

Hemi-Isoindigo Polymers and Oligomers for Temperature Sensing Applications

by

John Polena

A thesis

presented to the University of Waterloo

in fulfillment of the

thesis requirement for the degree of

Master of Applied Science

in

Chemical Engineering

Waterloo, Ontario, Canada, 2021

© John Polena 2021

Author's Declaration

I hereby declare that I am the sole author of this thesis. This is a true copy of the thesis, including any required final revisions, as accepted by my examiners. I understand that this work may be made electronically available to the public.

Abstract

Organic semiconductors are extensively used for electronic applications such as OFETs and OPVs due to their low-cost and well-defined manufacturing processes. This includes vacuum deposition, solution processing, and roll-to-roll printing mainly for the production of electronics on flexible substrates. Organic semiconductor-based sensors have garnered much attention from the scientific community for a wide range of applications including point-of-care diagnostics, artificial skin, microfluidic monitoring, wastewater treatment, etc. Organic temperature sensors are of great interest in the medical field, specifically for vital signal monitoring where accurate temperature determination is imperative for the diagnosis and treatment of a patient. Besides that, other important parameters such as humidity, pH, etc. may have an inherent temperature dependence, hence sensors for said parameters must also include a way of determining and correcting for the environmental temperature. Organic materials, including small molecules and polymers, have demonstrated promising results for temperature monitoring but these materials often require the introduction of dopants to achieve sufficient conductivity. The resulting sensor devices still suffer from poor long-term stability, low selectivity, low reversibility, and solution-processable films often require the use of toxic chlorinated solvents which damage the environment.

This thesis work aims to overcome the issues of poor long-term stability and the use of toxic chlorinated solvents by developing novel donor-acceptor hemi-isoindigo copolymers and hemi-isoindigo oligomers to fabricate sensors for real-time temperature monitoring. This work reports several strategies to achieve these goals including:

- i. Introducing functional groups on the thiophene unit of the hemi-isoindigo structure to improve sensor performance and dopant complex stability
- ii. Using thermally removable sidechains instead of aliphatic chains to improve electronic properties while maintaining solubility
- iii. Using well-defined oligomeric structures to improve the processability of the hemi-isoindigo material in less toxic solvents

First, the synthesis of three hemi-isoindigo donor-acceptor copolymers **PEEhB**, **PMEhB**, and **PTEhB** utilizing a **DDOBT** donor unit are reported. The polymers are doped with **F4TCNQ**, and the resulting films are used to fabricate temperature sensors on flexible PET substrates with TCRs

of $-1.09\%/^{\circ}\text{C}$, $-1.09\%/^{\circ}\text{C}$, and $-1.02\%/^{\circ}\text{C}$ respectively. While these TCR values indicate good sensitivity, the complexes formed using the **PTEhB** and **PMEhB** crystalline polymers are not stable after four and twelve days, respectively. Conversely, the amorphous polymer **PEEhB**, with the highest E_{HOMO} , forms a complex stable for over thirty-two days and has a significantly wider working range (25-120 $^{\circ}\text{C}$) than the other two polymers (25-60 $^{\circ}\text{C}$) which suggests it is a promising candidate for real-time temperature sensing applications.

Then, the hemi-isoindigo structure was converted from polymers to two oligomers. **OG-D1**, derived from the **M1** monomer structure of **PEEhB**, and **OG3**, derived from the **M3** monomer structure of **PTEhB**. **OG-D1**, which is essentially a dimer of the **M1** structure, utilizes thermally cleavable carbamate sidechains. These may be removed under moderate conditions which should lead to better coplanarity, and thus impart advantageous electronic properties in the oligomer film. Once annealed the resulting film, which is renamed **OG-D1_A**, has a significantly lower E_{HOMO} (-5.16 eV) than the three HID polymers. This material doped with **F4TCNQ** yielded a sensor with good sensitivity (TCR = $-1.39\%/^{\circ}\text{C}$) and working range (25-120 $^{\circ}\text{C}$) comparable to that of **PEEhB** due to the removal of sidechains impeding the formation of insulating regions. However, the conductivity of the material drops over 80% in four days signaling poor complex stability. **OG3** utilizes the same **DDOBT** donor unit as the polymers between two **M3** acceptor units. The corresponding device using **F4TCNQ** has a TCR of $-2.66\%/^{\circ}\text{C}$, significantly better than the previous devices which should be due to a different mechanism of charge transport, but a narrower working range (25-55 $^{\circ}\text{C}$). This film conductivity also drops within four days but not as dramatically as the **OG-D1_A** device. To take advantage of the oligomeric nature of this material, it is then dispersed in isopropanol with **PSS** dopant and the corresponding film is moderately conductive ($5.34 \times 10^{-4}\text{ S/cm}$) as conceptual proof for fabricating conductive films using these materials without the need for toxic solvents.

Acknowledgements

I would like to thank my supervisor, Prof. Yuning Li for welcoming me into his research group and giving me the opportunity to complete this work. His knowledge and expertise have been invaluable to helping me develop as a researcher and of course assisting with the completion of my thesis. His valuable advice and guidance throughout my graduate studies helped me to become a better researcher and prepare me for a future working in the organic electronics industry.

I would also like to thank Prof. Ahmad Ghavami and Prof. Neil McManus of the Nanotechnology Engineering program at the University of Waterloo. I am grateful to them for allowing me to TA their laboratory courses continuously throughout my graduate studies as well as for their valuable advice and comradery.

I want to extend a special thank you to my colleague Jenner Ngai for all his guidance throughout this whole process. His contributions included XRD testing, AFM testing, general training on device fabrication and characterization techniques. The patience, advice, and assistance he provided for me throughout the more than two years that I spent conducting this research was incredibly helpful and for that I am indebted to him.

I would like to thank Janet Venne from NMR facility in the Chemistry Department at the University of Waterloo for allowing me the use of the NMR machine to confirm compound purity. I would also like to thank Dr. Haitao Liu from Henan Academy of Sciences in Zhengzhou, Henan, China for conducting the HT-GPC experiments on the polymeric materials cited in this work.

Also, I would like to recognize all my other colleagues in the PEML group Dr. Zhong Ma, Dr. Keqiang He, Xiguang Gao, Pankaj Kumar, Yi Yuan, Wuqi Li, Chenyang Guo, Danial Afzal, Zhaoyi Yin, and Yunsheng Jiang for helping me with experiments and analyses. I would like to acknowledge them as well as other members of the group during my time in graduate school for their support and friendship over these last two years.

I would like to thank my committee members, Prof. Yuning Li, Prof. Eric Croiset, and Prof. Ting Tsui for taking the time to review this work and participate in the oral defence.

This research presented in this work was financially supported by the Natural Sciences and Engineering Research Council (NSERC), specifically their Green Electronics Network (GreEN).

Lastly, I want to extend a thank you to my family including my parents Koco and Viktori Polena, as well as my brother Enio Polena. Without the support they provided me over my time at the University of Waterloo, completing this work would not have been possible.

Table of Contents

Author's Declaration	ii
Abstract.....	iii
Acknowledgements	v
List of Figures.....	ix
List of Tables	xiii
List of Abbreviations	xiv
List of Symbols.....	xv
Chapter 1: Introduction.....	1
1.1 Overview of Organic Temperature Sensors	1
1.2 Structure of Organic Temperature Sensor Devices	4
1.3 Working Principles of Organic Temperature Sensor Devices.....	6
1.4 Donor-Acceptor Principles	7
1.5 Doping Mechanism	9
1.6 Thesis Objective and Summary	12
Chapter 2: Synthesis, Characterization, and Performance of HID Polymers.....	14
2.1 Introduction	14
2.2 3,3'-Bis(dodecyloxy)-2,2'-bithiophene (DDOBT) Monomer	18
2.2.1 3,3'-Bis(dodecyloxy)-2,2'-bithiophene (DDOBT) Molecular Design	18
2.2.2 Structures and Energy Levels Simulation by Density Functional Theory (DFT)	19
2.2.3 Synthesis of 3,3'-Bis(dodecyloxy)-2,2'-bithiophene (DDOBT) Monomer	22
2.3 Hemi-Isoindigo (HID) Monomers M1, M2, and M3	22
2.3.1 Hemi-Isoindigo (HID) Monomers Molecular Design	22
2.3.2 Structures and Energy Levels Simulation by Density Functional Theory (DFT)	23
2.3.3 Synthesis of HID Monomers with Alkyl Sidechains	28
2.4 Synthesis and Characterization of HID Polymers PEEhB, PMEhB, PTEhB.....	29
2.4.1 Synthesis of HID Polymers	29
2.4.2 Characterization of HID Polymers by HT-GPC, UV-Vis-NIR Spectroscopy, CV, DSC, AFM, and XRD	30
2.4.3 Temperature Sensing Performance of HID Polymer Devices.....	53
2.5 Summary and Future Directions.....	58
2.6 Experimental Section.....	60

2.6.1	Materials and Characterization	60
2.6.2	Fabrication of Temperature Sensor Devices	62
2.6.3	Synthesis Procedures	64
Chapter 3: Synthesis, Characterization, and Performance of HID Oligomers		77
3.1	Introduction	77
3.2	3,3'-((2,2',3,3'-tetrahydro-[5,5'-bithieno[3,4-b][1,4]dioxine]-7,7'- diyl)bis(methaneylylidene))-bis(2-oxoindoline-1-carboxylate) Dimer (OG-D1)	80
3.2.1	3,3'-((2,2',3,3'-tetrahydro-[5,5'-bithieno[3,4-b][1,4]dioxine]-7,7'- diyl)bis(methaneylylidene))-bis(2-oxoindoline-1-carboxylate) Molecular Design	80
3.2.2	Structure Simulation by Density Functional Theory (DFT).....	80
3.2.3	Synthesis of 3,3'-((2,2',3,3'-tetrahydro-[5,5'-bithieno[3,4-b][1,4]dioxine]-7,7'- diyl)bis(methaneylylidene))-bis(2-oxoindoline-1-carboxylate)	82
3.2.4	Characterization of OG-D1 by UV-Vis-NIR and CV	84
3.2.5	Temperature Sensing Performance of OG-D1	90
3.3	3,3'-((3'',4'-bis(dodecyloxy)-[2,2':5',2'':5'',2'''-quaterthiophene]-5,5'''- diyl)bis(methaneylylidene))bis(1-(2-ethylhexyl)indolin-2-one) (OG3).....	94
3.3.1	3,3'-((3'',4'-bis(dodecyloxy)-[2,2':5',2'':5'',2'''-quaterthiophene]-5,5'''- diyl)bis(methaneylylidene))bis(1-(2-ethylhexyl)indolin-2-one) Molecular Design	94
3.3.2	Structure Simulation by Density Functional Theory (DFT).....	94
3.3.3	Synthesis of 3,3'-((3'',4'-bis(dodecyloxy)-[2,2':5',2'':5'',2'''-quaterthiophene]-5,5'''- diyl)bis(methaneylylidene))bis(1-(2-ethylhexyl)indolin-2-one)	96
3.3.4	Characterization of OG3 by UV-Vis-NIR and CV	97
3.3.5	Temperature Sensing Performance of OG3	101
3.3.6	OG3:PSS Dispersion Results	105
3.4	Summary and Future Directions.....	108
3.5	Experimental Section.....	111
3.5.1	Materials and Characterization.....	111
3.5.2	Fabrication of Temperature Sensor Devices	111
3.5.3	Synthesis Procedures	112
Chapter 4: Conclusions and Direction for Future Work		118
4.1	Conclusions	118
4.2	Future Work.....	119
Bibliography		122
Appendix A		136

List of Figures

Figure 1-1: Architecture of bottom-contact interdigitated electrode design with both long and short channels.	5
Figure 1-2: Literature reported (a) donor and (b) acceptor units for organic electronics.....	8
Figure 1-3: (a) D-A bilayer junction and corresponding energy band diagram, (b) ideal morphology of D-A bulk heterojunction and corresponding energy band diagram.....	9
Figure 1-4: Chemical structures of F4TCNQ and PSSA dopants used in this work.....	10
Figure 1-5: Energy level diagram illustrating the electron transfer mechanism from polymer to dopant as is conventional of p-type semiconductor doping.	11
Figure 1-6: Counterion interaction between a short PEDOT chain with the PSS dopant chain showing the sulfur cations in the resonance structure interacting with oxygen anions from the sulfonate groups ⁸⁷	12
Figure 2-1: Various conformations of the functionalized thiophene dimers that can be extrapolated into a polymer chain.	14
Figure 2-2: Chemical structure of (a) isoindigo and its four most common derivatives (b) halogenated isoindigo, (c) heterocycle-substituted isoindigo, (d) peripherally expanded isoindigo, and (e) core-expanded isoindigo.	18
Figure 2-3: (a) Geometry of BT optimized by DFT simulation in Gaussian software, (b) HOMO/(c) LUMO orbitals of the BT and the DFT calculation of the orbital energy levels with respect to vacuum (0 eV).....	20
Figure 2-4: (a) Geometry of DDOBT optimized by DFT simulation in Gaussian software, (b) HOMO/(c) LUMO orbitals of the DDOBT and the DFT calculation of the orbital energy levels with respect to vacuum (0 eV).....	21
Figure 2-5: Chemical structures of HID monomers M1 , M2 , and M3	23
Figure 2-6: (a) Geometry of M1 optimized by DFT simulation in Gaussian software, (b) HOMO/(c) LUMO orbitals of the M1 and the DFT calculation of the orbital energy levels with respect to vacuum (0 eV).....	25
Figure 2-7: (a) Geometry of M2 optimized by DFT simulation in Gaussian software, (b) HOMO/(c) LUMO orbitals of the M2 and the DFT calculation of the orbital energy levels with respect to vacuum (0 eV).....	26

Figure 2-8: (a) Geometry of M3 optimized by DFT simulation ins Gaussian software, (b) HOMO/(c) LUMO orbitals of the M3 and the DFT calculation of the orbital energy levels with respect to vacuum (0 eV).....	27
Figure 2-9: Molecular weight distributions of (a) PEEhB , (b) PMEhB , (c) PTEhB from HT-GPC at 150 °C with 1,2,4-trichlorobenzene as the eluent.	32
Figure 2- 10: UV-Vis-NIR spectra of PEEhB in solution, as a film, and as a doped film.....	36
Figure 2-11: UV-Vis-NIR spectra of PMEhB in solution, as a film, and as a doped film.....	36
Figure 2-12: UV-Vis-NIR spectra of PTEhB in solution, as a film, and as a doped film.....	37
Figure 2-13: The CV trace of (a) PEEhB , (b) PMEhB , (c) PTEhB at a scan rate of 0.1 V/s in 0.1 M tetrabutylammonium hexafluorophosphate with anhydrous acetonitrile as the solvent.	38
Figure 2-14: Energy level diagram depicting the relative E_{HOMO} and E_{LUMO} of PEEhB , PMEhB , PTEhB , and the F4TCNQ dopant with respect to vacuum (0 eV).	39
Figure 2-15: Benzodithiophene donor and benzothiadiazole acceptor copolymers with a) DMT sidechains and b) EDOT side chains on the donor. ^{137,138}	40
Figure 2-16: The DSC analysis of (a) PEEhB , (b) PMEhB , and (c) PTEhB at a heating cooling rate of 10 °C min ⁻¹ under nitrogen atmosphere between -20 °C and 200 °C.	42
Figure 2-17: AFM images (4 μm x 4 μm) indicating relative height on films of PEEhB spin-coated on DDTS-modified SiO ₂ /Si substrates and annealed at RT, 100 °C, 150 °C, and 200 °C respectively.....	44
Figure 2-18: AFM images (4 μm x 4 μm) indicating relative height on films of PMEhB spin-coated on DDTS-modified SiO ₂ /Si substrates and annealed at RT, 100 °C, 150 °C, and 200 °C respectively.....	45
Figure 2-19: AFM images (4 μm x 4 μm) indicating relative height on films of PTEhB spin-coated on DDTS-modified SiO ₂ /Si substrates and annealed at RT 100 °C, 150 °C, and 200 °C respectively.....	46
Figure 2-20: The root-mean-square surface roughness (R_q) of PEEhB , PMEhB , and PTEhB at each different T_a	47
Figure 2-21: (a) One-dimensional and (b) two-dimensional XRD spectra of PEEhB film on DDTS-modified SiO ₂ /Si substrate annealed at RT, 100 °C, 150 °C, and 200 °C respectively.....	50
Figure 2-22: (a) One-dimensional and (b) two-dimensional XRD spectra of PMEhB film on DDTS-modified SiO ₂ /Si substrate annealed at RT, 100 °C, 150 °C, and 200 °C respectively.	51

Figure 2-23: (a) One-dimensional and (b) two-dimensional XRD spectra of PTEhB film on DDTS-modified SiO ₂ /Si substrate annealed at RT, 100 °C, 150 °C, and 200 °C respectively.	52
Figure 2-24: (a) Real-time current vs time (I-t) graph of PEEhB:F4TCNQ device at varying temperatures, (b) current vs adjusted absolute temperature (I-T ^{-0.25}) graph of PEEhB:F4TCNQ interdigitated device.	54
Figure 2-25: (a) Real-time current vs time (I-t) graph of PMEhB:F4TCNQ device at varying temperatures, (b) current vs adjusted absolute temperature (I-T ^{-0.25}) graph of PMEhB:F4TCNQ interdigitated device.	55
Figure 2-26: (a) Real-time current vs time (I-t) graph of PTEhB:F4TCNQ device at varying temperatures, (b) current vs adjusted absolute temperature (I-T ^{-0.25}) graph of PTEhB:F4TCNQ interdigitated device.	55
Figure 2-27: Normalized resistance vs temperature plots for TCR determination of sensor devices fabricated using (a) PEEhB:F4TCNQ , (b) PMEhB:F4TCNQ , and (c) PTEhB:F4TCNQ	56
Figure 2-28: Conductivity vs. time stability of PEEhB:F4TCNQ , PMEhB:F4TCNQ , and PTEhB:F4TCNQ	58
Figure 2-29: Process flow schematic for the blade-coating preparation of the doped HID polymer films onto the flexible PET/Ag substrates provide by the NSERC Green Electronics Network (GreEN).	63
Figure 3-1: Conjugated oligomer materials used in organic electronics; (a) simple α -sexithiophene, (b) DBP- α -6T ¹⁵⁸ , (c) BT ₂ B ¹⁵⁹ , (d) the family of methylsulphanyl substituted α -6T oligomers ¹⁵⁷ , (e) trifluoromethylphenyl substituted bithiazole ¹⁵² , (f) X-shaped anthracene oligomer ¹⁶¹ , (g) heteroatom-bridged oligophenylene ¹⁶⁰	79
Figure 3-2: (a) Geometry of OG-D1_A optimized by DFT simulation in Gaussian software, (b) HOMO/(c) LUMO orbitals of the OG-D1_A and the DFT calculation of the orbital energy levels with respect to vacuum (0 eV).	82
Figure 3-3: UV-Vis-NIR spectra for (a) OG-D1 in solution and as a thin film and (b) OG-D1_A as a thin film post annealing and doped with F4TCNQ dopant.	87
Figure 3-4: Energy level diagram depicting the relative E _{HOMO} and E _{LUMO} of OG-D1 , OG-D1_A and the F4TCNQ dopant with respect to vacuum (0 eV).	89
Figure 3-5: The CV trace of (a) OG-D1 and (b) OG-D1_A at a scan rate of 0.1 V/s in 0.1 M tetrabutylammonium hexafluorophosphate with anhydrous acetonitrile as the solvent.	90

Figure 3-6: (a) Real-time current vs time (I-t) graph of OG-D1_A:F4TCNQ device at varying temperatures, (b) current vs adjusted absolute temperature ($I-T^{-0.25}$) graph of OG-D1_A:F4TCNQ interdigitated device.	91
Figure 3-7: Normalized resistance vs temperature plots for TCR determination of sensor device fabricated using OG-D1_A:F4TCNQ	92
Figure 3-8: Conductivity vs. time stability of OG-D1_A:F4TCNQ	93
Figure 3-9: (a) Geometry of OG3 optimized by DFT simulation in Gaussian software, (b) HOMO/(c) LUMO orbitals of the OG3 and the DFT calculation of the orbital energy levels with respect to vacuum (0 eV).....	96
Figure 3-10: UV-Vis-NIR spectra of OG3 in solution, as a film, and as a doped film.	99
Figure 3-11: The CV trace of OG3 at a scan rate of 0.1 V/s in 0.1 M tetrabutylammonium hexafluorophosphate with anhydrous acetonitrile as the solvent.	100
Figure 3-12: Energy level diagram depicting the relative E_{HOMO} and E_{LUMO} of OG3 , OG-D1_A , PTEhB , and the F4TCNQ dopant with respect to vacuum (0 eV).	101
Figure 3-13: (a) Real-time current vs time (I-t) graph of OG3:F4TCNQ device at varying temperatures, (b) current vs adjusted absolute temperature ($I-T^{-0.25}$) three-dimensional VRH, (c) current vs adjusted absolute temperature ($I-T^{-0.5}$) one-dimensional VRH, (d) current vs adjusted absolute temperature ($I-T^{1/3}$) two-dimensional VRH graphs of OG3:F4TCNQ interdigitated device.....	103
Figure 3-14: Normalized resistance vs absolute temperature plots for TCR determination of sensor device fabricated using OG3:F4TCNQ	104
Figure 3-15: Conductivity vs. time stability of OG3:F4TCNQ	105
Figure 3-16: Real-time current vs time (I-t) graph of OG3:PSS device at varying temperatures.	107
Figure 3-17: Current response of OG3:PSS device when probed between -1 V to 1 V.	108
Figure 4-1: The original structure of OG-D1 and the structures of potential modifications that may yield enhanced properties for the corresponding doped film.	121

List of Tables

Table 2-1: DFT calculation results for both donors and all three acceptors.....	27
Table 2-2: Molecular weight distribution of the HID polymers PEEhB , PMEhB , and PTEhB from HT-GPC analysis.	30
Table 2-3: Summary of the UV-Vis-NIR spectroscopy results for PEEhB , PMEhB , and PTEhB showing the shifts in the absorbance λ_{\max} from solution to film to doped film and film λ_{onset}	37
Table 2-4: Summary of the molecular orbital energy levels of the HID polymers and the F4TCNQ dopant molecule along with E_T values.	39
Table 2-5: Summary of the calculated R_q for each AFM sample of the HID polymers.....	47
Table 2-6: Temperature sensing performance of the three devices fabricated on PET/Ag substrates using the HID polymers doped with F4TCNQ	56
Table 3-1: DFT calculation results for DDOBT , M1 , and OG-D1_A	82
Table 3-2: Summary of the UV-Vis-NIR spectroscopy results for OG-D1 and OG-D1_A showing the shifts in the absorbance λ_{\max} from solution to film to doped film and film λ_{onset}	88
Table 3-3: Summary of the molecular orbital energy levels of the OG-D1 , OG-D1_A , and the F4TCNQ dopant molecule along with E_T values.	89
Table 3-4: Temperature sensing performance of the PEEhB:F4TCNQ and OG-D1_A:F4TCNQ devices fabricated on PET/Ag substrates.	92
Table 3-5: DFT calculation results for OG3 , M3 , and OG-D1_A	96
Table 3-6: Summary of the UV-Vis-NIR spectroscopy results for OG3 showing the shifts in the absorbance λ_{\max} from solution to film to doped film and film λ_{onset}	99
Table 3-7: Summary of the molecular orbital energy levels of the OG3 , OG-D1_A , PTEhB , and the F4TCNQ dopant molecule along with E_T values.	101
Table 3-8: Temperature sensing performance of the OG3:F4TCNQ and OG-D1_A:F4TCNQ devices fabricated on PET/Ag substrates.	104
Table 3-9: Conductivity determination results and metrics for OG3:PSS device.	108

List of Abbreviations

α -6T: Alpha-sexithiophene	LUMO: Lowest unoccupied molecular orbital
1-D: One-dimensional	MTR: Multiple trapping and releasing
2-D: Two-dimensional	NBS: N-Bromosuccinimide
A-A: Acceptor-acceptor	NMR: Nuclear magnetic resonance
AFM: Atomic Force Microscopy	NO ₂ : Nitrogen dioxide
BDOPV: Benzodifuran-based oligo-p-phenylenevinylene	NTC: Negative temperature coefficient
CO ₂ : Carbon dioxide	OFET: Organic-field-effect transistor
CP: Conjugated Polymer	OLED: Organic light-emitting diode
CV: Cyclic voltammetry	OPV: Organic photovoltaic
D-A: Donor-acceptor	OSC: Organic solar cell
D-D: Donor-donor	P3HT: Poly(3-hexylthiophene)
DCE: 1,2-dichloroethane	PDI: Polydispersity index
DCM: Dichloromethane	PEDOT: Poly(3,4-ethylenedioxythiophene)
DFT: Density functional theory	PET: Polyethylene terephthalate
DI: Deionized	PMMA: poly(methyl methacrylate)
DMF: <i>N,N</i> -dimethylformamide	PSSA: Polystyrene sulfonic acid
DMT: 3,4-dimethoxythiophene	PSS: Polystyrene sulfonate
DOC: Degree of crystallinity	PT: Polythiophene
DPP: Diketopyrrolopyrrole	PTC: Positive temperature coefficient
DSC: Differential scanning calorimetry	PVDF: polyvinylidene fluoride
ECL: Effective conjugation length	PZT: Lead zirconate titanate
EDOT: Ethylenedioxythiophene	r.t: Room temperature
FET: Field-effect transistor	RT: Room temperature
HBr: Hydrobromic acid	Si: Silicon
HH: Head-to head	SiO ₂ : Silicon oxide
HID: Hemi-isoinidigo	TCR: Temperature coefficient of resistance
HOMO: Highest occupied molecular orbital	TFT: Thin-film transistor
HPLC: High-performance liquid chromatography	THF: Tetrahydrofuran
HT-GPC: High-temperature gel-permeation chromatography	TLC: Thin-layer chromatography
HT: Head-to-tail	TT: Tail-to-tail
ICT: Integer charge transfer	UV-Vis-NIR: Ultraviolet-visible-near-infrared
IPA: Isopropanol	VRH: Variable range hopping
ITO: Indium tin oxide	XRD: X-ray diffraction

Other abbreviations are defined in the text.

List of Symbols

σ : Conductivity	q : Elementary charge constant
σ_0 : Reference conductivity	R : Resistance
ΔT : Difference between temperature and reference temperature	R_0 : Resistance at reference temperature
c : Speed of light	R_{ij} : Separation between sites i and j
C-C: carbon-carbon single bond	R_q : Root-mean-square roughness parameter
C=C: carbon-carbon double bond	T : Temperature
E_a : Activation energy	t : Time
E_g : Bandgap Energy	T_α : Annealing temperature
E_{HOMO} : HOMO energy level	T_0 : Reference Temperature
E_{LUMO} : LUMO energy level	t_{10} : Recovery time
$E_{\text{ox}}^{\text{onset}}$: Oxidation onset potential	t_{90} : Response time
E_T : Trap energy	T_C : Crystallization temperature
h : Planck's constant	T_g : Glass transition temperature
I : Current	t_h : Thickness
I_D : Drain Current	T_m : Melting temperature
k : Boltzmann constant	V : Voltage
L : Length of the sensor channel	W : Total width of the sensor channel
m : Slope of the I/V curve	W/L : Width to length aspect ratio of interdigitated sensor
M_n : Number-average molecular weight	W_{ij} : Energy separation between sites i and j
M_w : Weight-average molecular weight	λ_{max} : Wavelength of incident light with maximum intensity
n : Electron carrier density	λ_{onset} : Onset wavelength of incident light
p : Hole carrier density	μ_h : hole mobility
P_{ij} : Probability of hopping between sites i and j	μ_n : electron mobility

Other symbols are defined in the text.

Chapter 1: Introduction

1.1 Overview of Organic Temperature Sensors

Organic materials consist of molecular compounds containing carbon-hydrogen bonds and may include other elements such as nitrogen or oxygen. The atoms in these molecules are held together by covalent bonds which allows them to share valence electrons. Therefore, most of these organic materials are electrical insulators due to their highly localized valence electrons. However, organic semiconductors contain extended π -conjugated systems normally composed of alternating C-C and C=C bonds. The hybridization of the molecular orbitals in these systems forms an extended highest occupied molecular orbital (HOMO) and lowest unoccupied molecular orbital (LUMO). These extended orbitals allow injected charge carriers (electrons in the HOMO and holes in the LUMO) to move relatively easily. These organic materials are held together by weak van der Waals or London dispersion forces which leads to a large intermolecular distance. Therefore, intermolecular charge transport in these systems is more difficult than intramolecular charge transport. For high molecular weight polymers, long-range π -conjugation leads to a band-like structure which reduces the bandgap of the material to rival that of typical inorganic semiconductors. These materials may also be doped with small amounts of inorganic or organic dopants to amplify the charge transport and increase the conductivity of the corresponding film.

A sensor is defined as a device which detects or measures a specific physical property and records, indicates, or otherwise responds to it. Organic-based sensing technologies have continuously evolved over time to introduce new devices that interact with environmental conditions including, but not limited to, humidity¹⁻³, target chemical concentration⁴⁻⁷, and pressure^{8,9} to allow for accurate detection of these parameters. However, temperature determination remains of the most common and arguably the most important application of organic environmental sensors. While being able to determine temperature is crucial for a variety of applications, many other environmental factors, such as humidity and pressure, inherently have their own temperature dependence¹⁰ hence, accurate temperature determination is also imperative to resolving these signals. Temperature sensing is of most interest in the medical field for vital signal monitoring. Humidifiers and ventilators require temperature monitoring to provide a comfortable breathing

situation and reduce sore throats caused by cold dry air¹¹. Essential procedures such as hemodialysis require very accurate temperature monitoring as active body temperature control improves tolerance in hypotension prone patients¹². Therapeutic hypothermia treatment is another example where temperature regulation and modulation are critical for the preservation of brain function in victims of cardiac arrest¹³. More recently the development of artificial skin or e-skin has become a very popular area of research. To effectively simulate skin, these new technologies require temperature sensing capabilities and multiple literature sources cite this application as the motivation behind their temperature sensor design¹⁴⁻¹⁸. Various groups have published works which include sensors that show excellent spatial resolution^{18,19}, high flexibility^{14,18,20-25}, and even the functionality to resolve environmental stimuli independently from one another¹⁴.

Early works involving organic temperature sensors started by depositing the active layer material between metal interdigitated electrodes to maximize the contact area^{26,27}. These types of configurations for resistive-type sensors are commonly referred to as thermistors. Conjugated polymers (CPs) are now popular candidates for electronics as they can be easily functionalized to tune properties such as bandgap energy (E_g) or solubility²⁸⁻³⁰. Once these CPs began showing promise as active layers for electronics, common semiconducting materials such as poly(3-hexylthiophene) (P3HT) became the focus of several organic electronic research publications including those focused on temperature sensors^{24,31}. Further studies were conducted showing that the temperature sensing properties of these organic materials could be enhanced by adding small amounts of both inorganic materials, such as silver nanoparticles^{19,23}, and organic materials, for example graphite¹⁸, to synthesize active layer composites.

Several challenges remain in the temperature sensor design and fabrication. Sensors that use CPs as their active layer are known to have issues with long-term stability due to the polymer:dopant complex undergoing phase segregation, coupling of polymer polarons, and counterion coupling between polymer and dopant³². All these phenomena reduce the number of polarons and consequently reduce the conductivity of the sensor over time. This means that these devices need to be replaced frequently which can be expensive and impractical. The choice of dopant for these polymer devices is also important as certain commonly used dopant materials are responsive to other environmental stimuli which may distort the signal of the device leading to inaccurate

measurements^{33,34}. Lastly, the fabrication of these devices using CPs often requires the use of halogenated solvents such as chloroform or 1,2-dichlorobenzene. These solvents are known to be harmful to the environment and thus the development of sensor materials that are solution processable in environmentally friendly solvents is a crucial area of research going forward^{35,36}.

Temperature sensors can be evaluated using a certain set of standardized metrics. Thermal sensitivity of the organic devices can be calculated using the temperature coefficient of resistance (TCR) which is defined as relative change in resistance per degree Celsius (Kelvin) and may be determined using **Equation (1-1)**:

$$TCR = \frac{R - R_0}{R_0} \times \frac{1}{\Delta T} \times 100\% \quad (1-1)$$

where R represents the resistance at a given temperature, and R₀ is a known resistance at a reference temperature with ΔT being the difference between the two temperatures³⁷. The response and recovery times of a sensor may also be used to determine if the device is suitable for certain applications that incur frequent temperature fluctuations. The response time (t₉₀) is denoted by the time taken, in seconds, for the device response to reach 90% of the final value upon application of a step pulse. The time required for the device to return to 10% of the final value upon removal of the step pulse is the recovery time (t₁₀)³⁸. Lastly, the time stability of the temperature sensor is measured by cycling a potential bias from -1 V to 1 V and assessing the current response. The slope of the current along with the dimensions of the sensor device and thickness of the film can be used to determine the conductivity of the device via **Equation (1-2)**:

$$\sigma = \frac{m \times L}{t_h \times W} \quad (1-2)$$

where m is the slope of the current response from the generated curve in A/V, L is the length of the sensor channel, W is the total width of the sensor channel, and t_h is the measured thickness of the active layer film. Repeating this measurement periodically over the course of a predetermined

time frame and then normalizing the conductivity to establish if and how quickly any conductivity loss has occurred allows one to evaluate the time stability of the device. In the context of this work, the time stability of the thermistor is dependent on the polymer/oligomer:dopant complex.

1.2 Structure of Organic Temperature Sensor Devices

The architecture of an interdigitated electrode temperature sensor can be seen in **Figure 1-1**. The first instance of this type of interdigitated structure is found in the patent by N. Tesla from 1891 where the electrodes were submerged in an insulating liquid and the overall capacitance of the proposed electrical condenser increased with increasing number of plates³⁹. In the 1960s this type of interdigitated design became popular for sensing techniques taking advantage of the high contact area design. The devices were used for rather complex sensing applications such as electric field sensing, magnetic field sensing, and acoustic sensing⁴⁰⁻⁴².

Common features of these types of designs include one-sided access which is especially advantageous for non-destructive testing sensors and pizeoacoustic transducers since only a single side is required to interact with the test material⁴³. In certain situations, the other side of the material of interest may be inaccessible due to design limitations and one-sided access becomes essential for device functionality. The signal strength is easily tuned in these types of devices by changing the area of the sensor, altering the number of fingers, or shifting spacing between them⁴³. This allows for optimizing the trade-off between the signal-to-noise ratio and the miniaturization of the device. For complex sensing applications such as electrical or acoustic interactions, an interdigitated electrode design can greatly simplify the modelling because it may be simulated as two-dimensional (2-D) which significantly decreases computational time⁴³.

The choice of substrate for these devices is application dependent. Rigid substrates such as silicon, G10 fiberglass circuit boards, or lead zirconate titanate (PZT) ceramics are suitable when a well-defined geometry must be maintained^{44,45}. Flexible substrates such as Teflon, Kapton, polyethylene terephthalate (PET), or Kynar (PVDF) are used when the sensor is required to conform to a target surface such as human skin^{46,47}. It is worth noting that the hydrophilicity of the substrate must also be considered during sensor design. Moisture absorption can cause swelling in

certain substrate materials which alters the signal of the sensor and hence, for direct measurements of bulk material hydrophobic substrates are used. Conversely, measuring moisture in liquid materials is accomplished by using a hydrophilic substrate and correlating the changes in substrate properties to the moisture levels of the system once equilibrium is reached⁴³.

With regards to the active layer coating for these sensors the requirements are application specific. One general requirement is that the material selected should not undergo any irreversible changes which is referred to as film poisoning⁴⁸. This poisoning will reduce the reliability and lifetime of the sensor. If the device is going to be in ambient air conditions, further protection of the coating maybe achieved by adding an electrically neutral layer on top of the film as a protective layer, high molecular weight poly(methyl methacrylate) (PMMA) is an excellent candidate for this. The final aspect of this type of sensor design is the electrode material choice and fabrication technique. Conductive metals like silver and gold are most frequently used as electrode layers for these devices often deposited via screen-printing to ensure intimate contact between electrode and substrate⁴⁹. Other methods of depositing the electrode material include electron beam deposition which has the advantage of controlling film thickness and deposition rate⁵⁰ or electroplating is also an option if excellent surface uniformity is a necessary requirement⁵¹.

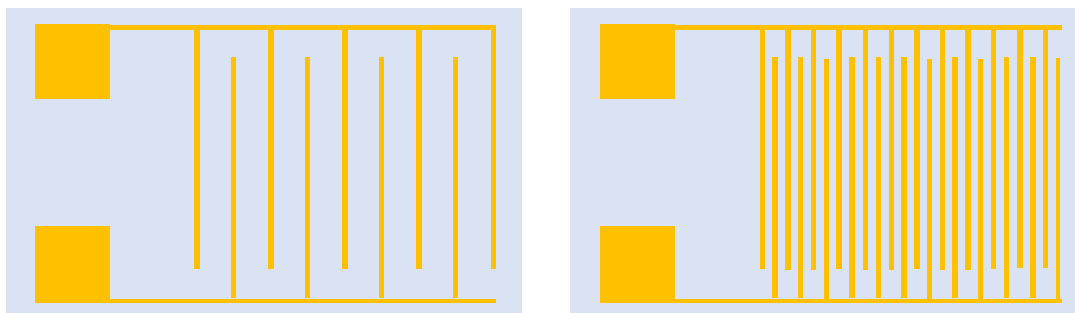


Figure 1-1: Architecture of bottom-contact interdigitated electrode design with both long and short channels.

For the purposes of this work, the sensor design aims to maximize contact area of the electrode with the organic material that is deposited inside of the channel. The aspect (W/L) ratio of the channel directly impacts the sensitivity of the device as it determines the surface contact area of the electrodes and the active layer. A higher aspect ratio increases the contact surface between the active material and the electrode which should yield a more conductive device⁵². However, since

channel dimensions are on the micrometer scale, capillary forces must be considered and thus depending on the active material and solvent used for fabrication there is a limit to how narrow the channels can be. After a certain critical aspect ratio these capillary forces may reduce the wettability of the device substrate with the active layer solution thus leading to a reduced conductivity in the deposited thin film.

1.3 Working Principles of Organic Temperature Sensor Devices

While there exist several types of temperature sensors, the two most common modes of operation utilizing organic materials are capacitive-type and resistive-type. In a capacitive sensor, the permittivity of the dielectric layer is temperature dependent and thus changes in temperature are detected by directly measuring the capacitance of the device^{53,54}. In this work, the focus is on resistive-type sensors hence the mechanism for these sensors will be discussed in greater detail. There are two common mechanisms that exist in these organic devices for temperature sensing, the variable-range hopping (VRH) mechanism and the multiple trapping and releasing (MTR) mechanism. Both are related to the simple governing conductivity equation which is shown in **Equation (1-3)**:

$$\sigma = q(n\mu_n + p\mu_p) \quad (1-3)$$

where σ is the conductivity, q is the elementary charge constant, n is the electron carrier density, p is the hole carrier density, and μ_n and μ_p are the electron and hole mobilities, respectively.

The MTR mechanism is often seen in field-effect transistor (FET) style temperature sensing devices where the semiconductor material is in contact with a dielectric layer. Dielectric engineering research has yielded promising results in improving the electronic properties of these transistors utilizing the MTR mechanism. The working principle involves the dielectric layer of the device inducing multiple charge traps of varying energy levels at the semiconductor/dielectric interface^{55,56}. These traps will decrease the carrier density and thus decrease the conductivity of the device measured via the drain current (I_D) response. Upon an increase in temperature, the

thermal excitation of these charge carriers is enough to release some of them from those traps and thus a higher I_D is observed as more charges are released with increasing thermal energy^{20,57,58}.

In this work, the VRH model is the proposed charge transport mechanism of the temperature sensitive active layer due to the excellent $I-T^{-0.25}$ fit observed in the results. Entropy laws dictate that a hopping electron will try to find the lowest activation energy (E_a) and the shortest hopping distance. Hence, probability of electron hopping from site i to site j will depend on both the spatial separation between the sites (R_{ij}) and the energy separation (W_{ij}). Mott showed that the probability of hopping between the two states (P_{ij}) can be modelled by **Equation 1-4**:

$$P_{ij} \sim \exp \left[-2\alpha R_{ij} - \frac{W_{ij}}{kT} \right] \quad (1-4)$$

This model proposes that thermal excitation of charge carriers increases the probability of hopping transport events occurring leading to enhanced charge carrier mobility⁵⁹⁻⁶¹. Both mechanisms described above are indicative of a positive current-temperature (I-T) correlation or rather a negative resistance-temperature (R-T) correlation. Hence, the organic active layer in this type of system is referred to as a negative temperature coefficient (NTC) material. Recent literature has shown that both the MTR and VRH mechanism can exist in the same device and that either of the two may be the dominant governing mechanism depending on the temperature range^{62,63}.

1.4 Donor-Acceptor Principles

Donor-acceptor (D-A) systems have been extensively researched in organic electronics due to the ease at which minor chemical alterations may tune their electronic properties for specific applications⁶⁴⁻⁶⁶. Most commonly, in photovoltaics, the engineering of the donor and acceptor units involves altering their HOMO and LUMO energy levels (E_{HOMO} and E_{LUMO}) leading to higher solar cell efficiency. Common donor materials used in the organic electronics field incorporate electron rich polythiophene derivatives. This includes the simple P3HT⁶⁷, triphenylamine (TPA) substituted polymers such as P3T-TPA, P3T-DDPTA, and PT5TTPA^{68,69}, as well as bithiophene donors such as DFDT⁷⁰. These donor materials may be combined with traditional acceptor units

include isoindigo derivatives such as IDIC⁷¹, Y6⁷², and ITIC⁷³, as well as pyridine and diazole based small molecules BX, BT, PX, PT⁷⁴ to improve the performance of organic electronics. The structures of some of these donor and acceptor materials are depicted in **Figure 1-2**.

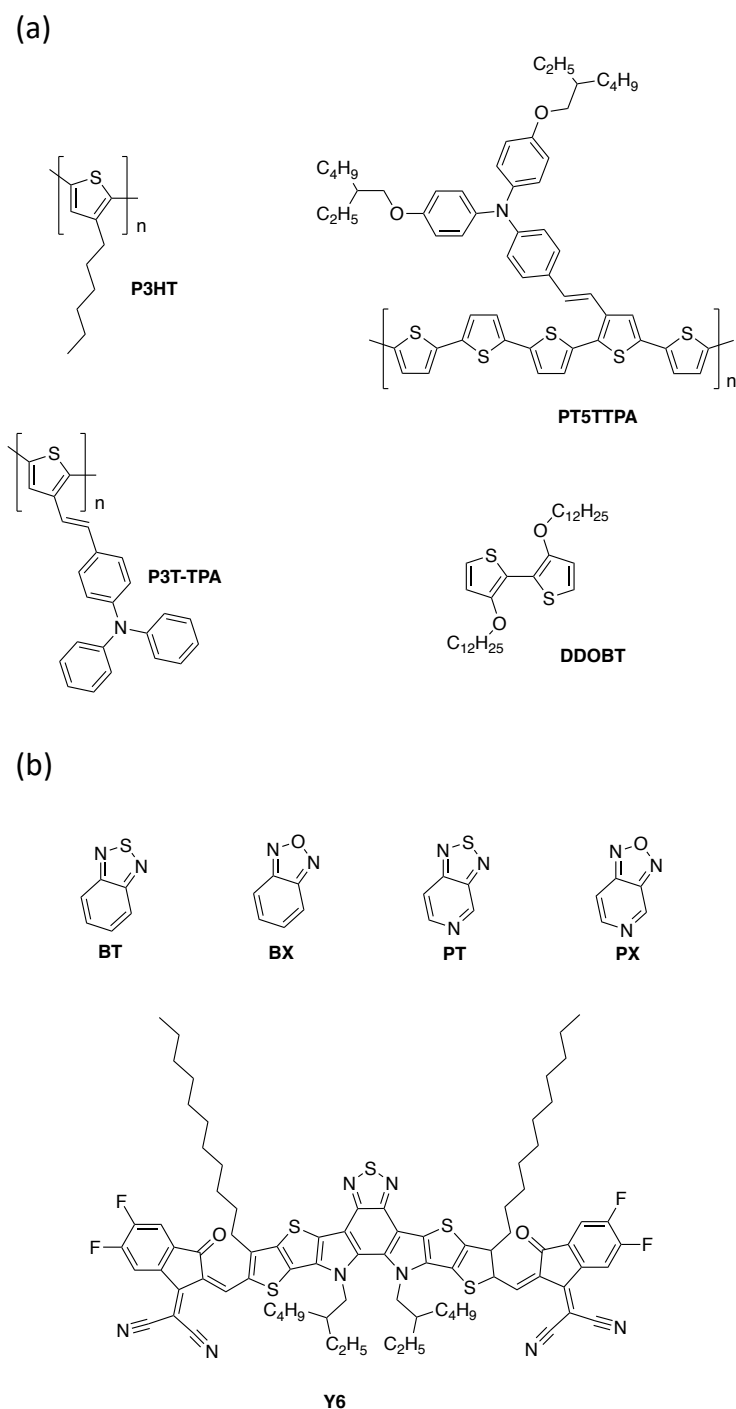


Figure 1-2: Literature reported (a) donor and (b) acceptor units for organic electronics.

The high E_{HOMO} of the donor and the low E_{LUMO} of acceptor work in combination to reduce the E_g of the copolymer. This is illustrated by the two models of D-A materials shown in **Figure 1-3** below. The bilayer structure incorporates both the donor and acceptor as individual materials stacked on top of one another and the resulting energy diagram illustrates an increased E_g . However, a more ideal morphology of a D-A system is the bulk heterojunction which would result in an energy diagram with a reduced E_g utilizing the E_{HOMO} of the donor and E_{LUMO} of the acceptor moiety⁷⁵.

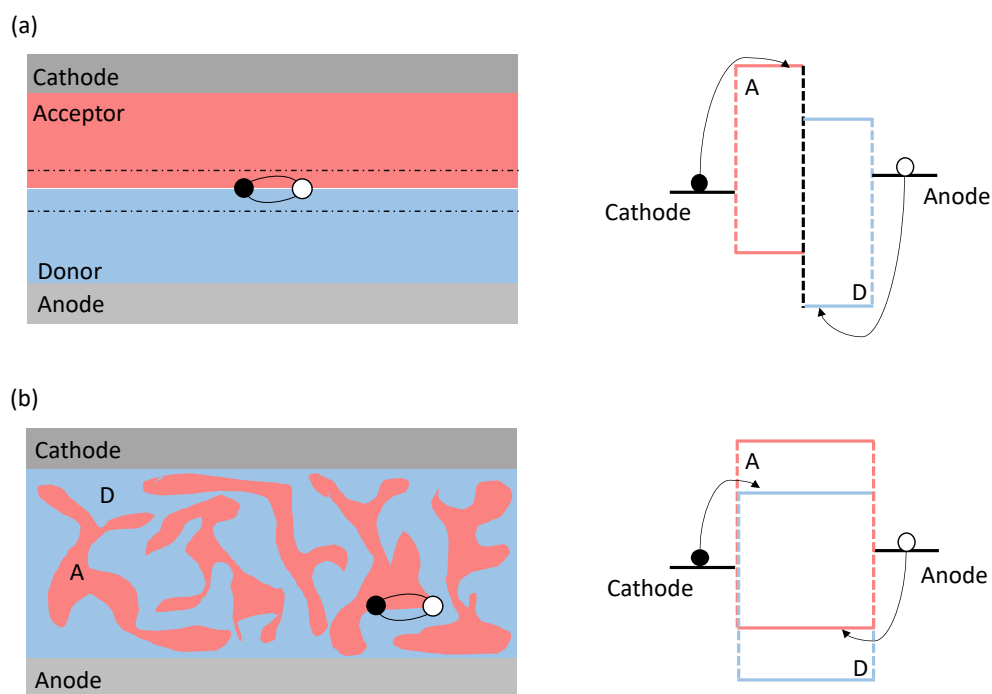


Figure 1-3: (a) D-A bilayer junction and corresponding energy band diagram, (b) ideal morphology of D-A bulk heterojunction and corresponding energy band diagram.

1.5 Doping Mechanism

In this work, two dopants are used to increase the conductivity of the polymers and oligomers. The two dopants in question are 2,3,5,6-tetrafluoro-7,7,8,8-tetracyanoquinodimethane (**F4TCNQ**) and polystyrene sulfonic acid (**PSSA**) the structures of which are shown in **Figure 1-4**.

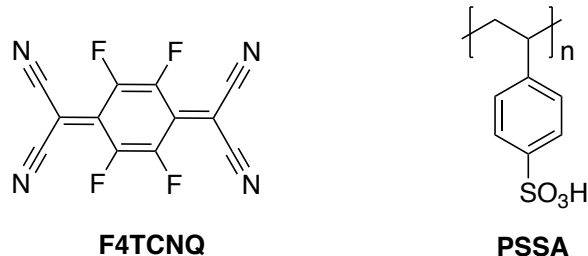


Figure 1-4: Chemical structures of **F4TCNQ** and **PSSA** dopants used in this work.

F4TCNQ as a p-type molecular dopant for CP electronics has received considerable attention with both solution coprocessing and sequential processing in both liquid and vapor phase⁷⁶⁻⁷⁸. In sequential processing, the polymer is left to solidify after deposition and the dopant is added either in solution or from the vapor phase to preserve the structure of the polymer film. For solution coprocessing the polymer and **F4TCNQ** are dissolved in the same solvent where polymer:dopant ion pairs readily form. However, this can lead to aggregates forming in the solution depending on the solvent which may reduce the conductivity of the film. To describe the doping mechanism of **F4TCNQ**, P3HT will be used as the reference polymer as numerous studies have used this polymer:dopant combination^{76,79,80}. The established physics state an integer charge transfer occurs from the E_{HOMO} of P3HT at ~ -4.8 eV and the E_{LUMO} of the **F4TCNQ** at ~ -5.2 eV^{79,81}. Electrons from the polymer E_{HOMO} may readily fall into the dopant E_{LUMO} to form charge carriers as is conventional for a p-type dopant and this is illustrated in the energy diagrams in **Figure 1-5**. Once the polarons are generated, basic semiconductor physics states that the charges are free to move through the lattice structure of the film thus increasing the conduction of the material. **F4TCNQ** is an excellent candidate for this type of doping due to its low E_{LUMO} since, theoretically, polymers with relatively high E_{HOMO} may be efficiently doped to form stable complexes^{82,83}.

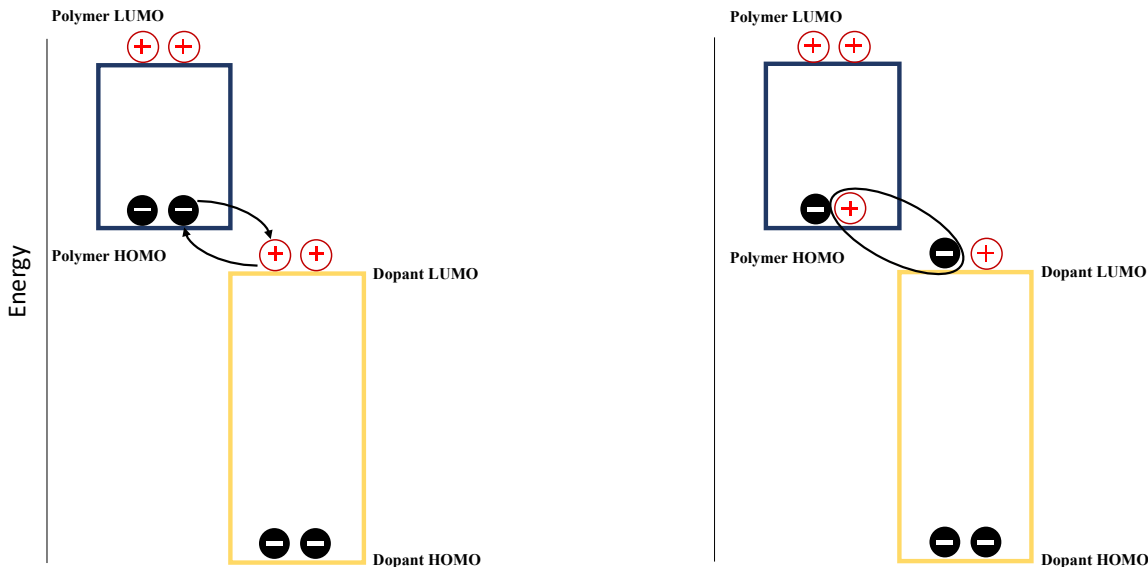


Figure 1-5: Energy level diagram illustrating the electron transfer mechanism from polymer to dopant as is conventional of p-type semiconductor doping.

The other dopant studied in this thesis work is **PSSA**, which ionizes into polystyrene sulfonate (**PSS**), and it is most referenced in conjunction with poly(3,4-ethylenedioxythiophene) (**PEDOT**) in **PEDOT:PSS** dispersions with hydrophilic solvents^{84–86}. The two polymers form an interpolymer complex that allows for a stable dispersion in water and then may be processed as a film using solution deposition techniques. Literature suggests that the negative charge carried by the sulfonate group on **PSS** building blocks interacts with the positive charge on the sulfur atom from resonance structures of **PEDOT** which is represented in **Figure 1-6**. Hence, the **PSS** not only acts as a dispersant for the **PEDOT** but also as a charge compensating counter polyanion. In literature studies E_{HOMO} and E_{LUMO} of **PEDOT** and **PEDOT:PSS** are compared by modelling a trimer and an eight-unit (8-mer) 3,4-ethylenedioxythiophene (**EDOT**) chain with a dimer and tetramer styrene sulfonate (**SS**) chain. The results show that the 8-mer **EDOT** chain has a E_g of 2.25 eV, and this is reduced to 1.09 eV when the dimer **SS** chain is introduced, then further reduced to 0.74 eV when the going from the dimer to tetramer **SS** chain⁸⁷. The studies also report that the E_{HOMO} is localized primarily on the **EDOT** portion whereas the E_{LUMO} is primarily localized on the **SS** portion and thus it can be visualized that an increase in ionic interaction between the two materials would lead to a reduced E_g . While this method is not the conventional route of doping semiconductors it is nonetheless effective and has the added benefit of potentially increasing the solubility of the organic polymer in hydrophilic, environmentally friendly solvents.

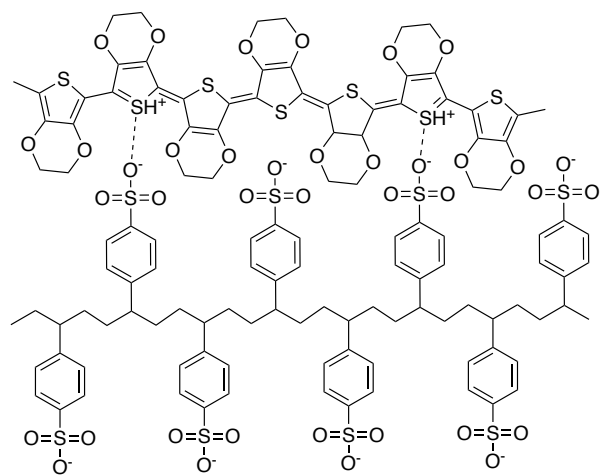


Figure 1-6: Counterion interaction between a short **PEDOT** chain with the **PSS** dopant chain showing the sulfur cations in the resonance structure interacting with oxygen anions from the sulfonate groups⁸⁷.

1.6 Thesis Objective and Summary

In this work, the issues of stability and processibility in environmentally friendly solvents for conjugated copolymer temperature sensing active materials are addressed. The stability of the device is dependent on polymer interaction with the dopant molecule and thus raising the E_{HOMO} level of the polymer should yield a more stable polymer:dopant complex. The crystallinity of the polymer and the effect thermal treatment has on the crystallinity of the material is also an important factor for the stability of the polymer:dopant complex. Higher degree of crystallinity (DOC) may serve to drive out dopant molecules from their lattice positions and thus destabilize the complex. Novel hemi-isoindigo (HID) materials are developed as the electron deficient acceptor monomers and are copolymerized with bithiophene donor units that include dodecyloxy chains at the β position of their structure to enhance the solubility and electron donating properties^{88,89}.

Here three HID copolymers are reported, each with different functionalities on the thiophene groups, and evaluated as temperature sensors. The monomers are alkylated with ethylhexyl groups to increase the solubility of the material for efficient polymerization. However, it is found that it is difficult to reach high molecular weights with these polymers as the HT-GPC results show that

the conjugation of the copolymers only extends to roughly up to 5.2 kDa. To improve the solubility in non-halogenated solvents two oligomers were synthesized using the same HID building blocks as the polymers but with a synthesis route that allows for better control of the final structure.

In chapter 2, the design and synthesis of the HID polymers **PEEhB**, **PMEhB**, and **PTEhB**, based on the monomers **M1**, **M2**, and **M3** is discussed. The three monomers are synthesized using the same route with each monomer having different functional groups on the β positions of the thiophene unit. The thiophene units are formylated on one side and a bromine group is added to the other side before a condensation reaction with an oxindole group forms the HID building block. An alkyl chain is added to improve the solubility of the material and each monomer is copolymerized with a bithiophene donor. The polymers are characterized using AFM, XRD, UV-Vis-NIR absorption spectroscopy, DSC, and CV. The polymers are deposited onto PET substrates with interdigitated silver electrodes and doped with **F4TCNQ** solution before being evaluated as temperature sensors.

Chapter 3 of this work discusses the transition from HID polymers to oligomers as initially, the donor unit is removed, and a similar synthesis route is taken to design an HID dimer unit **OG-D1**. The alkyl sidechain is replaced with the same length carbamate sidechain in an attempt to improve electronic properties and solvent processability. However, low solubility of intermediate reaction products leads to an inefficient synthesis procedure, so the donor unit is re-introduced to synthesize a similar structure as **PTEhB** but as an oligomer material with well-defined structure denoted as **OG3**. Both materials are evaluated as temperature sensors on a flexible PET substrate after being characterized by UV-Vis-NIR absorption spectroscopy and CV. While neither oligomer exhibits sufficient time-stability when processed as a film with the **F4TCNQ** dopant, **OG3** is dispersed with **PSS** in the environmentally friendly isopropanol (IPA) solvent. This dispersion produces a moderately conductive film as a proof of concept for **PSS** doping of these materials.

In chapter 4, the thesis findings are summarized, and conclusions are presented along with directions for future work and further study on this class of materials for sensor applications.

Chapter 2: Synthesis, Characterization, and Performance of HID Polymers

2.1 Introduction

Polythiophenes (PTs) have been extensively used as the donor entity of conjugated copolymers in electronics perhaps most frequently for organic photovoltaic (OPV) applications^{67,69,70}. The important characteristics of these types of polymers include:

- i. Easily tunable optical properties via early chemical modification
- ii. Solution processability for ease of manufacturing
- iii. Higher stability for OPV devices

The performance of these PTs and their derivatives is heavily dependent on the degree of π - π interactions between and within the polymer chains. In the case of an alkylated PT such as P3HT, polymerization without controlled coupling can lead to several different regioregular structures that impact the performance of the PT. This includes head-to-tail (HT), tail-to-tail (TT), and head-to-head (HH) orientations which are depicted in **Figure 2-1**⁹⁰⁻⁹².

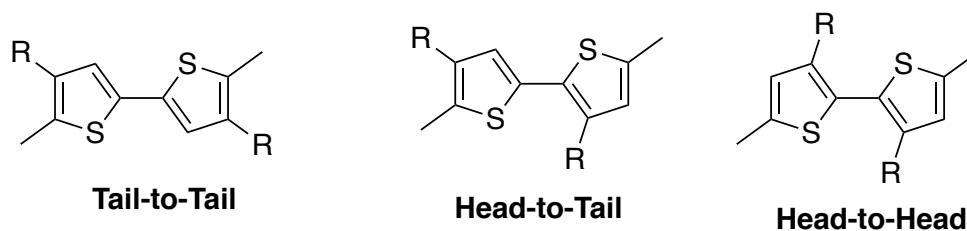


Figure 2-1: Various conformations of the functionalized thiophene dimers that can be extrapolated into a polymer chain.

More complex regioregularity occurs as the PT chain extends further but it is well understood that that HT orientation is preferred and displays the best performance in electronics⁹³. The functional R group on the thiophene unit may enhance the electrical properties of the polymer depending on its electron donating or electron withdrawing characteristics. The R groups may also introduce steric effects depending on their nature and this will impact the chain packing. This may alter the crystalline properties of thin films and can affect thin film transistor (TFT) and OPV charge carrier performance.

Functionalizing the thiophene unit with a long alkyl or alkoxy sidechains will improve the solubility of the material however, the polymer chains may stack further away from each other with increasing alkyl/alkoxy sidechain length. This can lead to increased steric hinderance which interrupts chain packing and the lamellar spacing of the polymer chains which may reduce the charge mobility⁹⁴. The sidechain can also impact the crystallinity of the thin film. Shorter sidechains may induce steric hinderance and reduce the crystallinity. However, a longer sidechain may be able to cocrystallize with the main chain and increase the overall crystallinity of the polymer⁹⁵. Generally speaking, a high degree of crystallinity (DOC) is advantageous for enhancing charge carrier mobility in OPV and OFET applications^{96,97}. Another benefit of adding alkyl or alkoxy chains is that they are electron donating moieties of the material, this is especially important when synthesizing copolymers as this will raise the E_{HOMO} of the polymer thus narrowing the E_g ^{94,98}. Lastly, these sidechains may also induce a steric effect during the polymerization step which may prevent α - α and α - β coupling of thiophene moieties and reduce the defects within the polymer chain³⁶.

Isoidindigo-based polymers have been excellent candidates for optoelectronics as they exhibit exceptional color control, flexibility, and long-term stability^{99,100}. The structure of an isoidindigo unit, which is shown in **Figure 2-2**, consists of two lactam rings fused to a benzene ring that are connected via an exocyclic double bond at the 3 and 3' positions. Smart windows, optical displays, and camouflage are examples of applications for these pigment polymers¹⁰¹⁻¹⁰³. Traditional acceptors will often make use of highly electronegative heteroatoms such as nitrogen or oxygen along with electron-accepting functional groups like esters or amides to receive electrons from donor materials. Over the years, research has picked up on these type of acceptor units and the copolymers of isoidindigo and oligothiophenes have become popular isoidindigo-based semiconductors for OPV applications.

Isoidindigo materials can generally be categorized into 5 categories, standard, halogenated, heterocycle-substituted, peripherally expanded, and core-expanded all of which are shown in **Figure 2-2**¹⁰⁴. It should also be noted that the nitrogen atom on the lactam ring is an important characteristic of these materials. That position is readily functionalized and thus, is often used to improve solubility of the material with alkyl or alkoxy sidechains. The halogenated structures, as

the name suggests, feature halogen atoms such as fluorine (**Figure 2-2b**) replacing the hydrogen atoms on the benzene ring. Early studies of these types of materials showed that the addition of fluorine atoms lowered both the E_{HOMO} and E_{LUMO} of the copolymer by ~ 0.18 eV as reported by Lei et al. in 2012¹⁰⁵. When incorporating this polymer into OFET devices the results showed improved charge carrier mobility. It was suggested this increase in mobility stems from the changes in interchain packing of the polymer which led to a higher DOC and improved charge transport.

Heterocyclic isoindigo units simply replace the benzene ring fused to the lactam ring with different heterocycles. The most common replacements for the benzene ring are nitrogen-containing pyridine groups or a thiophene ring (**Figure 2-2c**)¹⁰⁶. The thiophene substituted isoindigo, referred to as thienoisindigo, was copolymerized with benzothiadiazole. The resulting system showed a low optical E_g of 0.92 eV and an increased charge carrier mobility. This was attributed to the increased planarity of the material as eliminating the benzene group removed the steric repulsion between the hydrogen at the 4 position and the lactam oxygen and replaced it with an advantageous interaction between the thiophene sulfur atom and lactam oxygen atom.

In the peripherally expanded isoindigo, aromatic units are fused to the benzene rings expanding the structure of the system. The addition of these aromatic groups was shown to induce a red shift in E_g of the material. Yue et al. were able to copolymerize a thieno[2,3-b] benzothiophene-fused isoindigo (**Figure 2-2d**) monomer with thiophene to yield a low E_g material (~ 1.6 eV) with a high E_{LUMO} (-3.5 eV) as an ideal p-type semiconductor for OPV applications¹⁰⁷. Of particular interest for this material is that it performs well without thermal annealing or solvent additives post-fabrication. However, several attempts at synthesizing these types of materials have led to production of the undesirable isatin isomer of isoindigo and hence literature on these types of materials is limited.

Core-expanded isoindigo materials feature conjugated units inserted between the lactam rings of isoindigo units. The most popular of these structures includes a benzodifurandione group as the middle-conjugated unit shown in **Figure 2-2e** and is referred to as benzodifuran-based oligo-p-phenylenevinylene (BDOPV). In 2013 Lei et al first reported a copolymer using this material and

it was discovered that the lactam and lactone moieties enhanced electron-withdrawing properties of the material and led to increased carrier mobility¹⁰⁸. Another approach to this material design is to use an isoindigo unit itself as the conjugated material to expand in the core referred to as bisisoindigo. It was believed that by extending the conjugation of the acceptor to a second isoindigo unit the E_{LUMO} could be lowered, and this was confirmed to be true when copolymers using this the bisisoindigo structure showed a reduced E_g reported by Randell in 2016¹⁰⁹.

For specifically temperature sensing applications isoindigo-based materials have scarcely been reported even though studies on D-A systems using isoindigo have been published for the purposes of NO_2 sensing, ammonia sensing, and photoelectric sensing^{99,110,111}. Polythiophenes on the other hand have been reported in works on water-soluble temperature sensor, organic field-effect transistor (OFET) temperature sensors, and dual pressure/temperature sensor devices^{14,24,112}. A common theme in these polythiophene sensors is the use of a dopant to improve electrical conductivity, however long-term stability of that polymer:dopant complex remains an issue. This thesis work aims to utilize the electron-donating oligothiophene units with modified hemi-isoindigo (HID) acceptor units to synthesize copolymers that will exhibit long-term stability in temperature sensing applications.

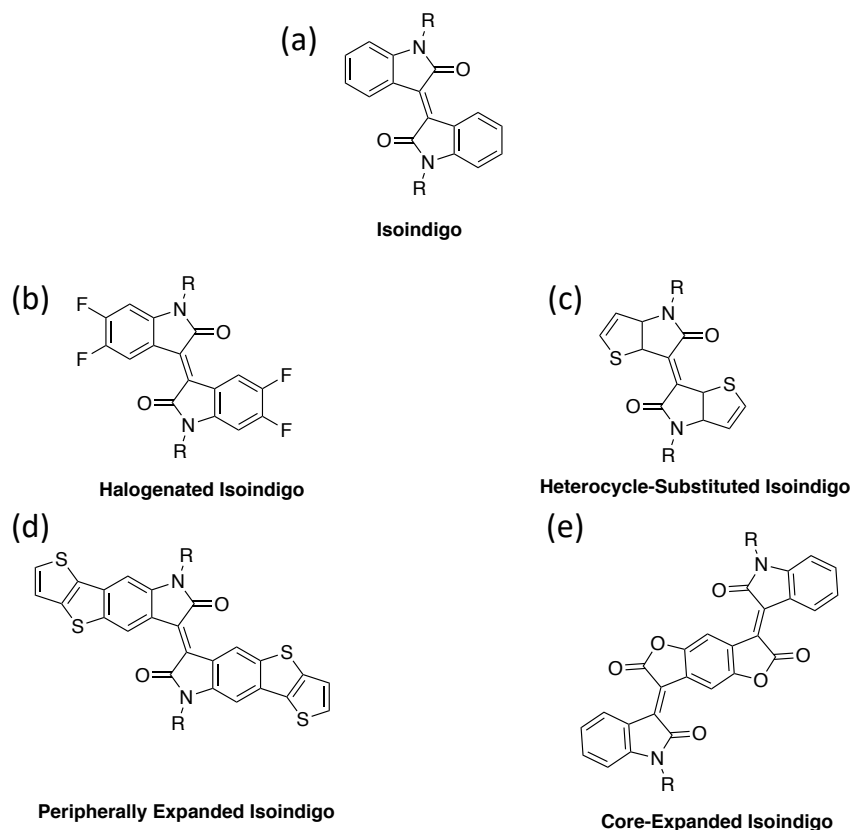


Figure 2-2: Chemical structure of (a) isoindigo and its four most common derivatives (b) halogenated isoindigo, (c) heterocycle-substituted isoindigo, (d) peripherally expanded isoindigo, and (e) core-expanded isoindigo.

2.2 3,3'-Bis(dodecyloxy)-2,2'-bithiophene (DDOBT) Monomer

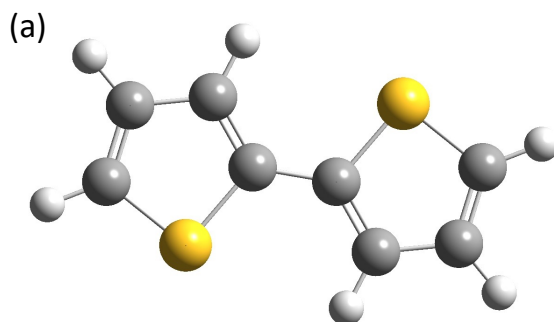
2.2.1 3,3'-Bis(dodecyloxy)-2,2'-bithiophene (DDOBT) Molecular Design

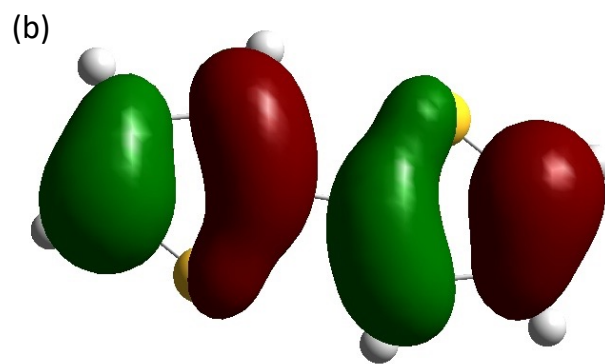
The donor unit chosen for the copolymers is 3,3'-bis(dodecyloxy)-2,2'-bithiophene (**DDOBT**) which consists of two thiophene units linked at the 2 and 2' positions in a HH orientation with each thiophene containing a dodecyloxy chain at their respective β position. The alkoxy groups on the thiophene units serve as electron donating groups that increase the donor characteristics of the standard 2,2'-bithiophene (**BT**), which itself is commonly used as the donor in copolymers. However, it has been reported that isoindigo-bithiophene copolymers using **DDOBT** have significantly increased the E_{HOMO} while having a less pronounced effect on the E_{LUMO} leading to a ~ 350 meV reduction in E_g ¹¹³. It is also noted that in the copolymers the frontier orbitals are much

more localized when using the **DDOBT** versus the **BT** which is attributed to the presence of the dodecyloxy groups leading to higher relative energies of the bithiophene π -orbitals. This agrees well with the expected results and the alkoxy groups have the added advantage of increasing solubility of the resulting copolymer. This may be beneficial when trying to process the material as an active layer via solution deposition methods.

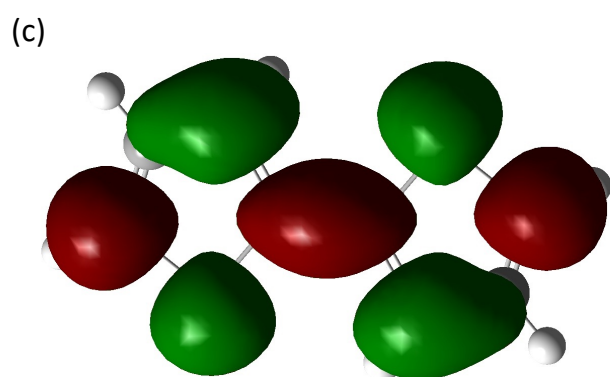
2.2.2 Structures and Energy Levels Simulation by Density Functional Theory (DFT)

The density functional theory (DFT) results for **BT** as a reference is shown in **Figure 2-3**. To simplify the calculation for the **DDOBT** a single methoxy group was used instead of the dodecyloxy group in **Figure 2-4** to illustrate the effect of these electron donating groups and it is reasonable to assume the trend would continue when using a longer alkoxy group. The electron distribution and $E_{\text{HOMO}}/E_{\text{LUMO}}$ with respect to vacuum (0 eV) are calculated for both structures. The simulation results show that the electrons in both structures are evenly delocalized around the two thiophene groups which implies that good π - π stacking is expected. The simulation also shows a significant difference in the E_{HOMO} and E_{LUMO} of the two donor units. The **BT** simulation yields a E_{HOMO} and E_{LUMO} of -5.48 eV and -1.24 eV respectively while the **DDOBT** has a E_{HOMO} at -4.62 eV and a E_{LUMO} level at -0.66 eV indicating that the alkoxy groups increase energy levels of the material which is a desirable characteristic for the donor.



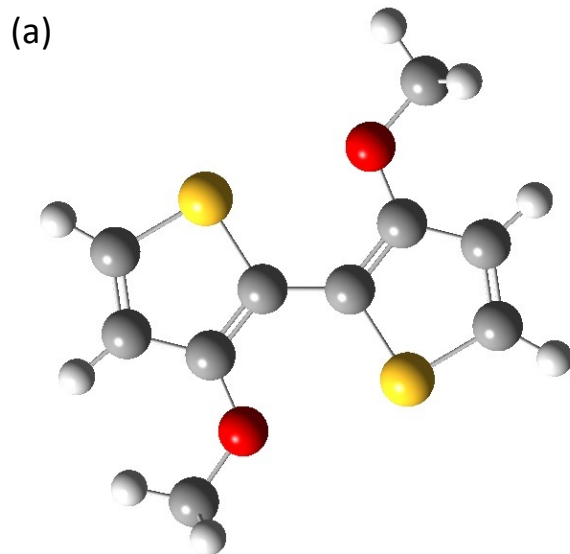


HOMO: -5.48 eV



LUMO: -1.24 eV

Figure 2-3: (a) Geometry of **BT** optimized by DFT simulation in Gaussian software, (b) HOMO/(c) LUMO orbitals of the **BT** and the DFT calculation of the orbital energy levels with respect to vacuum (0 eV).



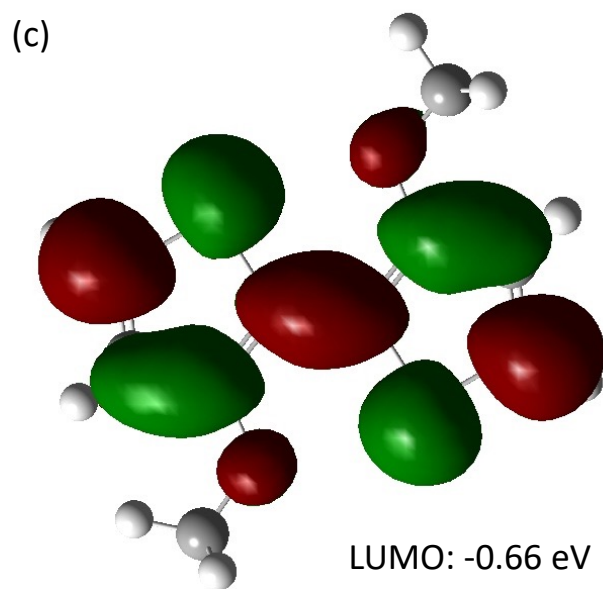
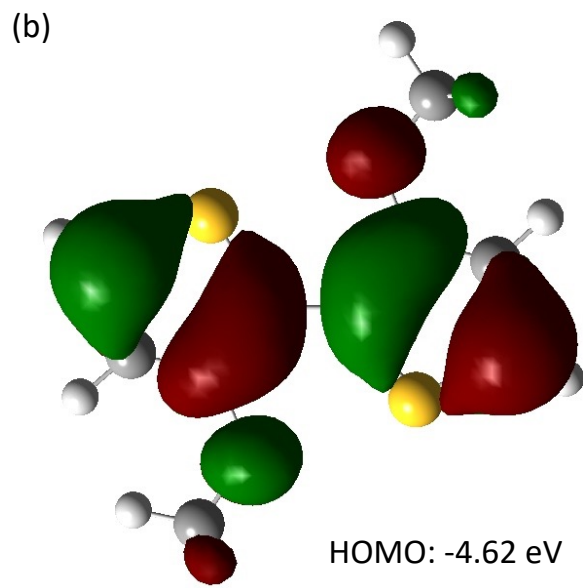
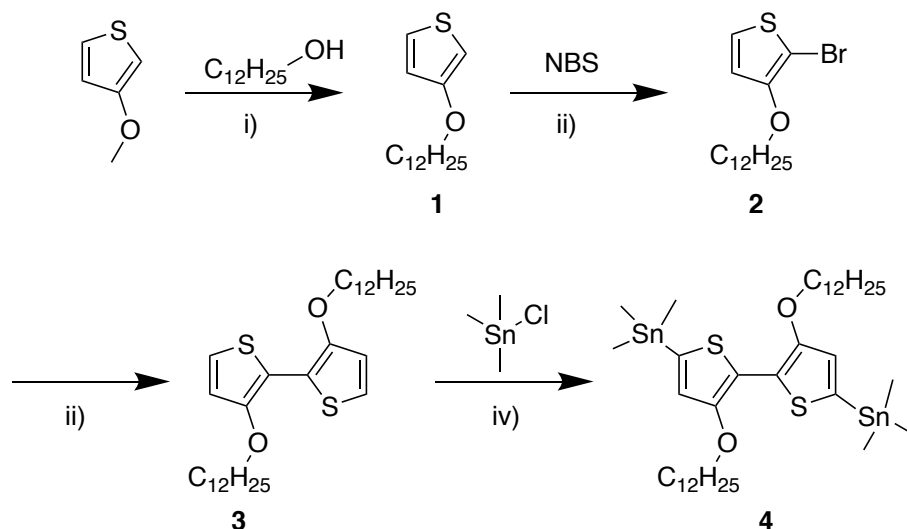


Figure 2-4: (a) Geometry of **DDOBT** optimized by DFT simulation in Gaussian software, (b) HOMO/(c) LUMO orbitals of the **DDOBT** and the DFT calculation of the orbital energy levels with respect to vacuum (0 eV).

2.2.3 Synthesis of 3,3'-Bis(dodecyloxy)-2,2'-bithiophene (DDOBT) Monomer

The following **Scheme 2-1** illustrates the synthesis route of the **DDOBT** donor monomer utilizing simple reactions and purification steps. It should be noted the product formed after step ii) is highly unstable and must be consumed immediately after NMR confirms purity. The synthesis details can be found in section 2.6.3 and the corresponding NMR for each reaction is found in Appendix A.



Scheme 2-1: Synthetic route towards the **DDOBT** monomer with trimethyltin groups required for copolymerization. Reaction conditions: i) lauryl alcohol/ p-toluene sulfonic acid/ toluene/ 100 °C 71.1% ii) N-bromosuccinimide/ HBr/ anhydrous chloroform/ r.t 61.0% iii) zinc powder/ triphenylphosphine/ nickel (II) chloride/ 2,2'-bipyridine/ anhydrous dimethylacetamide/ 80 °C 41.4% iv) n-butyllithium/ trimethyltin chloride/ anhydrous THF/ -78 °C to r.t 65.2%.

2.3 Hemi-Isoindigo (HID) Monomers M1, M2, and M3

2.3.1 Hemi-Isoindigo (HID) Monomers Molecular Design

While isoindigo acceptor monomers have been studied for copolymer use in various applications including logic circuits and OPVs amongst others^{114,115}, less literature exists on HID acceptor units in copolymer systems. At the time of this project commencing, it was found that HID materials had yet to be reported as potential temperature sensor active layers. The HID design employs a

thiophene spacer unit between the indigo moiety and the bithiophene donor instead of the traditional secondary indigo unit. In this section three novel HID monomers **M1**, **M2**, and **M3** shown in **Figure 2-5**, are introduced each with a different functionalization group on the thiophene unit. **M3** includes a simple thiophene ($R = H$) unit and is used as a reference as it is theorized that the addition of short alkoxy groups on the thiophenes in **M1** ($R+R = -OCH_2CH_2O-$) and **M2** ($R = OCH_3$) may further increase the E_{HOMO} of the polymers to improve the stability of the polymer:dopant complex. Furthermore, an ethylhexyl alkyl group is introduced at the indigo nitrogen atom to improve the solubility of these monomers which is crucial for the solution processing of the polymers as well as the practicality of the polymerization reaction itself.

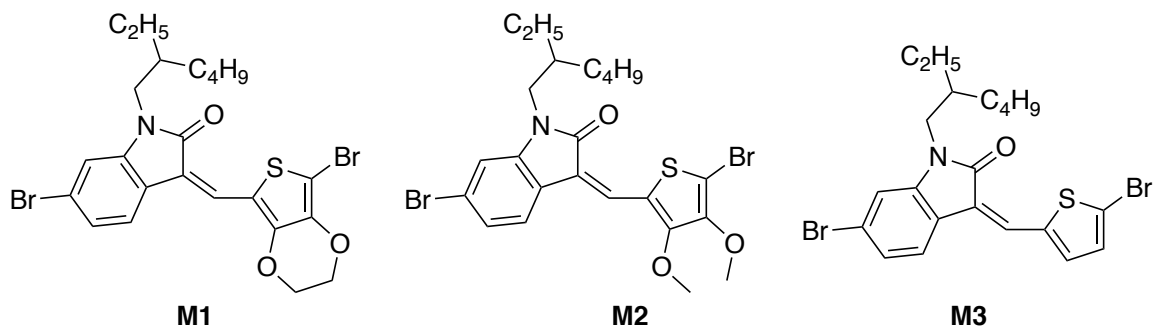
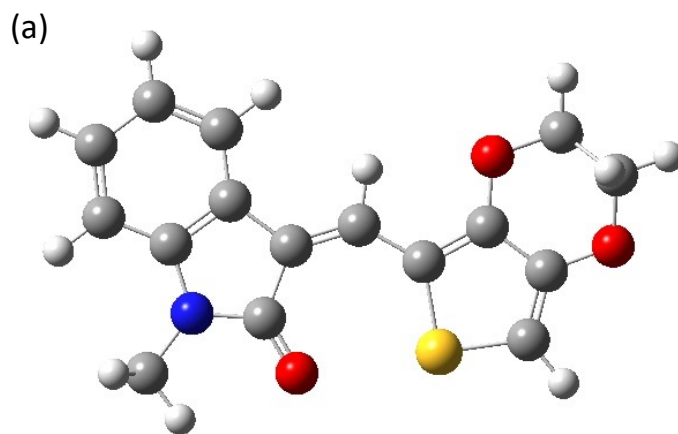


Figure 2-5: Chemical structures of HID monomers **M1**, **M2**, and **M3**.

2.3.2 Structures and Energy Levels Simulation by Density Functional Theory (DFT)

The DFT simulations and the calculated energy level estimates for **M1**, **M2**, and **M3** are shown in **Figure 2-6**, **Figure 2-7**, and **Figure 2-8** respectively supporting the theory that alkoxy-substituted thiophene monomers are expected to have higher E_{HOMO} and E_{LUMO} . Instead of an ethylhexyl alkyl chain on the indigo moiety of the monomers a simple methyl group was used to reduce computation complexity and time. The higher E_{LUMO} is normally undesired for acceptor units however, in this case it is more important to raise the E_{HOMO} for a stable polymer:dopant complex than it is to reduce the E_g so the trade-off is acceptable. It may also be noted that the E_{LUMO} from DFT calculations may deviate largely from actual values. This is because the LUMO orbital itself is empty of electrons hence the calculations assume that excited electrons fill the imaginary molecular orbitals. The DFT simulation results show that **M3** should have the lowest E_{HOMO} and E_{LUMO} of -5.44 eV and -2.10 eV. The methoxy groups on the β positions of the thiophene in **M2**

exhibit a significant increase in the energy levels with a E_{HOMO} and E_{LUMO} at -5.24 eV and -1.80 eV respectively. The highest simulated E_{HOMO} belongs to **M1** at -5.18 eV however the E_{LUMO} is predicted to be slightly lower than **M2** at -1.87 eV. A summary of the DFT calculations for both the donor and acceptor molecules proposed is provided in **Table 2-1**. The higher E_{HOMO} exhibited by the alkoxy functionalized monomers should yield a more stable polymer:dopant complex which is crucial for the time-stability of the organic sensor. The electrons in all three monomers are evenly delocalized in both the HOMO and LUMO levels which indicates that the HID materials should exhibit good π - π stacking. During the synthesis of these materials a double bond linkage between the thiophene and indigo units gives rise to potential geometric isomerization of the product. It is noted that no isomerization occurs after the Knoevenagel condensation reaction in any of the monomers and only the Z-form geometric isomer is present. However, after the alkylation reaction, **M1** and **M2** show that a small amount of E-form isomer is present with a Z:E ratio of $\sim 7:1$ and these isomers may not be separated using column chromatography, so this mixture of isomers remains in the final **M1** and **M2** products. Conversely, **M3** does not show any isomerization throughout the synthesis process so the final product is only the Z-form isomer.



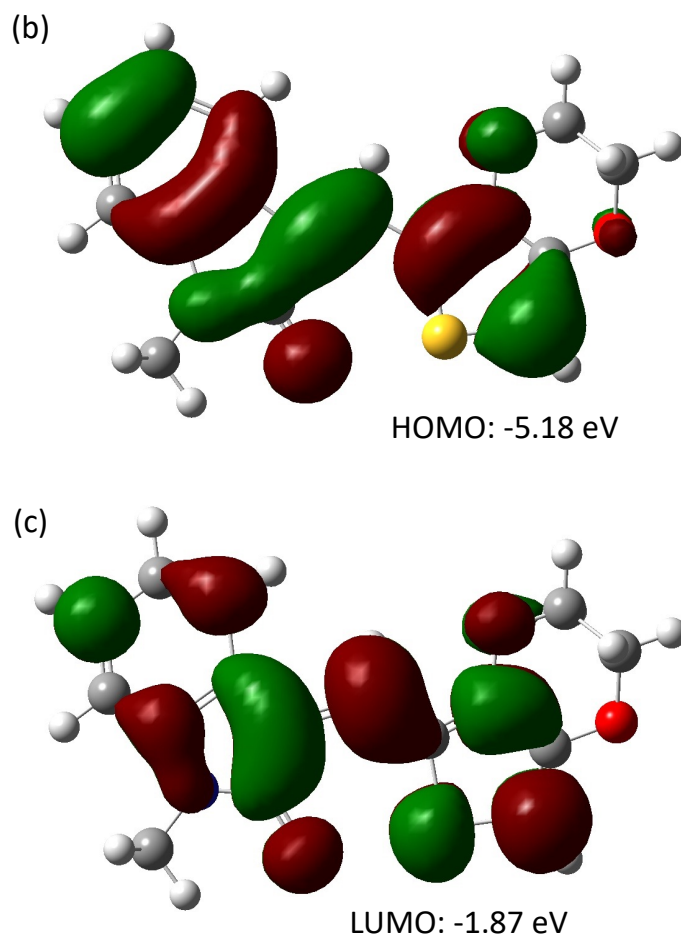
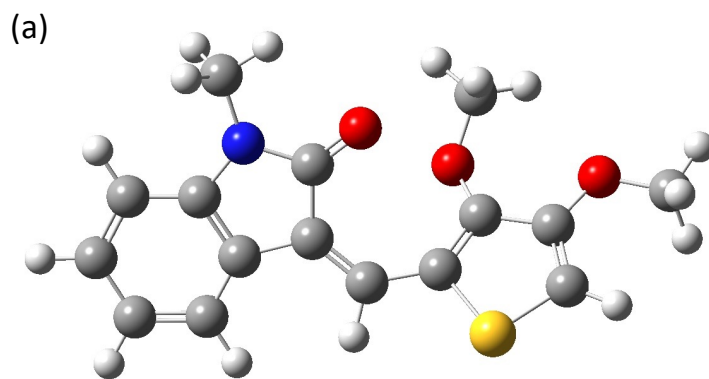


Figure 2-6: (a) Geometry of **M1** optimized by DFT simulation in Gaussian software, (b) HOMO/(c) LUMO orbitals of the **M1** and the DFT calculation of the orbital energy levels with respect to vacuum (0 eV).



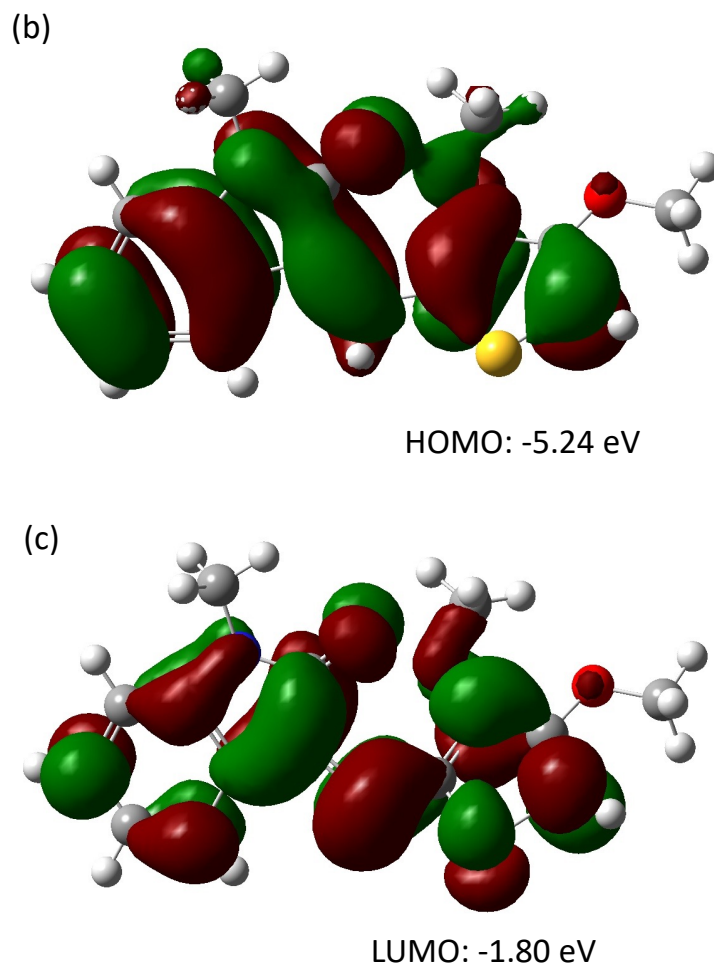
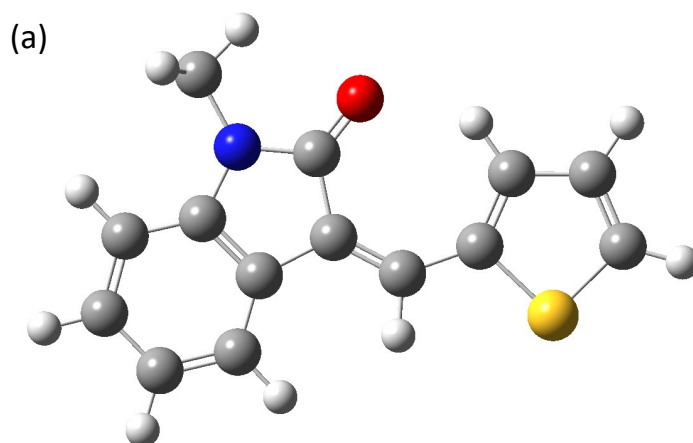


Figure 2-7: (a) Geometry of **M2** optimized by DFT simulation in Gaussian software, (b) HOMO/(c) LUMO orbitals of the **M2** and the DFT calculation of the orbital energy levels with respect to vacuum (0 eV).



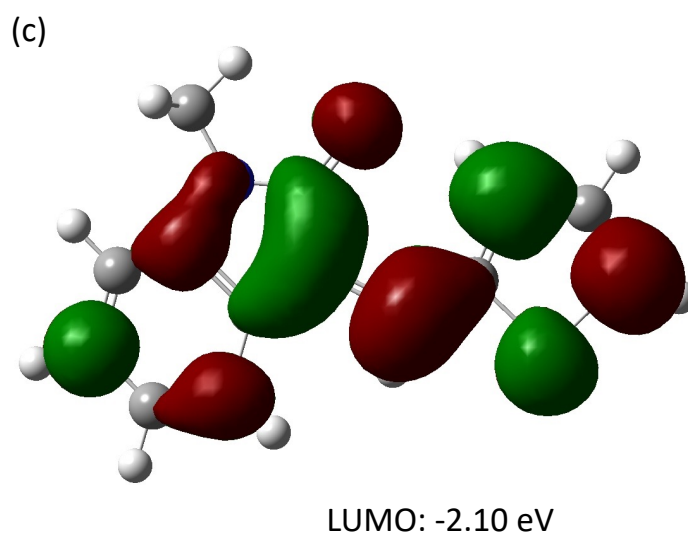
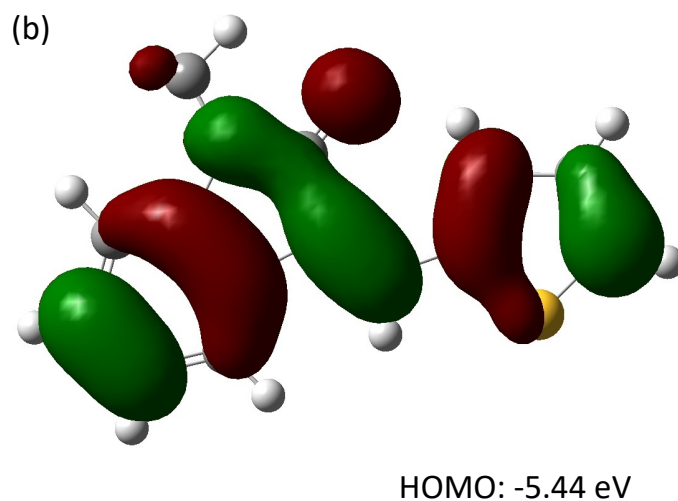


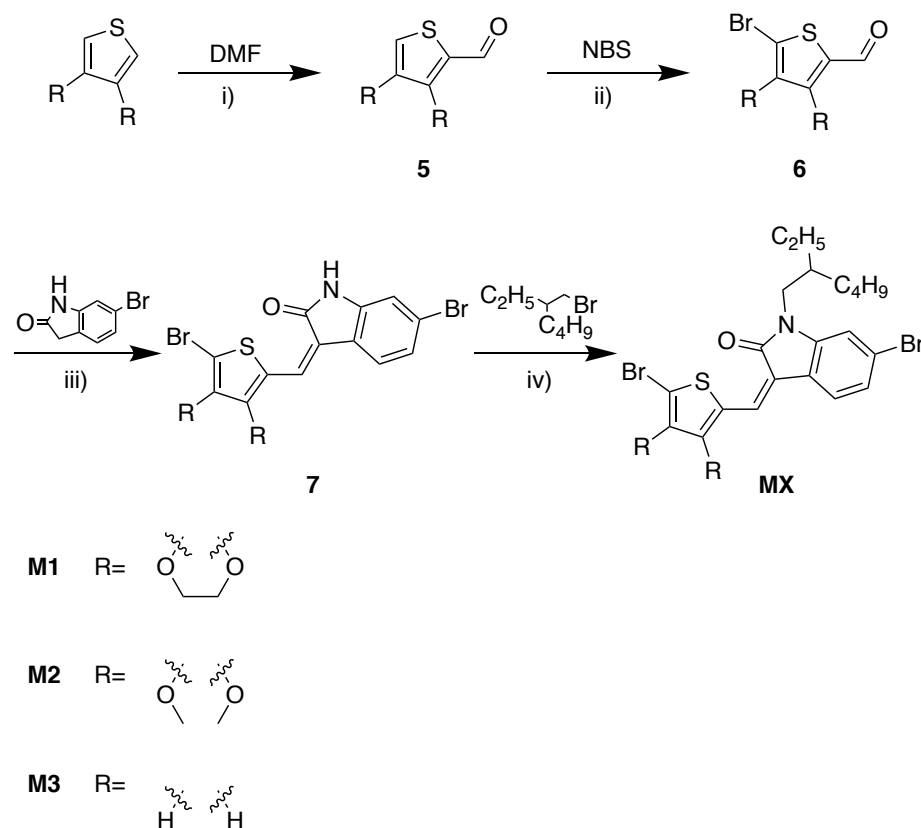
Figure 2-8: (a) Geometry of **M3** optimized by DFT simulation ins Gaussian software, (b) HOMO/(c) LUMO orbitals of the **M3** and the DFT calculation of the orbital energy levels with respect to vacuum (0 eV).

Table 2-1: DFT calculation results for both donors and all three acceptors.

	E_{HOMO}	E_{LUMO}	E_g
BT	-5.48 eV	-1.24 eV	4.24 eV
DDOBT	-4.62 eV	-0.66 eV	3.96 eV
M1	-5.18 eV	-1.87 eV	3.31 eV
M2	-5.24 eV	-1.80 eV	3.44 eV
M3	-5.44 eV	-2.10 eV	3.34 eV

2.3.3 Synthesis of HID Monomers with Alkyl Sidechains

Scheme 2-2 illustrates the HID monomer synthesis via a four-step series of reactions and purification procedures. Briefly, the **M1-3** monomers are synthesized starting from their thiophene derivative with a formylation reaction to anchor an aldehyde group to the α position followed by a bromination reaction with N-bromosuccinimide (NBS) to add the bromine group opposite the aldehyde, then a Knoevenagel condensation reaction to create the HID unit, and finally an alkylation reaction to improve solubility. The details for the synthesis and purification of each of the individual materials are discussed in section 2.6.3 and the corresponding NMR spectra are presented in Appendix A.

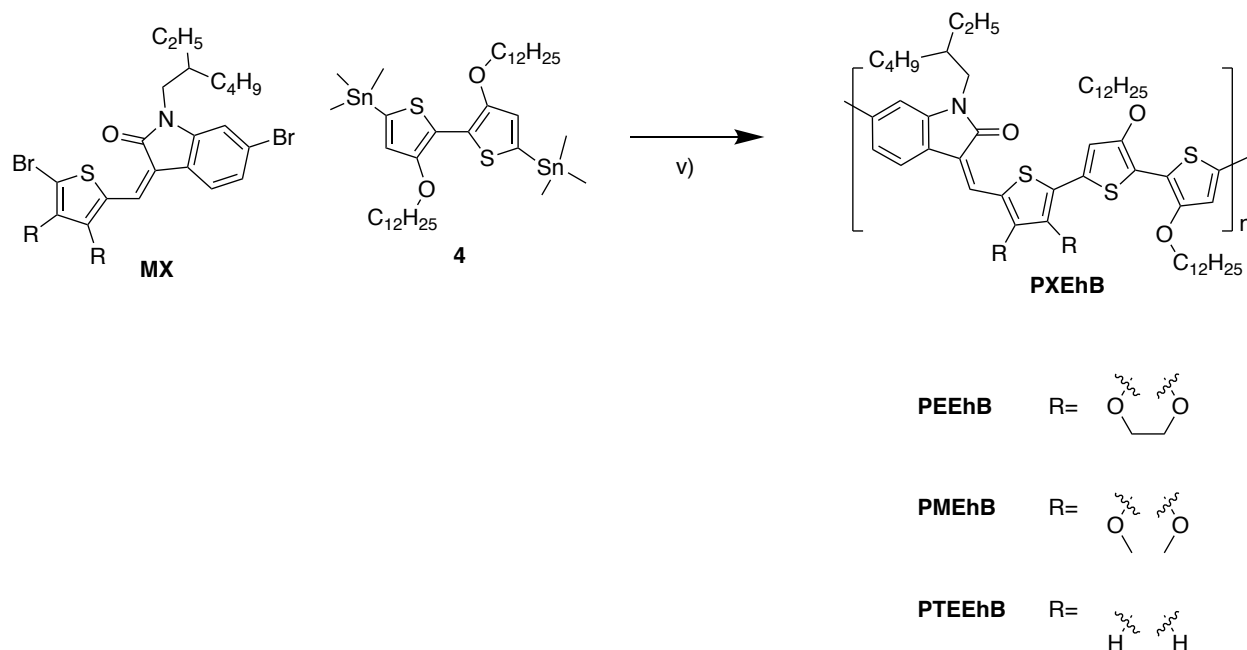


Scheme 2-2: Synthetic route towards HID monomers **M1**, **M2**, and **M3** with bromine groups required for copolymerization. Reaction conditions: i) n-butyllithium/ anhydrous DMF/ anhydrous THF/ -78 °C to r.t 69.5% ii) N-bromosuccinimide/ HBr/ anhydrous chloroform/ r.t 70.3% iii) 6-bromooxindole/ piperidine/ anhydrous ethanol/ 90 °C 76.8% iv) potassium carbonate/ 2-ethylhexyl bromide/ anhydrous DMF/ 100 °C 55.6%.

2.4 Synthesis and Characterization of HID Polymers PEEhB, PMEhB, PTEhB

2.4.1 Synthesis of HID Polymers

The three HID copolymers were synthesized using the Stille coupling mechanism in the presence of $\text{Pd}_2(\text{dba})_3/\text{P}(o\text{-tolyl})_3$ in degassed chlorobenzene, as indicated in **Scheme 2-3** with one of the **M1-3**, acceptor monomers and the **DDOBT** donor monomer. The polymers were then purified via Soxhlet extraction using methanol, acetone, hexane, and chloroform in that order each showing good solubility in chlorinated solvents such as chloroform, chlorobenzene, and 1,2-dichloromethane. The full details on the synthesis procedures for each polymer are available in section 2.6.3.



Scheme 2-3: Synthetic route towards HID copolymers **PEEhB**, **PMEhB**, and **PTEhB**. Reaction conditions: v) tri(*o*-tolyl)phosphine/ tris(dibenzylideneacetone)dipalladium(0)/ degassed anhydrous chlorobenzene/ 80 °C. Purified using Soxhlet extraction with methanol, acetone, hexane, chloroform in that order 71.7%.

2.4.2 Characterization of HID Polymers by HT-GPC, UV-Vis-NIR Spectroscopy, CV, DSC, AFM, and XRD

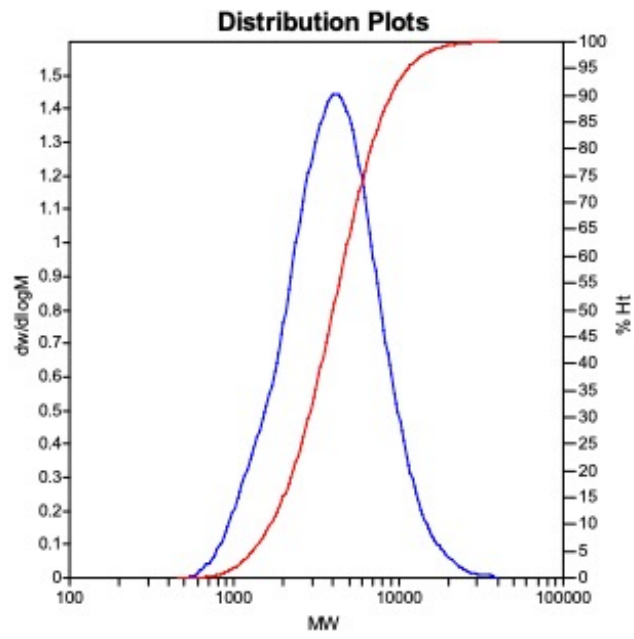
The molecular weight of **PEEhB**, **PMEhB**, and **PTEhB** were measured using high-temperature gel-permeation chromatography (HT-GPC) at 150 °C using 1,2,4-trichlorobenzene as the eluent with polystyrene standards. The number average (M_n), weight average (M_w), and polydispersity index (PDI) are shown in **Table 2-2** below with distributions shown in **Figure 2-9**. **PTEhB** showed the highest molecular weight of the three polymers with M_n of 5.2 kDa and a PDI of 1.38. The data from **PEEhB** and **PMEhB**, M_n of 3.2 kDa and 1.7 kDa respectively, implies that short oligomer chains were formed during polymerization.

The molecular weight distribution for the **PMEhB** polymer (**Figure 2-9b**) exhibits bimodal characteristics with one peak centered at ~ 1300 Da and the other centered at ~ 2500 Da. This should be due to the low molecular weight of the material meaning any additional monomer units added to the chain will have a pronounced impact on the molecular weight. The 1300 Da peak is close to the molecular weight of an oligomer consisting of two **M2** monomers with a single **DDOBT** unit between them while the ~ 2500 Da peak could represent a chain with the combination of three **M2** monomers with two **DDOBT** units. While **PMEhB** may be classified as an oligomer due to its short chains, the electronic properties and temperature sensing performance are still evaluated and reported in this work.

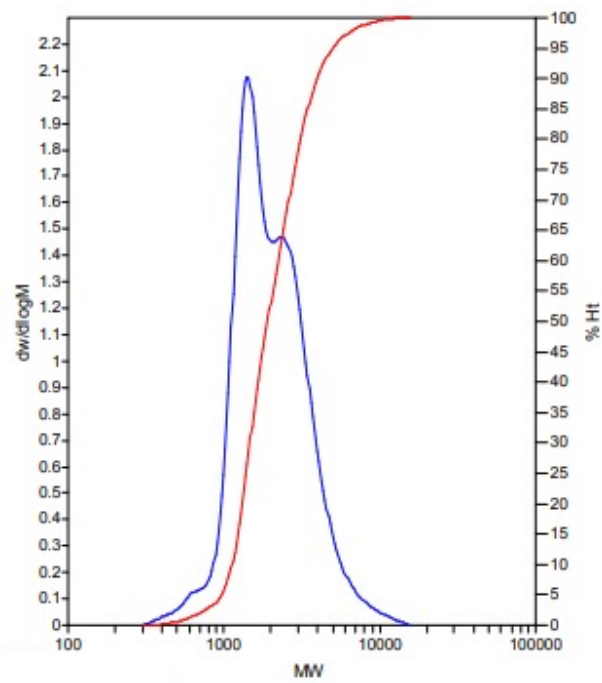
Table 2-2: Molecular weight distribution of the HID polymers **PEEhB**, **PMEhB**, and **PTEhB** from HT-GPC analysis.

	M_n	M_w	PDI
PEEhB	3158 Da	4816 Da	1.52
PMEhB	1739 Da	2305 Da	1.32
PTEhB	5165 Da	7143 Da	1.38

(a)



(b)



(c)

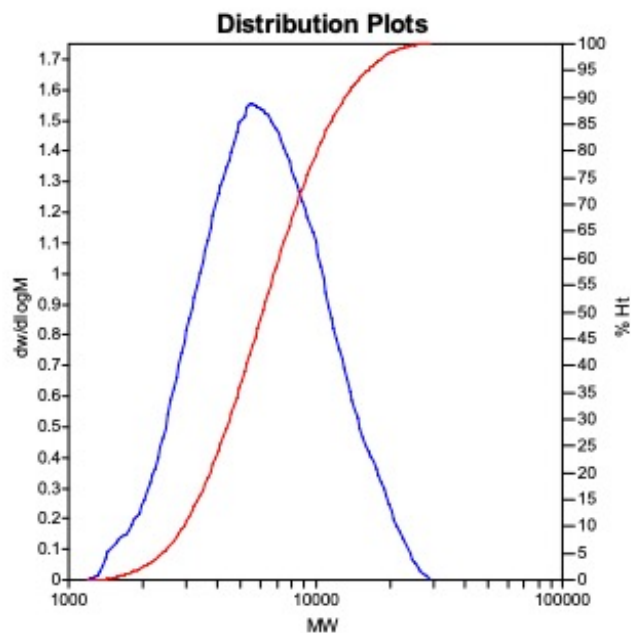


Figure 2-9: Molecular weight distributions of (a) **PEEhB**, (b) **PMEhB**, (c) **PTEhB** from HT-GPC at 150 °C with 1,2,4-trichlorobenzene as the eluent.

The ultraviolet-visible-near-infrared (UV-Vis-NIR) absorbance spectra of each polymer in solution (chloroform solvent), deposited as a thin film on a glass slide, and as a doped film with **F4TCNQ** on that same glass slide is shown in **Figure 2-10**, **Figure 2-11**, and **Figure 2-12** below. The onset wavelength (λ_{onset}) from the thin film spectra of each polymer is used in **Equation (2-1)** to determine the optical E_g :

$$E_g = \frac{hc}{\lambda_{\text{onset}}} \quad (2-1)$$

where h represents Planck's constant and c is the speed of light with E_g reported in units of electron volts (eV) as is convention. In each instance going from solution to thin film the absorbance curve undergoes a red shift towards higher wavelengths. The shifts of the peaks formed below 1000 nm, along with the film λ_{onset} are summarized in **Table 2-3** below. **PEEhB** exhibits the narrowest E_g at 1.41 eV while **PMEhB** and **PTEhB** exhibit optical E_g of 1.43 eV and 1.48 eV respectively.

While **PTEhB** has the highest molecular weight ($M_n \sim 5.2$ kDa) of the three copolymers, it still exhibits the widest bandgap. Conjugation theory dictates that an increased number of repeating units (n), leads to stronger π - π stacking between polymer chains and a narrower bandgap following the relationship shown in **Equation 2-2**¹¹⁶:

$$E_g(n) = E_{g,\infty} + (E_{g,1} - E_{g,\infty})\exp[-\alpha(n - 1)] \quad (2-2)$$

where $E_{g,1}$ and $E_{g,\infty}$ are the E_g for a single monomer unit and that of an infinitely long polymer chain respectively, while the α parameter represents how fast $E_g(n)$ will saturate towards $E_{g,\infty}$. This saturation occurs when the polymer reaches its effective conjugation length (ECL) at which point $E_g(n) \approx E_{g,\infty}$ and no additional monomer units being added to the chain will affect the electronic properties of the material¹¹⁷.

The results in this work indicate that the alkoxy-substituted thiophene spacer unit of the HID polymer has a more pronounced effect on the E_g than the conjugation length. Literature provides an example where poly(3,4-alkoxythiophene)s have exhibited reduced E_g and this has been attributed to the presence of the two strong electron donating oxygen atoms¹¹⁸ or potentially a more coplanar conformation which has previously been reported in poly(3-alkoxythiophene)s¹¹⁹. Shi et al. reported similar results where the conjugated copolymer **POT-co-DOT**, made up of two thiophene monomers, one with a 3-alkyl sidechain and the other with a 3-alkoxy sidechain had a higher molecular weight than homopolymer **P3DOT** which consisted of just the alkoxy-substituted thiophene monomer. However, the E_g of **P3DOT** was evaluated to be less than that of the **POT-co-DOT**. This was attributed it to the alkyl sidechain being less effective in lowering the bandgap of the polymer than the alkoxy analog¹²⁰. In that same work, **COPF-1**¹²¹ and **COPF-2**¹²² fluorene copolymers were directly compared with the fluorene copolymer **PF-co-DTB**. **COPF-1** and **COPF-2** had no sidechain on their thiophene units while **PF-co-DTB** included a decoxy group on both thiophene moieties and the material exhibited a E_g 240 meV and 280 meV narrower than **COPF-1** and **COPF-2** respectively.

Integer charge transfer (ICT) may be used to explain the doping effects in several conjugated polymers¹²³. The electron in the HOMO level of the polymer drops into the LUMO level of the p-type dopant to form the polaron. This is referred to as single electron transfer and is the most common mechanism of doping. Bipolarons may also form when a double electron transfer occurs, but this process occurs much less frequently in CPs¹²⁴. The optical E_g of each polymer is found to be significantly lowered, as is expected with conventional semiconductor doping, and broad peaks emerge in the NIR region (1200-2200 nm) when the film is doped with **F4TCNQ**¹²⁵. Towards the lower end of the spectrum the same peak forming with $\lambda_{\text{onset}} \sim 500$ nm is present in all three doped films, and this may be attributed to the presence of neutral **F4TCNQ**¹²⁶. In **Figures 2-10, 2-11, and 2-12** a small hump is seen in the doped films with a peak intensity maximum around 750 nm which indicates the presence of the **F4TCNQ**⁻ anion serving as evidence that the electron transfer should be a single electron transferring from polymer to **F4TCNQ** molecule to form a polaron¹²⁷. Characteristic of this mechanism are the sub-bandgap absorption peaks in the NIR region as seen in all three doped films. This peak is thought to stem from the polaron formation in the polymer structure and the P1 or P2 optical transition which appears in the NIR region of **F4TCNQ** doped conjugated polymers¹²⁸. The broad NIR-peaks show a λ_{max} at 1618 nm, 1241 nm, and 1508 nm for **PEEhB**, **PMEhB**, and **PTEhB** doped films respectively. The broad peak positions of **PEEhB** and **PTEhB** may be explained by the absorbance peak positions of the neat film with the former having a λ_{max} at a higher wavelength. Hence, one could assume that the transitions occurring from the corresponding polarons would follow a similar trend in λ_{max} . However, the significant shift in the λ_{max} of the **PMEhB** NIR broad peak warrants further explanation. This may be due the molecular weight of **PMEhB** which indicates that the polymer sample is made up of extremely short chains according to the HT-GPC data.

These extremely short chains may lead to **PMEhB** behaving more like a small molecule than the other polymers. **Equation 2-3** depicts the energy equation for a one-dimensional particle in a box of length L. The energy level (E_n) is inversely proportional to L^2 and thus increasing the length of the box has a significant impact on E_n ¹²⁹⁻¹³². In this equation n is some integer, h is Planck's constant and m is the mass of the particle.

$$E_n = \frac{n^2 h^2}{8mL^2} \quad (2-3)$$

The length of this box is analogous to the conjugation length of a polymer chain and thus increases approximately linearly with the number of C=C bonds in the system which correlates directly with molecular weight. Therefore, the polarons formed when the short chain **PMEhB** is doped with **F4TCNQ** may exhibit higher energy transitions. This is opposite the effect observed with the undoped films as the thiophene spacer unit has a greater impact on the optical E_g . However, it is reasonable to assume that the characteristics exhibited by charged species, generated from doping, may be more impacted by the molecular weight. To clarify, a shorter polymer chain would have fewer doping sites than a longer polymer chain and thus the interchain interactions generated by this doping would be weaker for the lower molecular weight species. In fact, it has been shown that neighbouring polymer chains being pulled closer together may effectively stabilize positively charged polarons leading to lower energy transitions^{133,134}. However, one would expect a similar effect in the **PEEhB:F4TCNQ** and **PTEhB:F4TCNQ** films. In the results presented here the former of the two has a lower molecular weight and still exhibits a higher energy transition as evidence by the NIR peak position. This may be due to the polymers nearing their ECL and thus the molecular weight effect is less pronounced in this case the thiophene spacer unit would be the root cause for the differences between the polaronic transitions of the two complexes.

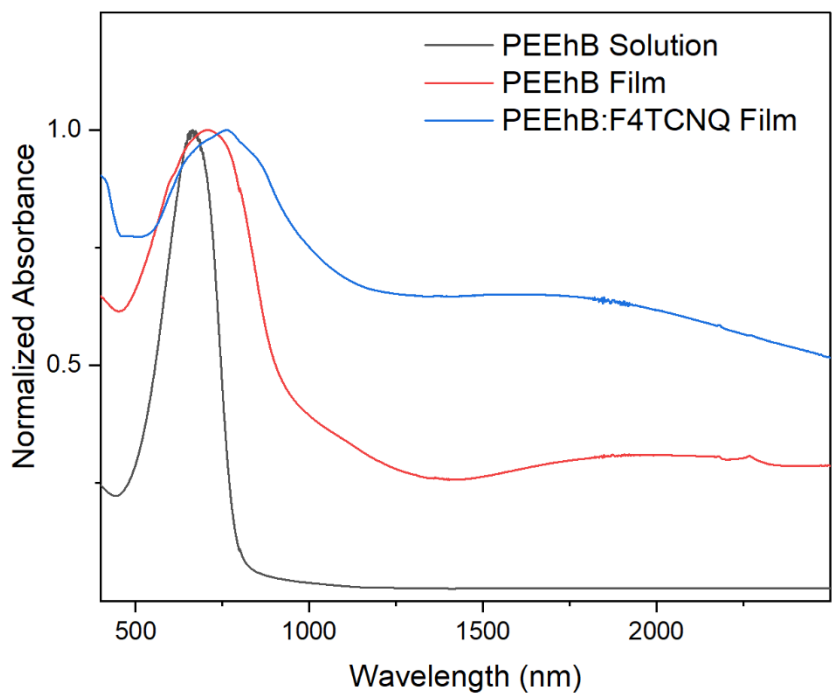


Figure 2- 10: UV-Vis-NIR spectra of **PEEhB** in solution, as a film, and as a doped film.

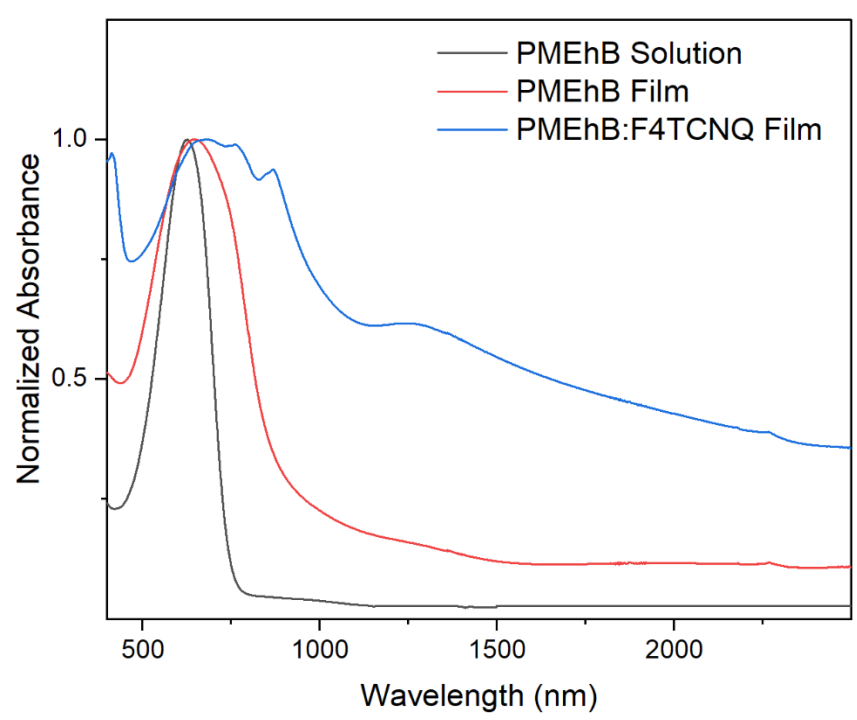


Figure 2-11: UV-Vis-NIR spectra of **PMEhB** in solution, as a film, and as a doped film.

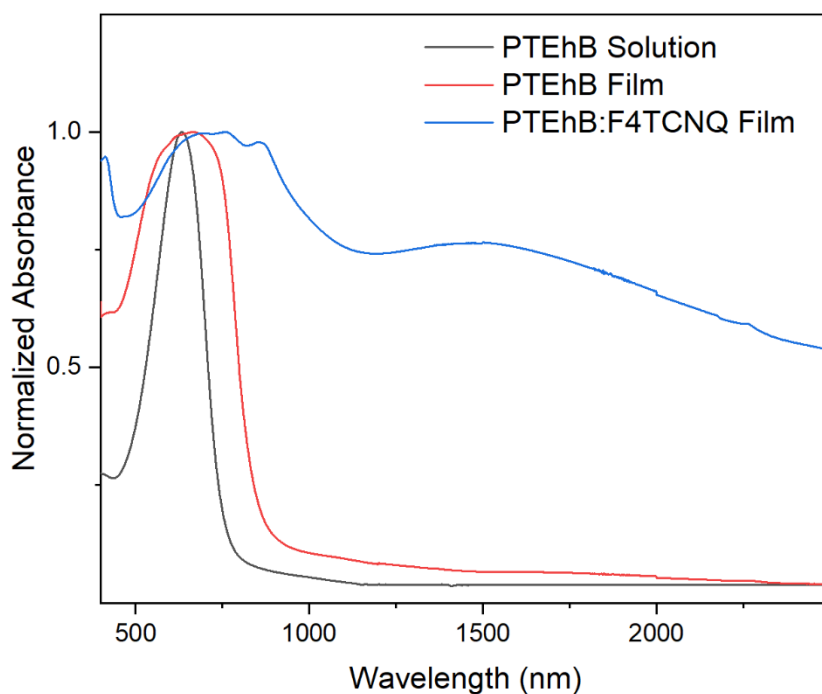


Figure 2-12: UV-Vis-NIR spectra of **PTEhB** in solution, as a film, and as a doped film.

Table 2-3: Summary of the UV-Vis-NIR spectroscopy results for **PEEhB**, **PMEhB**, and **PTEhB** showing the shifts in the absorbance λ_{\max} from solution to film to doped film and film λ_{onset} .

	Film λ_{onset}	Solution λ_{\max}	Film λ_{\max}	Doped λ_{\max}
PEEhB	875 nm	665 nm	696 nm	762 nm
PMEhB	855 nm	627 nm	656 nm	689 nm
PTEhB	839 nm	634 nm	665 nm	761 nm

Another noteworthy feature from this data is the positioning of the undoped film baseline. The normalized absorbance baseline for **PTEhB** is quite low (< 0.1) and approaches the solution baseline which indicates that only reflection from the film is causing this elevated absorbance. The UV-Vis-NIR spectra for **PMEhB** and **PEEhB** show increased baselines (~ 0.15 and ~ 0.25 respectively). This can be attributed to air oxidation of the alkoxy groups on the thiophene unit of the HID structure which are not present in the **PTEhB** structure. This oxidation may dope the polymers to a certain degree depending on how many groups are oxidized and thus a broad peak emerges in the NIR region similar to the peaks formed when doped with **F4TCNQ**.

The E_{HOMO} of each polymer is determined by using a cyclic voltammetry (CV) with a tetrabutylammonium hexafluorophosphate solution (0.1M) prepared in anhydrous acetonitrile using an Ag electrode for reference. The CV results for each of the HID polymers are shown in **Figure 2-13**. The oxidation redox is measured to determine the onset potential (E_{ox}^{onset}). Ferrocene was used as the reference for calculating the E_{HOMO} for each polymer via **Equation (2-4)**:

$$E_{HOMO} = -e [E_{ox}^{onset} - E_{FC/FC^+}] - 4.8 eV \quad (2-4)$$

where e represents the elementary charge, and E_{FC/FC^+} represents the measured E_{ox}^{onset} of ferrocene from the same CV device. The E_{LUMO} of each polymer was determined via the difference between the calculated E_{HOMO} and optical E_g of each polymer. The trap energy (E_T) is defined as the difference between the polymer E_{HOMO} and the dopant E_{LUMO} and is imperative for polymer:dopant complex stability. The energy levels of **PEEhB**, **PMEhB**, and **PTEhB**, along with the **F4TCNQ** dopant, determined using this method are presented in **Figure 2-14** and summarized in **Table 2-4** below along with the E_T value for each polymer.

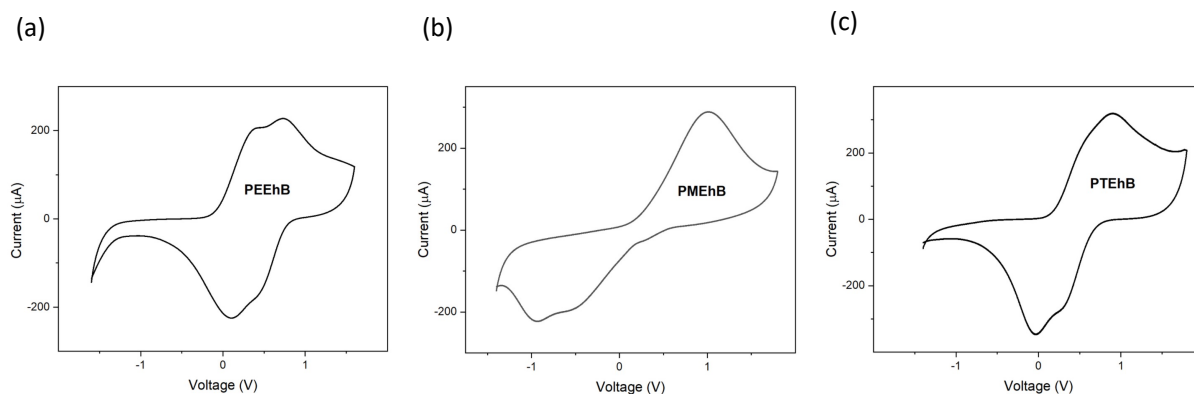


Figure 2-13: The CV trace of (a) **PEEhB**, (b) **PMEhB**, (c) **PTEhB** at a scan rate of 0.1 V/s in 0.1 M tetrabutylammonium hexafluorophosphate with anhydrous acetonitrile as the solvent.

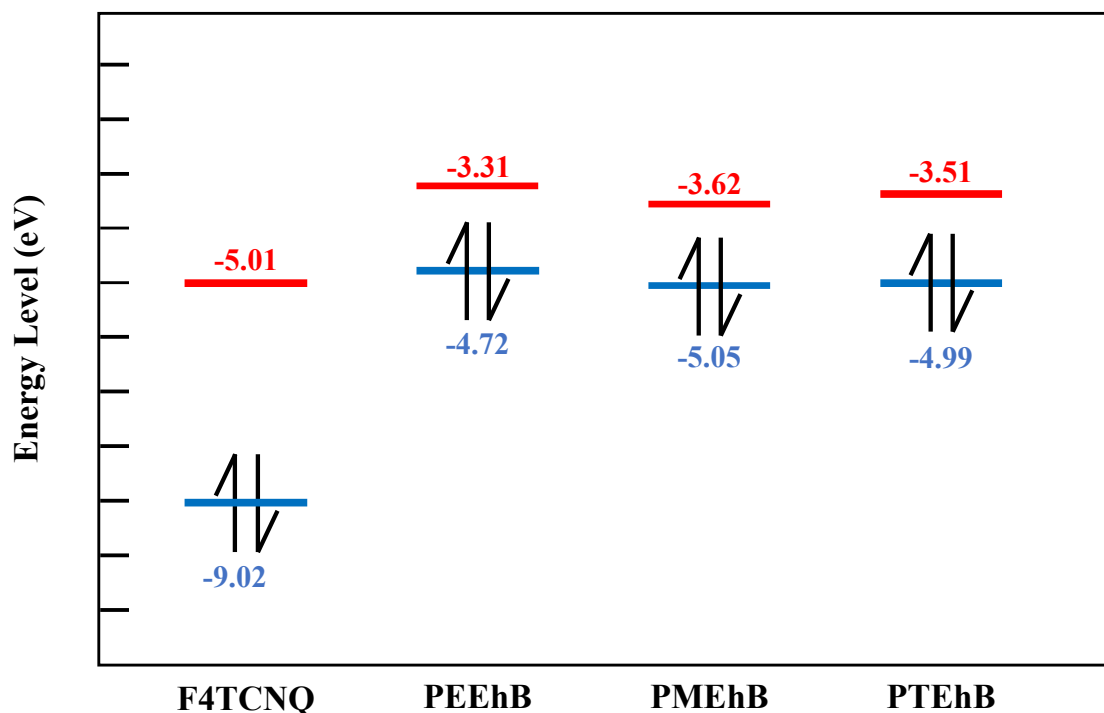


Figure 2-14: Energy level diagram depicting the relative E_{HOMO} and E_{LUMO} of **PEEhB**, **PMEhB**, **PTEhB**, and the **F4TCNQ** dopant with respect to vacuum (0 eV).

Table 2-4: Summary of the molecular orbital energy levels of the HID polymers and the **F4TCNQ** dopant molecule along with E_{T} values.

	E_{HOMO}	E_{LUMO}	E_{g}	E_{T}
PEEhB	-4.72 eV	-3.31 eV	1.41 eV	0.29 eV
PMEhB	-5.04 eV	-3.59 eV	1.43 eV	-0.03 eV
PTEhB	-4.95 eV	-3.51 eV	1.48 eV	0.06 eV
F4TCNQ	-9.02 eV	-5.01 eV	4.02 eV	-

It is noteworthy that while all three polymers exhibit an optical E_{g} between 1.4-1.5 eV, the **PEEhB** polymer is shown to have a significantly higher E_{HOMO} (~ 0.30 eV) than the other two. This may potentially be attributed to interactions between the sulfur atoms on the thiophene moieties of the copolymer and the oxygen atoms on the **EDOT** moieties. As previously mentioned, the alkoxy groups on the thiophene spacer induce strong electron donating properties which both reduce the E_{g} and increase the E_{HOMO} . Since **PEEhB** and **PMEhB** have very similar chemical structures one would expect similar electronic properties from the two materials. This is not the case when

comparing the E_{HOMO} of the two materials and there are two potential explanations for this. The first being the conjugation length of **PMEhB** is $\sim 60\%$ of the conjugation length of **PEEhB**, however literature suggests that the molecular weight does not have a significant impact on the E_{HOMO} of CPs^{135,136}. The other potential explanation for this phenomenon has to do with the difference in the solid-state packing of the polymers. The **EDOT** may form donor domains more effectively than the 3,4-dimethoxythiophene (**DMT**) thus yielding stronger electron donating properties which would lead to a higher E_{HOMO} in **PEEhB** relative to **PMEhB**. Evidence of this may be seen when comparing the work from Wang et al.¹³⁷ with that of Feng et al.¹³⁸ whom each synthesized D-A copolymers using benzodithiophene donors substituted with thiophene sidechains. The chemical structures of the four polymers are depicted in **Figure 2-15** below. The results from Wang et al., which include the **DMT** sidechains, show that the non-fluorinated polymer has an E_{HOMO} of -5.25 eV while the fluorinated polymer exhibits an E_{HOMO} of -5.46 eV. While Feng et al. were able to achieve a E_{HOMO} of -5.22 eV and -5.32 eV for the non-fluorinated and fluorinated polymers respectively using the **EDOT** sidechains instead of the **DMT** analog.

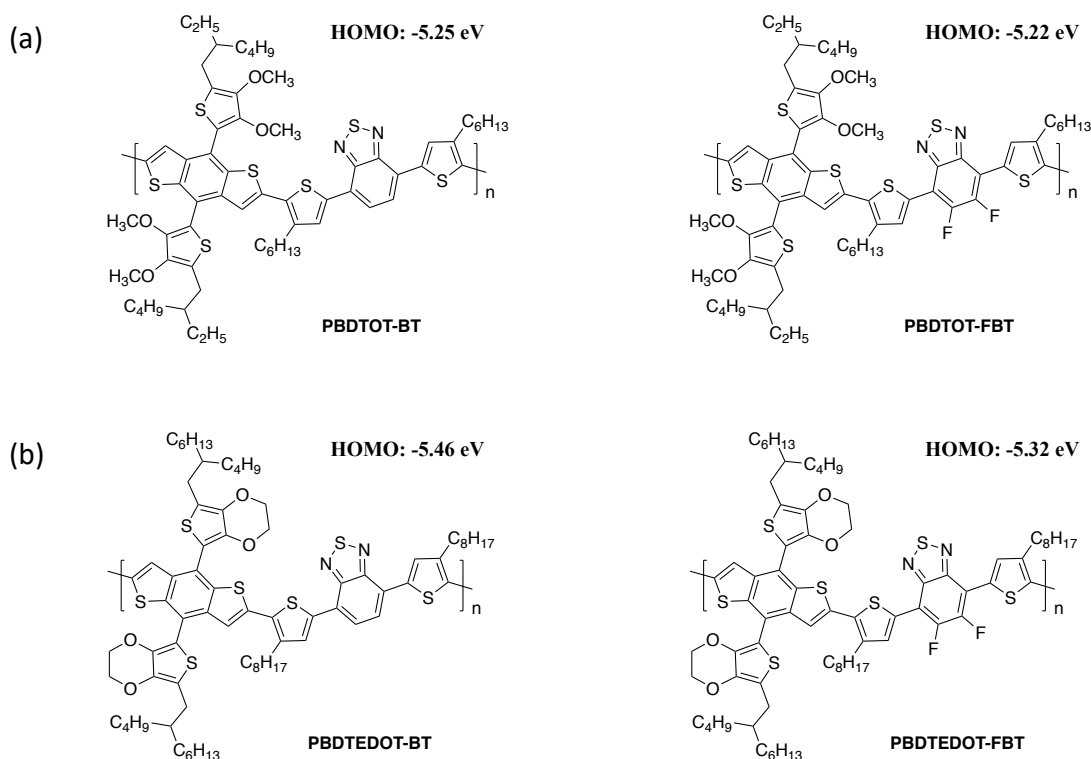


Figure 2-15: Benzodithiophene donor and benzothiadiazole acceptor copolymers with a) **DMT** sidechains and b) **EDOT** side chains on the donor.^{137,138}

This indicates that the **EDOT** group is indeed a stronger electron donating moiety and explains the E_{HOMO} results between **PEEhB** and **PMEhB**. However, the difference in E_{HOMO} reported between the two groups is not as large as the one reported in this work. This should be due to the **EDOT** and **DMT** units of their copolymers being sidechains in contrast with **PEEhB** and **PMEhB** where the **EDOT** and **DMT** units are on the polymer backbone. It has been demonstrated in literature that the further a functional group or sidechain is from the polymer backbone the less prominent the effect it will have on the electrical properties of the corresponding CP^{139,140}.

The E_{HOMO} , specifically, is integral for the stability of the polymer:dopant complex. The dopant can be considered as a “trap” for the charge carriers, in the case of **F4TCNQ** these carriers are electrons. Literature has indicated that to achieve a stable complex E_{T} should be ~ 0.25 eV or greater and these are referred to as deep traps^{82,83}. According to the results, only **PEEhB** should be able to form these deep traps and thus it is expected that the **PEEhB:F4TCNQ** complex ought to exhibit better time stability.

Differential scanning calorimetry (DSC) analysis was conducted on all three polymer samples and the results are shown in **Figure 2-16**. **PEEhB** and **PTEhB** exhibit no noticeable endothermic or exothermic transitions up to 200 °C. **PMEhB** exhibited an exothermic transition which corresponds to the crystallization temperature (T_{C}) at ~ 124 °C. The material also exhibits an endothermic transition with an onset of ~ 148 °C corresponding to the melting temperature (T_{m}) which is found to be ~ 156 °C. **PMEhB** having that lower molecular weight will correspond to a lower melting temperature than **PEEhB** and **PTEhB** due to weaker intermolecular forces between polymer chains and thus the melting point and the crystallization temperature is observed¹⁴¹.

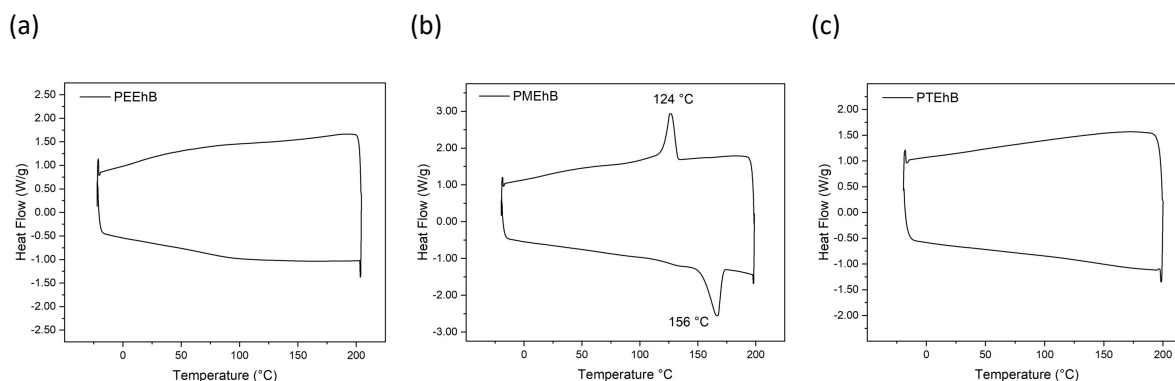


Figure 2-16: The DSC analysis of (a) **PEEhB**, (b) **PMEhB**, and (c) **PTEhB** at a heating cooling rate of $10\text{ }^{\circ}\text{C min}^{-1}$ under nitrogen atmosphere between $-20\text{ }^{\circ}\text{C}$ and $200\text{ }^{\circ}\text{C}$.

The surface morphology and crystalline features of each polymer were determined by spin coating the polymer solutions onto dodecyltrichlorosilane (DDTS)-modified SiO_2/Si substrates. Each polymer was spin-coated onto four separate substrates each heated at a different annealing temperature (T_{α}); room temperature (RT), $100\text{ }^{\circ}\text{C}$, $150\text{ }^{\circ}\text{C}$, and $200\text{ }^{\circ}\text{C}$ for 30 minutes. The films were then subjected to atomic force microscopy (AFM) and X-ray diffraction (XRD) analysis.

Figure 2-17, **Figure 2-18**, and **Figure 2-19** below show the AFM scans of the materials at the four different T_{α} . The surface coarseness of the film is denoted by the root-mean-square roughness parameter R_q , and the results at each T_{α} are plotted in **Figure 2-20** then summarized in **Table 2-5** for each polymer. **PEEhB** exhibits a very smooth film surface ($R_q = 1.14\text{ nm}$) with very small particles present in the AFM image at RT. Fewer larger particles are observed when annealed at $100\text{ }^{\circ}\text{C}$ indicating that agglomeration occurs at that temperature and the roughness decreases ($R_q = 0.85$). When annealed at $150\text{ }^{\circ}\text{C}$ the particles on the surface are very small and high in number so the overall roughness of the film increases slightly ($R_q = 0.97\text{ nm}$) from $100\text{ }^{\circ}\text{C}$. At $200\text{ }^{\circ}\text{C}$ deep cracks in the film are noticeable and that increases the roughness of the film ($R_q = 1.33\text{ nm}$). These cracks may form discontinuous domains in the film, and this would decrease charge carrier mobility. For the **PMEhB** film small particulates are visible at RT with a significantly rougher film than the other two polymers at RT ($R_q = 4.98\text{ nm}$) and when T_{α} increases to $100\text{ }^{\circ}\text{C}$ the scale decreases from 50 nm to 28 nm indicating the roughness is decreasing ($R_q = 4.15\text{ nm}$). The film also goes from a smooth surface with discernible small particles to wider, uneven particles. The DSC thermogram for this material shows a small hump before the T_m onset which may be the

beginning of the polymer melting transition or partial melting of the material leading to the blotchy AFM image at $T_{\alpha} = 100$ °C. At 150 °C and 200 °C large agglomerations of particles can be seen on the surface of the film but with a blurry resolution. These features are attributed to the melting of the polymer which was confirmed to occur at ~ 156 °C from the DSC thermogram. While the roughness slightly decreases from RT to 100 °C, once the polymer is melted the agglomerated particles significantly increase the roughness of the film at 150 °C ($R_q = 11.27$ nm) and 200 °C ($R_q = 11.45$ nm). The **PTEhB** film annealed at RT showed sub-micron-sized particles scattered on the smooth surface of the film ($R_q = 2.16$ nm). The roughness of the film is decreased slightly ($R_q = 1.66$ nm) when annealed at 100 °C and there is a higher number of smaller particles observed. At 150 °C the roughness increases ($R_q = 2.73$ nm) and it is difficult to discern small particles as the film now exhibits more uniform roughness across the surface. When annealed at 200 °C the roughness increases dramatically ($R_q = 4.96$ nm) due to a high number of deep cracks or holes observed in the otherwise uniform film.

PEEhB

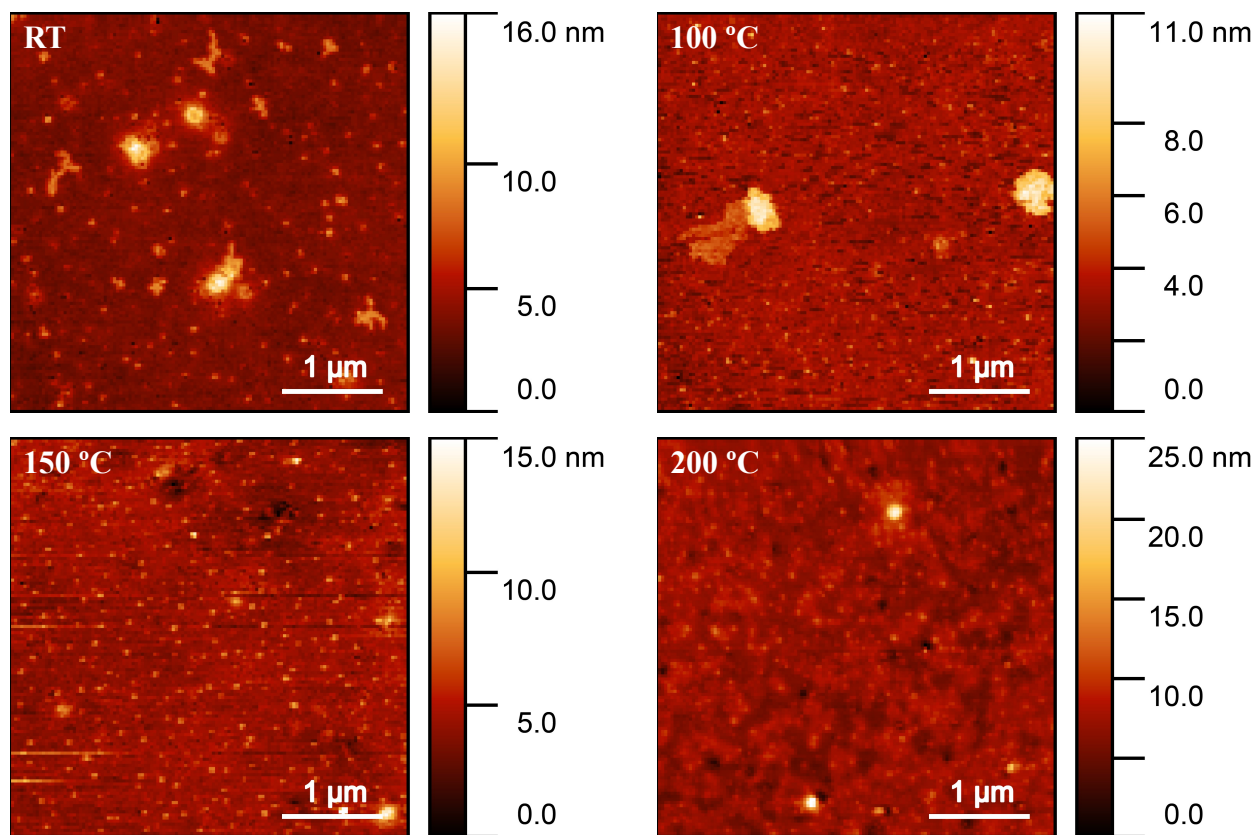


Figure 2-17: AFM images (4 μm x 4 μm) indicating relative height on films of **PEEhB** spin-coated on DDTS-modified SiO₂/Si substrates and annealed at RT, 100 °C, 150 °C, and 200 °C respectively.

PMEhB

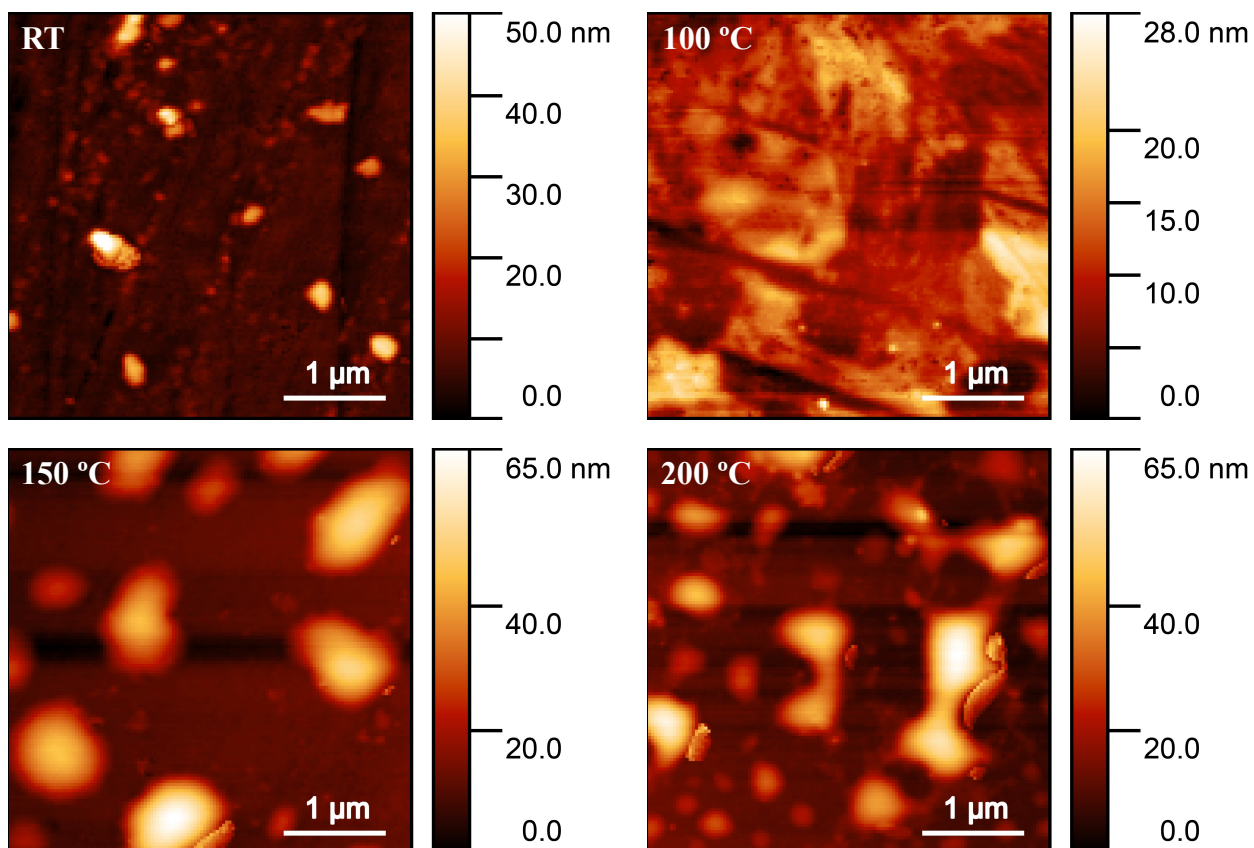


Figure 2-18: AFM images (4 μm x 4 μm) indicating relative height on films of **PMEhB** spin-coated on DOTS-modified SiO₂/Si substrates and annealed at RT, 100 °C, 150 °C, and 200 °C respectively.

PTEhB

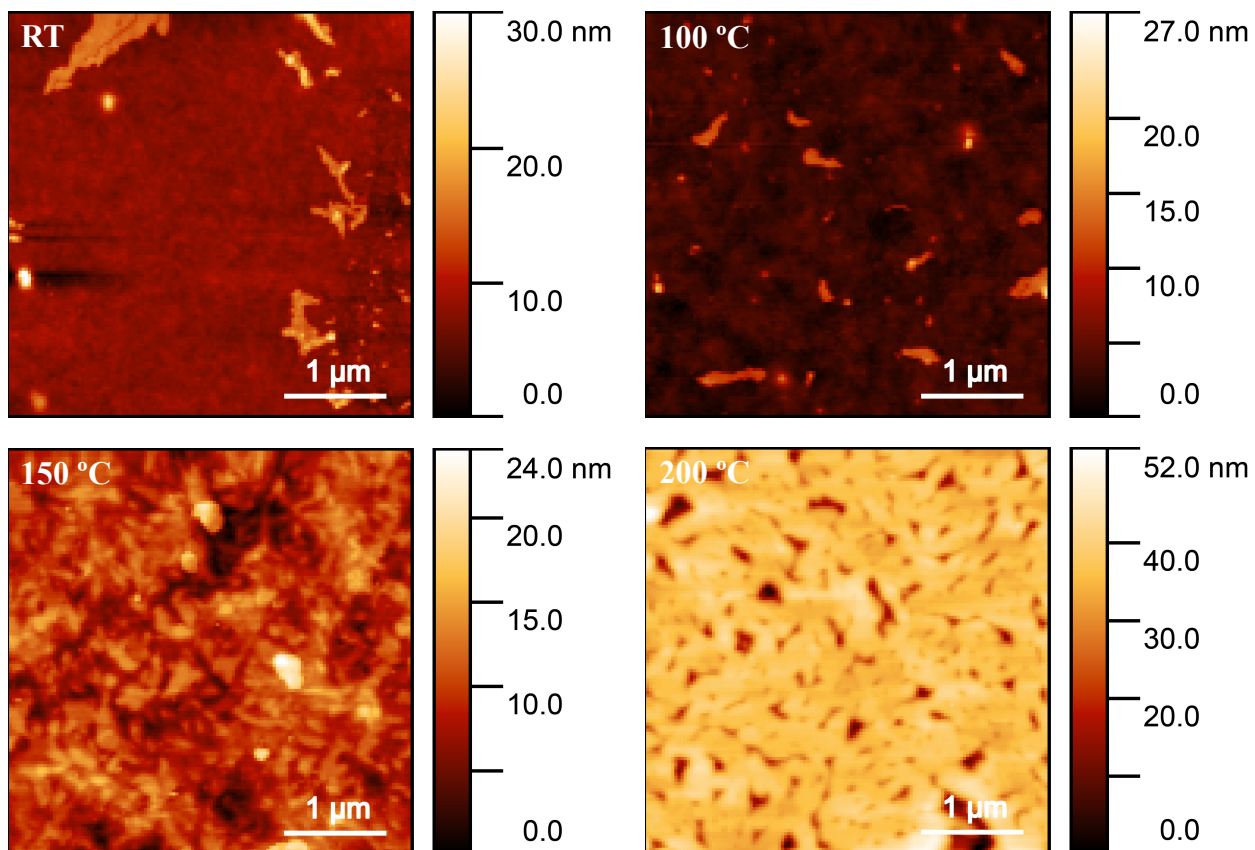


Figure 2-19: AFM images (4 μm x 4 μm) indicating relative height on films of **PTEhB** spin-coated on DDTS-modified SiO₂/Si substrates and annealed at RT 100 °C, 150 °C, and 200 °C respectively.

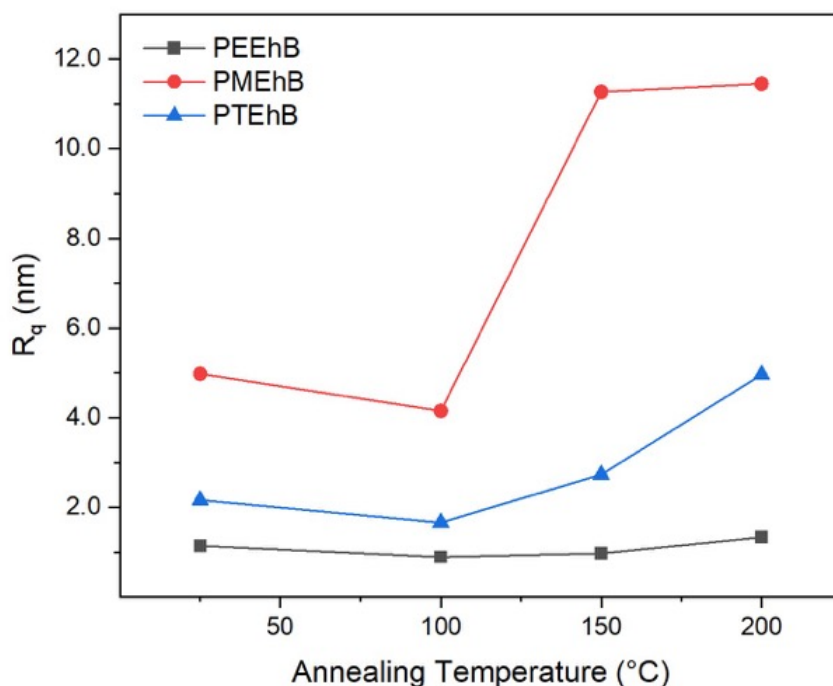


Figure 2-20: The root-mean-square surface roughness (R_q) of **PEEhB**, **PMEhB**, and **PTEhB** at each different T_α .

Table 2-5: Summary of the calculated R_q for each AFM sample of the HID polymers.

	R_{q-RT}	$R_{q-100\text{ }^\circ\text{C}}$	$R_{q-150\text{ }^\circ\text{C}}$	$R_{q-200\text{ }^\circ\text{C}}$
PEEhB	1.14 nm	0.85 nm	0.97 nm	1.33 nm
PMEhB	4.98 nm	4.15 nm	11.27 nm	11.45 nm
PTEhB	2.16 nm	1.66 nm	2.73 nm	4.96 nm

To evaluate these results, it must first be understood the impact of film roughness of the performance of organic electronic materials. It has been reported that π -conjugated materials with smoother surfaces exhibit better charge mobility and thus a smoother film is desirable¹⁴². It can be concluded that at $T_\alpha = 200\text{ }^\circ\text{C}$ the three polymer films are the roughest and thus the device performance may be negatively impacted. Furthermore, since much of the research in the field of temperature sensors is geared towards flexible applications, high temperature annealing may impact the integrity of flexible plastic substrates and thus a lower temperature process is optimal so that the films may be used more universally in these applications. At $T_\alpha = 150\text{ }^\circ\text{C}$ an increase in the film roughness is apparent, most significantly for **PMEhB** which is due to the melting

transition. At this temperature the formation of deep cracks is observed in the **PTEhB** and **PEEhB** films which explains the increased surface roughness. This may lead to the formation of discontinuous regions in the film resulting in decreased mobility. While RT annealing leads to relatively smooth films when compared to the high temperature processes ($T_\alpha = 150\text{ }^\circ\text{C}$, and $T_\alpha = 200\text{ }^\circ\text{C}$), annealing at $T_\alpha = 100\text{ }^\circ\text{C}$ exhibits the smoothest film in all three HID polymers. This temperature is also high enough to evaporate any solvent molecules on the substrate (chloroform or acetonitrile) post deposition and thus from these AFM results and the practicality of using flexible substrates $T_\alpha = 100\text{ }^\circ\text{C}$ is chosen for device fabrication.

The packing characteristics of **PEEhB**, **PMEhB**, and **PTEhB** film are indicated by the two-dimensional and one-dimensional (1D) XRD measurements shown below in **Figure 2-21**, **Figure 2-22**, and **Figure 2-23** respectively. The presence of peaks signifies crystalline domains in the film and the intensity of these peaks positively correlates with the DOC. **PEEhB** annealed at each temperature does not show any significant crystalline peak in the XRD measurements so it may be concluded that the polymer film is virtually completely amorphous and thermal treatment does not impact the packing characteristics. The **PEEhB** HID monomer **M1** has a C-C bond that locks the ring structure of the thiophene substituent group in place. Hence, it is difficult for the bonds to move and rotate on the thiophene spacer which can explain why this polymer inhibits chain packing most effectively leading to no crystalline peaks in the XRD analysis. In contrast to those results **PMEhB** shows a faint peak at $2\theta = 4.70^\circ$ (100) when annealed at $100\text{ }^\circ\text{C}$, a more intense peak at $2\theta = 4.99^\circ$ (100) when annealed at $150\text{ }^\circ\text{C}$, and the most intense peak at $2\theta = 5.08^\circ$ (100) when annealed at $200\text{ }^\circ\text{C}$. These peaks correspond to an interlayer lamellar d -spacing of 18.8 \AA , 17.7 \AA , and 17.4 \AA respectively. The methoxy substituent groups on the thiophene spacer in **M2** may also inhibit chain packing explaining why the film is not crystalline when annealed at RT. However, due to the low molecular weight and the ability of those methoxy groups to rotate freely, the polymer may orient itself into crystalline domains at elevated T_α . Hence, upon thermal treatment crystalline peaks are observed in the **PMEhB** film. Similar results are shown when evaluating the **PTEhB** measurements, however no thermal treatment is required for this film to exhibit crystallinity as peaks are observed at 4.74° , 4.66° , 4.69° , and 4.77° (100) corresponding to interlayer lamellar d -spacing of 18.6 \AA , 18.9 \AA , 18.8 \AA , and 18.5 \AA at RT, $100\text{ }^\circ\text{C}$, $150\text{ }^\circ\text{C}$, and $200\text{ }^\circ\text{C}$ respectively. This can be attributed to the lack of a substituent group on the thiophene

spacer in the **M3** structure which promotes chain packing. Interestingly, the peak intensity for the **PTEhB** measurements increases from RT to 100 °C which follows the DOC- T_α trend observed with **PMEhB**. However, the peak intensity decreases slightly when going from a T_α of 100 °C to 150 °C and decreases significantly at T_α of 200 °C. The peak intensity dropping suggests that the polymer chain may begin to undergo re-organization to more disordered chain packing. However, the AFM image for **PTEhB** with $T_\alpha = 200$ °C indicate a high degree of order. This suggests that the polymer chain may be re-organizing from predominantly edge-on orientation to a more isotropic packing orientation. This is evidence by the widening of the ring in the 2D XRD measurements as the T_α goes from 100 °C to 150 °C and the significant widening when $T_\alpha = 200$ °C indicating a reduction in edge-on orientation.

In OFET applications edge-on orientation is favorable for better charge transport between electrodes, while for OPV applications face-on orientation is preferred for better carrier transport in the vertical direction of active layers¹⁴³. In general, higher DOC semiconducting materials are desirable in both cases. Conversely, for the purposes of these polymers the amorphous films may be more advantageous. It is hypothesized that the crystalline domains, or the development of such domains upon thermal treatment, may drive the dopant molecules out of the polymer phase which would destabilize the complex and lead to reduced conductivity over time. Hence, from the results of the XRD analysis, it is postulated that the polymer:dopant complex generated with the **PEEhB** polymer may exhibit better stability due to its amorphous nature. Conveniently, this aligns with the results of the CV analysis where **PEEhB** is expected to show better dopant stability due to E_{HOMO} being high enough to generate deep traps with the proposed dopant.

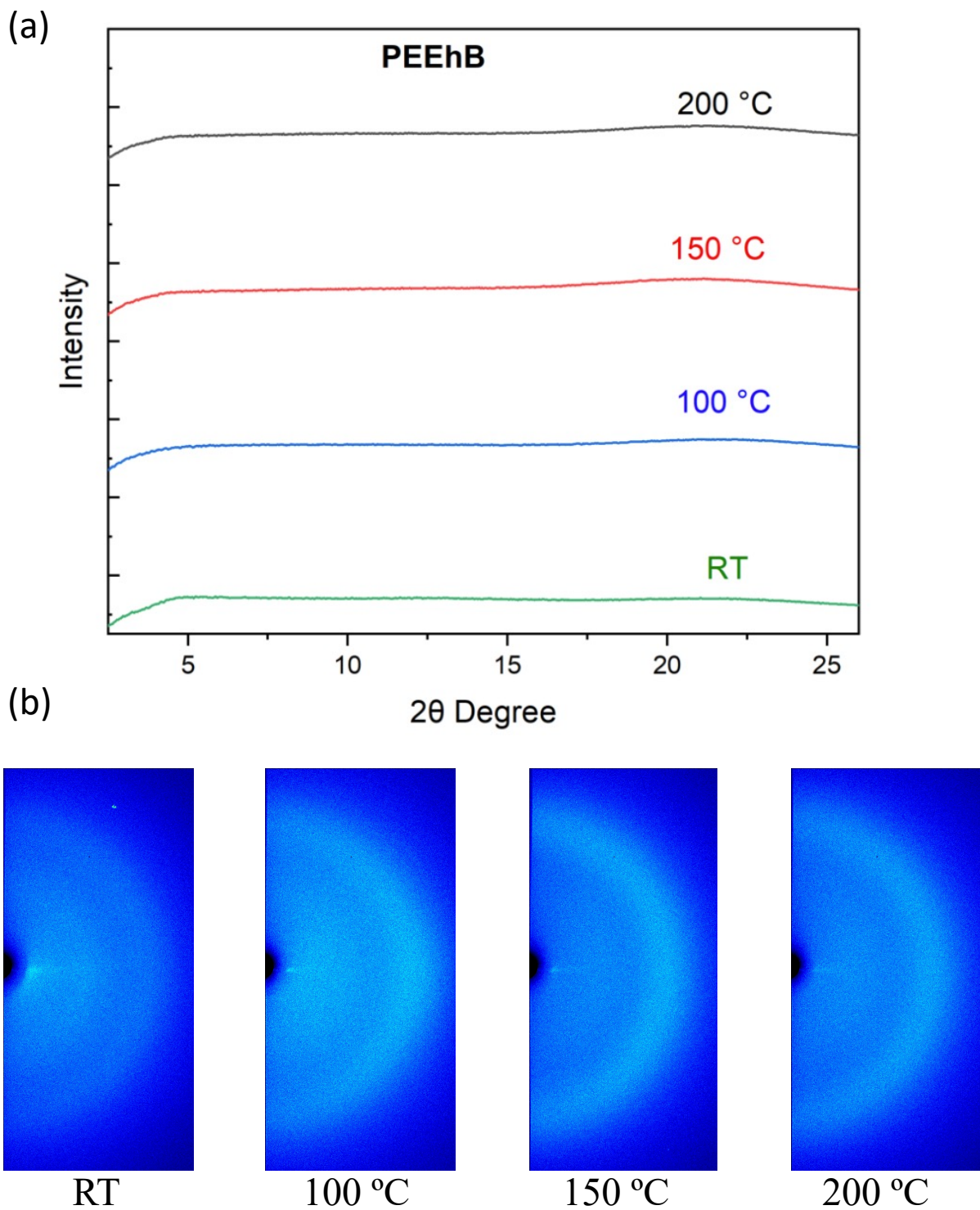


Figure 2-21: (a) One-dimensional and (b) two-dimensional XRD spectra of **PEEhB** film on DDTs-modified SiO₂/Si substrate annealed at RT, 100 °C, 150 °C, and 200 °C respectively.

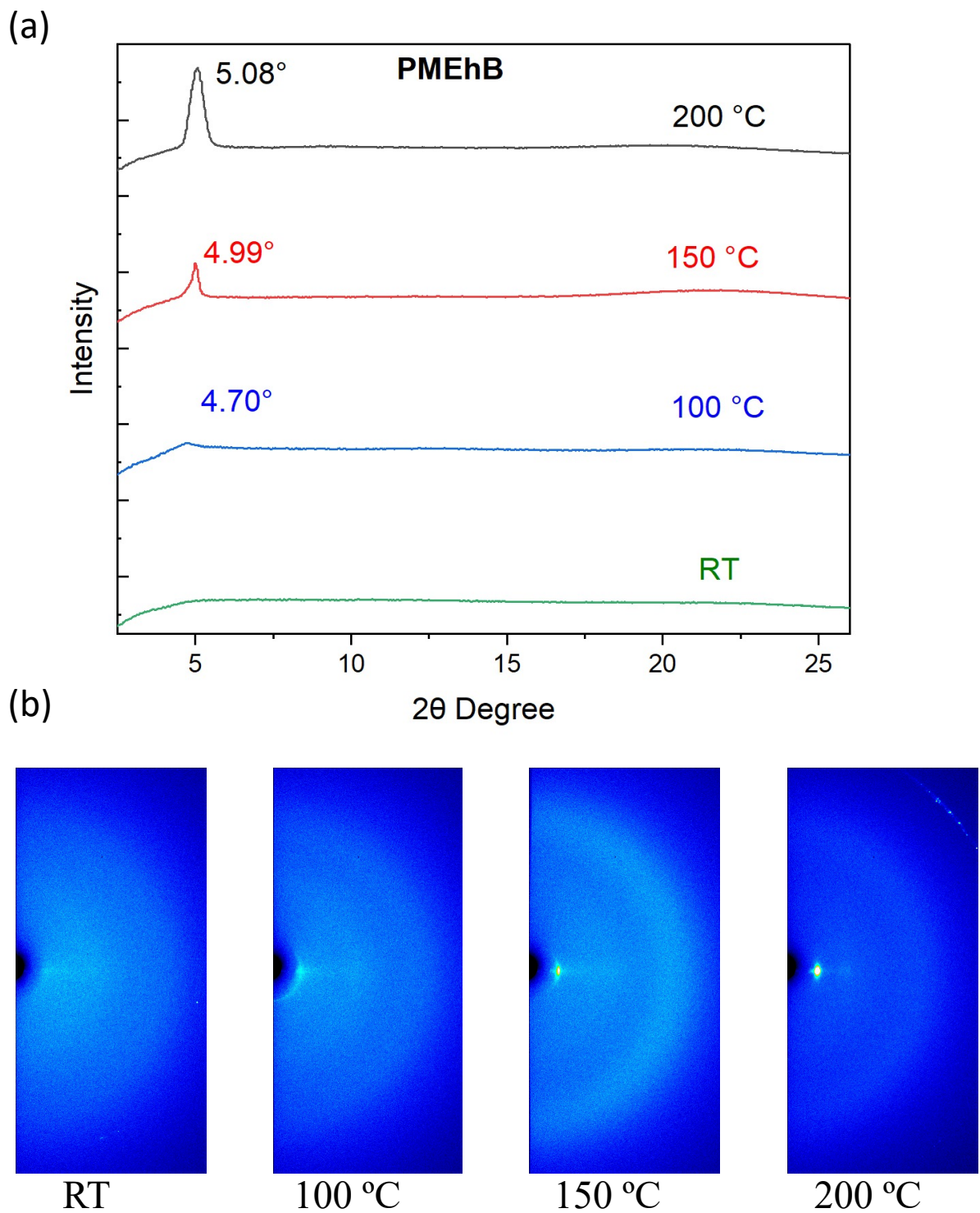


Figure 2-22: (a) One-dimensional and (b) two-dimensional XRD spectra of **PMEhB** film on DDTs-modified SiO₂/Si substrate annealed at RT, 100 °C, 150 °C, and 200 °C respectively.

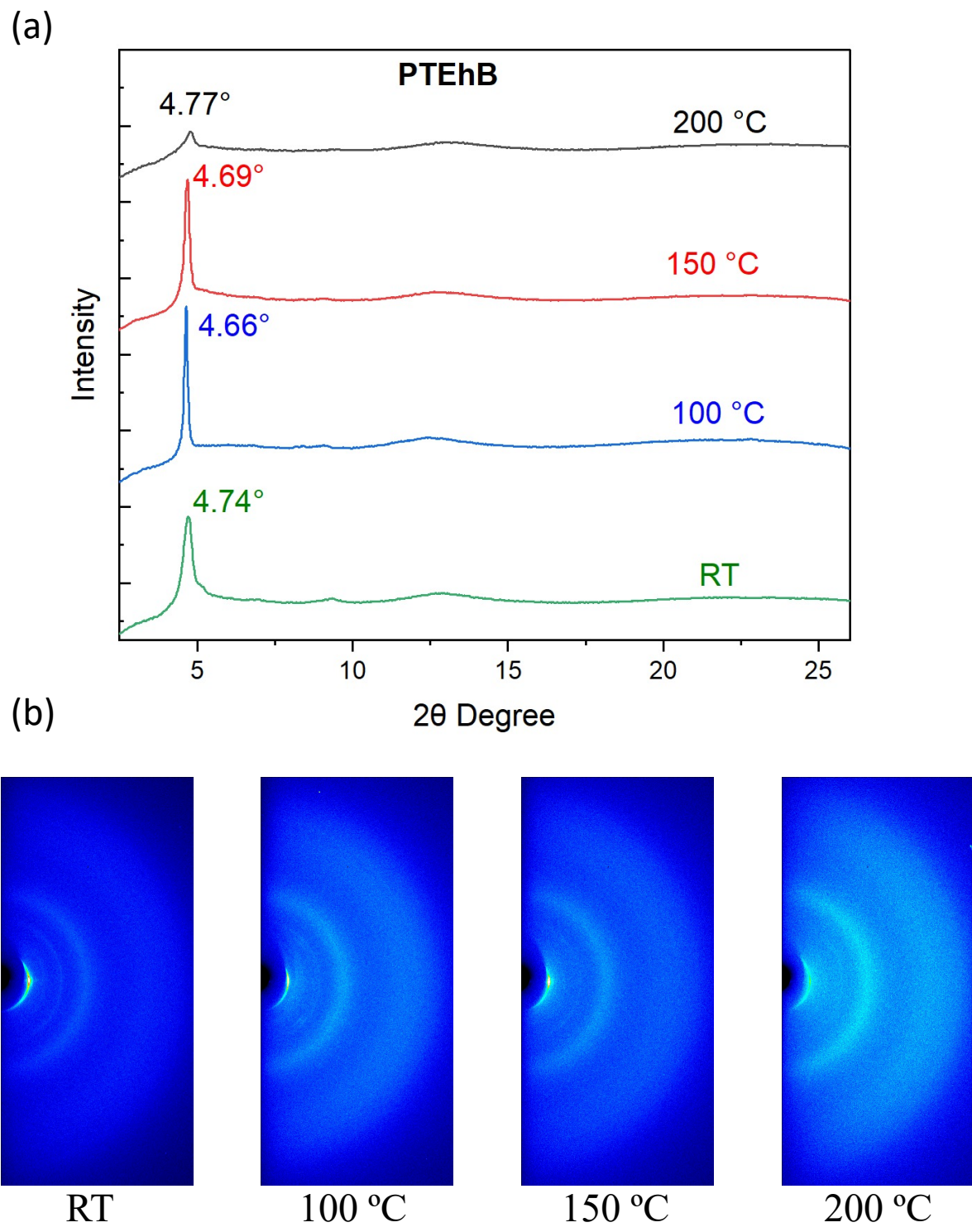


Figure 2-23: (a) One-dimensional and (b) two-dimensional XRD spectra of **PTEhB** film on DDTs-modified SiO₂/Si substrate annealed at RT, 100 °C, 150 °C, and 200 °C respectively.

2.4.3 Temperature Sensing Performance of HID Polymer Devices

The temperature sensing capabilities of each polymer doped with **F4TCNQ** were evaluated by depositing the films on interdigitated silver electrode devices with PET substrates. The sensor fabrication and experimental methodology are described in detail in section 2.6.2. A heating stage was used to increase temperature by 5-8 °C per interval and the current was allowed to stabilize for ~ 250 s per interval. All three devices exhibited a step function response where a sharp rise in current was observed as the temperature increased before the response stabilized at a current value corresponding to the heating stage temperature.

Figure 2-24, **Figure 2-25**, and **Figure 2-26** below represent the real-time current as a function of temperature (I-T) relationship for **PEEhB:F4TCNQ**, **PMEhB:F4TCNQ**, and **PTEhB:F4TCNQ**, sensors respectively. The step-function response is clearly depicted in each plot and the current at a given temperature is recorded and then plotted against the reciprocal of the absolute temperature taken to the one-quarter power ($T^{-0.25}$). This secondary plot provides the calibration curve for the sensor devices and a strong $I-T^{-0.25}$ correlation is apparent for all three devices. This agrees well with the hypothesized VRH mechanism of charge transport as proposed by Mott in 1968 where **Equation 2-4** was used to describe low temperature conductivity⁶¹:

$$\sigma = \sigma_0 e^{-\left(\frac{T_0}{T}\right)^{\frac{1}{4}}} \quad (2-4)$$

where σ_0 is the conductivity at the reference temperature T_0 and σ is the conductivity at a given temperature T . Each device exhibited this step-function response until the upper limit of their temperature working range. Above this upper limit, a sharp decrease in current was exhibited by all three devices which is referred to as the device breakdown. The device fabricated using **PEEhB:F4TCNQ** active layer showed an excellent working range as the device breakdown did not occur until after 120 °C was reached while the upper limit of both the **PMEhB:F4TCNQ** and **PTEhB:F4TCNQ** devices was only 60 °C respectively. This breakdown may be attributed to the thermal expansion of the polymer and the crystallization of the alkyl sidechains on the HID monomer units leading to the formation of insulating domains. Both of these effects will increase

the hopping distance for charge carriers which reduces their mobility^{144–146}. This is a positive-temperature coefficient (PTC) effect that conflicts with the NTC effect from the proposed VRH mechanism. At the breakdown temperature the PTC effect will begin to dominate the NTC effect and thus the device will not function as an NTC thermistor above this temperature. The device fabricated using **PEEhB:F4TCNQ** active layer has been shown to remain completely amorphous upon thermal treatment thus it is more difficult for the sidechains to interact with one another and form these insulating domains. Hence, the temperature required for the PTC effect to dominate in this device may be higher than that of the other two ordered complexes where the insulating domains may form more readily due to the polymer crystallinity.

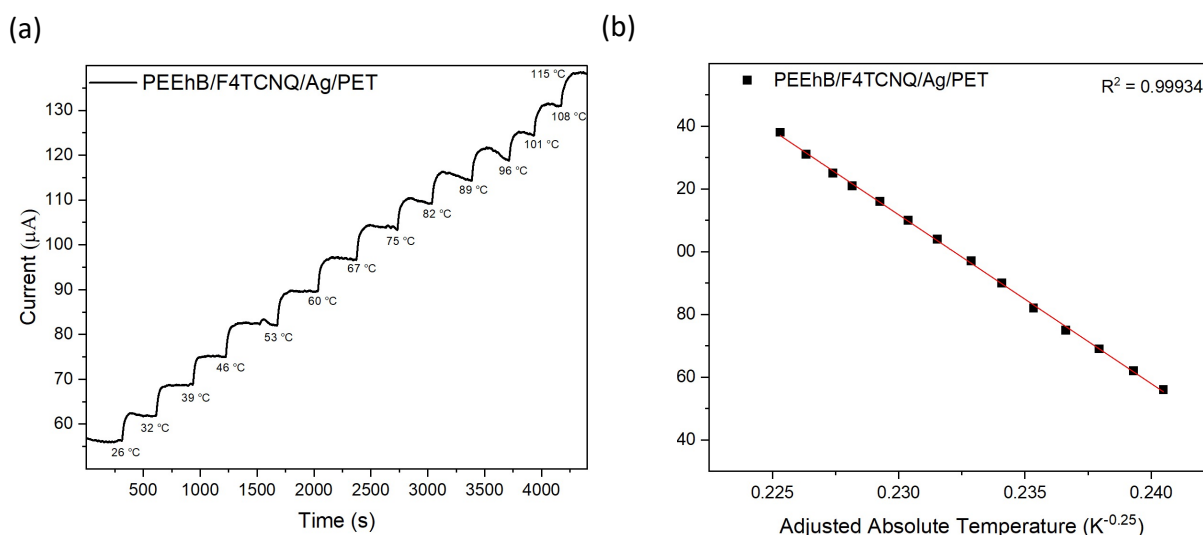


Figure 2-24: (a) Real-time current vs time (I-t) graph of **PEEhB:F4TCNQ** device at varying temperatures, (b) current vs adjusted absolute temperature ($I-T^{-0.25}$) graph of **PEEhB:F4TCNQ** interdigitated device.

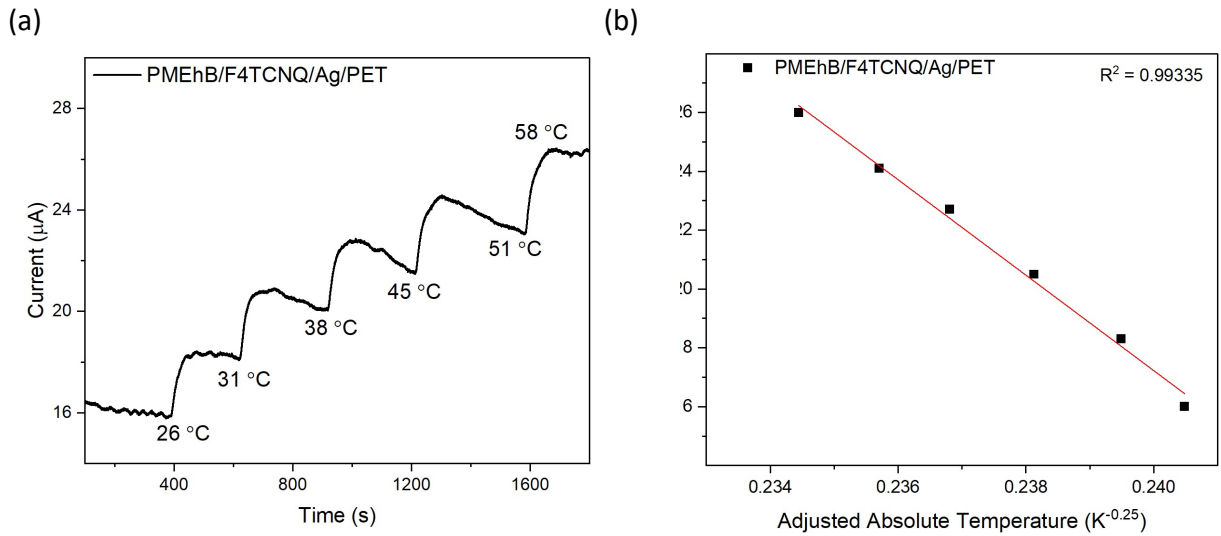


Figure 2-25: (a) Real-time current vs time (I-t) graph of **PMEhB:F4TCNQ** device at varying temperatures, (b) current vs adjusted absolute temperature ($I-T^{-0.25}$) graph of **PMEhB:F4TCNQ** interdigitated device.

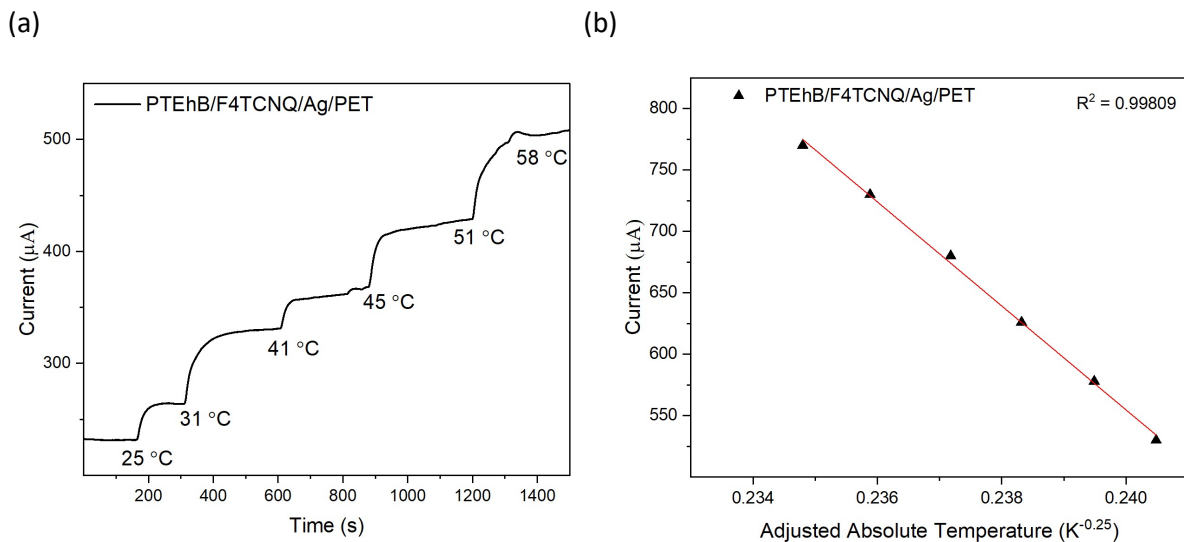


Figure 2-26: (a) Real-time current vs time (I-t) graph of **PTEhB:F4TCNQ** device at varying temperatures, (b) current vs adjusted absolute temperature ($I-T^{-0.25}$) graph of **PTEhB:F4TCNQ** interdigitated device.

The TCR of each device was estimated using the method described in section 2.6.2 and the corresponding plots are shown below in **Figure 2-27**. The response time, film thickness, working range, and initial conductivity of each device is summarized in **Table 2-6**. The response time of each device was measured to be on the order of 10s of seconds. It is determined that the

PEEhB:F4TCNQ and **PMEhB:F4TCNQ** devices displayed the highest sensitivity up to 60 °C with a TCR of $-1.09\%/^{\circ}\text{C}$ while **PTEhB:F4TCNQ** were slightly less sensitive with a TCR of $-1.02\%/^{\circ}\text{C}$. It is noted that the TCR curve of the **PEEhB:F4TCNQ** device does not follow a linear trend instead it exhibited a TCR of $-1.09\%/^{\circ}\text{C}$ at 25-60 °C and a TCR of $-0.38\%/^{\circ}\text{C}$ at 60-120 °C. This nonlinearity maybe due to the amorphous nature of the polymer itself which allows the highly disordered polymer chains to move and reorient themselves more easily at temperatures higher than 60 °C. This may lead to a large distance between polymer chains and creates a PTC effect that will reduce the sensitivity of the device at higher temperatures. It may also be noted that the low molecular weight of the **PMEhB** made the film difficult to process and it took several layers of the polymer and dopant to fabricate a practical working sensor device.

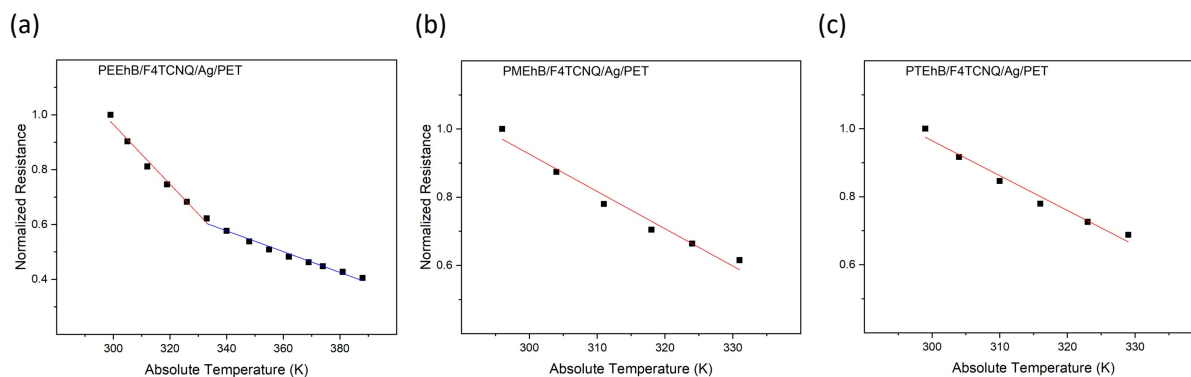


Figure 2-27: Normalized resistance vs temperature plots for TCR determination of sensor devices fabricated using (a) **PEEhB:F4TCNQ**, (b) **PMEhB:F4TCNQ**, and (c) **PTEhB:F4TCNQ**.

Table 2-6: Temperature sensing performance of the three devices fabricated on PET/Ag substrates using the HID polymers doped with **F4TCNQ**.

	Thickness (nm)	Working Range (°C)	TCR (%/°C)	Response Time (s)	Conductivity (S/cm)
PEEhB:F4TCNQ	43	25 - 60 60 -120	-1.09 ± 0.07 -0.38 ± 0.02	54.4 ± 10.9	1.23×10^{-3}
PMEhB:F4TCNQ	82	25 - 60	-1.09 ± 0.09	24.2 ± 8.8	2.26×10^{-4}
PTEhB:F4TCNQ	55	25 - 60	-1.02 ± 0.08	97.2 ± 14.4	1.15×10^{-2}

The polymer:dopant complex stability was evaluated by measuring the conductivity of the device periodically every four days and plotting the normalized conductivity over a thirty-two-day period. The results of this stability study are shown in **Figure 2-28** below. It may be noted that the devices were stored under ambient conditions in a petri dish with no encapsulation layer to best mimic environmental settings that sensors would be exposed to. The **PTEhB:F4TCNQ** complex remained stable after four days but beyond that, underwent a steady degradation in conductivity to below 20% of its original value after thirty-two days. The **PMEhB:F4TCNQ** device showed better stability as the device remained stable for twelve days before significant degradation occurred. The degradation of this device occurred at a much slower rate than that of **PTEhB:F4TCNQ** and the conductivity was only reduced to roughly 60% of its original value by the end of the study period. The device using **PEEhB:F4TCNQ** maintains a constant conductivity, within measurement error, over the thirty-two-day period. The E_{HOMO} of the **PEEhB** polymer was the only one that met the criteria for forming deep traps with the **F4TCNQ** dopant and hence it is not surprising that it was the only polymer to form a stable complex with the dopant. However, **PTEhB** had a higher lying E_{HOMO} than **PMEhB** so that it would be expected that **PTEhB** should exhibit better time stability. This was not case in this study as the **PTEhB:F4TCNQ** complex deteriorated much faster and more significantly than the **PMEhB:F4TCNQ** complex. Therefore, the E_{HOMO} of the polymer alone cannot be used to predict the stability of the polymer:dopant complex for these materials. The results indicate that the crystallinity of the polymer thin film does indeed play a significant role in engineering a stable complex. The **PEEhB** polymer was virtually completely amorphous while the **PMEhB** polymer exhibited increasing crystallinity upon thermal treatment and the **PTEhB** film was crystalline at RT with its highest crystallinity being at $T_{\alpha} = 100$ °C. The DOC of the polymer film (**PTEhB** > **PMEhB** > **PEEhB**) may be directly correlated to the instability of the polymer:dopant complex as the result supports the hypothesis that crystalline domains drive the dopant molecules out of the polymer phase. While further investigation is necessary to quantify the significance of E_{HOMO} and DOC relative to each other in forming stable complexes with this family of polymers, it can be concluded that HID polymers consisting of mostly amorphous domains are more successful at retaining dopant molecules and thus display better complex stability over time.

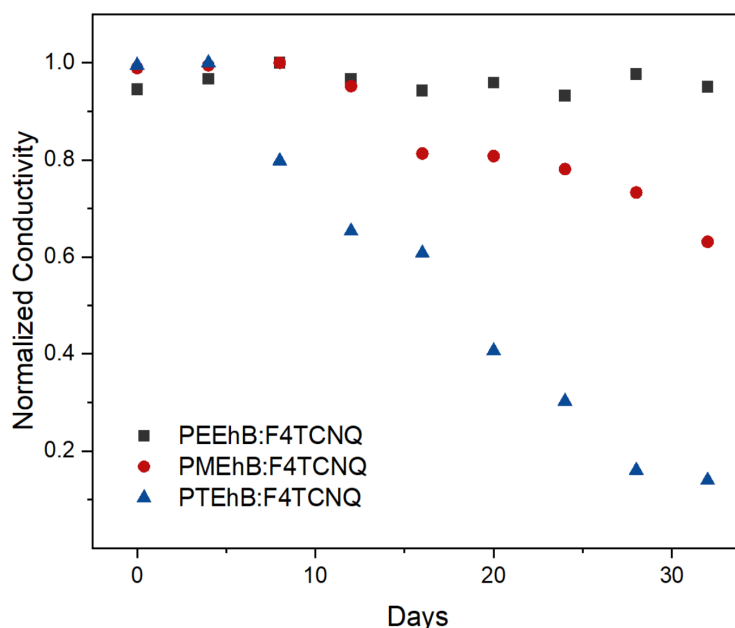


Figure 2-28: Conductivity vs. time stability of **PEEhB:F4TCNQ**, **PMEhB:F4TCNQ**, and **PTEhB:F4TCNQ**.

2.5 Summary and Future Directions

The synthesis of three new D-A copolymers **PEEhB**, **PMEhB**, and **PTEhB** is reported using HID acceptor and **DDOBT** donor units. E_{HOMO} of the polymers are calculated to be 4.72 eV, 5.05 eV, and 4.95 eV respectively. All three polymers exhibit a narrow E_g which are calculated to be 1.41 eV, 1.43 eV, and 1.48 eV respectively using UV-Vis-NIR absorption spectroscopy. The three polymers are relatively low molecular weight (< 10 kDa) materials and are processable in chlorinated solvents such as chloroform or chlorobenzene.

The polymers may be doped using p-type dopant **F4TCNQ** to fabricate conductive films of polymer:dopant complexes **PEEhB:F4TCNQ**, **PMEhB:F4TCNQ**, and **PTEhB:F4TCNQ** which are coated onto PET substrates with interdigitated silver electrodes to create NTC-type temperature sensors or thermistors. The current response of all three devices displayed a strong temperature dependence ($I \propto T^{-0.25}$) between 25-60 °C for **PTEhB** and **PMEhB** and between 25-120 °C for **PEEhB**. The devices also displayed excellent sensitivity to ambient temperatures up to 60 °C with TCRs between -1.02 %/°C to -1.09 %/°C. Above 60 °C, the device fabricated using

PEEhB:F4TCNQ as the active layer exhibited nonlinearity and the TCR decreased to $-0.38\%/^{\circ}\text{C}$ between $60\text{-}120\text{ }^{\circ}\text{C}$ while the other two devices with **PMEhB:F4TCNQ** and **PTEhB:F4TCNQ** active layers experienced device breakdown above $60\text{ }^{\circ}\text{C}$. These TCR values are quite good for organic thermistors^{76,147,148} and they may partially be attributed to the thin PET substrate that allows for better heat transfer from the heating stage to the active layer compared to thicker rigid substrates.

The device stability over time was assessed by monitoring the conductivity and it was determined that while the **PEEhB:F4TCNQ** complex may remain stable for over thirty-two days, the **PMEhB:F4TCNQ** and **PTEhB:F4TCNQ** complexes degrade after twelve and four days respectively. A relationship between DOC and polymer:dopant stability is established in that amorphous polymers hold onto dopant molecules more tightly as the crystalline domains drive out dopant molecules to destabilize the complex. Therefore, it may be concluded these polymers with lower DOC minimize the effect of phase segregation in the polymer:dopant complex and are thus better suited for long-term sensing applications where dopants are required to synthesize a conductive film.

These novel polymers exhibited tremendous real-time sensitivity and the thin film sensors show potential for applications for accurate temperature monitoring. These sensors on the highly flexible PET substrate may also lend themselves towards wearable electronic devices and artificial e-skin applications using thermal arrays for tactile sensing^{19,20,27}. Future work on these materials should aim to take advantage of this polymer:dopant complex stability-DOC relationship by synthesizing highly amorphous polymers. This may be done by using monomers with a high degree of geometric isomerism which can reduce the DOC in the corresponding copolymer. Other potential avenues for future work may include different functionalization on the HID acceptor monomers at the nitrogen atom or on the thiophene spacer unit to improve the sensitivity of the film or to work towards developing HID-based sensor devices for various other analytes such as ion detection, gas sensing, and chemical sensing, amongst others.

2.6 Experimental Section

2.6.1 Materials and Characterization

Materials

All chemicals used in the synthesis procedures were purchased from Sigma-Aldrich, VWR, TCI, Fluka, and Armstrong. Solvents used during synthesis procedures were analytical grade and anhydrous or used as received. Solvents used for the fabrication of devices or setting up any samples for characterization experiments were HPLC grade. Arsenic n-doped 6-inch silicon dioxide wafers with 300 nm polished oxide layers were purchased from the University of Waterloo. All column chromatography purification procedures were performed using silica gel (230-400 mesh) slurries purchased from the University of Waterloo.

High Temperature Gel Permeation Chromatography (HT-GPC)

HT-GPC analysis was performed to obtain the molecular weight characteristics of each of the three polymers. The chromatograms provide details on the number average (M_n) and weight average (M_w) molecular weight of each polymer, and the polydispersity index (PDI) is calculated using the two. The measurements were performed using a Viscotek Malvern 350 HT-GPC system with 300 mm Jordi Gel DVB Mixed Bed liquid chromatography column. 1,2,4-trichlorobenzene was used as the eluent for polystyrene standards at 150 °C and the samples were detected using a refractive index (RI) detector.

Atomic Force Microscopy (AFM)

Atomic force microscopy (AFM) images were taken using a Dimension 3100 scanning probe microscope. AFM analysis was used for the determination of the surface morphology and roughness of the thin film samples. The films used for AFM were spin-coated on a bare or dodecyltrichlorosilane modified $\text{SiO}_2/\text{p}^{++}\text{Si}$ substrate.

X-Ray Diffraction (XRD)

The X-Ray diffraction (XRD) measurements were conducted using a Bruker D8 Advance diffractometer with Cu K α radiation ($\lambda = 0.15418$ nm) with the polymer films spin coated onto dodecyltrichlorosilane modified SiO₂/p++Si substrates annealed at different temperatures.

Nuclear Magnetic Resonance (NMR) Spectroscopy

¹H NMR analysis is conducted for structural identification and purity confirmation of the target compounds routinely after each synthesis step. The samples are dissolved in either deuterated chloroform (CDCl₃, ALDRICH 99.8% atom % D, contains 0.1 % (v/v) TMS) or deuterated dimethoxy sulfoxide (DMSO-d₆, ALDRICH, 99.5% atom % D, contains 0.1 % (v/v) TMS). The NMR spectra is recorded using a Bruker 300 Ultrashield 300 MHz FT-NMR spectrometer.

Differential Scanning Calorimetry (DSC)

Differential scanning calorimetry (DSC) was used to determine melting temperature (T_m) and crystallization temperature (T_c) of materials in this work. A TA Instruments Q20 Differential Scanning Calorimeter was used to take these measurements. The samples were scanned for one heating and one cooling cycle under nitrogen atmosphere at a rate of 10 °C min⁻¹.

Cyclic Voltammetry (CV)

Cyclic voltammetry (CV) is used to determine the oxidative potentials for the synthesized polymers to establish the E_{HOMO}. The samples are casted on a platinum (Pt) working electrode as a thin film and submersed in a 0.1M tetrabutylammonium hexafluorophosphate (Bu₄NPF₆) solution in HPLC grade acetonitrile as the electrolyte. The scan rate is 50 mV/s between -1.6 to 1.6 V and Ferrocene is used as the internal standard with a known E_{HOMO} of -4.80 eV. The reference electrode is silver/silver chloride while the auxiliary electrode is a blank platinum rod.

Ultraviolet-Visible-Near-Infrared (UV-Vis-NIR) Spectroscopy

The UV-Visible-NIR spectroscopy measurements are conducted using a Thermo Scientific GENESYS™ 10S VIS spectrophotometer or using the Cary 7000 UMS UV-Vis-NIR spectrophotometer. Solutions are prepared using chloroform as the solvents while thin films are prepared via either spin-coating or drop-casting the sample solution onto a thin glass slide and

using a blank glass slide as the reference. The optical E_g for each polymer is obtained using the UV-Vis-NIR spectra in which the λ_{onset} is used to estimate E_g .

Film Thickness Determination

Film thickness of the sensor devices is determined using an Alpha-Step D-500 Profiler. The PET substrate is fixed onto a glass slide as a thicker surface is required for an accurate measurement. The film is scratched off both ends of the device to leave behind just the substrate surface. The tip of the profiler is swept across both ends of the device at a scan rate of 0.03 mm/s starting and finishing on the scratched off areas of the device.

2.6.2 Fabrication of Temperature Sensor Devices

The thermistors used in this chapter were fabricated on polyethylene terephthalate (PET) substrates with interdigitated bottom/top-contact silver (Ag) electrodes that were provided to us by the NSERC-Green Electronics Network (GreEN) network to design flexible, more environmentally friendly devices. The fabrication procedure as described by the GreEN network consists of using silver (Ag) nanoparticle ink in water procured from NovaCentrix (PFI500). The ink is transferred onto a printing form to define the pattern information. The devices are then printed with an OMET Varyflex V2 Roll-to-Roll (R2R) Continuous Press with flexography printing units at a speed of 15 m/min on a 125 μm -thick PET substrate. The printed devices are then dried in-line with hot air at a temperature of 100 °C and the produced samples have a conductivity of 4.40 MS/m with a thickness of 352 nm¹⁴⁹.

The device substrates used in this work had a W/L ratio of 10,000 and were first cleaned using ultrasonication in DI water, isopropanol, and then acetone each for 15 min. Due to the size of the devices spin coating was not very practical given the size of the spin coater used in the PEML laboratory. Instead, 40 μL of a 5 mg/mL solution **PEEhB/PMEhB/PTEhB** in chloroform was casted onto the substrate and then a clean glass slide is lightly dragged back and forth to across the substrate to mimic blade coating. Once the solvent has evaporated (\sim 30 s of blade coating) the device is then thermally annealed at 100 °C for 30 min. The sample is then washed with ethanol before the doping procedure. To dope the sample 40 μL of a 1 mg/mL solution of **F4TCNQ** in

acetonitrile was casted onto the organic film using the same blade coating technique to deposit the dopant until the solvent evaporates. Once the acetonitrile is evaporated the device is annealed at 100 °C for 30 mins to remove any excess solvent. The process of depositing the polymer films and doping them is depicted below in **Figure 2-29**.

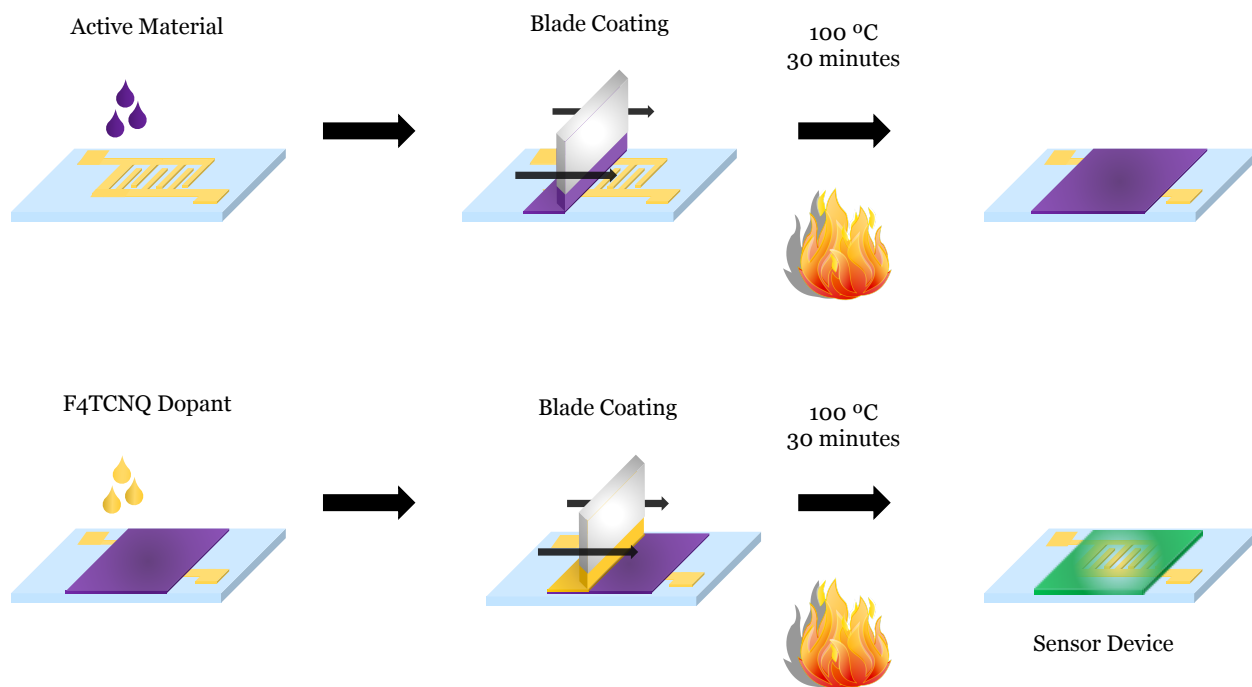


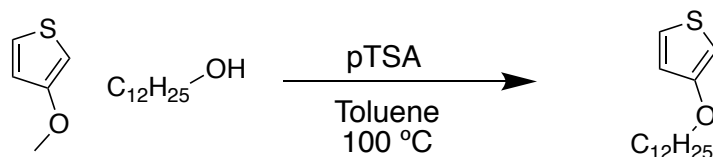
Figure 2-29: Process flow schematic for the blade-coating preparation of the doped HID polymer films onto the flexible PET/Ag substrates provide by the NSERC Green Electronics Network (GreEN).

The thermal sensing of the device was done using ambient conditions outside of a glovebox. The device is placed on a heating stage and a thermal probe is placed on the device surface connected to a Uni-T UT33C Multimeter to yield a temperature readout. The electrodes of the sensor are connected to an Agilent B2912A Precision Source/Measure Unit. A current versus time measurement (I-t) is conducted to first establish a stable baseline before the heating stage temperature is set to ~ 26 °C to begin temperature measurement. Once the current stabilizes to the corresponding temperature the device is left at that temperature for ~ 250 s before the heating stage is turned up by 5-8 °C per interval. This procedure is repeated until a temperature is reached where the current readout is no longer stable which also defines the working range of each thermistor.

At each interval the temperature and IV response are recorded so that resistance may be determined. The resistance values are normalized and then plotted against absolute temperature. This data is fitted via linear regression and the slope is taken as the estimated TCR of the device. This method for TCR determination was adapted from Wang et al.¹⁵⁰ To evaluate the time stability of the temperature sensor devices the I-V response is measured at room temperature in ambient conditions with no encapsulation layer. The conductivity of the device is determined, and this measurement is repeated every four days for thirty-two days. The conductivity values are then normalized over this time frame, and this is plotted to determine whether or not the polymer:dopant complex has degraded over time.

2.6.3 Synthesis Procedures

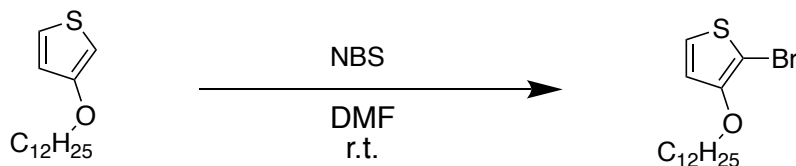
Synthesis of 3-(dodecyloxy)thiophene (3DDT)



A solution of 3-methoxythiophene (3.00 g, 26.3 mmol), dodecanol (19.6 g, 105.1 mmol), and p-toluene sulfonic acid (450 mg, 2.63 mmol) in 25 mL anhydrous toluene all in a 100 mL three-neck oven-dried round bottom flask was heated to 100 °C using a silicon oil bath. The mixture was allowed to react at temperature overnight before being extracted with chloroform and washed with DI water and saturated sodium bicarbonate. The solvent was removed with the rotary evaporator and the mixture was purified via flash column chromatography using pure hexane as the eluent to afford a white crystal material as the 3-(dodecyloxy)thiophene product. Yield: 5.03 g (71.1%)

¹H NMR (300 MHz, chloroform-*d*) δ 7.19 (dd, 1H), 6.77 (dd, 1H), 6.25 (dd, 1H), 3.96 (t, 2H), 1.79 (m, 2H), 1.40 (m, 18H), 0.91 (t, 3H)

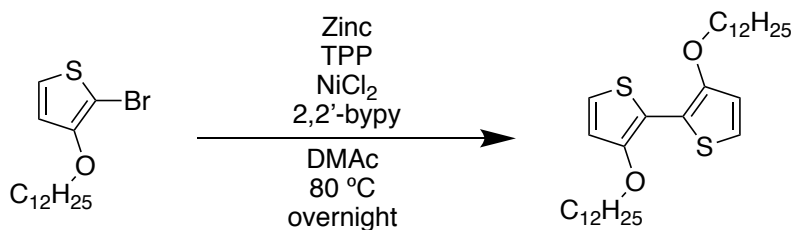
Synthesis of 2-bromo-3-(dodecyloxy)thiophene (3DDT-Br)



A solution of 3-(dodecyloxy)thiophene (2.50 g, 9.31 mmol) and N-bromosuccinimide (1.66 g, 9.31 mmol) was dissolved in 20 mL of anhydrous DMF in a 100 mL three-neck oven-dried round bottom flask and was stirred vigorously at room temperature while being monitored via TLC. After two hours the starting material was fully consumed, and the mixture was extracted with diethyl ether and washed with DI water and saturated sodium bicarbonate solution then further purified via flash column chromatography using hexane as the eluent to afford a yellow-white crystal as the 2-bromo-3-(dodecyloxy)thiophene product. Yield: 1.97 g (61.0%)

$^1\text{H NMR}$ (300 MHz, chloroform-*d*) δ 7.20 (d, 1H), 6.77 (t, 1H), 4.05 (t, 2H), 1.76(dd, 2 H), 1.41 (m, 19H), 0.90 (t, 3H)

Synthesis of 3,3'-Bis(dodecyloxy)-2,2'-bithiophene (DDOBT)

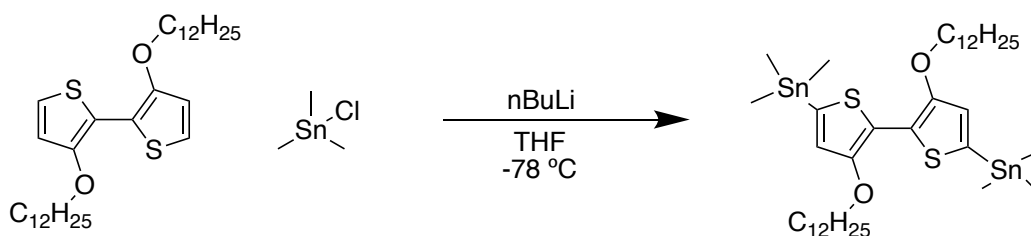


To a solution of 2-bromo-3-(dodecyloxy)thiophene (830 mg, 2.40 mmol) in 15 mL of anhydrous dimethylacetamide, zinc powder (941 mg, 14.39 mmol), triphenylphosphine (377 mg, 1.44 mmol), nickel(II) chloride (62 mg, 0.48 mmol), and 2,2'-bipyridine (75 mg, 0.48 mmol) were all added in a 50 mL oven-dried two-neck round bottom flask. The mixture was heated to 80 °C and reacted overnight before water was added to quench the reaction. The mixture was filtered, and the black solid was dissolved using isopropanol and washed again with isopropanol. The filtrate was collected, and the solvent was removed before the product was purified via flash column

chromatography with hexane as the eluent to afford a yellow solid as the 3,3'-bis(dodecyloxy)-2,2'-bithiophene. Yield: 266 mg (41.4%)

$^1\text{H NMR}$ (300 MHz, chloroform-*d*) δ 7.05 (d, 2H), 6.81 (d, 2H), 4.07 (t, 4H), 1.81 (dd, 4H), 1.24 (s, 38H), 0.86 (t, 8H)

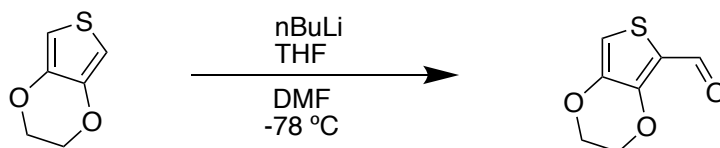
Synthesis of (3,4'-bis(dodecyloxy)-[2,2'-bithiophene]-5,5'-diyl)bis(trimethylstannane) (DDOBT-TMT)



A solution of 3,3'-bis(dodecyloxy)-2,2'-bithiophene (200 mg, 0.37 mmol) in 10 mL of THF all in a two-neck oven-dried 50 mL round bottom flask was cooled to $-78\text{ }^\circ\text{C}$ using a dry ice in acetone bath. *N*-butyllithium (0.33 mL, 0.82 mmol) was added dropwise over the course of 15 minutes and the reaction was allowed to mix at $-78\text{ }^\circ\text{C}$ for two hours. A solution of trimethyltin chloride (0.93 mL, 0.93 mmol) in 10 mL THF was added dropwise to the mixture and the dry ice bath was removed allowing the mixture to warm up and react for 90 minutes. The reaction mixture was extracted with DCM and washed with DI water and brine and the organic layer was dried using anhydrous sodium sulfate drying salt. The solvent was removed via rotary evaporation and the product was recrystallized using hexane to afford a brown crystal solid as the (3,4'-bis(dodecyloxy)-[2,2'-bithiophene]-5,5'-diyl)bis(trimethylstannane) product. Yield: 266 mg (65.2%)

$^1\text{H NMR}$ (300 MHz, chloroform-*d*) δ 6.86 (s, 2H), 4.09 (t, 4H), 1.83 (m, 4 H), 1.40 (m, 36H), 0.86 (t, 6H), 0.34 (m, 18H)

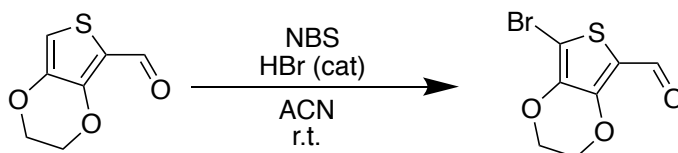
Synthesis of 2,3-dihydrothieno[3,4-b][1,4]dioxine-5-carbaldehyde (EDOT-CHO)



A solution of 3,4-ethylenedioxythiophene (1.50 g, 10.55 mmol) in 20 mL of anhydrous THF all in a 100 mL oven dried three-neck round bottom flask was cooled to -78 °C using a dry ice in acetone bath. N-butyllithium 2.5 M in hexanes (4.22 mL, 10.55 mmol) was added dropwise through the auxiliary neck over the course of 30 minutes. The mixture was left to stir vigorously for two hours when it became a pale slurry. Anhydrous DMF (3.08 g, 42.20 mmol) was added quickly to the mixture and the mixture was left to react for another two hours. The reaction is quenched by adding DI water and extracted with DCM then washed with DI water twice. The mixture is dried over anhydrous sodium sulfate drying salt and recrystallized using DCM/methanol to afford 2,3-dihydrothieno[3,4-b][1,4]dioxine-5-carbaldehyde as a white crystal product. Yield: 1.19 g, (66.1%)

¹H NMR (300 MHz, chloroform-*d*) δ 10.00 (d, 1H) 6.82 (s, 1H), 4.35 (m, 4H)

Synthesis of 7-bromo-2,3-dihydrothieno[3,4-b][1,4]dioxine-5-carbaldehyde (EDOT-CHO-Br)

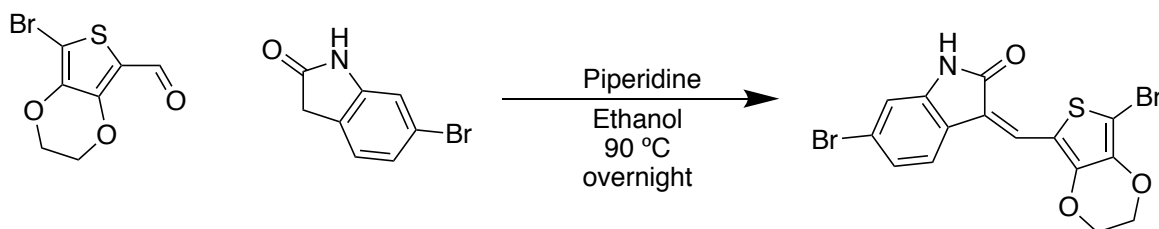


A solution of 2,3-dihydrothieno[3,4-b][1,4]dioxine-5-carbaldehyde (1.00 g, 5.876 mmol) and N-Bromosuccinimide (1.15 g, 6.464 mmol) in 20 mL of anhydrous acetonitrile in a 100 mL oven dried three-neck round bottom flask was stirred and a single drop of 48% hydrobromic acid was added as a catalyst to the reaction. The reaction was monitored by TLC and when the starting material was consumed DI water was added to quench the reaction and DCM was used to extract

the mixture which was then washed with DI water and saturated sodium bicarbonate solution before drying with anhydrous sodium sulfate drying salt. The solvent was removed using rotary evaporation and the further purified via flash column chromatography using hexane: ethyl acetate (4:1) to yield 7-bromo-2,3-dihydrothieno[3,4-*b*][1,4]dioxine-5-carbaldehyde as a light tan crystal product. Yield: 1.29 g (88.1%)

^1H NMR (300 MHz, chloroform-*d*) δ 9.85 (s, 1H), 4.39 (m, 4H)

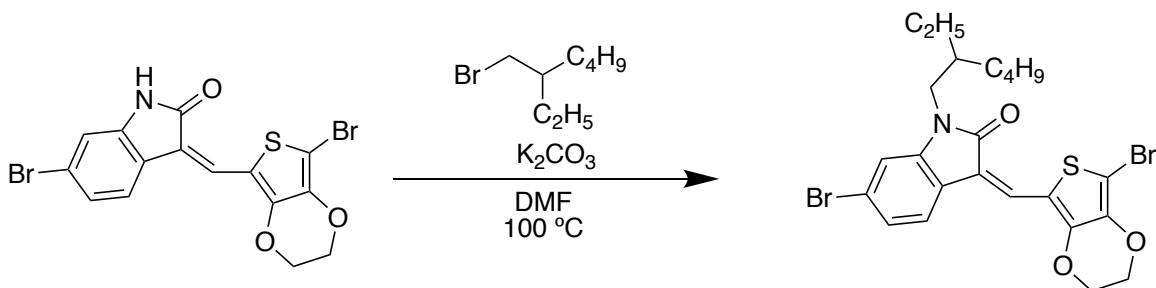
Synthesis of (Z)-6-bromo-3-((7-bromo-2,3-dihydrothieno[3,4-*b*][1,4]dioxin-5-yl)methylene)indolin-2-one (EEI-dBr)



7-bromo-2,3-dihydrothieno[3,4-*b*][1,4]dioxine-5-carbaldehyde (1.00 g, 4.02 mmol) and 6-bromooxindole (851 mg, 4.02 mmol) were dispersed in 30 mL of anhydrous ethanol in a 100 mL oven-dried two-neck round bottom flask. Piperidine (820 mg, 4.82 mmol) was added to the dispersion dropwise over the course 10 minutes and the dispersion was then heated to 90 °C using a silicon oil bath. The mixture was left to react overnight when the mixture became an orange slurry which was allowed to cool to room temperature before being filtered to afford a single isomer of (Z)-6-bromo-3-((7-bromo-2,3-dihydrothieno[3,4-*b*][1,4]dioxin-5-yl)methylene)indolin-2-one as an orange crystal product. Yield: 1.63 g (91.6%)

^1H NMR (300 MHz, dimethyl sulfoxide-*d*₆) δ 10.77 (s, 1H), 7.79 (s, 1H), 7.61 (s, 1H), 7.13 (s, 1H), 6.99 (s, 1H), 4.42 (dd, 4H)

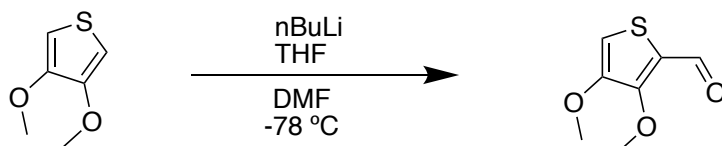
Synthesis of 6-bromo-3-((7-bromo-2,3-dihydrothieno[3,4-*b*][1,4]dioxin-5-yl)methylene)-1-(2-ethylhexyl)indolin-2-one (M1)



(Z)-6-bromo-3-((7-bromo-2,3-dihydrothieno[3,4-*b*][1,4]dioxin-5-yl)methylene)indolin-2-one (250 mg, 0.56 mmol) and potassium carbonate (187 mg, 1.36 mmol) were dissolved in 10 mL anhydrous DMF in a 25 mL two-neck oven-dried round bottom flask and the mixture is stirred at room temperature for 20 minutes before heating the mixture to 100 °C using a silicon oil bath. 2-ethylhexyl bromide (131 mg, 0.68 mmol) is added dropwise to the solution over the course of 15 minutes and the reaction is monitored using TLC. Upon the full consumption of the starting material the solution is cooled to room temperature and filtered out with the organic portion being collected then washed with DI water and brine. The solvent was removed and the crude product was precipitated using a minimum amount of methanol before further purification via flash column chromatography using hexane: ethyl acetate (1:1) as the eluent to yield a red-orange crystal material as a mixture of Z and E (~ 7:1, Z:E ratio) isomers of 6-bromo-3-((7-bromo-2,3-dihydrothieno[3,4-*b*][1,4]dioxin-5-yl)methylene)-1-(2-ethylhexyl)indolin-2-one as the product. Yield: 174 mg (55.6%)

¹H NMR (300 MHz, chloroform-*d*) δ 7.93/7.73 (s, 1H), 7.91/7.13 (d, 1H), 7.35/7.17 (d, 1H), 6.93 (s, 1H), 4.34 (q, 4H), 3.60 (m, 2H), 1.84 (s, 1H), 1.30 (m, 8 H), 0.89 (dd, 6 H)

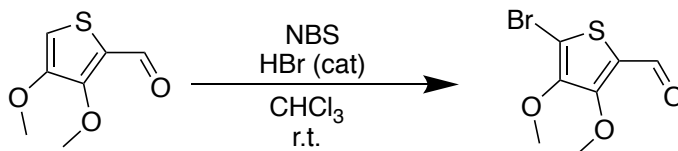
Synthesis of 3,4-dimethoxythiophene-2-carbaldehyde (3,4-DMT-CHO)



A solution of 3,4-dimethoxythiophene (2.50 g, 17.34 mmol) in 30 mL of anhydrous THF all in a 100 mL oven dried three-neck round bottom flask was cooled to -78 °C using a dry ice in acetone bath. N-butyllithium 2.5 M in hexanes (7.28 mL, 18.205 mmol) was added dropwise through the auxiliary neck over the course of 30 minutes. The mixture was left to stir vigorously for two hours when it became a pale slurry. Anhydrous DMF (5.07 g, 69.35 mmol) was added quickly to the mixture and the mixture was left to react for another two hours. The reaction is quenched by adding DI water and extracted with DCM then washed with DI water twice. The mixture is dried over anhydrous sodium sulfate drying salt and recrystallized using DCM/methanol to afford 3,4-dimethoxythiophene-2-carbaldehyde as a light tan crystal product. Yield: 2.07 g (69.5%)

$^1\text{H NMR}$ (300 MHz, chloroform-*d*) δ 10.04 (s, 1H), 6.67 (s, 1H), 4.01 (d, 6H)

Synthesis of 5-bromo-3,4-dimethoxythiophene-2-carbaldehyde (3,4-DMT-CHO-Br)



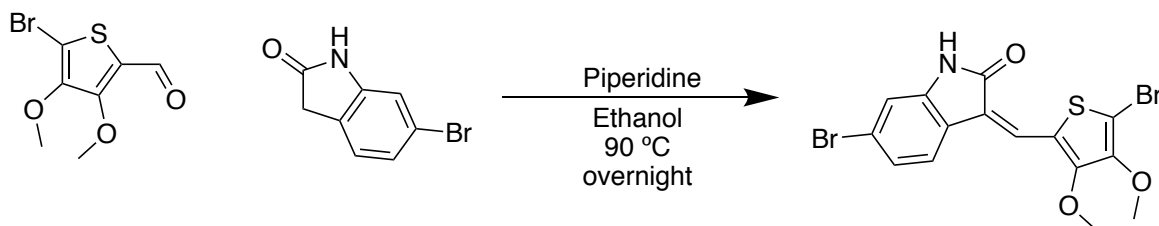
A solution of 3,4-dimethoxythiophene-2-carbaldehyde (1.40 g, 8.13 mmol) and N-bromosuccinimide (1.75 g, 9.76 mmol) in 40 mL of anhydrous chloroform in a 100 mL oven dried three-neck round bottom flask was stirred and a single drop of 48% hydrobromic acid was added as a catalyst to the reaction. The reaction was monitored by TLC and when the starting material was consumed DI water was added to quench the reaction and DCM was used to extract the mixture which was then washed with DI water and saturated sodium bicarbonate solution before

drying with anhydrous sodium sulfate drying salt. The solvent was removed using rotary evaporation and the further purified via flash column chromatography using hexane: ethyl acetate (4:1) to yield 5-bromo-3,4-dimethoxythiophene-2-carbaldehyde as a light-yellow crystal product.

Yield: 1.43 g (70.3%)

$^1\text{H NMR}$ (300 MHz, chloroform-*d*) δ 9.93 (s, 1H), 4.05 (d, 6H)

Synthesis of (*Z*)-6-bromo-3-((5-bromo-3,4-dimethoxythiophen-2-yl)methylene)indolin-2-one (MEI-dBr)

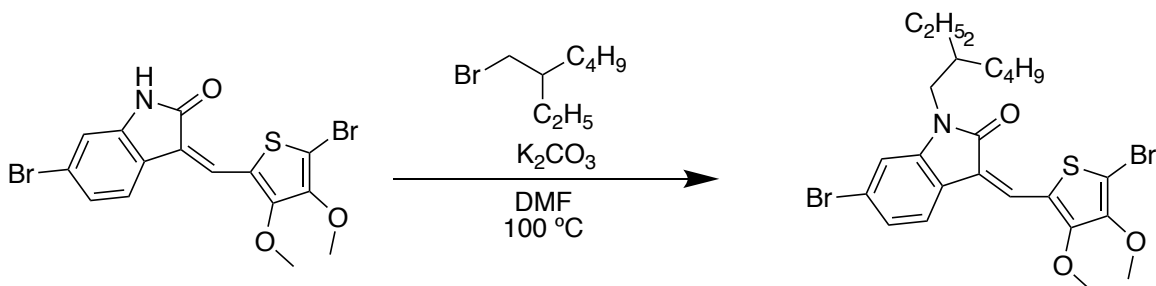


5-bromo-3,4-dimethoxythiophene-2-carbaldehyde (700 mg, 2.788 mmol) and 6-bromooxindole (591 mg, 2.788 mmol) were dispersed in 20 mL of anhydrous ethanol in a 50 mL oven-dried two-neck round bottom flask. Piperidine (570 mg, 5.74 mmol) was added to the dispersion dropwise over the course 10 minutes and the dispersion was then heated to 90 °C using a silicon oil bath. The mixture was left to react overnight when the mixture becomes a yellow slurry which was allowed to cool to room temperature before being filtered to afford a single isomer of (*Z*)-6-bromo-3-((5-bromo-3,4-dimethoxythiophen-2-yl)methylene)indolin-2-one as an orange crystal product.

Yield: 953 mg (76.8%)

$^1\text{H NMR}$ (300 MHz, dimethyl sulfoxide-*d*₆) δ 10.80 (s, 1H), 7.84 (s, 1H), 7.67 (d, 1H), 7.16 (d, 1H), 7.00 (s, 1H), 3.96 (m, 6H)

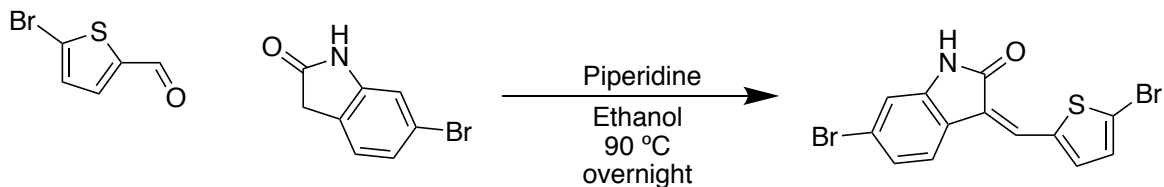
Synthesis of 6-bromo-3-((5-bromo-3,4-dimethoxythiophen-2-yl)methylene)-1-(2-ethylhexyl)indolin-2-one (M2)



(Z)-6-bromo-3-((5-bromo-3,4-dimethoxythiophen-2-yl)methylene)indolin-2-one (600 mg, 1.35 mmol) and potassium carbonate (447 mg, 3.24 mmol) are dissolved in 20 mL anhydrous DMF in a 100 mL two-neck oven-dried round bottom flask and the mixture is stirred at room temperature for 20 minutes before heating the mixture to 100 °C using a silicon oil bath. 2-ethylhexyl bromide (286 mg, 1.48 mmol) is added dropwise to the solution over the course of 15 minutes and the reaction is monitored using TLC. Upon the full consumption of the starting material the solution is cooled to room temperature and filtered out with the organic portion being collected then washed with DI water and brine. The solvent was removed and the crude product was precipitated using a minimum amount of methanol before further purification via flash column chromatography using hexane: ethyl acetate (2:1) as the eluent to yield an orange crystal material as a mixture of Z and E (~ 7:1, Z:E ratio) isomers of 6-bromo-3-((5-bromo-3,4-dimethoxythiophen-2-yl)methylene)-1-(2-ethylhexyl)indolin-2-one as the product. Yield: 487 mg (64.8%)

¹H NMR (300 MHz, chloroform-*d*) δ 7.81 (s, 1H), 7.42 (d, 1H), 7.19 (d, 1H), 6.98 (s, 1H), 3.98 (m, 6H), 3.96 (m, 2H), 1.88 (s, 1H), 1.34 (dt, 8H), 0.93 (m, 6H)

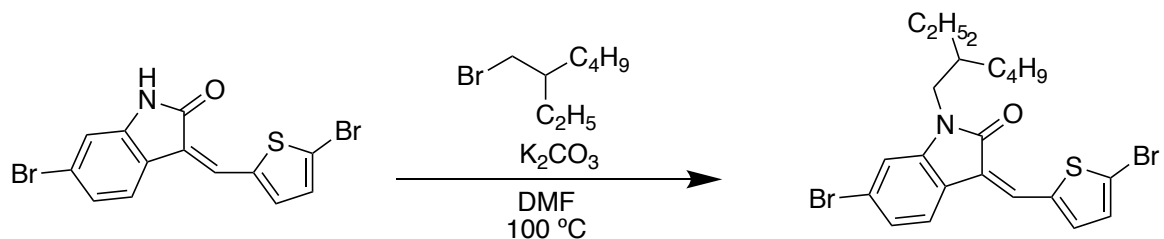
Synthesis of (Z)-6-bromo-3-((5-bromothiophen-2-yl)methylene)indolin-2-one (TEI-dBr)



5-bromothiophene-2-carbaldehyde (700 mg, 3.64 mmol) and 6-bromooxindole (777 mg, 3.64 mmol) were dispersed in 20 mL of anhydrous ethanol in a 50 mL oven-dried two-neck round bottom flask. Piperidine (749 mg, 8.794 mmol) was added to the dispersion dropwise over the course 10 minutes and the dispersion was then heated to 90 °C using a silicon oil bath. The mixture was left to react overnight when the mixture becomes a yellow slurry which was allowed to cool to room temperature before being filtered to afford a single isomer of (Z)-6-bromo-3-((5-bromo-3,4-dimethoxythiophen-2-yl)methylene)indolin-2-one as a yellow crystal product. Yield: 1.23 mg (87.2%)

¹H NMR (300 MHz, dimethyl sulfoxide-*d*₆) δ 10.78 (s, 1H), 7.99 (d, 1H), 7.74 (s, 1H), 7.70 (d, 1H), 7.47 (d, 1H), 7.25 (m, 1H), 7.06 (d, 1H)

Synthesis of (Z)-6-bromo-3-((5-bromothiophen-2-yl)methylene)-1-(2-ethylhexyl)indolin-2-one (M3)

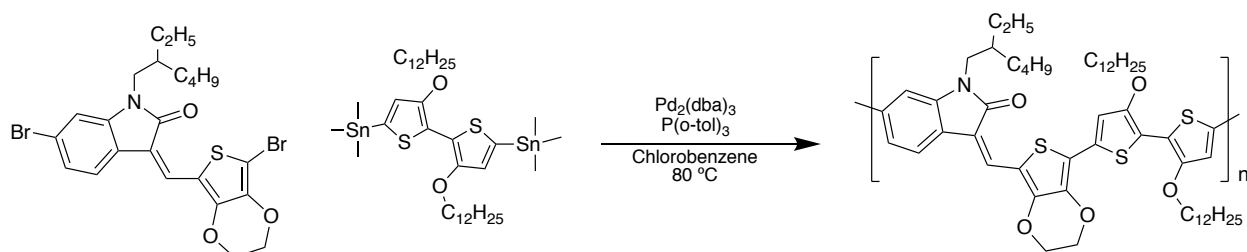


(Z)-6-bromo-3-((5-bromothiophen-2-yl)methylene)indolin-2-one (600 mg, 1.56 mmol) and potassium carbonate (517 mg, 3.74 mmol) are dissolved in 20 mL anhydrous DMF in a 100 mL two-neck oven-dried round bottom flask and the mixture is stirred at room temperature for 20 minutes before heating the mixture to 100 °C using a silicon oil bath. 2-ethylhexyl bromide (331 mg, 1.71 mmol) is added dropwise to the solution over the course of 15 minutes and the reaction

is monitored using TLC. Upon the full consumption of the starting material the solution is cooled to room temperature and filtered out with the organic portion being collected then washed with DI water and brine. The solvent was removed and the crude product was precipitated using a minimum amount of methanol before further purification via flash column chromatography using hexane: ethyl acetate (2:1) as the eluent to yield a yellow crystal material as a mixture of Z and E (~ 7:1, Z:E ratio) isomers of 6-bromo-3-((5-bromo-3,4-dimethoxythiophen-2-yl)methylene)-1-(2-ethylhexyl)indolin-2-one as the product. Yield: 423 mg (54.6%)

¹H NMR (300 MHz, chloroform-*d*) δ 7.60 (s, 1H), 7.41 (d, 1H), 7.38 (d, 1H), 7.20 (d, 1H), 7.15 (d, 1H), 6.99 (s, 1H), 3.70 (dd, 2H), 1.89 (s, 1H), 1.37 (m, 8H), 0.94 (dd, 6H)

Synthesis of Poly(3-((7-(3,3'-bis(dodecyloxy)-[2,2'-bithiophen]-5-yl)-2,3-dihydrothieno[3,4-*b*][1,4]dioxin-5-yl)methylene)-1-(2-ethylhexyl)indolin-2-one) (PEEhB)



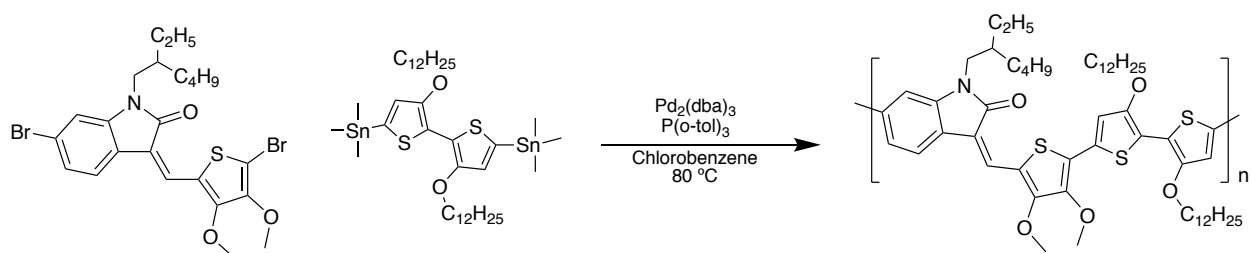
In a 25 mL two-neck oven dried round bottom flask, 6-bromo-3-((7-bromo-2,3-dihydrothieno[3,4-*b*][1,4]dioxin-5-yl)methylene)-1-(2-ethylhexyl)indolin-2-one (26 mg, 0.05 mmol), (3,4'-bis(dodecyloxy)-[2,2'-bithiophene]-5,5'-diyl)bis(trimethylstannane) (40 mg, 0.05 mmol), and tri(*o*-tolyl)phosphine (1.13 mg, 0.004 mmol) are dissolved in 1.5 mL of degassed anhydrous chlorobenzene. Tris(dibenzylideneacetone)dipalladium(0) (0.85 mg, 0.001 mmol) is dissolved in 1 mL of the degassed anhydrous chlorobenzene and added to the reaction mixture under anhydrous conditions. The reaction mixture was heated to 80 °C using a silicon oil bath and the Stille coupling reaction was allowed to proceed for 24 hours before the reaction was cooled to room temperature where the reaction mixture went from a dark red color to a blue color to signal the reaction is proceeding. Methanol is added to the reaction mixture to crash out the polymer and the polymer is purified using Soxhlet extraction using methanol, acetone, hexane, and chloroform in that order to

afford the Poly(3-((7-(3,3'-bis(dodecyloxy)-[2,2'-bithiophen]-5-yl)-2,3-dihydrothieno[3,4-*b*][1,4]dioxin-5-yl)methylene)-1-(2-ethylhexyl)indolin-2-one) [PEEhB] polymer product.

Acetone Yield: 12.2 mg (27.3%)

Chloroform Yield: 32.0 mg (71.7%)

Synthesis of Poly(3-((3',4'-bis(dodecyloxy)-3,4-dimethoxy-[2,2':5',2''-terthiophen]-5-yl)methylene)-1-(2-ethylhexyl)indolin-2-one) (PMEhB)

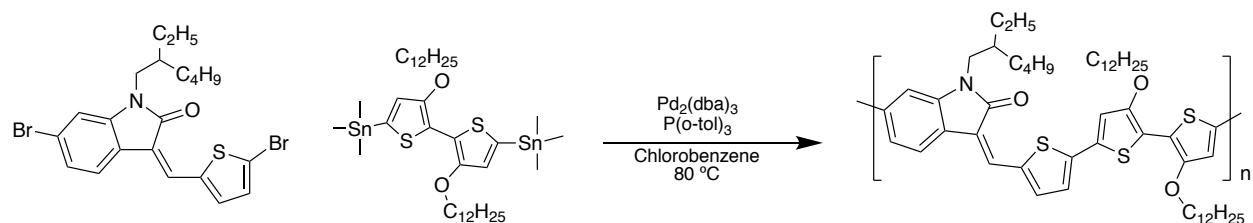


In a 25 mL two-neck oven dried round bottom flask, 6-bromo-3-((5-bromo-3,4-dimethoxythiophen-2-yl)methylene)-1-(3-ethylheptyl)indolin-2-one (27 mg, 0.05 mmol), (3,4'-bis(dodecyloxy)-[2,2'-bithiophene]-5,5'-diyl)bis(trimethylstannane) (40 mg, 0.05 mmol), and tri(*o*-tolyl)phosphine (1.13 mg, 0.004 mmol) are dissolved in 1.5 mL of degassed anhydrous chlorobenzene. Tris(dibenzylideneacetone)dipalladium(0) (0.85 mg, 0.001 mmol) is dissolved in 1 mL of the degassed anhydrous chlorobenzene and added to the reaction mixture under anhydrous conditions. The reaction mixture was heated to 80 °C using a silicon oil bath and the Stille coupling reaction was allowed to proceed for 24 hours before the reaction was cooled to room temperature where the reaction mixture went from a dark red color to a blue color to signal the reaction is proceeding. Methanol is added to the reaction mixture to crash out the polymer and the polymer is purified using Soxhlet extraction using methanol, acetone, hexane, and chloroform in that order to afford the Poly(3-((3',4'-bis(dodecyloxy)-3,4-dimethoxy-[2,2':5',2''-terthiophen]-5-yl)methylene)-1-(2-ethylhexyl)indolin-2-one) [PMEhB] polymer product.

Acetone Yield: 10.7 mg (24.2%)

Chloroform Yield: 29.2 mg (66.0%)

Synthesis of Poly(3-((3',4'-bis(dodecyloxy)-[2,2':5',2''-terthiophen]-5-yl)methylene)-1-(2-ethylhexyl)indolin-2-one) (PTEhB)



In a 25 mL two-neck oven dried round bottom flask, 6-bromo-3-((5-bromothiophen-2-yl)methylene)-1-(2-ethylhexyl)indolin-2-one (100 mg, 0.20 mmol), (3,4'-bis(dodecyloxy)-[2,2':5',2''-bithiophene]-5,5'-diyl)bis(trimethylstannane) (173 mg, 0.20 mmol), and tri(o-tolyl)phosphine (4.89 mg, 0.02 mmol) are dissolved in 2.5 mL of degassed anhydrous chlorobenzene. Tris(dibenzylideneacetone)dipalladium(0) (3.68 mg, 0.004 mmol) is dissolved in 1 mL of the degassed anhydrous chlorobenzene and added to the reaction mixture under anhydrous conditions. The reaction mixture was heated to 80 °C using a silicon oil bath and the Stille coupling reaction was allowed to proceed for 24 hours before the reaction was cooled to room temperature where the reaction mixture went from a dark red color to a blue color to signal the reaction is proceeding. Methanol is added to the reaction mixture to crash out the polymer and the polymer is purified using Soxhlet extraction using methanol, acetone, hexane, and chloroform in that order to afford the Poly(3-((3',4'-bis(dodecyloxy)-[2,2':5',2''-terthiophen]-5-yl)methylene)-1-(2-ethylhexyl)indolin-2-one) [PTEhB] polymer product.

Hexane Yield: 10.4 mg (5.4%)

Chloroform Yield: 181 mg (93.0%)

Chapter 3: Synthesis, Characterization, and Performance of HID Oligomers

3.1 Introduction

Oligomeric π -conjugated organic molecules have been the subject of extensive study for the development of new electronic materials. These oligomeric materials have been researched comprehensively for the purposes of organic solar cells (OSCs)¹⁵¹, OFETs¹⁵², organic light emitting diodes (OLEDs)¹⁵³, chemical sensing¹⁵⁴, pH sensing¹⁵⁵, and temperature sensing¹⁵⁶. These organic oligomers possess inherent advantages relevant to their analogous CPs which includes:

- i. Well-defined chemical structure allows for high purity reproducibility of the oligomer leading to repeatable device performance
- ii. Oligomer films favor long-range order (high DOC) which leads to enhanced charge carrier transport
- iii. Readily fabricated by both solution-deposition and vacuum deposition techniques

Of these organic oligomers, oligothiophenes are of the most studied materials due to the structural versatility of thiophene moieties which allow for the synthesis of tailor-made materials for tuning of the electrical properties. The oligothiophene, α -sexithiophene (α -6T) has a wide range of electronic and optoelectronic applications which include OPVs, OLEDs, spatial modulators, and luminescent diodes making it the most heavily researched oligothiophene. Barbarella et al functionalized the generic structure with methylsulphanyl groups on the β positions of each thiophene in the inner quaterthiophene as well as on all six thiophenes of α -6T¹⁵⁷. These functionalized compounds were shown to be solvent processable which the unsubstituted α -6T is not but had significantly lower melting points (~ 150 - 170 °C) than their unsubstituted analog (~ 303 °C). The UV-Vis analysis of these compounds showed that the methylsulphanyl groups incurred a small shift to wider E_g , but this was considered the trade-off for functionalizing the oligomer such that it can be processed in chloroform. Later, Afzali et al. functionalized the α positions of the terminal thiophenes in the α -sexithiophene structure with dibutylphosphonate groups to synthesize dibutylphosphonate- α -sexithiophene (DBP- α -6T)¹⁵⁸. These polar terminal groups yielded a chloroform-soluble oligomer without the need for alkyl sidechains on the β

positions of the inner thiophenes which can often reduce the coplanarity of the material due to steric hinderance and significantly decrease its electronic performance. When this material was used to fabricate TFT devices, they exhibited a modest carrier mobility, but the high purity material afforded by the Ullmann-type synthesis route yielded high on/off ratios in the TFTs.

A second family of oligomer electronic material is oligothiazoles as n-type semiconducting materials. Regioselective thiazole oligomers were synthesized in a study by Ando et al. along with thiazole-thiophene co-oligomers with terminal trifluoromethylphenyl groups on each end of the molecule¹⁵². Upon treating the SiO₂ substrates used to fabricate top-contact OFETs with octadecyltrichlorosilane (OTS) the electron mobility (μ_n) of the 5,5'-bithiazole-core oligomer was reported to be 1.83 cm²/V·s which, at the time, was of the highest reported values. This work was expanded on in 2008 by Moon et al who developed the “push-pull” co-oligomer using a bi-EDOT core with β -alkylated bithiazole terminal units to form the donor-acceptor oligomer BT₂B. This novel oligomer was fabricated onto a top-contact TFT device with an indium tin oxide (ITO) glass substrate and a PMMA dielectric layer via both solution and vacuum deposition methods. The theoretical hole mobility (μ_h) for these devices was calculated to be 0.86 cm²/V·s but it was hypothesized this could be enhanced to 3.5 cm²/V·s with a more favorable eclipsed geometry¹⁵⁹.

While thiazole and thiophene oligomers and co-oligomers are of the most popular for electronic applications there several other π -conjugated structures that warrant further study. Grimsdale and Müllen introduced oligo(ladder-phenylene)s to overcome the issue of incomplete bridge formations in synthesis of polyphenylenes¹⁶⁰. These oligomers are bridged with heteroatoms such as nitrogen or sulfur and were shown to be successfully used as the active material in light-emitting diodes, solar cells, and TFTs. Sun et al. introduced a solution processable oligomer based on an anthracene core that exhibited a glass transition temperature (T_g) above 200 °C. This X-shaped oligomer was solution deposited as the active layer in conjunction with PEDOT:PSS for OLED devices¹⁶¹. The high T_g of anthracene oligomer material allowed for device fabrication to be conducted at elevated temperature without destabilizing the thin film morphology. The structures for some of the discussed π -conjugated oligomers are shown in **Figure 3-1**.

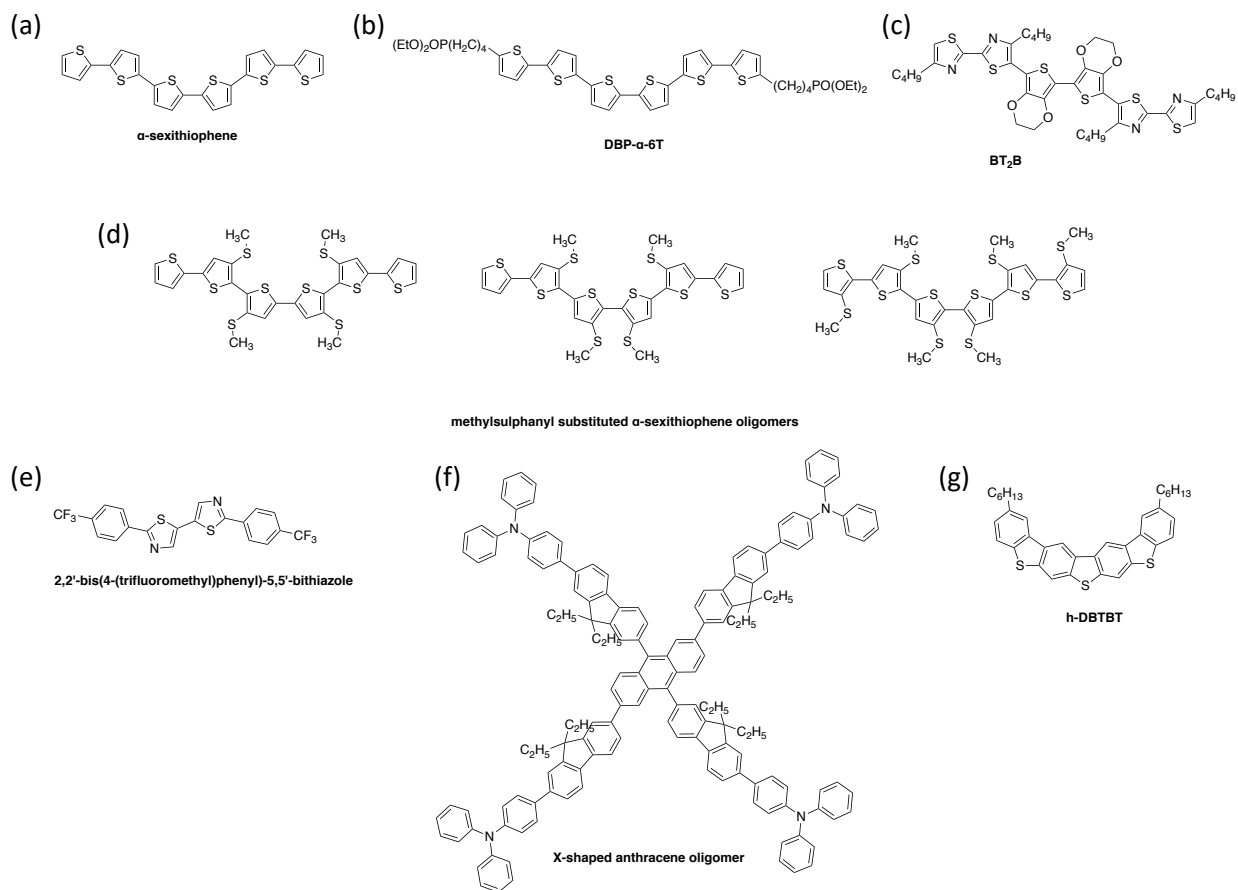


Figure 3-1: Conjugated oligomer materials used in organic electronics; (a) simple α -sexithiophene, (b) DBP- α -6T¹⁵⁸, (c) BT₂B¹⁵⁹, (d) the family of methylsulphonyl substituted α -6T oligomers¹⁵⁷, (e) trifluoromethylphenyl substituted bithiazole¹⁵², (f) X-shaped anthracene oligomer¹⁶¹, (g) heteroatom-bridged oligophenylene¹⁶⁰.

Analyzing the results from the previous chapter indicates that the molecular weight of polymers did not correlate strongly with device performance. The device that used the higher molecular weight **PTEhB** doped with **F4TCNQ** exhibited the lowest sensitivity, the worst time stability, and, along with **PMEhB** doped with **F4TCNQ**, the narrowest working range. Hence, it was hypothesized that the HID materials may exhibit sufficient π - π stacking without the need for copolymerization for the purposes of temperature sensing applications. Therefore, this chapter focuses on the development of two HID oligomers **OG-D1** derived from the **M1** chemical structure and **OG3** which stems from the monomer structure of **M3**. These oligomer materials were designed to be doped with the same **F4TCNQ** p-type dopant for real-time temperature sensing applications. Compared to the copolymers discussed in previous chapter, oligomers allow for complete control of the chemical structure as the molecular weight is defined.

3.2 3,3'-((2,2',3,3'-tetrahydro-[5,5'-bithieno[3,4-*b*][1,4]dioxine]-7,7'-diyl)bis(methaneylylidene))-bis(2-oxoindoline-1-carboxylate) Dimer (OG-D1)

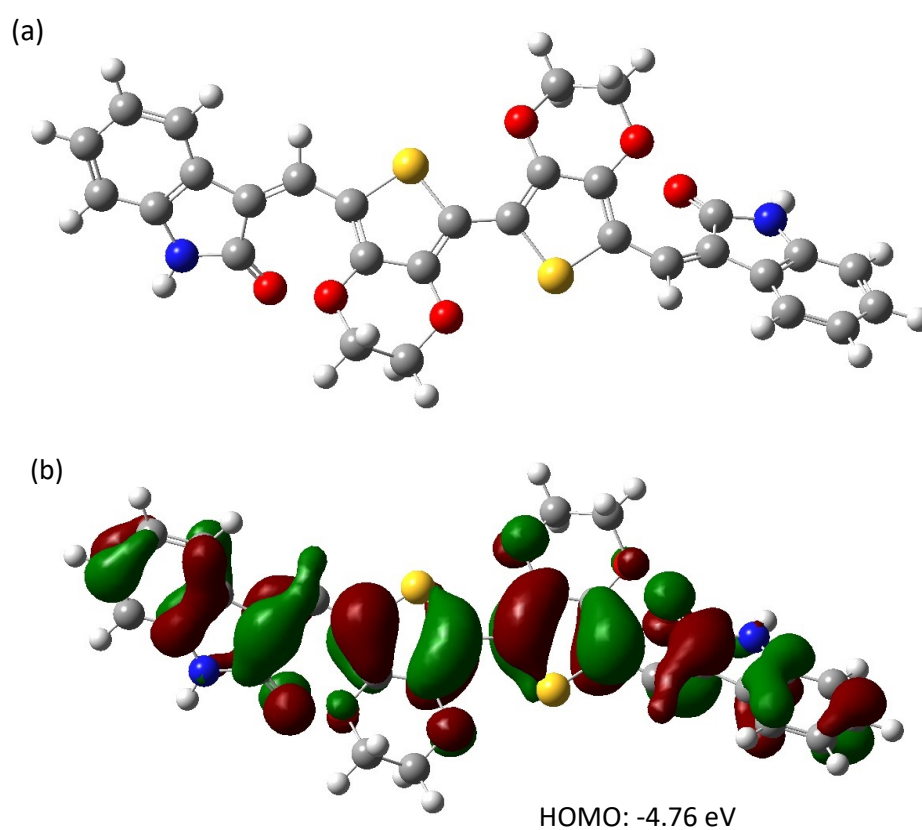
3.2.1 3,3'-((2,2',3,3'-tetrahydro-[5,5'-bithieno[3,4-*b*][1,4]dioxine]-7,7'-diyl)bis(methaneylylidene))-bis(2-oxoindoline-1-carboxylate) Molecular Design

Due to the **PEEhB** polymer considerably outperforming the other two polymers discussed in the previous chapter, as well as the high frequency at which successful **EDOT** materials are reported for electronic applications^{162–164} the **M1** structure was adopted for the design of the dimer. **OG-D1** The molecular structure of the material consists of two **M1** units coupled together at the α position of their respective thiophene moieties. In this dimer structure, a solubilizing sidechain, similar to the ethylhexyl chain in the **M1** structure, is still required for solution processability. In the case of **OG-D1**, the sidechain is converted from the simple ethylhexyl carbon chain to an ethylhexyl carbamate chain on both the indigo moieties. This change may provide several advantageous properties for the material. The carbamate sidechain is significantly more polar than the aliphatic sidechain which may enable better solubility in non-halogenated, more environmentally friendly solvents. These carbamate sidechains may also be thermally cleaved under moderate conditions hence the resulting oligomer structure would exhibit reduced steric hinderance. This should induce a higher degree of coplanarity between oligomer molecules that can reduce the E_g of the resulting material and enhance conductivity. Without the sidechains the PTC effect discussed in the previous chapter is reduced and removing the sidechain leaves behind N-H groups on the indigo unit which induces intermolecular hydrogen bonding to prevent separation of neighboring molecules with increasing temperature and thus both effects should improve temperature stability and reversibility of the corresponding sensor device.

3.2.2 Structure Simulation by Density Functional Theory (DFT)

The DFT simulation results for **OG-D1** upon removal of the carbamate sidechains (referred to as **OG-D1_A**) are shown in **Figure 3-2** and the results are compared with that of **M1** and **DDOBT** in **Table 3-1**. The even delocalization of electrons across the molecule is apparent and implies that good π -stacking should occur. Extending the conjugation of the **M1** monomer to a dimer structure

has significantly impacted the simulated energy levels of the material. The E_{HOMO} and E_{LUMO} for **OG-D1_A** without the sidechains are simulated to be -4.76 eV and -2.25 eV respectively which is a 0.42 eV increase in E_{HOMO} and a 0.38 eV decrease in the E_{LUMO} relative to the simulation results for **M1**. Moreover, the E_{HOMO} of this material calculated by the DFT simulation is comparable to that of the **DDOBT** donor material which was simulated to be -4.62 eV. Therefore, it stands to reason that if a sufficient percentage of the carbamate sidechains are removed, the donor-acceptor structure may not be necessary as the corresponding **OG-D1_A** film could already exhibit the necessary electronic properties for developing a stable oligomer:dopant complex.



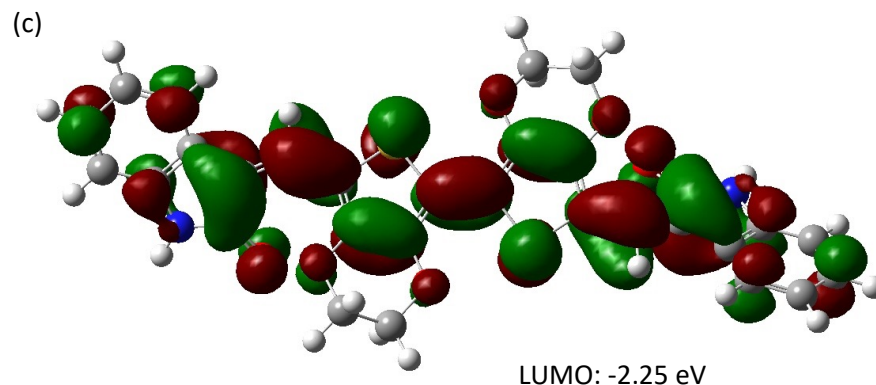


Figure 3-2: (a) Geometry of **OG-D1_A** optimized by DFT simulation in Gaussian software, (b) HOMO/(c) LUMO orbitals of the **OG-D1_A** and the DFT calculation of the orbital energy levels with respect to vacuum (0 eV).

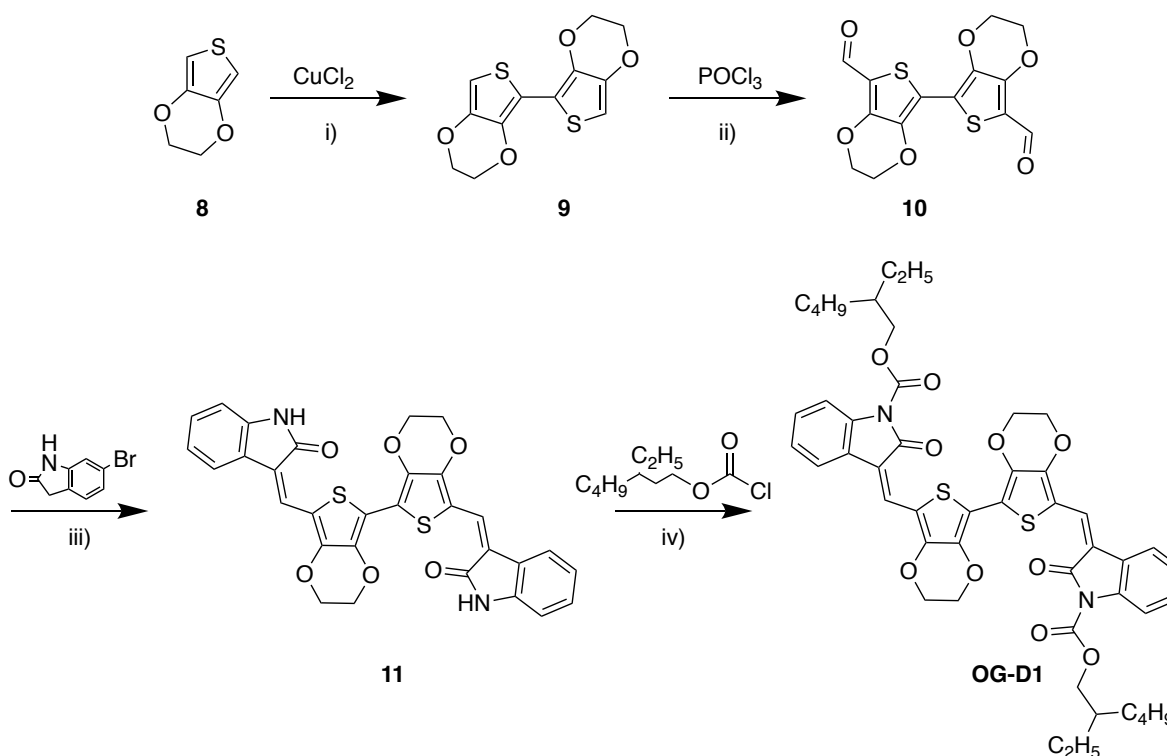
Table 3-1: DFT calculation results for **DDOBT**, **M1**, and **OG-D1_A**.

	E_{HOMO}	E_{LUMO}	E_g
DDOBT	-4.62 eV	-0.66 eV	3.96 eV
M1	-5.18 eV	-1.87 eV	3.31 eV
OG-D1_A	-4.76 eV	-2.25 eV	2.51 eV

3.2.3 Synthesis of 3,3'-((2,2',3,3'-tetrahydro-[5,5'-bithieno[3,4-*b*][1,4]dioxine]-7,7'-diyl)bis(methaneylylidene))-bis(2-oxoindoline-1-carboxylate)

The synthetic route of **OG-D1** is depicted in **Scheme 3-1** using similar reactions that were introduced in chapter 2 for the HID polymers. The first step is an aromatic coupling reaction using *n*-butyllithium and copper (II) chloride. This is followed by a Vilsmeier-Haack reaction to formlyate both aromatic units which is then proceeded by the same Knoevenagel condensation reaction from chapter 2. The final reaction adds an ethylhexyl carbamate side chain instead of the alkyl analog for increased solubility and the additional functionality of being able to remove the carbamate sidechain upon sufficient thermal treatment. It is important to note that after steps ii) and iii) the materials produced are quite insoluble and thus NMR analysis and column purification was not possible for these products. Instead, the crude solid material yielded from these two reactions was used for the next stage of the series with no purification, this leads to a low yield of the final product which may be purified via column chromatography due to the carbamate

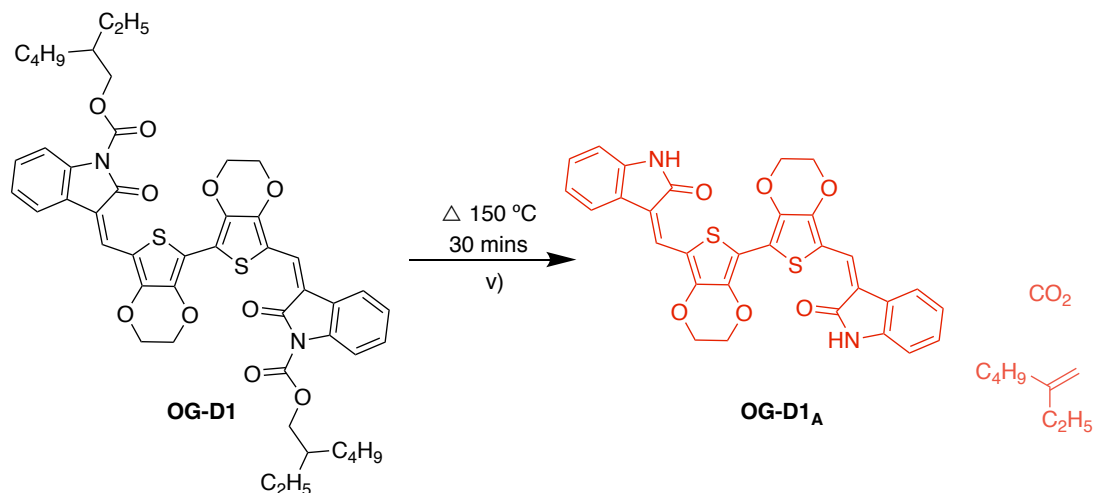
sidechains improving solubility. The yield of 67 mg (21.6%) is reported under the assumption that the mass of starting material used in reaction iv) was purely material **11**. While the dimer was successfully synthesized, this reaction scheme may not be practical for larger scale synthesis and different avenues of producing **OG-D1** should be explored. Details of each reaction are available in section 3.5.3 and the NMR analysis after steps i) and iv) are shown in Appendix A.



Scheme 3-1: Synthetic route towards the **OG-D1** dimer. Reaction conditions: i) n-butyllithium/ copper(II) chloride/ anhydrous THF/ $-78\text{ }^\circ\text{C}$ to r.t 56.8% ii) anhydrous DMF/ phosphorous(V) oxychloride/ anhydrous 1,2-dichloroethane/ $100\text{ }^\circ\text{C}$ iii) oxindole/ piperidine/ anhydrous ethanol/ $90\text{ }^\circ\text{C}$ / iv) sodium hydride/ anhydrous THF/ 2-ethylhexyl chloroformate/ $50\text{ }^\circ\text{C}$ 21.6%.

The thermal removal of the carbamate sidechains along with the potential reaction byproducts are depicted in **Scheme 3-2** below where literature reports that significant cleavage of these carbamate chains can be achieved by annealing at $\sim 100\text{-}150\text{ }^\circ\text{C}$ in air^{165,166}. Upon thermal treatment the carbamate sidechains will decompose and react with air to form carbon dioxide (CO_2) and the corresponding olefins. This reaction will leave behind a single hydrogen bonded at the atom where the carbamate chain previously was. In the case of **OG-D1** an N-H group is left behind to provoke

a hydrogen bonding network. This type of process where the carbamate chain is used to design a solution processable material and then removed to optimize the electronic properties of the deposited film has been reported to improve the performance of diketopyrrolopyrrole (DPP) materials for OFET, OPV, and sensor applications¹⁶⁷⁻¹⁶⁹.



Scheme 3-2: Thermal treatment at 150 °C to remove the carbamate sidechains from **OG-D1** to yield **OG-D1_A** and the byproducts of CO₂ and 2-ethyl-1-hexene.

3.2.4 Characterization of **OG-D1** by UV-Vis-NIR and CV

The UV-Vis-NIR spectra of **OG-D1** in solution, and as a film is depicted in **Figure 3-3a** alongside the spectra for **OG-D1_A** as a thin film and as a doped film deposited on a glass slide in **Figure 3-3b**. The results of this UV-Vis-NIR absorbance analysis are summarized in **Table 3-2** below which includes the λ_{max} peak positions for the multimodal distributions. Initially, the solution spectrum exhibits a bimodal distribution but only a single peak is observed when that solution is deposited on a glass slide as a thin film. The two peaks in the solution spectrum must be due to either the presence of two compounds in the solution or two distinct electronic transitions between two different electronic or vibronic states. The latter case would require a material with high crystallinity and since this absorbance spectrum is in solution it is more likely the bimodal peak is due to a mixture of two compounds. This may arise due to the high degree of geometric isomerization in the **OG-D1** structure stemming from the two C=C bonds between the **EDOT**

spacers and indigo units. While there is also isomerization in the **M1** and **M2** structures from the previous chapter, a distinct bimodal absorbance spectrum is not observed for either of the corresponding polymers **PEEhB** and **PMEhB**. Several factors may contribute to this, the first of which being that the polymers incur a molecular weight distribution which gives them broader peaks in the UV-Vis-NIR analysis. This is apparent when comparing the film peaks for **OG-D1** to the film peaks of the three polymers and noting that the dimer peaks are significantly narrower. Thus, the excitation of the geometric isomers with varied molecular weight may be encompassed within that single broad peak. Also, the geometric isomerization is only a $\sim 1:7$ ratio so it may not have a very significant impact on the absorbance properties of the material. Lastly, the polymer chains for **PEEhB**, **PMEhB**, and **PTEhB** may only exist as one of their Z-form or E-form isomers. The structure of **OG-D1** gives rise to three potential geometric isomers Z-Z, Z-E, and E-E. It is difficult to discern the percentage of each isomer in the NMR analysis, but it stands to reason that since sharp, narrow peaks exist for this oligomer as opposed to the polymers, isomers with significant enough structural differences, specifically Z-Z versus E-E, may lead to different electronic transitions and thus a multimodal absorbance spectrum is observed. Interestingly, when going from the solution to a thin film, the single film peak has undergone a hypsochromic shift (~ 57 nm) to higher energy wavelengths relative to the two solution peaks. This is the opposite of what is normally expected as in most cases the solid-state packing of π -conjugated materials in a thin film leads to absorbance peaks of lower energy. This should be due to the formation of H-aggregates in the film. When H-aggregation occurs the individual molecules stack predominantly face-to-face as opposed when J-aggregation occurs the molecules will orient themselves in predominantly a head-to-tail arrangement¹⁷⁰. In D-A systems, H-aggregation phenomenon occurs when the oligomer materials stack in a donor-donor (D-D) and (A-A) orientation and this leads to a hypsochromic shift as reported by Bricks et al. which is observed in **Figure 3-3a**.

After annealing at 150 °C for 30 minutes to remove the carbamate sidechains and yield **OG-D1_A**, the UV-Vis-NIR spectrum shows significant differences relative to the **OG-D1** film. The single peak film spectrum evolves into two distinctive peaks with a shoulder on lower wavelength peak. The overall curve shifts significantly towards lower energy absorption ($\lambda_{\text{max}} = 698$ nm, 609 nm) relative to the non-annealed film ($\lambda_{\text{max}} = 552$ nm). This may be attributed to the partial removal of the carbamate sidechains upon annealing at 150 °C which increases the coplanarity of the oligomer

that enhances the π - π stacking and reduces the E_g . The thermal treatment may also impact the aggregation of the molecules as annealing imparts energy for solid-state rearrangement. This may lead to the evolution of J-aggregation and would cause a bathochromic shift from the **OG-D1** film to the **OG-D1_A** film. Hence, when annealed the corresponding **OG-D1_A** film may include a mixture of H-aggregation and J-aggregation as well as different crystalline regions as thermal treatment may allow the molecules to rearrange themselves into more ordered solid-state packing. The combination of these effects is likely what led to the multimodal absorbance distribution of the annealed film. This effect may not be observed in the HID polymers because of the higher molecular weight and thus this leads to more randomness in both the solution and film. Hence, all these characteristics described in the oligomer structure are encompassed within the single broad absorbance peak that the HID polymer solutions and films exhibit as reported in section 2.4.2.

Upon doping, the emergence of a broader peak in the UV-Vis region spanning between 502-715 nm is observed. The peak also undergoes a bathochromic shift relative to the neat **OG-D1_A** film when doped which is consistent with the results from the previous chapter and agrees with the conventional p-type doping mechanism. This broad peak may encompass the absorption characteristics of the **OG-D1_A** doped regions, the **F4TCNQ⁻** anion, as well as any remaining undoped **OG-D1_A** molecules. As with the polymer materials discussed in the previous chapter, the baseline level is increased when going from solution to film due to reflection from the film. However, upon doping, the baseline is only slightly increased in the NIR region which indicates that there is some formation of the NIR-polaron broad peak, but it is nowhere near as intense as that of the polymeric samples. This should indicate that the doping for the **OG-D1_A** material is not as efficient as for the HID polymers and it may be more difficult to fabricate a conductive film using this oligomer:dopant complex.

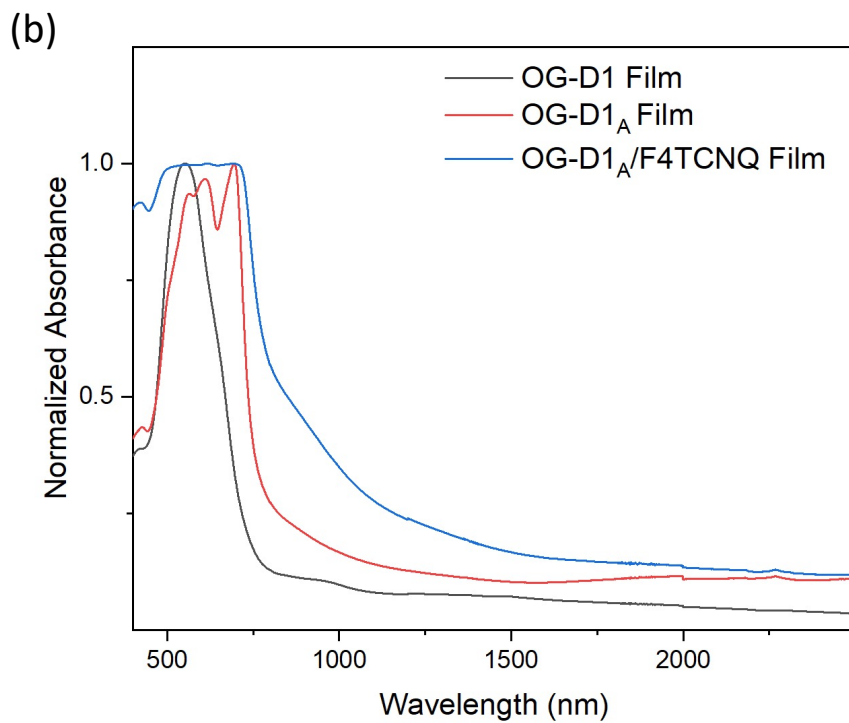
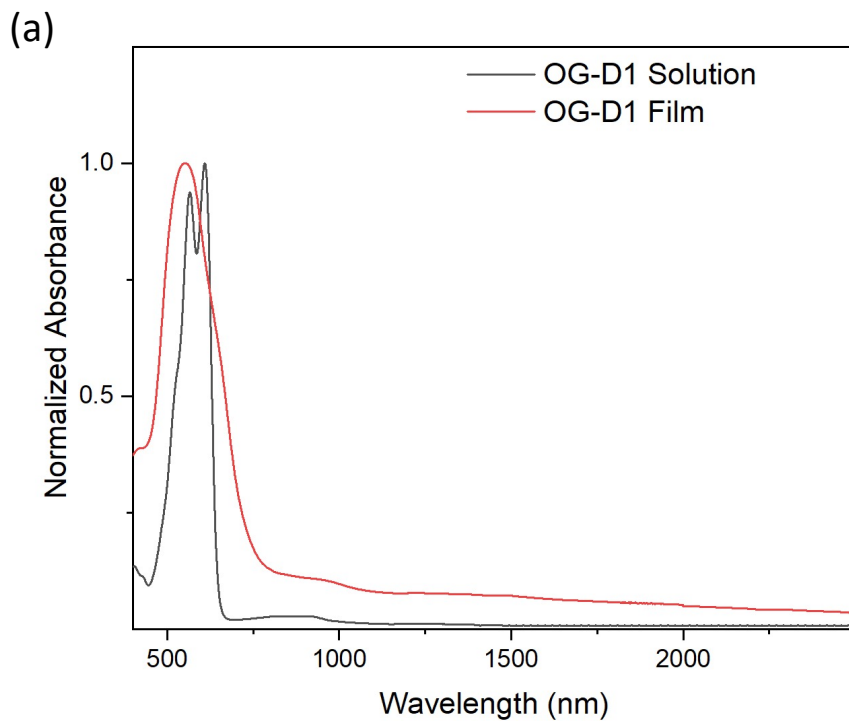


Figure 3-3: UV-Vis-NIR spectra for (a) **OG-D1** in solution and as a thin film and (b) **OG-D1_A** as a thin film post annealing and doped with **F4TCNQ** dopant.

Table 3-2: Summary of the UV-Vis-NIR spectroscopy results for **OG-D1** and **OG-D1_A** showing the shifts in the absorbance λ_{max} from solution to film to doped film and film λ_{onset} .

	Film λ_{onset}	Solution λ_{max}	Film λ_{max}	Doped λ_{max}
OG-D1	737 nm	609 nm 556 nm	552 nm	-
OG-D1_A	771 nm	-	698 nm 609 nm	618 nm (502-715 nm)

CV analysis was conducted to determine the E_{HOMO} of the oligomer film using the same procedure as the previous chapter. The E_{LUMO} is once again determined using the optical E_{g} from the UV-Vis-NIR results. The energy levels for **OG-D1** and **OG-D1_A** including the E_{T} values are summarized in **Table 3-3** and illustrated in the energy diagram in **Figure 3-4** along with the **F4TCNQ** dopant for reference. The CV trace for both the **OG-D1** and **OG-D1_A** films are presented in **Figure 3-5**. The neat **OG-D1** film has a E_{HOMO} of -5.18 eV with respect to vacuum (0 eV) and this increases slightly upon thermal annealing to yield a E_{HOMO} of -5.16 eV for the **OG-D1_A** film. The bandgap is also slightly decreased by ~ 70 meV when the film is annealed, and these phenomena may be due to the partial removal of the carbamate sidechains. Another potential reason for the shift in energy levels is that the thermal annealing may impact the solid-state packing of the film. For organic materials, thermal treatment normally increases the DOC of the π -conjugated system and leads to a lower E_{g} as is the case here. Nevertheless, the E_{HOMO} of both **OG-D1** and **OG-D1_A** is well below the E_{LUMO} of the **F4TCNQ** dopant hence one would not expect this oligomer:dopant complex to form deep traps. However, as was noted in the previous chapter, the E_{HOMO} alone cannot be used to determine whether a complex will be stable. Upon thermal treatment of the film electrons can use the thermal energy to jump to higher energy levels in the oligomer and thus they may be high enough to readily fall into the E_{LUMO} level of the dopant if annealed at high enough temperatures. Hence, an attempt was still made to deposit a conductive film using the **OG-D1_A:F4TCNQ** complex onto the PET substrate to evaluate as a temperature sensor.

Table 3-3: Summary of the molecular orbital energy levels of the **OG-D1**, **OG-D1_A**, and the **F4TCNQ** dopant molecule along with E_T values.

	E_{HOMO}	E_{LUMO}	E_g	E_T
OG-D1	-5.18 eV	-3.50 eV	1.68 eV	-0.17 eV
OG-D1_A	-5.16 eV	-3.55 eV	1.61 eV	-0.15 eV
F4TCNQ	-9.02 eV	-5.01 eV	4.02 eV	-

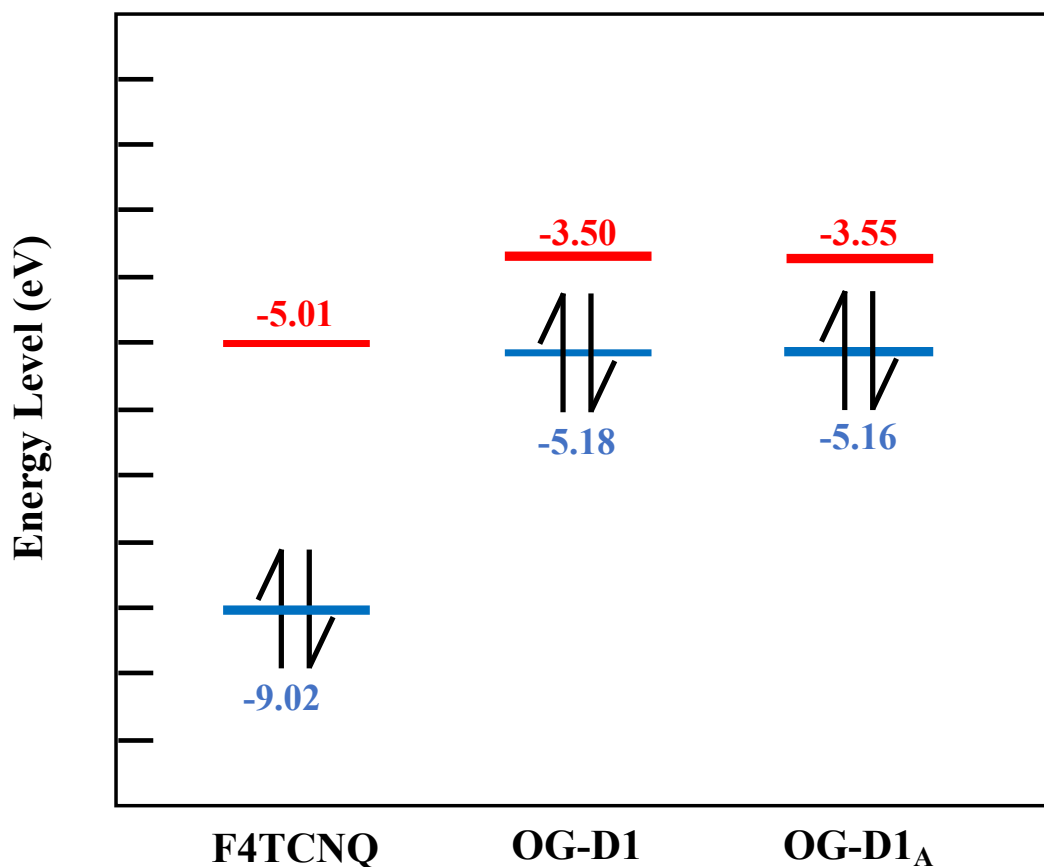


Figure 3-4: Energy level diagram depicting the relative E_{HOMO} and E_{LUMO} of **OG-D1**, **OG-D1_A** and the **F4TCNQ** dopant with respect to vacuum (0 eV).

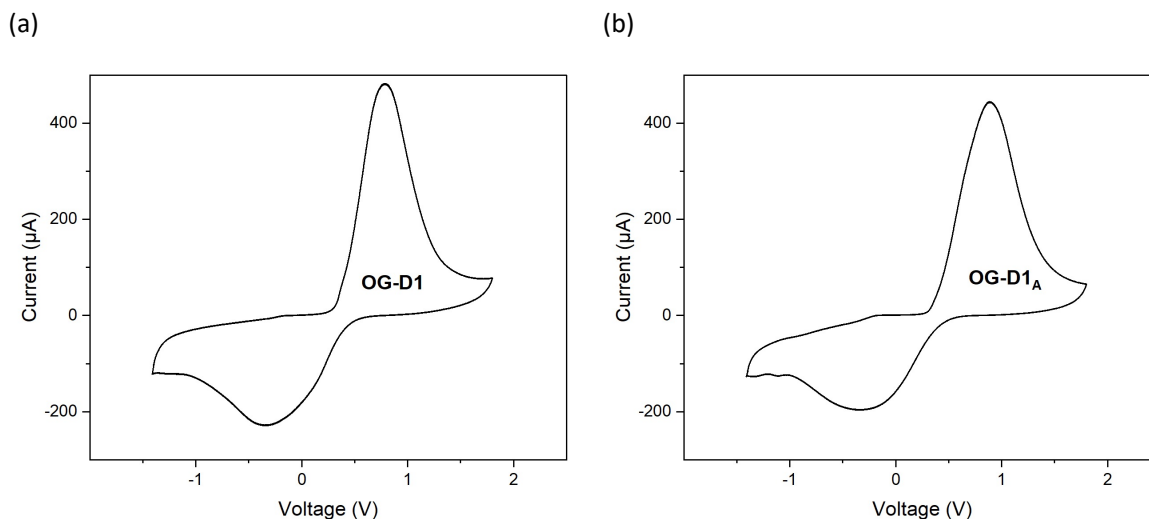


Figure 3-5: The CV trace of (a) **OG-D1** and (b) **OG-D1_A** at a scan rate of 0.1 V/s in 0.1 M tetrabutylammonium hexafluorophosphate with anhydrous acetonitrile as the solvent.

3.2.5 Temperature Sensing Performance of OG-D1

The temperature sensing performance of the **OG-D1_A:F4TCNQ** complex was evaluated by fabricating temperature sensors using the same technique described in the previous chapter with interdigitated silver electrodes on a PET substrate. Any deviations from the original fabrication technique are detailed in section 3.5.2. The results of the temperature sensing trials are presented in **Figure 3-6** where a step function response is once again observed upon increasing the temperature in the real-time current measurement. Interestingly, while this device doesn't suffer from the device breakdown described in the previous section until ~ 120 °C, after reaching 66 °C the current signal exhibits visible noise relative to the signal at lower temperatures. As the temperature increases, the step-function shape of the response is maintained but at each temperature interval the noise is increased. This supports the theory that the removal of the carbamate sidechain may inhibit the formation of the insulating regions leading to the PTC effect described in the previous chapter. These insulating regions will form more slowly with less sidechain present and thus this effect will increase the working range of the sensor as evidence by the absence of device breakdown below 120 °C. The signal noise increasing with temperature is likely also due to the carbamate sidechains and the process of which they are removed. While the sensors are washed with minimal amounts of ethanol after fabrication to remove any impurities,

the 2-ethyl-1-hexene byproduct of the carbamate cleavage reaction is reported to be an aliphatic liquid material¹⁷¹. Hence, any of it that is in the bulk of the film may not be removed by ethanol wash. This material is reported to have a boiling point of 120 °C so it should be mostly in the liquid phase during the temperature sensing trial. As the temperature is increased this will affect the viscosity of the liquid olefins which may interact with the solid doped film and distort the signal. Also, as the temperatures get closer to ~ 100 °C more carbamate sidechains may be thermally cleaved from the film. This will impact the nature of the doped film as well as lead to the production of more byproduct which can further distort the signal, and this should explain why the noise in the signal is larger as the temperature increases. The $I-T^{-0.25}$ response is plotted in **Figure 3-6b**, and a relatively good fit is depicted which indicates that this material may also follow the VRH theory of thermal conduction. The TCR of the device exhibits nonlinearity similar to that of the **PEEhB:F4TCNQ** device from the previous chapter. At 25-60 °C the TCR is determined to be -1.39%/°C and at 60-120 °C the TCR is -0.53%/°C (**Figure 3-7**). This should be due to the ability of the lower molecular weight oligomer molecules to move at higher temperatures. It is easier for these oligomers to reorganize as they don't suffer from any chain entanglements like the polymers of the previous chapter. This movement may again result in larger distances between the conductive polymer chains leading to the same PTC effect discussed for the **PEEhB:F4TCNQ** device. The device performance is summarized in **Table 3-5** along with the results of the **PEEhB** polymer for comparison.

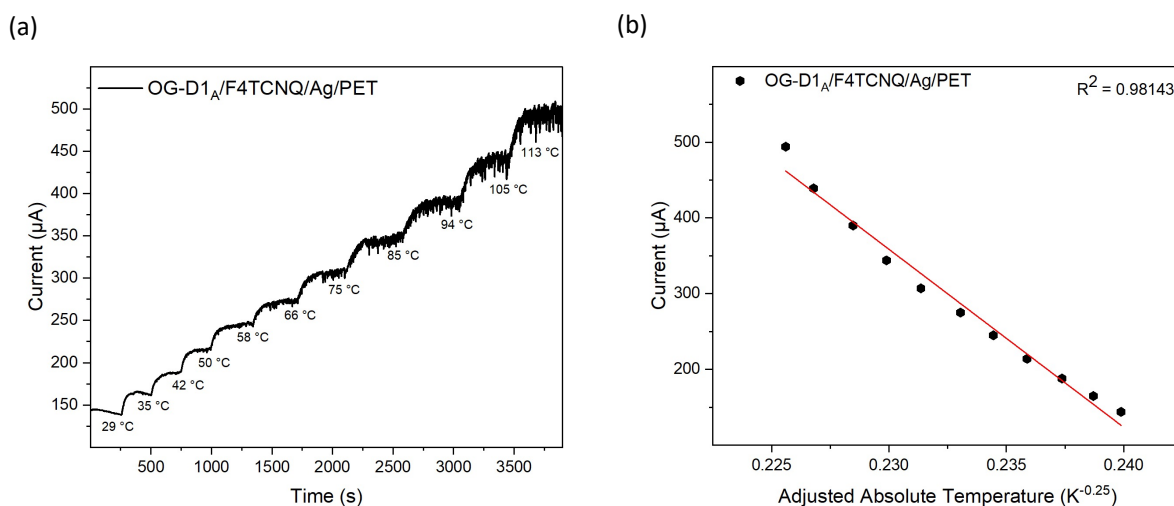


Figure 3-6: (a) Real-time current vs time (I-t) graph of **OG-D1A:F4TCNQ** device at varying temperatures, (b) current vs adjusted absolute temperature ($I-T^{-0.25}$) graph of **OG-D1A:F4TCNQ** interdigitated device.

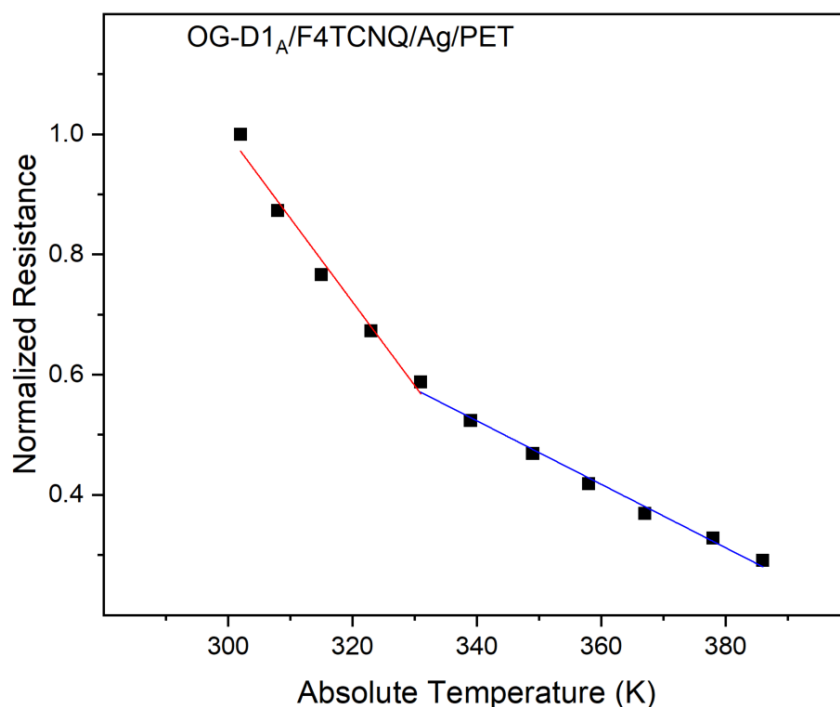


Figure 3-7: Normalized resistance vs temperature plots for TCR determination of sensor device fabricated using **OG-D1_A:F4TCNQ**.

Table 3-4: Temperature sensing performance of the **PEEhB:F4TCNQ** and **OG-D1_A:F4TCNQ** devices fabricated on PET/Ag substrates.

	Thickness (nm)	Working Range (°C)	TCR (%/°C)	Response Time (s)	Conductivity (S/cm)
PEEhB:F4TCNQ	43	25 - 60	-1.09 ± 0.07	54.4 ± 10.9	1.23 x 10 ⁻³
		60 -120	-0.38 ± 0.02		
OG-D1_A:F4TCNQ	115	25 - 60	-1.39 ± 0.11	67.2 ± 12.1	3.02 x 10 ⁻³
		60 -120	-0.53 ± 0.02		

The **OG-D1_A:F4TCNQ** complex was successfully deposited as a conductive film as is evident from the results of the temperature sensing trials. The stability of the device was then evaluated over the thirty-two-day time frame tested every periodically every four days. The results of this stability study are shown in **Figure 3-8**. While the film was conductive upon fabrication, the complex deteriorated rapidly as the corresponding device had its conductivity drop to ~ 10% of

the original value (σ_0) after just four days. The current continued to drop over the time frame but at a more gradual rate. As previously mentioned, the E_{HOMO} of the oligomer is theoretically unable to form deep traps and is above the E_{LUMO} level of the dopant so the doping process is reliant on the thermal excitation of electrons from their ground state. However, since the sensor is stored at room temperature, the electrons may fall from the dopant LUMO level back into the oligomer HOMO level and this along with the other polymer/oligomer:dopant destabilizing mechanisms mentioned in the introductory chapter lead to the very poor time stability of this device. Even though the **OG-D1_A:F4TCNQ** device had poor time stability, a conductive film was still produced that when evaluated shortly after fabrication exhibited excellent temperature sensing capabilities. This implies that the dimer structure can still be used as part of an active layer without needing to engineer a donor-accepter conjugated system. Future work on these HID dimer materials may include different functional groups that induce stronger electron donating effects in the structure such that deeper charge traps may be created. Also, a more efficient synthesis route should be explored that leads to more soluble and processable intermediate products for purification and characterization purposes.

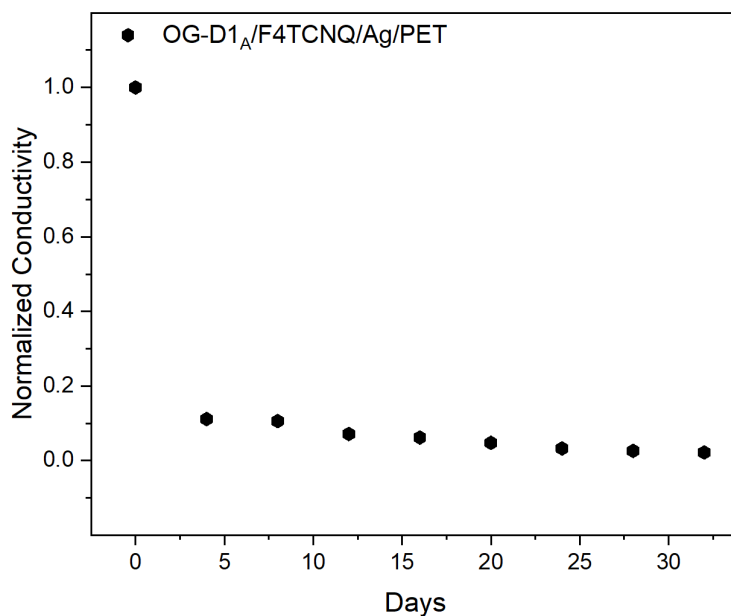


Figure 3-8: Conductivity vs. time stability of **OG-D1_A:F4TCNQ**

3.3 3,3'-((3'',4'-bis(dodecyloxy)-[2,2':5',2'':5'',2'''-quaterthiophene]-5,5'''-diyl)bis(methaneylylidene))bis(1-(2-ethylhexyl)indolin-2-one) (OG3)

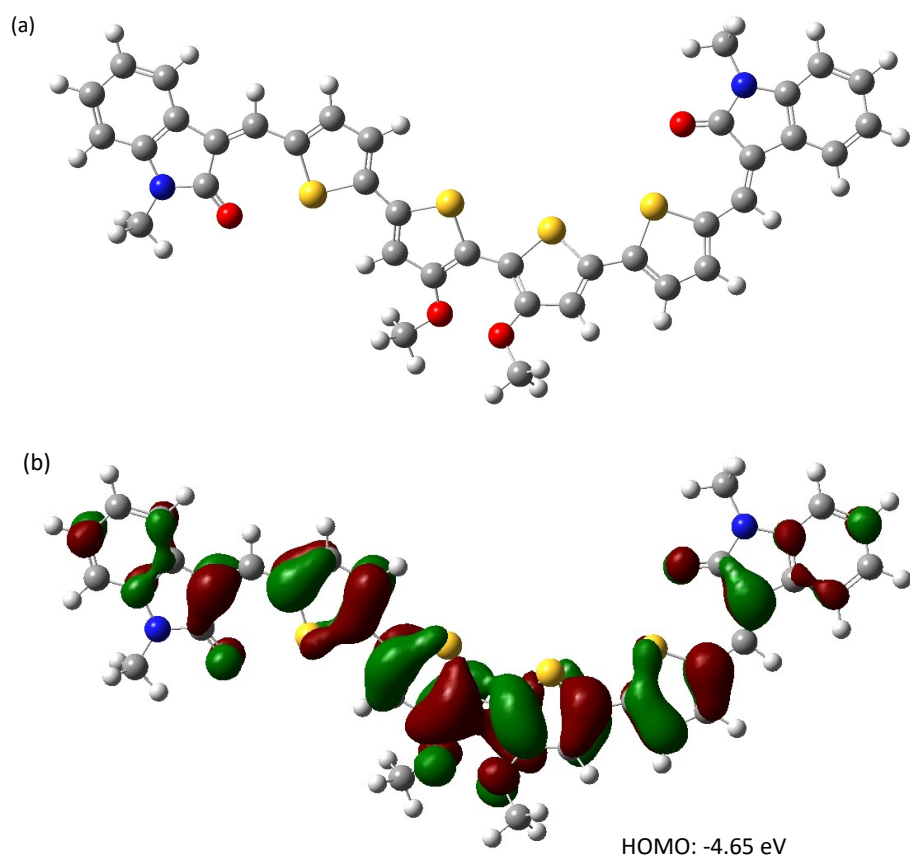
3.3.1 3,3'-((3'',4'-bis(dodecyloxy)-[2,2':5',2'':5'',2'''-quaterthiophene]-5,5'''-diyl)bis(methaneylylidene))bis(1-(2-ethylhexyl)indolin-2-one) Molecular Design

While the previous oligomer **OG-D1_A** was able to be doped with **F4TCNQ** to yield a temperature sensitive conductive film, the relatively low E_{HOMO} level led to poor stability of the material. Hence, it was believed that increasing the conjugation length of the oligomer with a donor unit should be able to increase the E_{HOMO} . Since the molecular weight of the polymers from the previous chapter didn't seem to have an impact on the time stability of the sensors it was theorized that using the same D-A system may be suitable for real-time sensing applications. Hence, **OG3** was designed by inserting the **DDOBT** donor units in between two **M3** monomer units to synthesize the D-A oligomer. The idea behind this design is to utilize the same D-A system for advantageous electronic properties such as higher E_{HOMO} and narrower E_{g} but maintain the defined structure of the oligomer unit. This lower molecular weight structure may also prove to be advantageous when trying to process in the material in less harmful, non-chlorinated solvents.

3.3.2 Structure Simulation by Density Functional Theory (DFT)

The DFT simulations and calculated energy level estimates for the **OG3** material are shown below in **Figure 3-9**. It is noted that as with the simulations for **M3**, the alkyl sidechain on the indigo unit was simulated as a simple methyl group to reduce computation time. **Table 3-5** summarizes the simulation results along with that of **M3** and the **OG-D1_A** to compare the effects of adding the donor unit as well as the effects of increasing the conjugation of the HID structure. As with the previous HID structures simulated using DFT, the **OG3** results indicate even delocalization of electrons across the whole structure to suggest good π - π stacking is expected. The E_{HOMO} of the **OG3** simulation is calculated to be -4.65 eV and the E_{LUMO} is calculated to be -2.38 eV. As anticipated, when compared to the **M3** simulation ($E_{\text{HOMO}} = -5.44$ eV), the E_{HOMO} is increased significantly due to the presence of the donor **DDOBT** even at a very low conjugation length which

in turn also leads to a significant reduction in E_g . When compared with the other oligomer reported in this work **OG-D1_A**, the inclusion of the **DDOBT** unit in between the two HID units leads to a 110 meV increase in the E_{HOMO} and a 130 meV decrease in the E_{LUMO} even without the ethylenedioxy group on the thiophene unit. Hence, the **OG3** simulation calculates an $E_g \sim 240$ meV less than that of the **OG-D1_A** even without the sidechains being thermally cleavable. These simulations suggest that the incorporation of the donor should bring about the increase in the E_{HOMO} to provide more efficient doping in the oligomer structure. Furthermore, the narrowing of the bandgap should yield a more conductive thin film when fabricating sensor devices.



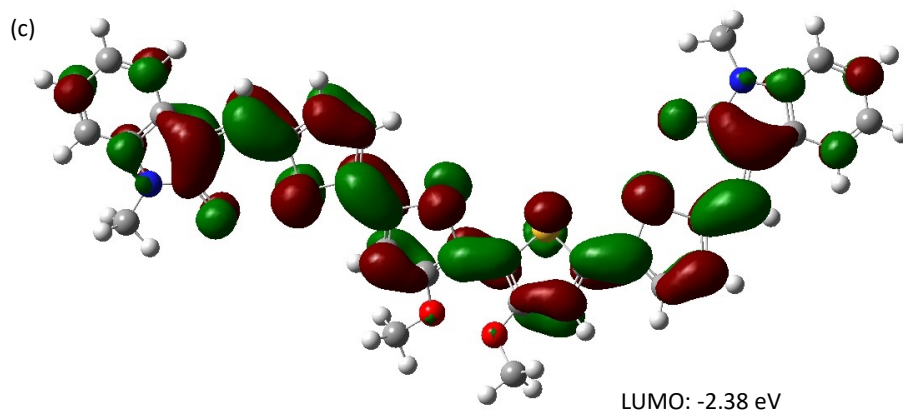


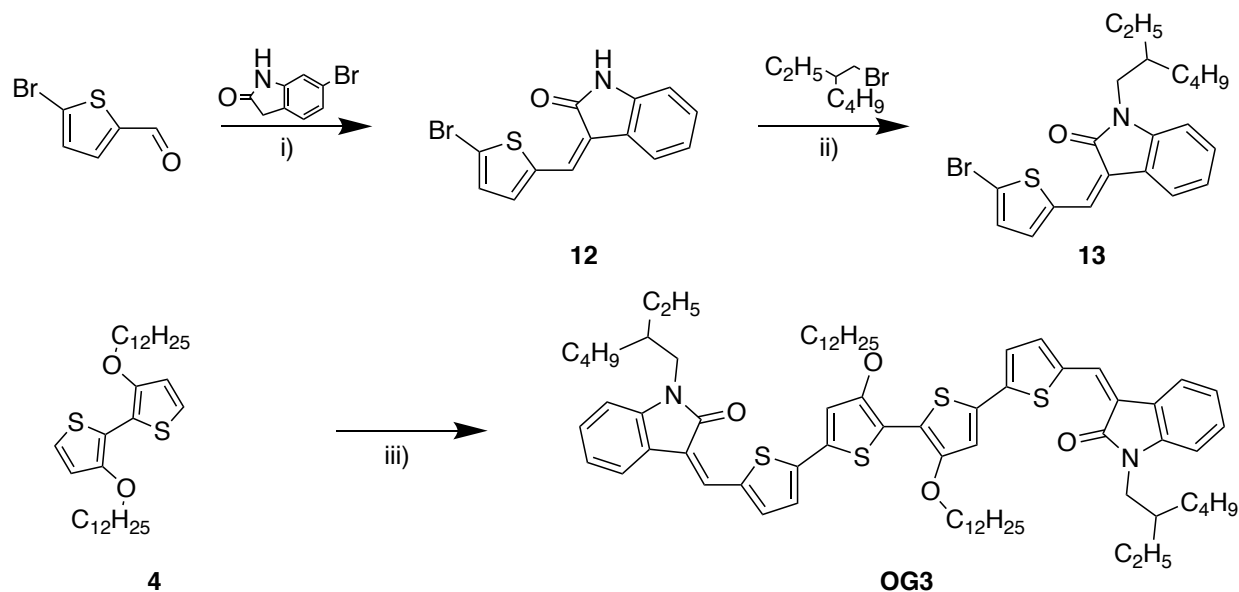
Figure 3-9: (a) Geometry of **OG3** optimized by DFT simulation in Gaussian software, (b) HOMO/(c) LUMO orbitals of the **OG3** and the DFT calculation of the orbital energy levels with respect to vacuum (0 eV).

Table 3-5: DFT calculation results for **OG3**, **M3**, and **OG-D1_A**.

	E_{HOMO}	E_{LUMO}	E_{g}
OG3	-4.65 eV	-2.38 eV	2.27 eV
M3	-5.44 eV	-2.10 eV	3.34 eV
OG-D1_A	-4.76 eV	-2.25 eV	2.51 eV

3.3.3 Synthesis of 3,3'-((3'',4'-bis(dodecyloxy)-[2,2':5',2'':5'',2'''-quaterthiophene]-5,5'''-diyl)bis(methaneylylidene))bis(1-(2-ethylhexyl)indolin-2-one)

Scheme 3-3 shows the synthetic route to yield the **OG3** oligomer utilizing the same reaction conditions as described in chapter 2 for synthesizing the HID monomers. The final step of this reaction once again utilizes the same Stille coupling mechanism but with only a single functional group on the HID units, thus further conjugation is not possible. The details for each reaction in the scheme and corresponding purification are available in section 2.6.3 with the NMR analysis for the materials are displayed in Appendix A.



Scheme 3-3: Synthetic route towards the OG3 oligomer. Reaction conditions: i) oxindole/ piperidine/ anhydrous ethanol/ 90 °C 94.2% ii) potassium carbonate/ anhydrous DMF/ 2-ethylhexyl bromide/ 100 °C 52.4% iii) tri(o-tolyl)phosphine/ tris(dibenzylideneacetone)dipalladium(0)/ degassed anhydrous chlorobenzene/ 80 °C 32.8%.

3.3.4 Characterization of OG3 by UV-Vis-NIR and CV

The UV-Vis-NIR absorbance spectra of **OG3** dissolved in chloroform, deposited as a thin film on a glass slide, and as a film doped with F4TCNQ is shown in **Figure 3-10** below. The results of this characterization are summarized in **Table 3-6** along with that of **PTEhB** to evaluate the effects that increasing the molecular weight has on this general HID structure. The solution absorbance peak of the **OG3** material is shifted towards higher energy wavelengths relative to that of the **PTEhB** material which is in accordance with conjugation theory as outlined in **Equation 2-2** from the previous chapter. An important aspect of this material is to note that while two C=C bonds are in the structure, only the Z-isomer form was present in the NMR analysis of **M3** and the NMR analysis of **OG3**. Hence, the absorbance spectra for this material in solution only shows the single sharp peak as opposed to that of **OG-D1** which showed the two distinct narrow peaks attributed to the geometric isomerization of the structure.

Upon going from solution to thin film the absorbance spectrum shifts to lower energy as expected but the λ_{onset} of the oligomer is ~ 100 nm blue-shifted relative to that of the polymer analog. This leads to **OG3** having a $E_g \sim 190$ meV wider than that of **PTEhB** so it would be expected that the corresponding **OG3** film will not be as conductive. Furthermore, going from solution to thin film, the single solution peak transforms into two discernible peaks with the lower energy peak having a noticeable shoulder which is similar to the results from the **OG-D1_A** absorbance. This effect should be characteristic of these HID oligomers due to the mixture of H- and J-aggregation imparted by the thermal annealing of the film as well as the thermal energy likely inducing the organization of the oligomers into different crystalline domains. These crystalline regions will have a different interlamellar spacing and which will impact the π - π stacking and in this case, these separate crystalline and amorphous regions will exhibit their own distinct absorption characteristics.

Upon doping, the peak in the UV-Vis region becomes a single peak again and the λ_{onset} is shifted to lower energy from the effect of conventional semiconductor doping. The same broad peak in the NIR region is observed for this material was observed for the doped polymers where the peak height is significantly higher than the baseline of the undoped film. This signals that efficient doping has occurred with this material unlike the **OG-D1_A**. It is also noted that the λ_{max} of this broad peak is ~ 1250 nm which is similar to that of the **PMEhB:F4TCNQ** film. This provides more evidence that the lower molecular weight materials will have their polaron peak shifted to higher energy wavelengths as hypothesized in the previous chapter.

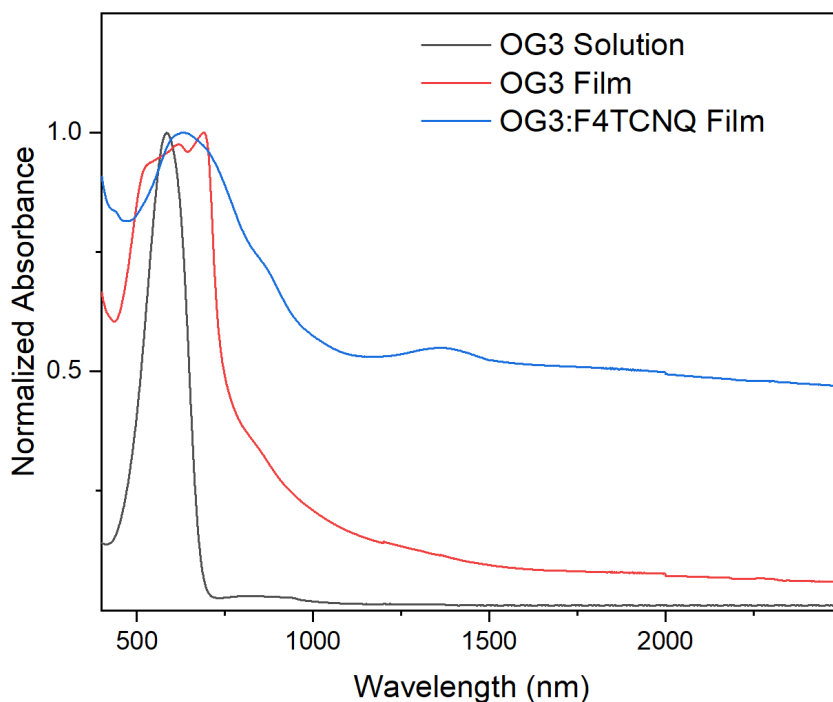


Figure 3-10: UV-Vis-NIR spectra of **OG3** in solution, as a film, and as a doped film.

Table 3-6: Summary of the UV-Vis-NIR spectroscopy results for **OG3** showing the shifts in the absorbance λ_{\max} from solution to film to doped film and film λ_{onset} .

	Film λ_{onset}	Solution λ_{\max}	Film λ_{\max}	Doped λ_{\max}
OG3	741 nm	585 nm	690 nm	633 nm
PTEhB	839 nm	634 nm	665 nm	761 nm

The CV trace shown in **Figure 3-11** below was used in conjunction with the λ_{onset} from the UV-Vis-NIR analysis to determine the molecular orbital energy levels of the oligomer and these are summarized along with **PTEhB** and **OG-D1_A** in **Table 3-7** below which also includes the relevant E_T values. The corresponding energy diagram in **Figure 3-12** represents the three materials alongside the energy levels determined for **F4TCNQ**. As expected, the introduction of the donor unit in the **OG3** structure ($E_{\text{HOMO}} = -4.91$ eV) significantly increased the E_{HOMO} compared to **OG-D1_A** ($E_{\text{HOMO}} = -5.16$ eV) even without the incorporation of the electron donating ethylenedioxy group. However, the E_g of the two oligomers was roughly the same indicating that further conjugation or functionalization is required if the bandgap needed to be narrowed further.

Interestingly, the E_{HOMO} level of the oligomer is ~ 40 meV higher at than the polymeric analog **PTEhB** indicating that for the unsubstituted thiophene HID structures, the molecular weight may not impact the E_{HOMO} too significantly. However, the same conclusion cannot be reached for the HID polymers that include the **EDOT** and **DMT** units as the substituent groups may interact differently as conjugation length is increased to affect the E_{HOMO} . Hence, strictly based on the E_{HOMO} , both the **OG3** and **PTEhB** materials should have a relatively equal probability of forming the deep traps required for good complex time stability.

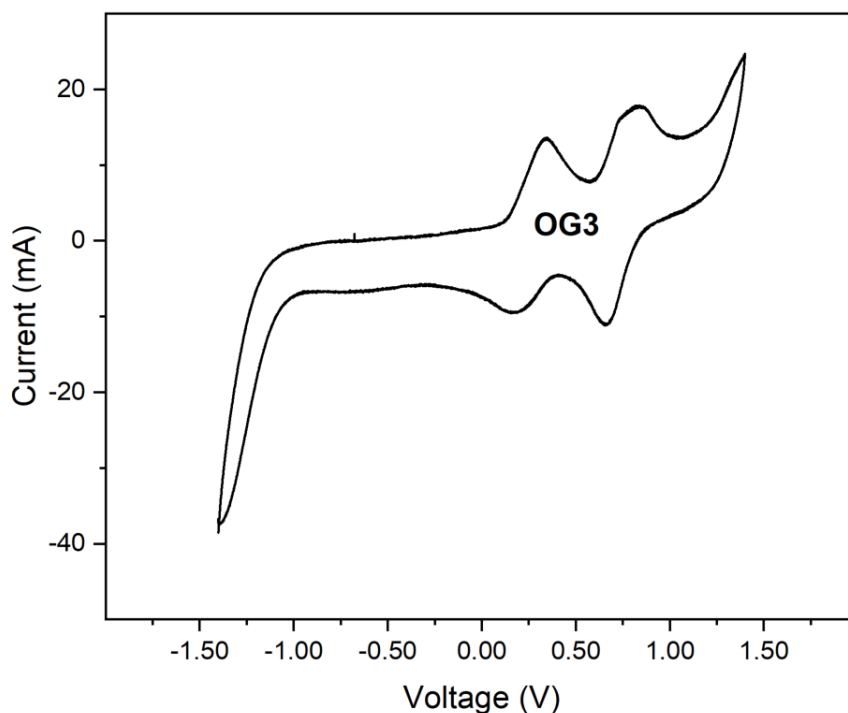


Figure 3-11: The CV trace of **OG3** at a scan rate of 0.1 V/s in 0.1 M tetrabutylammonium hexafluorophosphate with anhydrous acetonitrile as the solvent.

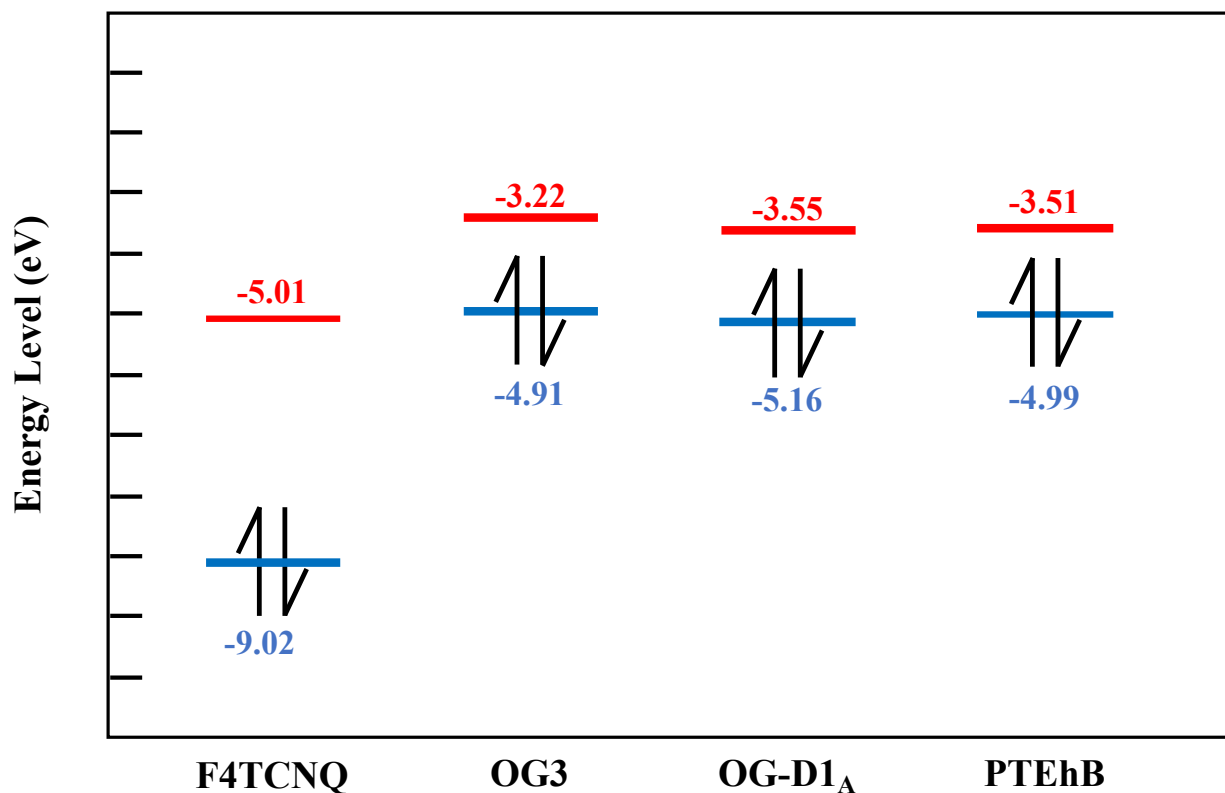


Figure 3-12: Energy level diagram depicting the relative E_{HOMO} and E_{LUMO} of **OG3**, **OG-D1_A**, **PTEhB**, and the **F4TCNQ** dopant with respect to vacuum (0 eV).

Table 3-7: Summary of the molecular orbital energy levels of the **OG3**, **OG-D1_A**, **PTEhB**, and the **F4TCNQ** dopant molecule along with E_{T} values.

	HOMO	LUMO	E_{g}	E_{T}
OG3	-4.91 eV	-3.22 eV	1.67 eV	0.10 eV
OG-D1_A	-5.16 eV	-3.55 eV	1.61 eV	-0.15 eV
PTEhB	-4.95 eV	-3.51 eV	1.48 eV	0.06 eV
F4TCNQ	-9.02 eV	-5.01 eV	4.02 eV	-

3.3.5 Temperature Sensing Performance of OG3

A device was fabricated using the **OG3:F4TCNQ** complex, with the same process as the **OG-D1_A:F4TCNQ** device, then was evaluated for its temperature sensing performance. The results of these experiments are shown in **Figure 3-13** and **Figure 3-14** as well as summarized and compared to **OG-D1_A:F4TCNQ** results in **Table 3-8**. The device current was on the order of microamperes which is the lowest of any of the devices discussed in this work leading to a noticeably noisier

signal. However, the same general step function shape of the curve was still observed but this device exhibited the lowest upper limit of working range at 55 °C. This may be due to the low conjugation length of the material which cannot remove its sidechains. The lower molecular weight of the material allows for easier movement and reorganization of **OG3** when compared to the HID polymers. This is due to a lower degree of both intermolecular (between molecules) and intramolecular (within the chain) interactions of the oligomeric material. Hence, it is easier for the insulating sidechain domains to form, and the PTC breakdown effect dominates at a lower temperature compared to the other materials. This does not occur with **OG-D1_A** due to the removal of sidechains upon thermal annealing as previously discussed. Surprisingly, the $I-T^{-0.25}$ fit is poor ($R^2 < 0.9$) with this complex so the correlation between conductivity and temperature discussed in **Equation 2-4** does not apply in this case. However, that equation strictly refers to the Mott VRH mechanism for three-dimensional charge transport while the general equation for VRH conduction is shown here in **Equation 3-1**:

$$\sigma = \sigma_0 e^{-\left(\frac{T_0}{T}\right)^{\frac{1}{d+1}}} \quad (3-1)$$

where d represents the dimensionality of the transport. Therefore, in **Figure 3-13** the fit between the current and temperature with each dimensionality is shown and none exhibit a strong correlation. These results indicate that the active layer of this device does not exhibit VRH transport, and a different mechanism or combination of mechanisms are dictating conduction in this temperature range. This is further supported by the significant difference in the TCR of this material compared to the four devices that displayed three-dimensional VRH transport properties.

Furthermore, the TCR of this device was determined to be -2.66%/°C which is substantially stronger than that of the previous four devices. This is likely due the different mechanism of charge transport occurring in this device which leads to a higher sensitivity. However, the device conductivity is relatively low (7.50×10^{-5} S/cm) which leads to the unstable signal and thus it may be difficult to use this oligomer:dopant active layer for practical temperature sensing applications. It may be possible that minor chemical alterations to the structure of the oligomer may increase the conductivity such that the resulting sensor device can operate with this enhanced sensitivity.

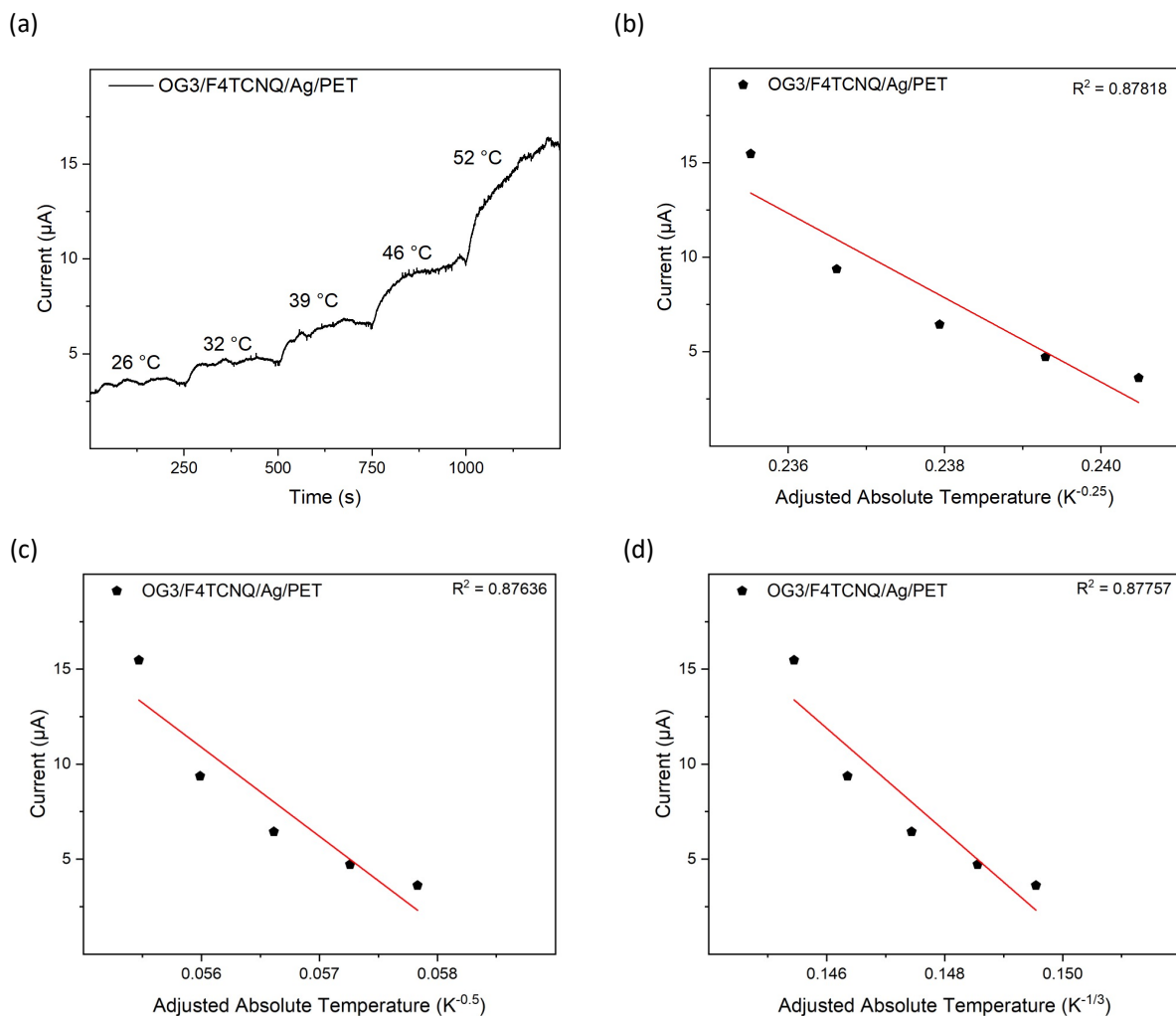


Figure 3-13: (a) Real-time current vs time (I-t) graph of **OG3:F4TCNQ** device at varying temperatures, (b) current vs adjusted absolute temperature ($I-T^{-0.25}$) three-dimensional VRH, (c) current vs adjusted absolute temperature ($I-T^{-0.5}$) one-dimensional VRH, (d) current vs adjusted absolute temperature ($I-T^{1/3}$) two-dimensional VRH graphs of **OG3:F4TCNQ** interdigitated device.

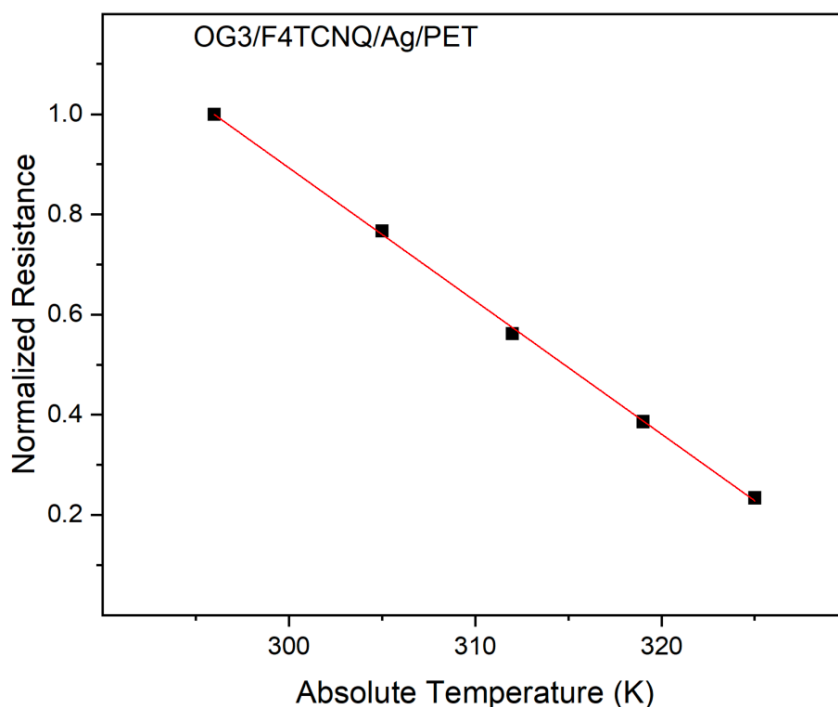


Figure 3-14: Normalized resistance vs absolute temperature plots for TCR determination of sensor device fabricated using **OG3:F4TCNQ**.

Table 3-8: Temperature sensing performance of the **OG3:F4TCNQ** and **OG-D1_A:F4TCNQ** devices fabricated on PET/Ag substrates.

	Thickness (nm)	Working Range (°C)	TCR (%/°C)	Response Time (s)	Conductivity (S/cm)
OG3:F4TCNQ	88	25 - 55	-2.66 ± 0.03	42.3 ± 27.6	7.50×10^{-5}
OG-D1_A:F4TCNQ	115	25 - 60	-1.39 ± 0.11	67.2 ± 12.1	3.02×10^{-3}
		60 - 120	-0.53 ± 0.02		

The time stability of the device using **OG3:F4TCNQ** was evaluated (**Figure 3-15**) and compared to the polymer analog **PTEhB:F4TCNQ** device. While the polymeric complex remained stable for four days before degradation, the **OG3:F4TCNQ** device already displayed conductivity loss when evaluated four days after fabrication. Both complexes showed a steady drop in conductivity over time after the initial degradation and both had reached less than 20% of their original conductivity by the end of the thirty-two-day period. These results indicate that while the E_{HOMO}

of **OG3** (-4.91 eV) is slightly higher than that of **PTEhB** (-4.95 eV) the latter material is better at holding onto dopant molecules. This should be due to the solid-state packing of the HID molecules with the **F4TCNQ** dopant and leads to the conclusion that increasing the conjugation length should lead to superior dopant efficiency for these materials. Therefore, it may be concluded that even though the **OG3** oligomer in conjunction with the **F4TCNQ** dopant has superb thermal sensitivity, the poor long-term stability of the **OG3:F4TCNQ** complex inhibits its applicability for real-time temperature monitoring. However, the well-defined structure may have more predictable changes to its properties with additional chemical modification compared to its polymeric analog and this could be advantageous in future work using these HID oligomers.

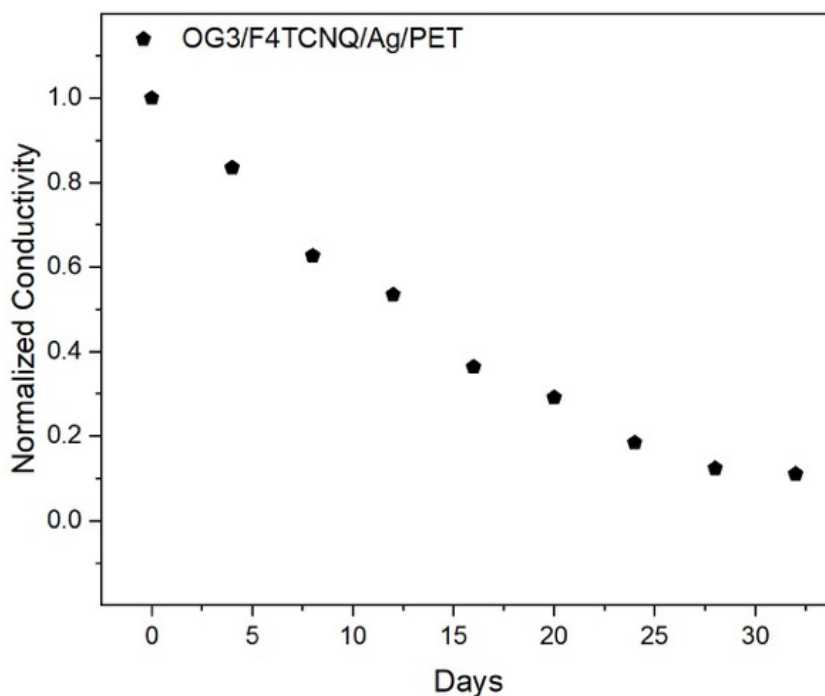


Figure 3-15: Conductivity vs. time stability of **OG3:F4TCNQ**.

3.3.6 **OG3:PSS Dispersion Results**

While the oligomers discussed in this chapter failed to form stable complexes with the **F4TCNQ** dopant, they were still able to form conductive films that were temperature sensitive. That implies that the materials still have some potential for use in organic electronics but instead of altering the

structure of the material, this work explores altering the dopant. Thanks to the relatively low molecular weight of the oligomers compared to the polymers it was believed that they may have a higher chance of being processed in less toxic solvents as they are free of chain entanglements that occur upon increasing conjugation length. Hence, inspired by the success of **PEDOT:PSS**, an effort was made to disperse the **OG3** material and **PSSA** dopant in a polar, non-chlorinated solvent using the doping mechanism of **PSS** as described in section 1.5. 3.84 mg of **OG3** was added to a small vial of 1.00 mL isopropanol and ultrasonicated before 13.7 μL of 18% **PSSA** solution in water was added to the vial. This should yield a $\sim 1.5:1$ ratio of **OG3** to **PSSA** and overall give a 0.8% weight dispersion of **OG3:PSS** in IPA. The mixture was stirred overnight, and the resulting dispersion was blade coated onto an interdigitated device.

The temperature sensing performance of the device was evaluated after a confirmed conductive film was deposited onto the PET device substrate. The results of the temperature sensing trial are shown in **Figure 3-16**. The results show that going from room temperature to 32 °C initially yields an increase in current but when further increasing the temperature, it is difficult to discern a noticeable change in the current response. While the signal stays relatively constant between 32 to 57 °C there is a small drop in current when the temperature is increased to 64 °C. It has been previously shown that the **PSS** dopant counterions can expand to form insulating regions. This swelling may increase the distance between **OG3** domains and lead to a similar PTC effect as previously discussed with the HID polymers. The NTC effect seems to be strong enough when going from 26 to 32 °C but afterwards the NTC effect may begin to compete with the PTC effect which would reduce the sensitivity of the device and, with this noisy signal, make it difficult to discern any sort of I-T relationship. Then after 57 °C, the PTC effect may begin to dominate enough such that a drop in the current is noticeable. It may also be noted that when establishing the baseline current large fluctuations occurred which may have led to the highly noisy signal. From these results it can be concluded that this **OG3:PSS** dispersion as currently processed and deposited may not yield a device suitable for practical real-time temperature monitoring.

Despite the device fabricated using **OG3:PSS** dispersion did not perform effectively as a temperature sensor, this work reports that a conductive film was able to be processed by doping **OG3** with **PSSA** and dispersing in isopropanol. The film was determined to be moderately

conductive as the conductivity was evaluated to be 5.34×10^{-4} S/cm and the metrics of the device are summarized in **Table 3-9** alongside **Figure 3-17** depicting the current response when probed between -1 V and 1 V. This proof of concept may lead to further investigation on HID materials dispersed using **PSSA** for fabrication of organic electronics using environmentally friendly solvent processing techniques. Furthermore, it may open the door for the evaluation of other thiophene-rich conjugated organic materials as candidates for **PSS** doping to determine whether dispersions with improved properties can be manufactured.

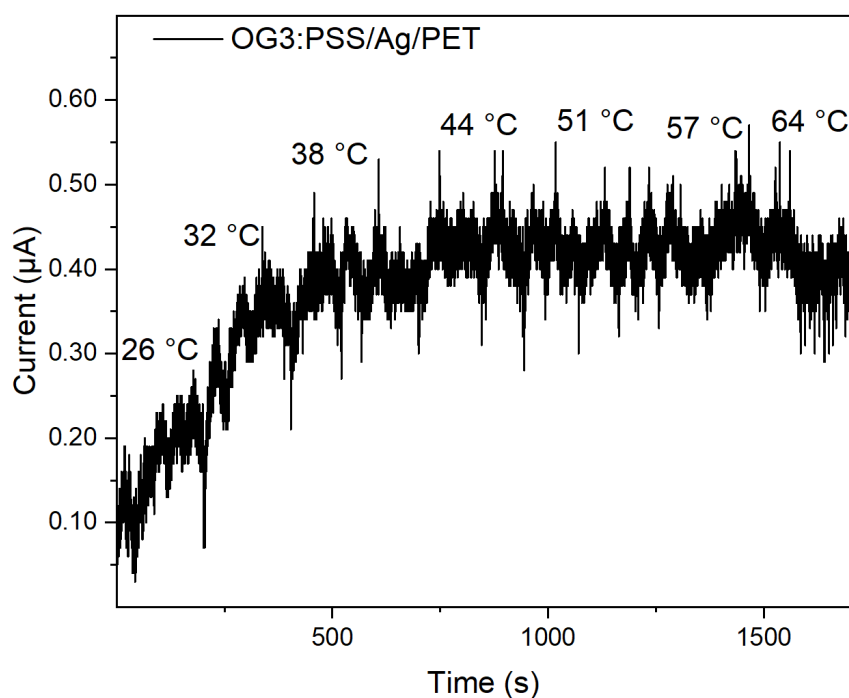


Figure 3-16: Real-time current vs time (I-t) graph of **OG3:PSS** device at varying temperatures.

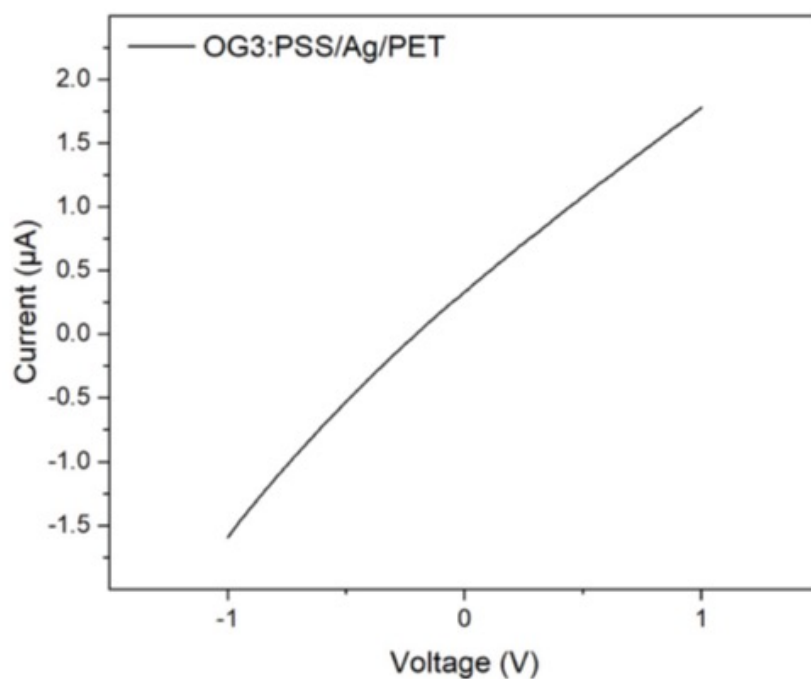


Figure 3-17: Current response of **OG3:PSS** device when probed between -1 V to 1 V.

Table 3-9: Conductivity determination results and metrics for **OG3:PSS** device.

	Thickness (nm)	Substrate/ Electrodes	W/L Ratio	Conductivity (S/cm)
OG3:PSS	270	PET/Ag	120	5.34×10^{-4}

3.4 Summary and Future Directions

In this chapter the synthesis of two HID oligomers **OG-D1** and **OG3** are reported derived from the **M1** and **M3** structures. The E_{HOMO} of the two oligomers are calculated to be -5.16 eV and -4.91 eV respectively. Both materials exhibit a significantly larger E_g relative to the HID D-A copolymers at 1.67 eV for **OG3** and 1.68 for **OG-D1** which is reduced slightly after annealing to 1.61 eV for **OG-D1_A**. Both materials are processable in chlorinated solvents such as chloroform or chlorobenzene, but a higher concentration is used in solution deposition as the film processability of these oligomers is worse than that of the polymer analogs.

OG-D1 exhibited H-aggregation properties upon deposition where the UV-Vis-NIR absorbance peak shifted towards lower wavelengths relative to the solution spectrum. Upon annealing to yield **OG-D1_A**, the single peak of the film was transformed into a multimodal distribution indicating that molecular re-arrangement has occurred leading to J-aggregation domains and potentially different crystalline regions. These effects may also be related to the removal of the carbamate sidechains used for this material to increase the coplanarity post-deposition and yield advantageous electronic properties. **OG-D1_A** was doped with **F4TCNQ** to fabricate an NTC-type temperature sensor on PET substrate. The device showed better sensitivity compared to the HID polymers with a TCR of -1.39%/°C at 25-60 °C which decreased to -0.53%/°C at 60-120 °C. Similar to the HID copolymers, a good $I \propto T^{-0.25}$ relationship was observed with this oligomeric device. Interestingly, the device did not breakdown until after 120 °C was reached which is twice the upper limit of the working range for the **PMEhB:F4TCNQ** and **PTEhB:F4TCNQ** devices. This is attributed to the removal of carbamate sidechains which slows down the evolution of insulating domains formed by the sidechains. The stability of the devices was evaluated and an immediate drop in conductivity to less than 20% of the original value was observed indicating that the **OG-D1_A:F4TCNQ** complex is not suitable for long-term temperature monitoring applications.

OG3 showed a similar E_{HOMO} compared to its polymer analog **PTEhB** ($E_{\text{HOMO}} \sim -4.95$ eV) via CV analysis so it was believed it should have similar probability of forming deep traps. The oligomer exhibited the same multimodal distribution as **OG-D1_A** which may be a unique phenomenon observed in these HID oligomers. An NTC-type temperature device was fabricated using a thin film of **OG3:F4TCNQ** and the device was shown to be thermally sensitive. However, this device did not exhibit a good $I \propto T^{-0.25}$ correlation nor did it correlate well with other dimensionalities of the VRH conduction, indicating that other mechanisms besides the proposed VRH mechanism may be governing the charge transport. The device had a slightly lower upper limit of working range at 55 °C which should be due to reduced intermolecular interactions allowing for the faster evolution of insulating regions. The sensitivity of the device was the best of the five films using **F4TCNQ** at -2.66%/°C which is attributed to different mechanisms other than three dimensional VRH dictating charge transport in the temperature range of interest. The stability of the complex was evaluated and compared to **PTEhB:F4TCNQ** and while the latter remained stable for four days, the **OG3:F4TCNQ** complex was less stable as it exhibited conductivity loss after four days.

However, due to the oligomeric nature of the material, it was able to form a dispersion in IPA with **PSSA** after sonication and overnight stirring. The dispersion was used to fabricate a temperature sensor. The I-T response of this **OG3:PSS** sensor was noisy and only a current increase from 26 °C to 32 °C was observed. From 32 °C to 57 °C it was difficult to discern any fluctuation in the current response due to the NTC effect of the organic material competing with the PTC effect of the **PSS** swelling as well as the potential **PSS** interaction with atmospheric moisture. At 64 °C a small dip in the current response is observed indicating that the PTC effect should be starting to dominate the NTC effect. While the device did not exhibit good temperature sensing properties, the film was moderately conductive with a conductivity of 5.34×10^{-4} S/cm. The processing of **OG3** in a non-chlorinated solvent is crucial discovery for reducing the environmental damage done by processing these types of conjugated organic materials in solvents like chloroform or chlorobenzene.

Two novel oligomers that demonstrate enhanced thermal sensitivity when doped with **F4TCNQ** compared to the polymers from the previous chapter are reported here. However, neither oligomer:dopant complex remains stable after initial deposition while the polymer:dopant complexes from the previous chapter exhibited superior time stability. This chapter also presents a proof of concept for processing an HID oligomeric material using the **PSS** dopant as a dispersion with IPA solvent for less toxic deposition. Future work on these materials should take advantage of their well-defined chemical structure and introduce different functional groups and sidechains to increase the E_{HOMO} or reduce the crystallinity of the material for better dopant stability. Other avenues for these materials may include optimizing the process for creating a dispersion using the HID materials. This may include use of different non-toxic solvents, changing the dopant, or other methods of breaking the bulk material into small particles for finer dispersions. For the purposes of temperature sensing, working towards mitigating the PTC effect via methods such as isolating the film from the environment with an inert protective layer should be considered for the further development of this technology.

3.5 Experimental Section

3.5.1 Materials and Characterization

The characterization techniques and devices used for the materials discussed in this chapter are the same as those discussed in section 2.6.1.

3.5.2 Fabrication of Temperature Sensor Devices

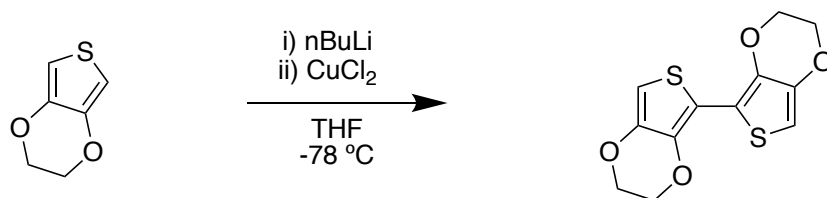
Temperature sensor devices in this chapter were fabricated using the same method as previously described in section 2.6.2 . Any deviations from the method are as follows:

- A solution of 10 mg/mL in chloroform instead of 5 mg/mL in chloroform was used for **OG-D1/OG3** as the processibility of the polymers was better compared to these lower molecular weight materials.
- The device using **OG-D1** was annealed at a T_{α} of 150 °C instead of 100 °C to maximize thermal cleavage of carbamate sidechains

The device fabricated using **OG3:PSS** dispersion was done so using the following technique. **OG3** solid was added to a 4 mL vial containing 1.00 mL of IPA. The mixture was sonicated using an ultra-sonication probe at medium setting for three hours until the mixture appeared visually uniform. A solution of 18% **PSSA** ($M_n \sim 75$ kDa) was micropipetted into the vial and a small stir bar was added. The mixture was stirred overnight at high setting and a visually uniform dispersion was observed the following day. The dispersion was deposited onto the interdigitated device on PET substrate using the same blade coating technique as previously described.

3.5.3 Synthesis Procedures

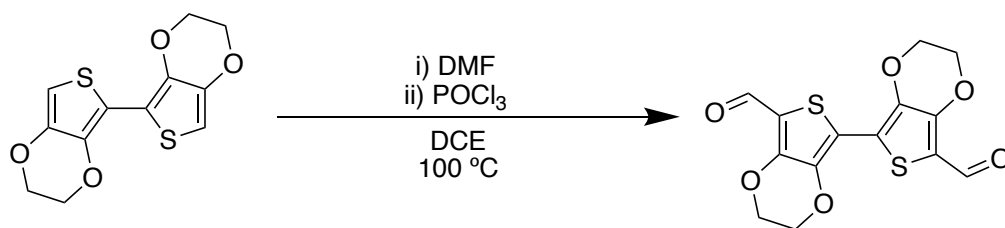
Synthesis of 2,2',3,3'-tetrahydro-5,5'-bithieno[3,4-*b*][1,4]dioxine (BEDOT)



A solution of 3,4-ethylenedioxythiophene (1.00 g, 7.03 mmol) in 15 mL of anhydrous THF all in a 50 mL oven dried three-neck round bottom flask was cooled to -78 °C using a dry ice in acetone bath. N-butyllithium 2.5 M in hexanes (2.81 mL, 7.03 mmol) was added dropwise through the auxiliary neck over the course of 30 minutes. The mixture was left to stir vigorously for two hours when it became a pale slurry. Anhydrous copper(II) chloride (946 mg, 7.03 mmol) was added quickly to the mixture and the mixture was left to react for another two hours. The reaction is quenched by adding DI water and the mixture is filtered with the precipitate being washed thoroughly with chloroform. The filtrate is collected and washed with water and brine before being dried over anhydrous sodium sulfate drying salt. The solvent is removed, and the material is recrystallized using the minimum amount of cold methanol to afford a pale white crystal solid as the 2,2',3,3'-tetrahydro-5,5'-bithieno[3,4-*b*][1,4]dioxine product. Yield: 564 mg, (56.8%)

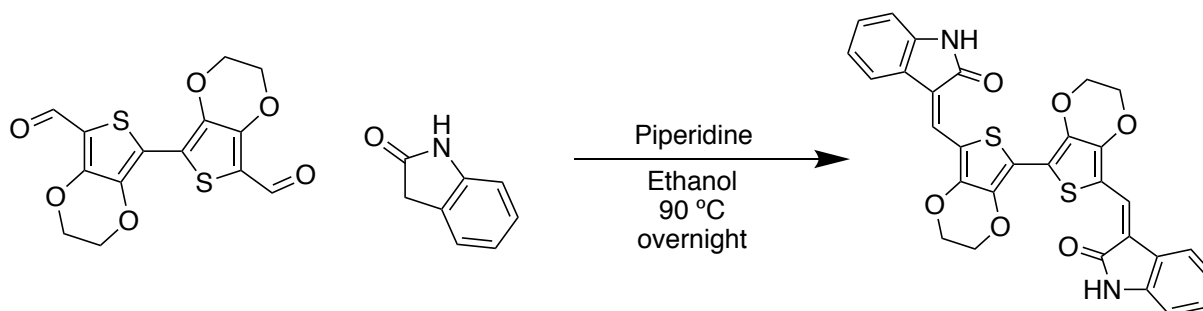
¹H NMR (300 MHz, chloroform-*d*) δ 6.29 (s, 2H), 4.31 (m, 8H)

Synthesis of 2,2',3,3'-tetrahydro-[5,5'-bithieno[3,4-*b*][1,4]dioxine]-7,7'-dicarbaldehyde (BEDOT-dCHO)



A solution of 2,2',3,3'-tetrahydro-5,5'-bithieno[3,4-*b*][1,4]dioxine (400 mg, 1.42 mmol) is dissolved in 2 mL of anhydrous dichloroethane in a two-neck oven-dried 50 mL round bottom flask and then anhydrous DMF is added to the solution (0.66 mL, 8.50 mmol) dropwise. Once the mixture becomes homogenous, phosphorous(V) oxychloride (0.79 mL, 8.50 mmol) dropwise to the solution. The flask is heated to reflux conditions at 100 °C using a silicon oil bath and the reaction is monitored by TLC until starting material is consumed. The reaction is quenched with DI water and extracted with DCM before being washed with water and saturated sodium bicarbonate solution before being dried over anhydrous sodium sulfate drying salt. The solvent is removed, and the resulting product is 263 mg of dark yellow material that NMR shows is partially monoaldehyde material but can proceed with the reactions as planned as due to the insolubility of the material it is difficult to separate the desired product from the side-products.

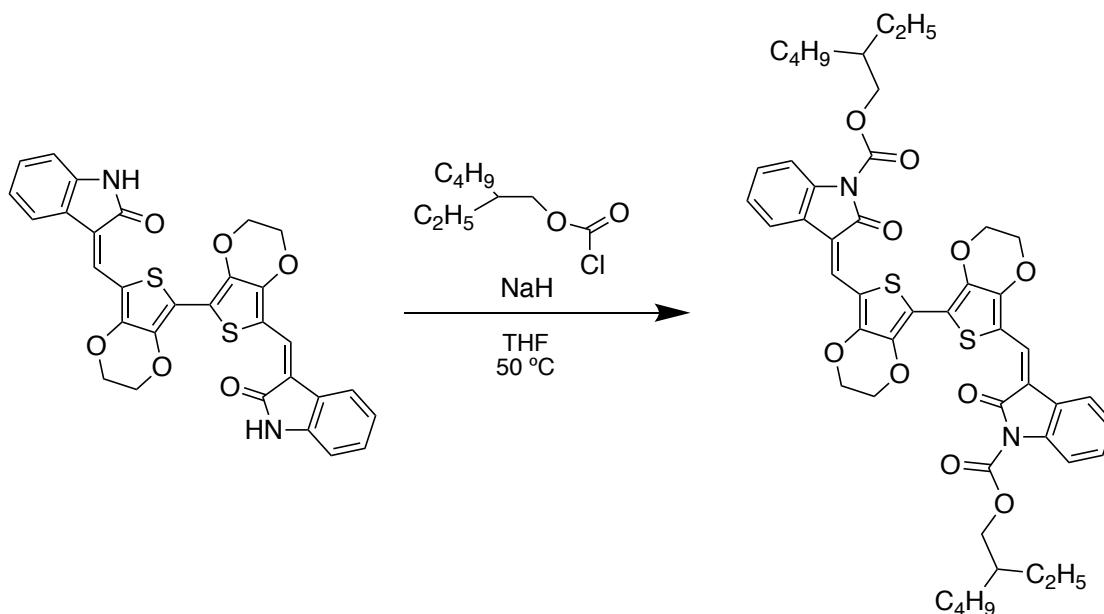
Synthesis of 3,3'-((2,2',3,3'-tetrahydro-[5,5'-bithieno[3,4-*b*][1,4]dioxine]-7,7'-diyl)bis(methaneylidene))bis(indolin-2-one) (BEEI)



The dark yellow material that according to NMR was mostly the 2,2',3,3'-tetrahydro-[5,5'-bithieno[3,4-*b*][1,4]dioxine]-7,7'-dicarbaldehyde (200 mg, 0.59 mmol) desired product from the previous reaction was dispersed with oxindole (157 mg, 1.18 mmol) in 4 mL of anhydrous methanol in an oven-dried two-neck round bottom flask. Piperidine (0.18 mL, 1.77 mmol) was added dropwise to the solution and the mixture was heated to 90 °C using a silicon oil bath and the mixture was allowed to react overnight. The reaction mixture was cooled to room temperature and the solvent was removed with the rotary evaporator and the resulting dark blue mixture was filtered out and washed with methanol and DCM. The resulting 298 mg of a dark blue crystal material was assumed to be at least partially the 3,3'-((2,2',3,3'-tetrahydro-[5,5'-bithieno[3,4-*b*][1,4]dioxine]-

7,7'-diyl)bis(methaneylylidene))bis(indolin-2-one) product but was insoluble and thus NMR could not be completed to confirm the purity of the material. Instead, the next step in the reaction series was conducted to add a carbamate sidechain to the material that should increase solubility to allow for purification and characterization.

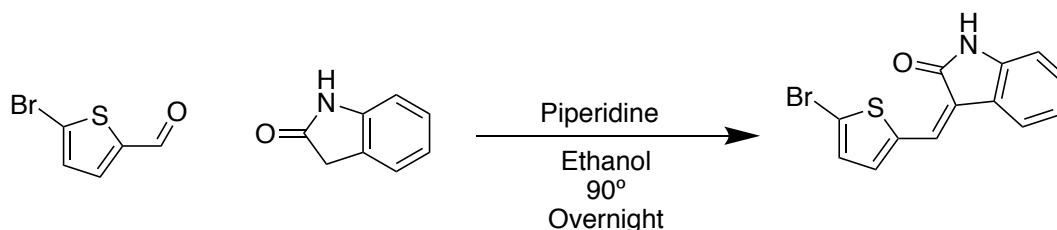
Synthesis of bis(2-ethylhexyl) 3,3'-((2,2',3,3'-tetrahydro-[5,5'-bithieno[3,4-*b*][1,4]dioxine]-7,7'-diyl)bis(methaneylylidene))-bis(2-oxoindoline-1-carboxylate) (OG-D1)



In a 100 mL two-neck oven-dried round bottom flask the dark blue material that is presumed to be partially the bis(2-ethylhexyl) 3,3'-((2,2',3,3'-tetrahydro-[5,5'-bithieno[3,4-*b*][1,4]dioxine]-7,7'-diyl)bis(methaneylylidene))-bis(2-oxoindoline-1-carboxylate) product from the previous reaction (200 mg, 0.35 mmol) and sodium hydride 60% in mineral oil (70 mg, 1.76 mmol) were dissolved in 7 mL of anhydrous THF. The reaction mixture was stirred for one hour and then 2-ethylhexyl chloroformate (0.17 mL, 0.879 mmol) was added dropwise to the solution. The reaction mixture was then warmed to 50 °C using a silicon oil bath and allowed to react for three hours while monitoring TLC. The mixture was extracted with diethyl ether and washed with water and brine. The organic portion was collected, and the solvent was reduced to a minimum before the reaction mixture was further purified via flash column chromatography using hexane: ethyl acetate (3:1) as the eluent. The resulting dark blue product yielded 67 mg of a mix of potentially three isomers of the 3,3'-((2,2',3,3'-tetrahydro-[5,5'-bithieno[3,4-*b*][1,4]dioxine]-7,7'-diyl)bis(methaneylylidene))-

bis(2-oxindoline-1-carboxylate) product but the NMR had the correct proton count hence the material was assumed to be pure isomers of the desired product. Yield: 67 mg (21.6%). NMR analysis difficult to assign isomer triplets to one another so it is excluded from this section.

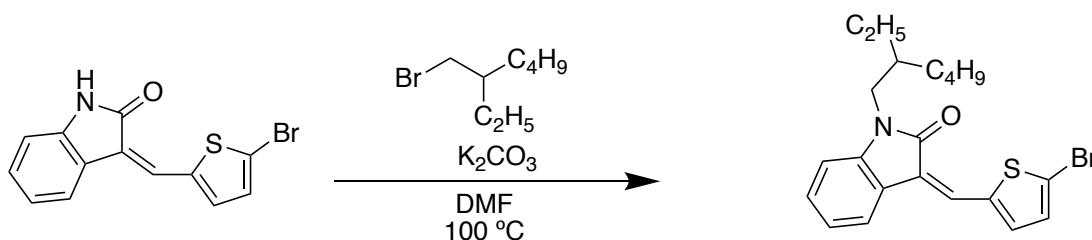
Synthesis of (Z)-3-((5-bromothiophen-2-yl)methylene)indolin-2-one (TEI-2-Br)



5-bromothiophene-2-carbaldehyde (2.00 g, 10.53 mmol) and oxindole (1.40 mg, 10.53 mmol) were dispersed in 40 mL of anhydrous ethanol in a 100 mL oven-dried three-neck round bottom flask. Piperidine (2.15, 25.28 mmol) was added to the dispersion dropwise over the course 10 minutes and the dispersion was then heated to 90 °C using a silicon oil bath. The mixture was left to react overnight when the mixture becomes an orange slurry which was allowed to cool to room temperature before being filtered to afford the single isomer of (Z)-3-((5-bromothiophen-2-yl)methylene)indolin-2-one one as a yellow crystal product. Yield: 3.03 g (94.2%)

¹H NMR (300 MHz, dimethyl sulfoxide-*d*₆) δ 10.69 (s, 1H), 8.07 (s, 1H), 7.67 (d, 1H), 7.61 (d, 1H), 7.37 (d, 1H), 7.23 (t, 1H), 7.01 (t, 1H), 6.87 (d, 1H)

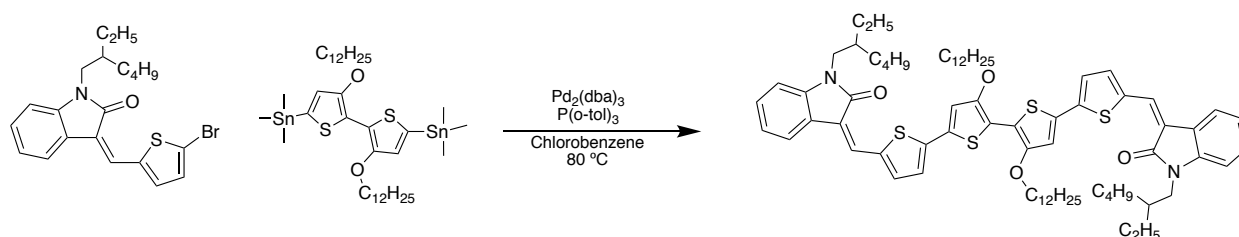
Synthesis (Z)-3-((5-bromothiophen-2-yl)methylene)-1-(2-ethylhexyl)indolin-2-one (TEI-2-Br-EH)



(Z)-3-((5-bromothiophen-2-yl)methylene)indolin-2-one (514 mg, 1.67 mmol) and potassium carbonate (855 mg, 6.18 mmol) are dissolved in 15 mL anhydrous DMF in a 50 mL three-neck oven-dried round bottom flask and the mixture is stirred at room temperature for 20 minutes before heating the mixture to 100 °C using a silicon oil bath. 2-ethylhexyl bromide (389 mg, 2.00 mmol) is added dropwise to the solution over the course of 15 minutes and the reaction is monitored using TLC. Upon the full consumption of the starting material the solution is cooled to room temperature and filtered out with the organic portion being collected then washed with DI water and brine. The solvent was removed, and the crude product was precipitated using a minimum amount of methanol before further purification via flash column chromatography using hexane: ethyl acetate (2:1) as the eluent to yield a yellow crystal material as the single isomer (Z)-3-((5-bromothiophen-2-yl)methylene)-1-(2-ethylhexyl)indolin-2-one product. Yield: 367 mg (52.4%)

¹H NMR (300 MHz, chloroform-*d*) δ 7.56 (s, 1H), 7.48 (s, 1H), 7.35 (s, 1H), 7.23 (m, 1H), 7.10 (t, 1H), 7.03 (dt, 1H), 6.82 (d, 1H), 3.67 (m, 2H), 1.86 (m, 1H), 1.33 (ddt, 8H), 0.87 (dt, 6H)

Synthesis of 3,3'-((3'',4'-bis(dodecyloxy)-[2,2':5',2'':5'',2''']-quaterthiophene)-5,5''-diyl)bis(methaneylylidene))bis(1-(2-ethylhexyl)indolin-2-one) (OG3)



In a 25 mL two-neck oven dried round bottom flask, 3-((5-bromothiophen-2-yl)methylene)-1-(2-ethylhexyl)indolin-2-one (97 mg, 0.23 mmol), (3,4'-bis(dodecyloxy)-[2,2'-bithiophene]-5,5'-diyl)bis(trimethylstannane) (100 mg, 0.12 mmol), and tri(*o*-tolyl)phosphine (2.83 mg, 0.009 mmol) are dissolved in 3 mL of degassed anhydrous chlorobenzene. Tris(dibenzylideneacetone)dipalladium(0) (2.13 mg, 0.002 mmol) is dissolved in 1 mL of the degassed anhydrous chlorobenzene and added to the reaction mixture under anhydrous conditions. The reaction mixture was heated to 80 °C using a silicon oil bath and the Stille coupling reaction was allowed to proceed for 24 hours before the reaction was cooled to room temperature where

the reaction mixture went from a dark red color to a blue color to signal the reaction is proceeding. The material was extracted with diethyl ether and washed with water and brine then further purified via flash column chromatography using DCM: hexane (3:1) as the eluent to yield a dark blue crystal material as the 3,3'-((3'',4'-bis(dodecyloxy)-[2,2':5',2'':5'',2'''-quaterthiophene]-5,5'''-diyl)bis(methaneylylidene))bis(1-(2-ethylhexyl)indolin-2-one) single isomer product. Yield: 46 mg (32.8%)

¹H NMR (300 MHz, chloroform-*d*) δ 7.64 (s, 2H), 7.54 (d, 2H), 7.49 (d, 2H), 7.19 (d, 4H), 7.03 (t, 2H), 6.84 (d, 2H), 4.19 (t, 4H), 3.71 (s, 4H), 1.91 (s, 7H), 1.59 (s, 5H), 1.24 (s, 47 H), 0.89 (m, 18 H)

Chapter 4: Conclusions and Direction for Future Work

4.1 Conclusions

In Chapter 2, three novel D-A HID copolymers **PEEhB**, **PMEhB**, **PTEhB**, were synthesized and characterized. Each polymer utilized a **DDOBT** donor unit along with their HID acceptor unit each with the different spacers **EDOT**, **DMT**, and thiophene respectively. Of the three polymers, only the **PEEhB** polymer exhibited a E_{HOMO} level high enough to theoretically form deep traps for reliable polymer:dopant complex stability. Characterization shows that the E_{HOMO} is governed by the spacer functional unit more strongly than the molecular weight of the polymer. The XRD analysis of these polymer films indicates that the **PEEhB** remains completely amorphous upon thermal treatment up to 200 °C while **PTEhB** is a crystalline material and **PMEhB** forms crystalline domains upon thermal treatment. These crystalline domains are thought to drive out dopant molecules from the polymer phase and negatively affect the polymer:dopant stability.

The three polymers were each deposited on an interdigitated electrode PET substrate and then doped with **F4TCNQ** to fabricate organic thermistors. The thermistors using **PEEhB:F4TCNQ**, **PMEhB:F4TCNQ**, and **PTEhB:F4TCNQ** exhibited excellent temperature sensing performance with TCRs of -1.09%/°C, -1.09%/°C, and -1.02%/°C at 25-60 °C. The **PEEhB** sensor exhibited a wider working range, up to 120 °C (TCR of -0.38%/°C at 60-120°C), than the other two polymers which only worked up to 60 °C. This was attributed to the amorphous nature of the polymer hindering the formation of sidechain insulating domains. While both **PMEhB:F4TCNQ** and **PTEhB:F4TCNQ** complexes degraded over time, conductivity loss after twelve and four days respectively, the **PEEhB:F4TCNQ** polymer remained stable for over thirty-two days. This was attributed more to the amorphous nature of the film than the elevated E_{HOMO} since if the latter was the dominant mechanism, one would expect the **PTEhB:F4TCNQ** complex to be more stable than the **PMEhB:F4TCNQ** complex which was shown to not be the case.

In Chapter 3, two HID oligomers were introduced derived from the **M1** and **M3** monomer structures. Both oligomeric devices doped with **F4TCNQ** exhibited better thermal sensitivity than the polymeric devices but both oligomeric devices had poor time stability. The **OG-D1** oligomer

incorporated the use of thermally removable carbamate sidechains to replace the alkyl sidechains used with the previous polymers. The oligomer exhibited interesting aggregation properties before and after the film was annealed. The removal of the carbamate sidechains should theoretically lead to better coplanarity and overall, a more conductive film. Annealing of the film to remove carbamate chains and leave an **OG-D1_A** film only led to ~ 70 meV reduction in E_g and the material exhibited quite a low E_{HOMO} at -5.16 eV. The oligomer was deposited and doped with **F4TCNQ** to yield an organic thermistor. The device showed good thermal sensitivity with a TCR -1.38%/°C at 25-60 °C and a working range of up to 120 °C (TCR of -0.53%/°C at 60-120°C) which is attributed to the removal of carbamate sidechains that should also impede the formation of insulating regions. The device stability was shown to be poor as after four days the conductivity rapidly degraded to less than 20% of its original value.

The **OG3** oligomer was synthesized and the E_{HOMO} (-4.91 eV) was determined to be similar to that of the polymeric analog (-4.95 eV). This further supports the argument that the E_{HOMO} does not solely govern HID material dopant stability. The same aggregation properties seen with **OG-D1** were present in the UV-Vis-NIR analysis of **OG3**. The corresponding temperature sensor with **F4TCNQ** had the strongest sensitivity with a TCR of -2.66%/°C and the working range was slightly narrower with an upper limit of 55 °C. The conductivity of the complex also degraded after four days but less dramatically than the **OG-D1_A:F4TCNQ** device. This was a less stable complex than the polymer analog which only destabilized after eight days even though the oligomeric material exhibited a higher E_{HOMO} . As a proof of concept, a device was fabricated using **OG3** dispersed in IPA with **PSSA** used as the dopant. The resulting film on the flexible PET substrate was moderately conductive with a conductivity of 5.34×10^{-4} S/cm.

4.2 Future Work

Future work regarding the HID copolymers introduced in Chapter 2 may include using different polymerization techniques to try and increase the molecular weight of the polymers. The three polymers have molecular weights less than 10 kDa which is unusual for polymer electronics. **PEEhB** and **PMEhB** specifically, had HT-GPC results that indicate the majority of polymer chains were no more than three repeating units long. While **PTEhB** and **OG3** have indicated that

extending the conjugation length will narrow the bandgap but have a minimal effect on the E_{HOMO} it cannot be assumed **PMEhB** and **PEEhB** will follow the same trend due to potential interactions stemming from the functional groups on the thiophene spacer. Increased conjugation may also be achieved by extending the alkyl sidechain on the HID structure of the monomers to increase the solubility of the material for the polymerization process leading to higher molecular weight polymers. This extension of the sidechain can also lead to better solubility of the resulting polymer, improving processability. Other avenues for exploring these materials may include changing the nature of the functional group on either the indigo unit or the thiophene spacer. While the alkyl chain serves its purpose in converting the HID intermediate from an insoluble material to a solution processable monomer the aliphatic chain does not provide much else in terms imparting useful properties on the resulting polymer. Altering these solubilizing sidechains to an electron donating group may further elevate the E_{HOMO} of the material to increase the probability of forming deep traps with the **F4TCNQ** dopant. Furthermore, polar chains such as oligoglycols may enhance the solubility of the material in environmentally friendly solvents and is worth exploring in future works. Both increasing the length of the sidechain and altering its nature may also impact the crystallinity of the material and research should focus on synthesis of highly amorphous films as those are shown to be advantageous for holding dopant molecules in the polymer phase.

Future work on the oligomeric materials may include further functionalizing **OG-D1** with electron donating groups to raise the E_{HOMO} which would reduce the E_g of the oligomer as well as theoretically improve oligomer:dopant complex stability. Since the **M1** may be synthesized with a bromine group on the end of the indigo unit, as was done when preparing the **PEEhB** monomer **M1**, that position of the molecule is a prime location for functionalizing **OG-D1**. Some potential modifications for the **M1** structure to synthesize a modified **OG-D1** material are shown below in **Figure 4-1**. Other prospects regarding these types of materials may include improving the synthesis procedure for a better yield that would allow for practical scale-up of the material. The current yield of the material is very low due to insoluble intermediate products making purification challenging. Methods of circumventing this may include the coupling of two **M1** units without the indigo bromine group after the sidechain has been added. Another potential optimization of the synthesis procedure may be the addition of the sidechain to the indigo unit before the condensation reaction which would at least remove one of the insoluble intermediates from the reaction scheme.

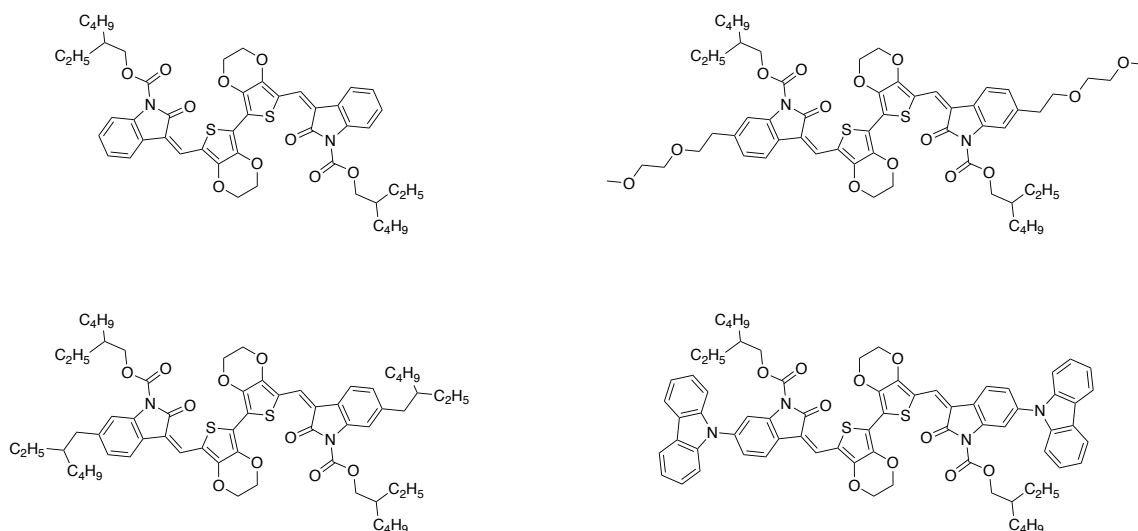


Figure 4-1: The original structure of **OG-D1** and the structures of potential modifications that may yield enhanced properties for the corresponding doped film.

Similar methods of exploring future work on the **OG3** structure may also be implemented to improve the electronic properties. More polar functional groups may improve the solubility in non-chlorinated solvents and thus lead to a more uniform dispersion. Other potential changes to explore may include using other polar dopants for these dispersions such as HCl along with different solvents to optimize the dispersion so that thinner, more uniform films may be fabricated. Another avenue worth exploring is working towards circumventing the issue with **PSS** swelling to form insulating layers by either isolating the film from the environment or via other means to properly characterize the temperature sensing capabilities of a device using **OG3:PSS** active layer.

Bibliography

1. Dzugan T, Kroupa M, Reboun J. Sensitivity of Organic Humidity Sensor Element on Organic Vapours. *Procedia Eng.* 2014;69:962-967.
2. Al-Sehemi AG, Al-Assiri MS, Kalam A, et al. Sensing performance optimization by tuning surface morphology of organic (D- π -A) dye based humidity sensor. *Sens Actuators B Chem.* 2016;231:30-37.
3. Rubinger CPL, Martins CR, De Paoli MA, Rubinger RM. Sulfonated polystyrene polymer humidity sensor: Synthesis and characterization. *Sens Actuators B Chem.* 2007;123(1):42-49.
4. Han S, Cheng J, Fan H, Yu J, Li L. Achievement of High-Response Organic Field-Effect Transistor NO₂ Sensor by Using the Synergistic Effect of ZnO/PMMA Hybrid Dielectric and CuPc/Pentacene Heterojunction. *Sensors.* 2016;16(10):1763.
5. Haasnoot W, Bienenmann-Ploum M, Lamminmäki U, Swanenburg M, van Rhijn H. Application of a multi-sulfonamide biosensor immunoassay for the detection of sulfadiazine and sulfamethoxazole residues in broiler serum and its use as a predictor of the levels in edible tissue. *Anal Chim Acta.* 2005;552(1-2):87-95.
6. Rizzo G, Arena A, Donato N, et al. Flexible, all-organic ammonia sensor based on dodecylbenzene sulfonic acid-doped polyaniline films. *Thin Solid Films.* 2010;518(23):7133-7137.
7. Liu J, Agarwal M, Varahramyan K. Glucose sensor based on organic thin film transistor using glucose oxidase and conducting polymer. *Sens Actuators B Chem.* 2008;135(1):195-199.
8. Someya T, Sekitani T, Iba S, Kato Y, Kawaguchi H, Sakurai T. A large-area, flexible pressure sensor matrix with organic field-effect transistors for artificial skin applications. *Proc Natl Acad Sci.* 2004;101(27):9966-9970.
9. Chakraborty P, Guterman T, Adadi N, et al. A Self-Healing, All-Organic, Conducting, Composite Peptide Hydrogel as Pressure Sensor and Electrogenic Cell Soft Substrate. *ACS Nano.* 2019;13(1):163-175.
10. Mansoor M, Haneef I, Akhtar S, De Luca A, Udrea F. Silicon diode temperature sensors - A review of applications. *Sens Actuators Phys.* 2015;232:63-74.
11. Hromadka J, Mohd Hazlan NN, Hernandez FU, et al. Simultaneous in situ temperature and relative humidity monitoring in mechanical ventilators using an array of functionalised optical fibre long period grating sensors. *Sens Actuators B Chem.* 2019;286:306-314.
12. Maggiore Q, Pizzarelli F, Santoro A, et al. The effects of control of thermal balance on vascular stability in hemodialysis patients: Results of the European randomized clinical trial. *Am J Kidney Dis.* 2002;40(2):280-290.

13. Varon J, Acosta P. Therapeutic Hypothermia. *Chest*. 2008;133(5):1267-1274.
14. Graz I, Krause M, Bauer-Gogonea S, et al. Flexible active-matrix cells with selectively poled bifunctional polymer-ceramic nanocomposite for pressure and temperature sensing skin. *J Appl Phys*. 2009;106(3).
15. Kanao K, Harada S, Yamamoto Y, et al. Highly selective flexible tactile strain and temperature sensors against substrate bending for an artificial skin. *RSC Adv*. 2015;5(38):30170-30174.
16. Harada S, Kanao K, Yamamoto Y, Arie T, Akita S, Takei K. Fully Printed Flexible Fingerprint-like Three-Axis Tactile and Slip Force and Temperature Sensors for Artificial Skin. *ACS Nano*. 2014;8(12):12851-12857.
17. Zhu C, Wu HC, Nyikayaramba G, Bao Z, Murmann B. Intrinsically Stretchable Temperature Sensor Based on Organic Thin-Film Transistors. *IEEE Electron Device Lett*. 2019;40(10):1630-1633.
18. Yokota T, Inoue Y, Terakawa Y, et al. Ultraflexible, large-area, physiological temperature sensors for multipoint measurements. *Proc Natl Acad Sci*. 2015;112(47):14533-14538.
19. Ren X, Pei K, Peng B, et al. A Low-Operating-Power and Flexible Active-Matrix Organic-Transistor Temperature-Sensor Array. *Adv Mater*. 2016;28(24):4832-4838.
20. Wu X, Ma Y, Zhang G, et al. Thermally stable, biocompatible, and flexible organic field effect transistors and their application in temperature sensing arrays for artificial skin. *Adv Funct Mater*. 2015;25(14):2138-2146.
21. Yuvaraja S, Nawaz A, Liu Q, et al. Organic field-effect transistor-based flexible sensors. *Chem Soc Rev*. 2020;49(11):3423-3460.
22. Someya T, Kato Y, Sekitani T, et al. Conformable, flexible, large-area networks of pressure and thermal sensors with organic transistor active matrixes. *Proc Natl Acad Sci*. 2005;102(35):12321-12325.
23. Ren X, Chan PKL, Lu J, Huang B, Leung DCW. High dynamic range organic temperature sensor. *Adv Mater*. 2013;25(9):1291-1295.
24. Song M, Seo J, Kim H, Kim Y. Flexible Thermal Sensors Based on Organic Field-Effect Transistors with Polymeric Channel/Gate-Insulating and Light-Blocking Layers. *ACS Omega*. 2017;2(7):4065-4070.
25. Mandal S, Banerjee M, Roy S, et al. Organic Field-Effect Transistor-Based Ultrafast, Flexible, Physiological-Temperature Sensors with Hexagonal Barium Titanate Nanocrystals in Amorphous Matrix as Sensing Material. *ACS Appl Mater Interfaces*. 2019;11(4):4193-4202.

26. Park S, Kang J, Park J, Mun S. One-bodied humidity and temperature sensor having advanced linearity at low and high relative humidity range. *Sens Actuators B Chem.* 2001;76(1-3):322-326.
27. Shih WP, Tsao LC, Lee CW, et al. Flexible Temperature Sensor Array Based on a Graphite-Polydimethylsiloxane Composite. *Sensors.* 2010;10(4):3597-3610.
28. Hou J, Park MH, Zhang S, et al. Bandgap and Molecular Energy Level Control of Conjugated Polymer Photovoltaic Materials Based on Benzo[1,2-*b*:4,5-*b'*]dithiophene. *Macromolecules.* 2008;41(16):6012-6018.
29. Meyers F, Heeger AJ, Brédas JL. Fine tuning of the band gap in conjugated polymers via control of block copolymer sequences. *J Chem Phys.* 1992;97(4):2750-2758.
30. Li L, Counts KE, Kurosawa S, Teja AS, Collard DM. Tuning the Electronic Structure and Solubility of Conjugated Polymers with Perfluoroalkyl Substituents: Poly(3-perfluorooctylthiophene), the First Supercritical CO₂-soluble Conjugated Polymer. *Adv Mater.* 2004;16(2):180-183.
31. Yang Y, Lin ZH, Hou T, Zhang F, Wang ZL. Nanowire-composite based flexible thermoelectric nanogenerators and self-powered temperature sensors. *Nano Res.* 2012;5(12):888-895.
32. Billingham NC, Calvert PD, Foot PJS, Mohammad F. Stability and degradation of some electrically conducting polymers. *Polym Degrad Stab.* 1987;19(4):323-341.
33. Oh JH, Hong SY, Park H, et al. Fabrication of High-Sensitivity Skin-Attachable Temperature Sensors with Bioinspired Microstructured Adhesive. *ACS Appl Mater Interfaces.* 2018;10(8):7263-7270.
34. Bießmann L, Kreuzer LP, Widmann T, Hohn N, Moulin JF, Müller-Buschbaum P. Monitoring the Swelling Behavior of PEDOT:PSS Electrodes under High Humidity Conditions. *ACS Appl Mater Interfaces.* 2018;10(11):9865-9872.
35. Jin Z, Su Y, Duan Y. An improved optical pH sensor based on polyaniline. Published online 2000:5.
36. Wen Y, Xu J. Scientific Importance of Water-Processable PEDOT-PSS and Preparation, Challenge and New Application in Sensors of Its Film Electrode: A Review. *J Polym Sci Part Polym Chem.* 2017;55(7):1121-1150.
37. Schafft HA, Suehle JS. The measurement, use and interpretation of the temperature coefficient of resistance of metallizations. *Solid-State Electron.* 1992;35(3):403-410.
38. Rieger L, Alex J, Winkler S, Boehler M, Thomann M, Siegrist H. Progress in sensor technology - progress in process control? Part I: Sensor property investigation and classification. *Water Sci Technol.* 2003;47(2):103-112.

39. Tesla N, inventor; Electrical Condenser. U. S. Patent No. 464 667. December 18, 1891.
40. Leidl A, Hartinger R, Roth M, Endres HE. A New So, Sensor System With Saw And Idc Elements. In: *Proceedings of the International Solid-State Sensors and Actuators Conference - TRANSDUCERS '95*. IEEE; 1995:818-820.
41. Sheiretov Y. *Deep Penetration Magnetoquasistatic Sensors*. Ph.D. Dissertation. Massachusetts Institute of Technology. 2001
42. Zaretsky MC, Li P, Melcher JR. Estimation of thickness, complex bulk permittivity and surface conductivity using interdigital dielectrometry. *IEEE Trans Electr Insul*. 1989;24(6):1159-1166.
43. A.V. Mamishev, Sundara-Rajan K, Fumin Yang, Yanqing Du, Zahn M. Interdigital sensors and transducers. *Proc IEEE*. 2004;92(5):808-845.
44. Xiang PH, Dong XL, Chen H, Zhang Z, Guo JK. Mechanical and electrical properties of small amount of oxides reinforced PZT ceramics. *Ceram Int*. 2003;29(5):499-503.
45. Hwang HJ, Yasuoka M, Sando M, Toriyama M, Niihara K. Fabrication, Sinterability, and Mechanical Properties of Lead Zirconate Titanate/Silver Composites. *J Am Ceram Soc*. 1999;82(9):2417-2422.
46. Mamishev AV, Lesieutre BC, Zahn M. Optimization of multi-wavelength interdigital dielectrometry instrumentation and algorithms. *IEEE Trans Dielectr Electr Insul*. 1998;5(3):408-420.
47. Varadan VK, Varadan VV, Bao XQ. IDT, SAW, and MEMS sensors for measuring deflection, acceleration, and ice detection of aircraft. In: Varadan VK, McWhorter PJ, eds. ; 1997:209-219.
48. Gardner JW. Intelligent gas sensing using an integrated sensor pair. *Sens Actuators B Chem*. 1995;27(1-3):261-266.
49. Huyberechts G, Frisson L. In situ formation of humidity-sensitive devices for the evaluation of solar panel encapsulations. *Sens Actuators B Chem*. 1995;27(1-3):308-311.
50. Kolesar ES, Wiseman JM. Interdigitated gate electrode field effect transistor for the selective detection of nitrogen dioxide and diisopropyl methylphosphonate. *Anal Chem*. 1989;61(21):2355-2361.
51. Reiß S, Hagen G, Moos R. Zeolite-based Impedimetric Gas Sensor Device in Low-cost Technology for Hydrocarbon Gas Detection. *Sensors*. 2008;8(12):7904-7916.
52. Castro HF, Correia V, Pereira N, Costab P, Oliveiraa J, Lanceros-Méndez S. Printed Wheatstone bridge with embedded polymer based piezoresistive sensors for strain sensing applications. *Addit Manuf*. 2018;20:119-125.

53. Salmaz U, Islam T, Sohail S. A Novel Linear Capacitive Temperature Sensor Using Polydimethylsiloxane. *IEEE Trans Instrum Meas.* 2020;69(10):7887-7894.
54. Ren QY, Wang LF, Huang JQ, Zhang C, Huang QA. A novel capacitive temperature sensor for a lab-on-a-chip system. In: *IEEE SENSORS 2014 Proceedings.* IEEE; 2014:436-439.
55. Monroe D, Kastner MA. Generalizations of multiple trapping. *Philos Mag B.* 1983;47(6):605-620.
56. Nenashev AV, Oelerich JO, Jandieri K, et al. Field-enhanced mobility in the multiple-trapping regime. *Phys Rev B.* 2018;98(3):035201.
57. Haque F, Lim S, Lee S, Park Y, Mativenga M. Highly Sensitive and Ambient Air-Processed Hybrid Perovskite TFT Temperature Sensor. *IEEE Electron Device Lett.* 2020;41(7):1086-1089.
58. Ye R, Ohta K, Baba M. Temperature Dependence of Electrical Properties of Organic Thin Film Transistors Based on pn Heterojunction and Their Applications in Temperature Sensors. *J Comput Commun.* 2016;04(05):10-15.
59. Apsley N, Hughes HP. Temperature-and field-dependence of hopping conduction in disordered systems. *Philos Mag.* 1974;30(5):963-972.
60. Shklovskii BI, Efros AL. *Electronic Properties of Doped Semiconductors.* Vol 45. Springer Berlin Heidelberg; 1984.
61. Mott NF. Conduction in Non-crystalline Materials III. Localized States in a Pseudogap and Near Extremities of Conduction and Valence Bands. In: *World Scientific Series in 20th Century Physics.* Vol 12. WORLD SCIENTIFIC; 1995:465-482.
62. Ye R, Baba M, Ohishi Y, Mori K, Suzuki K. On the correlation between morphology and electronic properties of fluorinated copper phthalocyanine (F16CuPc) thin films. *Mol Cryst Liq Cryst.* 2006;444:203-210.
63. Subbarao NVV, Mandal S, Gedda M, Iyer PK, Goswami DK. Effect of temperature on hysteresis of dipolar dielectric layer based organic field-effect transistors: A temperature sensing mechanism. *Sens Actuators Phys.* 2018;269:491-499.
64. Peng Q, Park K, Lin T, Durstock M, Dai L. Donor- π -Acceptor Conjugated Copolymers for Photovoltaic Applications: Tuning the Open-Circuit Voltage by Adjusting the Donor/Acceptor Ratio. *J Phys Chem B.* 2008;112(10):2801-2808.
65. Gross YM, Trefz D, Tkachov R, et al. Tuning Aggregation by Regioregularity for High-Performance n-Type P(NDI2OD-T₂) Donor-Acceptor Copolymers. *Macromolecules.* 2017;50(14):5353-5366.

66. Ko S, Mondal R, Risko C, et al. Tuning the Optoelectronic Properties of Vinylene-Linked Donor–Acceptor Copolymers for Organic Photovoltaics. *Macromolecules*. 2010;43(16):6685-6698.
67. Silva Sousa DF, Rosso Dotto ME, Eccher J, Bock H, Bechtold IH. Blending with a phthalocyanine leads to improved P3HT donor layers for OPVs. *Synth Met*. 2020;263:116367.
68. Zhou W, Zhang ZG, Ma L, Li Y, Zhan X. Dithienocoronene diimide based conjugated polymers as electron acceptors for all-polymer solar cells. *Sol Energy Mater Sol Cells*. 2013;112:13-19.
69. Li Y, Xue L, Xia H, Xu B, Wen S, Tian W. Synthesis and properties of polythiophene derivatives containing triphenylamine moiety and their photovoltaic applications. *J Polym Sci Part Polym Chem*. 2008;46(12):3970-3984.
70. Wang K, Xu Z, Guo B, Guo X, Zhang M, Li Y. TPD-based polythiophene derivatives with higher V_{oc} for polymer solar cells. *RSC Adv*. 2016;6(68):63338-63346.
71. Lin Y, Zhao F, Prasad SKK, et al. Balanced Partnership between Donor and Acceptor Components in Nonfullerene Organic Solar Cells with >12% Efficiency. *Adv Mater*. 2018;30(16):1706363.
72. Yuan J, Zhang Y, Zhou L, et al. Single-Junction Organic Solar Cell with over 15% Efficiency Using Fused-Ring Acceptor with Electron-Deficient Core. *Joule*. 2019;3(4):1140-1151.
73. Huang S, Wu F, Liu Z, Cui Y, Chen L, Chen Y. Novel polymer acceptors achieving 10.18% efficiency for all-polymer solar cells. *J Energy Chem*. 2021;53:63-68.
74. Pandey L, Risko C, Norton JE, Brédas JL. Donor–Acceptor Copolymers of Relevance for Organic Photovoltaics: A Theoretical Investigation of the Impact of Chemical Structure Modifications on the Electronic and Optical Properties. *Macromolecules*. 2012;45(16):6405-6414.
75. Nakashima M, Otsura T, Naito H, Ohshita J. Synthesis of new D-A polymers containing disilanobithiophene donor and application to bulk heterojunction polymer solar cells. *Polym J*. 2015;47(11):733-738.
76. Jacobs IE, Aasen EW, Oliveira JL, et al. Comparison of solution-mixed and sequentially processed P3HT:F4TCNQ films: effect of doping-induced aggregation on film morphology. *J Mater Chem C*. 2016;4(16):3454-3466.
77. Fontana MT, Stanfield DA, Scholes DT, Winchell KJ, Tolbert SH, Schwartz BJ. Evaporation vs Solution Sequential Doping of Conjugated Polymers: F4TCNQ Doping of Micrometer-Thick P3HT Films for Thermoelectrics. *J Phys Chem C*. 2019;123(37):22711-22724.

78. Hynynen J, Kiefer D, Müller C. Influence of crystallinity on the thermoelectric power factor of P3HT vapour-doped with F₄TCNQ. *RSC Adv.* 2018;8(3):1593-1599.
79. Watts KE, Neelamraju B, Moser M, McCulloch I, Ratcliff EL, Pemberton JE. Thermally Induced Formation of HF₄TCNQ⁻ in F₄TCNQ-Doped Regioregular P3HT. *J Phys Chem Lett.* 2020;11(16):6586-6592.
80. Lim E, Peterson KA, Su GM, Chabinyc ML. Thermoelectric Properties of Poly(3-hexylthiophene) (P3HT) Doped with 2,3,5,6-Tetrafluoro-7,7,8,8-tetracyanoquinodimethane (F₄TCNQ) by Vapor-Phase Infiltration. *Chem Mater.* 2018;30(3):998-1010.
81. Yim KH, Whiting GL, Murphy CE, et al. Controlling Electrical Properties of Conjugated Polymers via a Solution-Based p-Type Doping. *Adv Mater.* 2008;20(17):3319-3324.
82. Li C, Duan L, Li H, Qiu Y. Universal Trap Effect in Carrier Transport of Disordered Organic Semiconductors: Transition from Shallow Trapping to Deep Trapping. *J Phys Chem C.* 2014;118(20):10651-10660.
83. Sun B, Hong W, Guo C, Suttly S, Aziz H, Li Y. Utilization of hole trapping effect of aromatic amines to convert polymer semiconductor from ambipolar into n-type. *Org Electron.* 2016;37:190-196.
84. Kim N, Kee S, Lee SH, et al. Highly Conductive PEDOT:PSS Nanofibrils Induced by Solution-Processed Crystallization. *Adv Mater.* 2014;26(14):2268-2272.
85. Wei Q, Mukaida M, Naitoh Y, Ishida T. Morphological Change and Mobility Enhancement in PEDOT:PSS by Adding Co-solvents. *Adv Mater.* 2013;25(20):2831-2836.
86. Fan Z, Ouyang J. Thermoelectric Properties of PEDOT:PSS. *Adv Electron Mater.* 2019;5(11):1800769.
87. Gangopadhyay R, Das B, Molla MR. How does PEDOT combine with PSS? Insights from structural studies. *RSC Adv.* 2014;4(83):43912-43920.
88. Ye G, Liu J, Qiu X, et al. Controlling n-Type Molecular Doping via Regiochemistry and Polarity of Pendant Groups on Low Band Gap Donor-Acceptor Copolymers. *Macromolecules.* 2021;54(8):3886-3896.
89. Guo X, Quinn J, Chen Z, et al. Dialkoxybithiazole: A New Building Block for Head-to-Head Polymer Semiconductors. *J Am Chem Soc.* 2013;135(5):1986-1996.
90. Mao H, Xu B, Holdcroft S. Synthesis and structure-property relationships of regioirregular poly(3-hexylthiophenes). *Macromolecules.* 1993;26(5):1163-1169.
91. Chen TA, Wu X, Rieke RD. Regiocontrolled Synthesis of Poly(3-alkylthiophenes) Mediated by Rieke Zinc: Their Characterization and Solid-State Properties. *J Am Chem Soc.* 1995;117(1):233-244.

92. McCullough RD, Lowe RD, Jayaraman M, Anderson DL. Design, synthesis, and control of conducting polymer architectures: structurally homogeneous poly(3-alkylthiophenes). *J Org Chem*. 1993;58(4):904-912.
93. Chen TA, Rieke RD. The first regioregular head-to-tail poly(3-hexylthiophene-2,5-diyl) and a regiorandom isopolymer: nickel versus palladium catalysis of 2(5)-bromo-5(2)-(bromozincio)-3-hexylthiophene polymerization. *J Am Chem Soc*. 1992;114(25):10087-10088.
94. He J, Su Z, Yan B, Xiang L, Wang Y. The Effects of Different Side Groups on the Properties of Polythiophene. *J Macromol Sci Part A*. 2007;44(9):989-993.
95. Malik S, Nandi AK. Crystallization mechanism of regioregular poly(3-alkyl thiophene)s. *J Polym Sci Part B Polym Phys*. 2002;40(18):2073-2085.
96. Chandrasekaran N, Gann E, Jain N, et al. Correlation between Photovoltaic Performance and Interchain Ordering Induced Delocalization of Electronics States in Conjugated Polymer Blends. *ACS Appl Mater Interfaces*. 2016;8(31):20243-20250.
97. Gundlach DJ, Royer JE, Park SK, et al. Contact-induced crystallinity for high-performance soluble acene-based transistors and circuits. *Nat Mater*. 2008;7(3):216-221.
98. García G, Timón V, Hernández-Laguna A, Navarro A, Fernández-Gómez M. Influence of the alkyl and alkoxy side chains on the electronic structure and charge-transport properties of polythiophene derivatives. *Phys Chem Chem Phys*. 2011;13(21):10091.
99. Lu CF, Shih CW, Chen CA, Chin A, Su WF. Tuning the Morphology of Isoindigo Donor-Acceptor Polymer Film for High Sensitivity Ammonia Sensor. *Adv Funct Mater*. 2018;28(40):1803145.
100. Ding Y, Jiang L, Du Y, et al. Linear hybrid siloxane-based side chains for highly soluble isoindigo-based conjugated polymers. *Chem Commun*. 2020;56(79):11867-11870.
101. Gu H, Wang K, Wu Z, et al. Stable low-bandgap isoindigo-bisEDOT copolymer with superior electrochromic performance in NIR window. *Electrochimica Acta*. 2021;399:139418.
102. Yang W, Yue HG, Zhao D, et al. Thienylmethylene Oxindole Based Conjugated Polymers via Direct Arylation Polymerization and Their Electrochromic Properties. *Chin J Polym Sci*. 2021;39(2):147-153.
103. Gu H, Ming S, Lin K, et al. Isoindigo as an electron-deficient unit for high-performance polymeric electrochromics. *Electrochimica Acta*. 2018;260:772-782.
104. Randell NM, Kelly TL. Recent Advances in Isoindigo-Inspired Organic Semiconductors. *Chem Rec*. 2019;19(6):973-988.

105. Lei T, Dou JH, Ma ZJ, et al. Ambipolar Polymer Field-Effect Transistors Based on Fluorinated Isoindigo: High Performance and Improved Ambient Stability. *J Am Chem Soc.* 2012;134(49):20025-20028.
106. Ashraf RS, Kronemeijer AJ, James DI, Sirringhaus H, McCulloch I. A new thiophene substituted isoindigo based copolymer for high performance ambipolar transistors. *Chem Commun.* 2012;48(33):3939.
107. Yue W, Ashraf RS, Nielsen CB, et al. A Thieno[3,2-*b*]benzothiophene Isoindigo Building Block for Additive- and Annealing-Free High-Performance Polymer Solar Cells. *Adv Mater.* 2015;27(32):4702-4707.
108. Lei T, Dou JH, Cao XY, Wang JY, Pei J. Electron-Deficient Poly(*p*-phenylene vinylene) Provides Electron Mobility over $1 \text{ cm}^2 \text{ V}^{-1} \text{ s}^{-1}$ under Ambient Conditions. *J Am Chem Soc.* 2013;135(33):12168-12171.
109. Randell NM, Boutin PC, Kelly TL. Bisisoindigo: using a ring-fusion approach to extend the conjugation length of isoindigo. *J Mater Chem A.* 2016;4(18):6940-6945.
110. Lin X, Lu Q, Yang C, et al. Multifunctional donor–acceptor conjugated polymers containing isoindigo and benzothiadiazole moieties for electrochromic, photoelectric sensor, 2,4,6-trinitrophenol detection and resistance memory device. *J Mater Sci.* 2021;56(20):12001-12017.
111. Zhou C, Zhao J, Ye J, et al. Printed thin-film transistors and NO₂ gas sensors based on sorted semiconducting carbon nanotubes by isoindigo-based copolymer. *Carbon.* 2016;108:372-380.
112. Chan EWC, Baek P, De la Rosa VR, Barker D, Hoogenboom R, Travas-Sejdic J. Thermoresponsive laterally-branched polythiophene phenylene derivative as water-soluble temperature sensor. *Polym Chem.* 2017;8(30):4352-4358.
113. Randell NM, Douglas AF, Kelly TL. 7-Azaisoindigo as a new electron deficient component of small molecule chromophores for organic solar cells. *J Mater Chem A.* 2014;2(4):1085-1092.
114. Xu L, Zhao Z, Xiao M, et al. π -Extended Isoindigo-Based Derivative: A Promising Electron-Deficient Building Block for Polymer Semiconductors. *ACS Appl Mater Interfaces.* 2017;9(46):40549-40555.
115. Deng P, Zhang Q. Recent developments on isoindigo-based conjugated polymers. *Polym Chem.* 2014;5(10):3298-3305.
116. Rissler J. Effective conjugation length of π -conjugated systems. *Chem Phys Lett.* 2004;395(1-3):92-96.
117. Mike JF, Lutkenhaus JL. Recent advances in conjugated polymer energy storage. *J Polym Sci Part B Polym Phys.* 2013;51(7):468-480.

118. Cui C, Wong WY. Effects of Alkylthio and Alkoxy Side Chains in Polymer Donor Materials for Organic Solar Cells. *Macromol Rapid Commun.* 2016;37(4):287-302.
119. Hu X, Xu L. Structure and properties of 3-alkoxy substituted polythiophene synthesized at low temperature. *Polymer.* 2000;41(26):9147-9154.
120. Shi C, Yao Y, Yang, Pei Q. Regioregular Copolymers of 3-Alkoxythiophene and Their Photovoltaic Application. *J Am Chem Soc.* 2006;128(27):8980-8986.
121. Inganäs O, Svensson M, Zhang F, et al. Low bandgap alternating polyfluorene copolymers in plastic photodiodes and solar cells. *Appl Phys A.* 2004;79(1):31-35.
122. Hou Q, Xu Y, Yang W, Yuan M, Peng J, Cao Y. Novel red-emitting fluorene-based copolymers. *J Mater Chem.* 2002;12(10):2887-2892.
123. Gao J, Niles ET, Grey JK. Aggregates Promote Efficient Charge Transfer Doping of Poly(3-hexylthiophene). *J Phys Chem Lett.* 2013;4(17):2953-2957.
124. Chance RR, Brédas JL, Silbey R. Bipolaron transport in doped conjugated polymers. *Phys Rev B.* 1984;29(8):4491-4495.
125. Dexter Tam TL, Ng CK, Lim SL, et al. Proquinoidal-Conjugated Polymer as an Effective Strategy for the Enhancement of Electrical Conductivity and Thermoelectric Properties. *Chem Mater.* 2019;31(20):8543-8550.
126. Mun J, Kang J, Zheng Y, et al. F4-TCNQ as an Additive to Impart Stretchable Semiconductors with High Mobility and Stability. *Adv Electron Mater.* 2020;6(6):2000251.
127. Hamidi-Sakr A, Biniek L, Bantignies JL, et al. A Versatile Method to Fabricate Highly In-Plane Aligned Conducting Polymer Films with Anisotropic Charge Transport and Thermoelectric Properties: The Key Role of Alkyl Side Chain Layers on the Doping Mechanism. *Adv Funct Mater.* 2017;27(25):1700173.
128. Méndez H, Heimel G, Winkler S, et al. Charge-transfer crystallites as molecular electrical dopants. *Nat Commun.* 2015;6(1):8560.
129. Onyia AI, Ikeri HI, Nwobodo AN. Theoretical Study of Quantum Confinement on Quantum Dots using Particle in a Box Model. *J. Ovonic Res.* 2018;14(1):49-54
130. Barford W, Paiboonvorachat N. Excitons in conjugated polymers: Wavefunctions, symmetries, and quantum numbers. *J Chem Phys.* 2008;129(16):164716.
131. Pedersen TG. Particle-in-a-box model of exciton absorption and electroabsorption in conjugated polymers. *Phys Rev B.* 2000;62(23):15424-15426.
132. Pedersen TG, Johansen PM, Pedersen HC. Particle-in-a-box model of one-dimensional excitons in conjugated polymers. *Phys Rev B.* 2000;61(15):10504-10510.

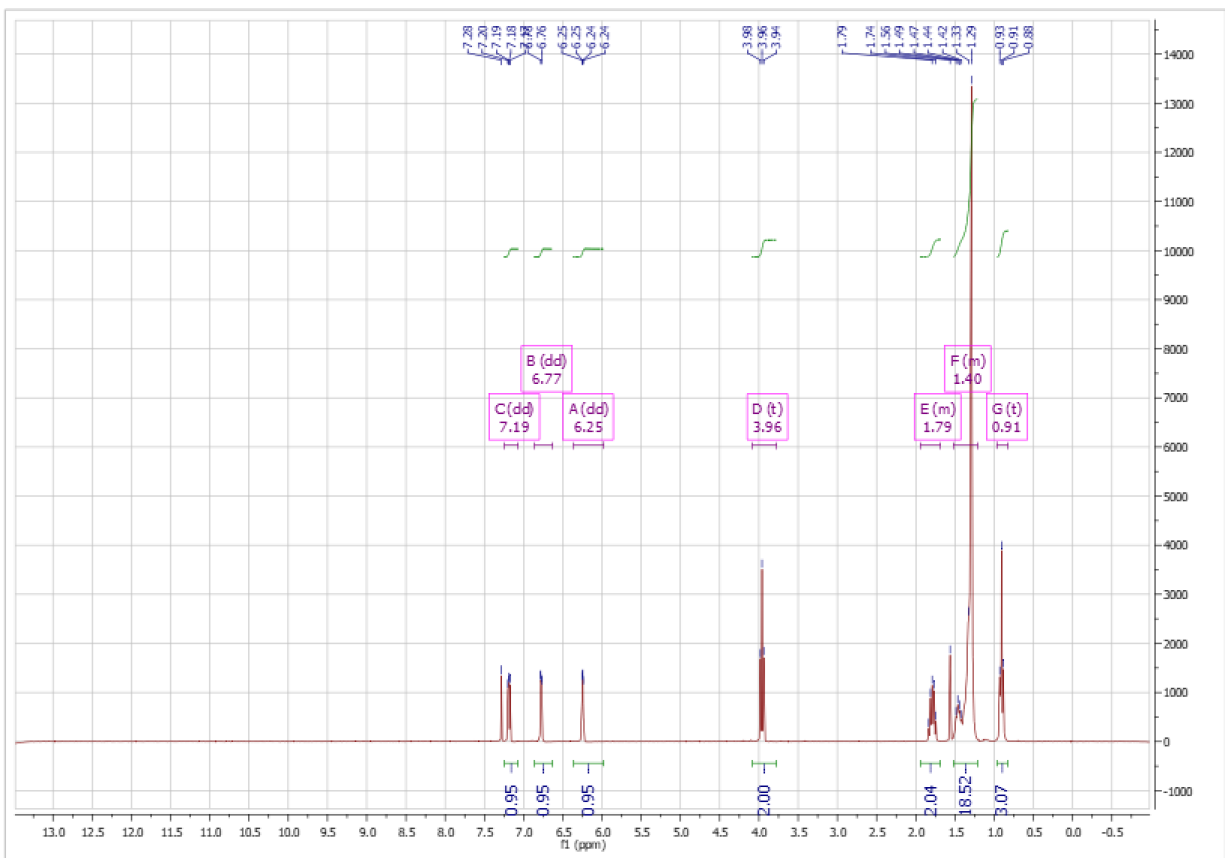
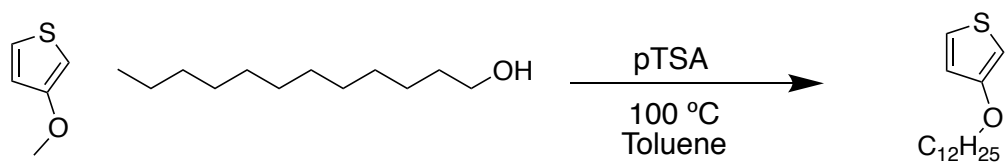
133. Liang Z, Zhang Y, Souril M, et al. Influence of dopant size and electron affinity on the electrical conductivity and thermoelectric properties of a series of conjugated polymers. *J Mater Chem A*. 2018;6(34):16495-16505.
134. Kellenberger A, Dmitrieva E, Dunsch L. Structure Dependence of Charged States in “Linear” Polyaniline as Studied by In Situ ATR-FTIR Spectroelectrochemistry. *J Phys Chem B*. 2012;116(14):4377-4385.
135. Liu C, Wang K, Hu X, et al. Molecular Weight Effect on the Efficiency of Polymer Solar Cells. *ACS Appl Mater Interfaces*. 2013;5(22):12163-12167.
136. Intemann JJ, Yao K, Yip HL, et al. Molecular Weight Effect on the Absorption, Charge Carrier Mobility, and Photovoltaic Performance of an Indacenodiselenophene-Based Ladder-Type Polymer. *Chem Mater*. 2013;25(15):3188-3195.
137. Wang W, Chen L, Wang G, Zhang ZG, Li Y, Shen P. Synthesis and Optoelectronic Properties of Benzo[1,2-*b*:4,5-*b'*]dithiophene-Based Copolymers with Conjugated 2-(2-Ethylhexyl)-3,4-dimethoxythiophene Side Chains. *Macromol Chem Phys*. 2016;217(14):1586-1599.
138. Feng K, Yang G, Xu X, et al. High-Performance Wide Bandgap Copolymers Using an EDOT Modified Benzodithiophene Donor Block with 10.11% Efficiency. *Adv Energy Mater*. 2018;8(6):1602773.
139. Liu X, He B, Garzón-Ruiz A, et al. Unraveling the Main Chain and Side Chain Effects on Thin Film Morphology and Charge Transport in Quinoidal Conjugated Polymers. *Adv Funct Mater*. 2018;28(31):1801874.
140. Cao Z, Galuska L, Qian Z, et al. The effect of side-chain branch position on the thermal properties of poly(3-alkylthiophenes). *Polym Chem*. 2020;11(2):517-526.
141. Chen X, Hou G, Chen Y, Yang K, Dong Y, Zhou H. Effect of molecular weight on crystallization, melting behavior and morphology of poly(trimethylene terephthalate). *Polym Test*. 2007;26(2):144-153.
142. Bräuer B, Kukreja R, Virkar A, et al. Carrier mobility in pentacene as a function of grain size and orientation derived from scanning transmission X-ray microscopy. *Org Electron*. 2011;12(11):1936-1942.
143. Yang H, Zhang R, Wang L, et al. Face-On and Edge-On Orientation Transition and Self-Epitaxial Crystallization of All-Conjugated Diblock Copolymer. *Macromolecules*. 2015;48(20):7557-7566.
144. Fang L, Zhou Y, Yao YX, et al. Side-Chain Engineering of Isoindigo-Containing Conjugated Polymers Using Polystyrene for High-Performance Bulk Heterojunction Solar Cells. *Chem Mater*. 2013;25(24):4874-4880.

145. Yan X, Zhao B, Liu J, Zhang X, He G. Tailoring the nanophase-separated morphology of anion exchange membrane by embedding aliphatic chains of different lengths into aromatic main chains. *J Membr Sci.* 2018;564:436-443.
146. Dan L, Elias AL. Flexible and Stretchable Temperature Sensors Fabricated Using Solution-Processable Conductive Polymer Composites. *Adv Healthc Mater.* 2020;9(16):2000380.
147. Nitani M, Nakayama K, Maeda K, Omori M, Uno M. Organic temperature sensors based on conductive polymers patterned by a selective-wetting method. *Org Electron.* 2019;71:164-168.
148. Turkani VS, Maddipatla D, Narakathu BB, Bazuin BJ, Atashbar MZ. A carbon nanotube based NTC thermistor using additive print manufacturing processes. *Sens Actuators Phys.* 2018;279:1-9.
149. Zhuldybina M, Ropagnol X, Bois C, Zednik RJ, Blanchard F. Printing accuracy tracking with 2D optical microscopy and super-resolution metamaterial-assisted 1D terahertz spectroscopy. *Npj Flex Electron.* 2020;4(1):21.
150. Wang YF, Sekine T, Takeda Y, et al. Fully Printed PEDOT:PSS-based Temperature Sensor with High Humidity Stability for Wireless Healthcare Monitoring. *Sci Rep.* 2020;10(1):2467.
151. Zhang F, Wu D, Xu Y, Feng X. Thiophene-based conjugated oligomers for organic solar cells. *J Mater Chem.* 2011;21(44):17590.
152. Ando S, Murakami R, Nishida J ichi, et al. n-Type Organic Field-Effect Transistors with Very High Electron Mobility Based on Thiazole Oligomers with Trifluoromethylphenyl Groups. *J Am Chem Soc.* 2005;127(43):14996-14997.
153. Zhen CG, Chen ZK, Liu QD, et al. Fluorene-Based Oligomers for Highly Efficient and Stable Organic Blue-Light-Emitting Diodes. *Adv Mater.* 2009;21(23):2425-2429.
154. Trul AA, Agina EV, Ponomarenko SA. Gas Sensors Based on Conjugated Oligomers and Polymers as Promising Sensitive Elements for Toxic Gases Monitoring in the Atmosphere. *Polym Sci Ser B.* 2021;63(5):443-458.
155. Wu HC, Lee WY, Lin CJ, Chen WC. Highly air stable branched octithiophene oligomer for organic field effect transistor and pH sensor applications. *Mater Chem Phys.* 2013;138(2-3):542-552.
156. Jung S, Ji T, Varadan VK. Point-of-care temperature and respiration monitoring sensors for smart fabric applications. *Smart Mater Struct.* 2006;15(6):1872-1876.
157. Barbarella G, Zambianchi M, Di Toro R, Colonna M, Antolini L, Bongini A. Functionalization of sexithiophene with electron-donating methylsulphonyl groups. *Adv Mater.* 1996;8(4):327-331.

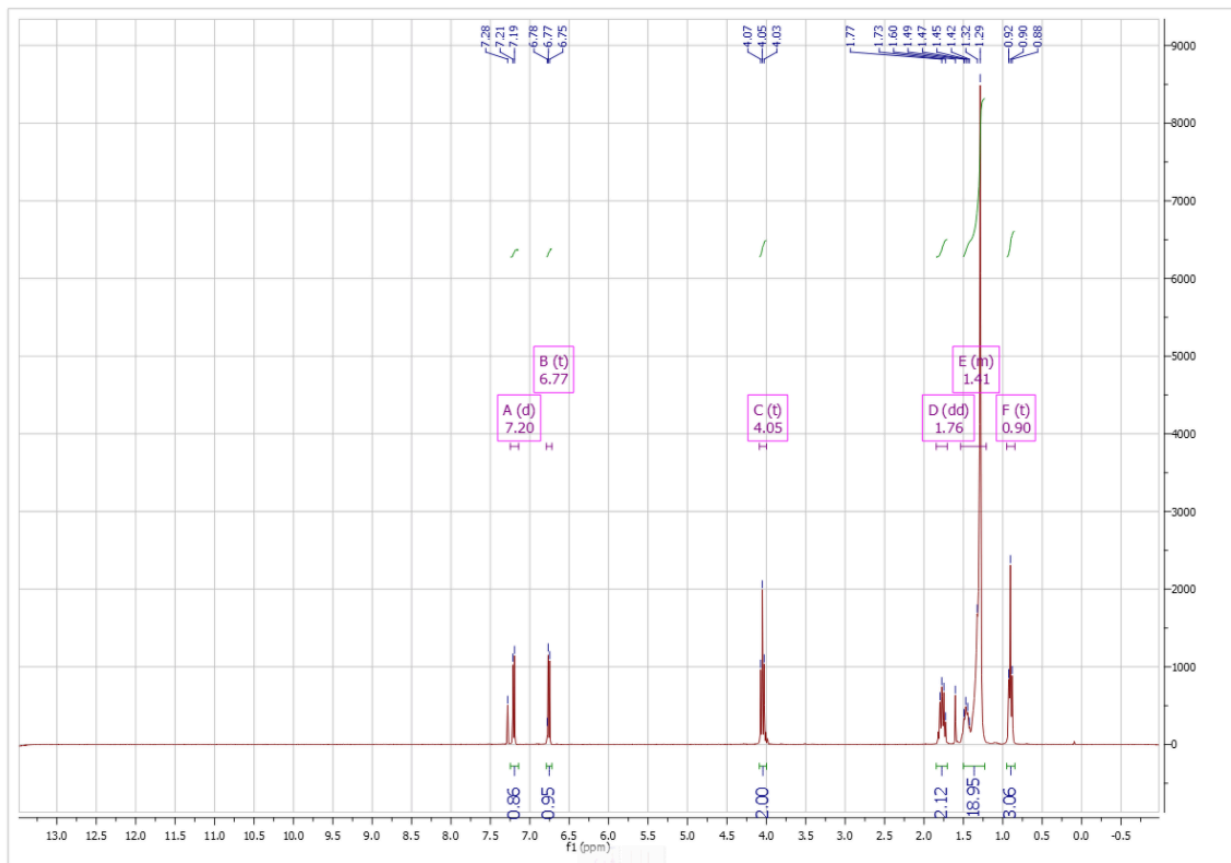
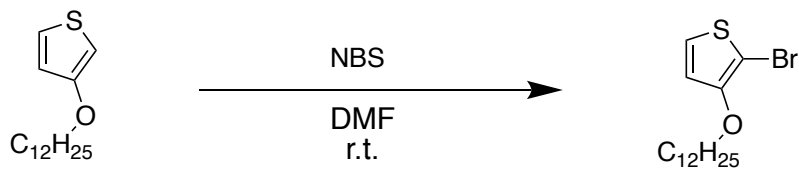
158. Afzali A, Breen TL, Kagan CR. An Efficient Synthesis of Symmetrical Oligothiophenes: Synthesis and Transport Properties of a Soluble Sexithiophene Derivative. *Chem Mater.* 2002;14(4):1742-1746.
159. Moon H, Jahng WS, Curtis MD. Transistor performance of a “push-pull”, π -stacked bithiazole-ethylenedioxythiophene co-oligomer. *J Mater Chem.* 2008;18(40):4856.
160. Grimsdale AC, Müllen K. Oligomers and Polymers Based on Bridged Phenylenes as Electronic Materials. *Macromol Rapid Commun.* 2007;28(17):1676-1702.
161. Sun J, Zhong H, Xu E, et al. An X-shaped solution-processible oligomer having an anthracene unit as a core: A new organic light-emitting material with high thermostability and efficiency. *Org Electron.* 2010;11(1):74-80.
162. Ponder JF, Österholm AM, Reynolds JR. Conjugated Polyelectrolytes as Water Processable Precursors to Aqueous Compatible Redox Active Polymers for Diverse Applications: Electrochromism, Charge Storage, and Biocompatible Organic Electronics. *Chem Mater.* 2017;29(10):4385-4392.
163. Algi F, Cihaner A. An ambipolar low band gap material based on BODIPY and EDOT. *Org Electron.* 2009;10(3):453-458.
164. Cansu Ergun EG, Eroglu D. An electrochemically and optically stable electrochromic polymer film based on EDOT and 1,2,3,4-tetrahydrophenazine. *Org Electron.* 2019;75:105398.
165. Krakowiak KE, Bradshaw JS. Thermal Removal of Boc-Protecting Groups During Preparation of Open-Chain Polyamines. *Synth Commun.* 1996;26(21):3999-4004.
166. Zambounis JS, Hao Z, Iqbal A. Latent pigments activated by heat. *Nature.* 1997;388(6638):131-132.
167. Ji J, Zhou D, Tang Y, et al. Partially removing long branched alkyl side chains of regioregular conjugated backbone based diketopyrrolopyrrole polymer for improving field-effect mobility. *J Mater Chem C.* 2018;6(48):13325-13330.
168. Ngai JHL, Gao X, Kumar P, Polena J, Li Y. A Highly Stable Diketopyrrolopyrrole (DPP) Polymer for Chemiresistive Sensors. *Adv Electron Mater.* 2021;7(3):2000935.
169. Tamayo AB, Walker B, Nguyen* TQ. A Low Band Gap, Solution Processable Oligothiophene with a Diketopyrrolopyrrole Core for Use in Organic Solar Cells. *J Phys Chem C.* 2008;112(30):11545-11551.
170. Más-Montoya M, Janssen RAJ. The Effect of H- and J-Aggregation on the Photophysical and Photovoltaic Properties of Small Thiophene-Pyridine-DPP Molecules for Bulk-Heterojunction Solar Cells. *Adv Funct Mater.* 2017;27(16):1605779.

171. Harvey BG, Quintana RL. Synthesis of renewable jet and diesel fuels from 2-ethyl-1-hexene. *Energy Environ Sci.* 2010;3(3):352.

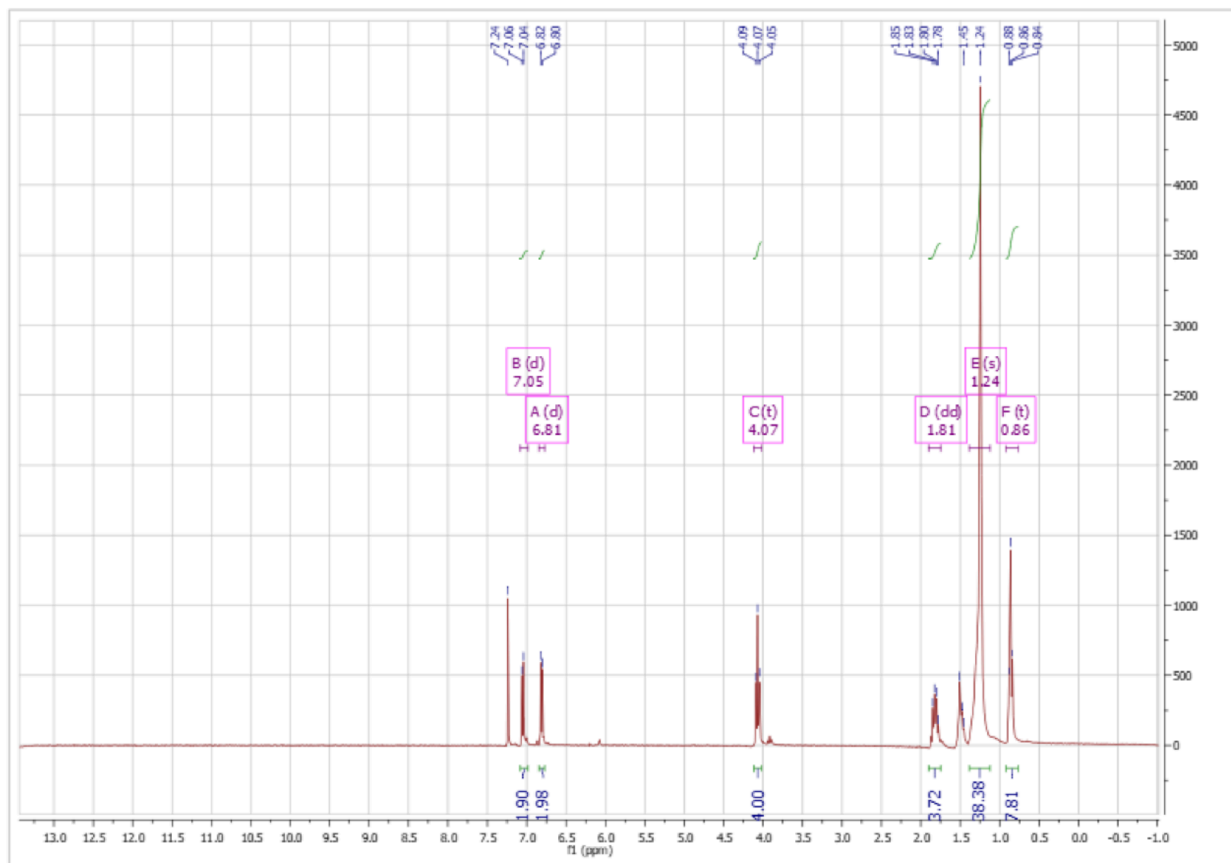
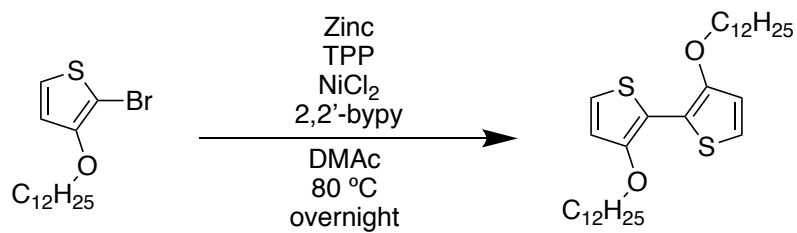
Appendix A



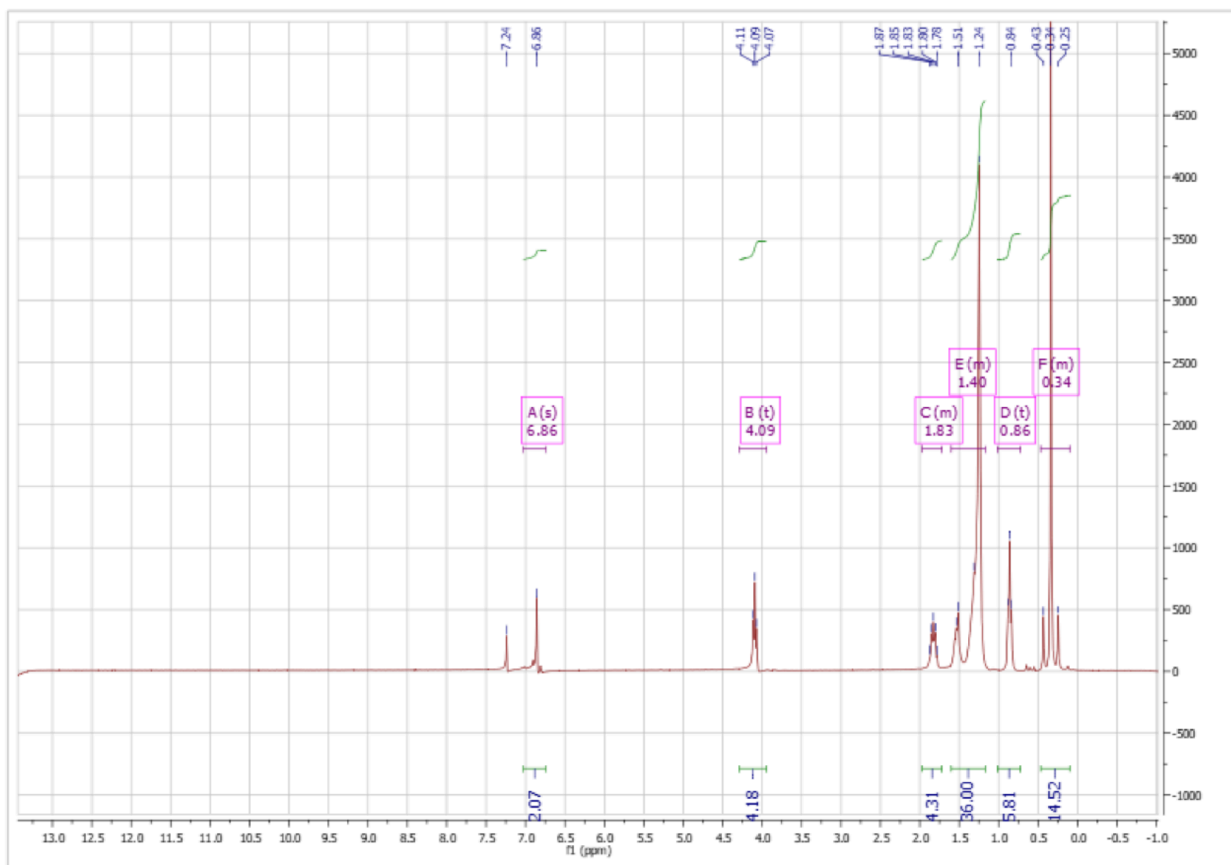
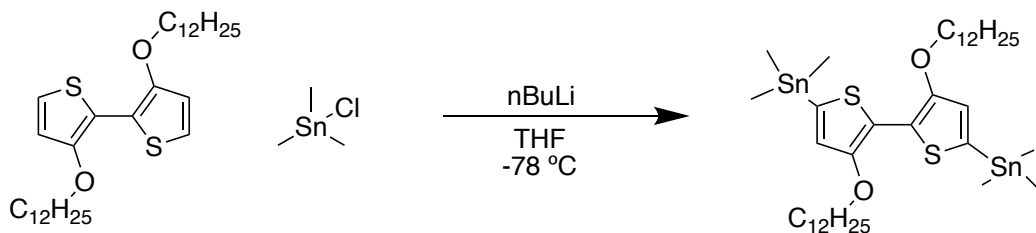
Appendix A-1: 300 MHz ¹H NMR Spectrum for the **3-(dodecyloxy)thiophene (3DDT)** in chloroform-d



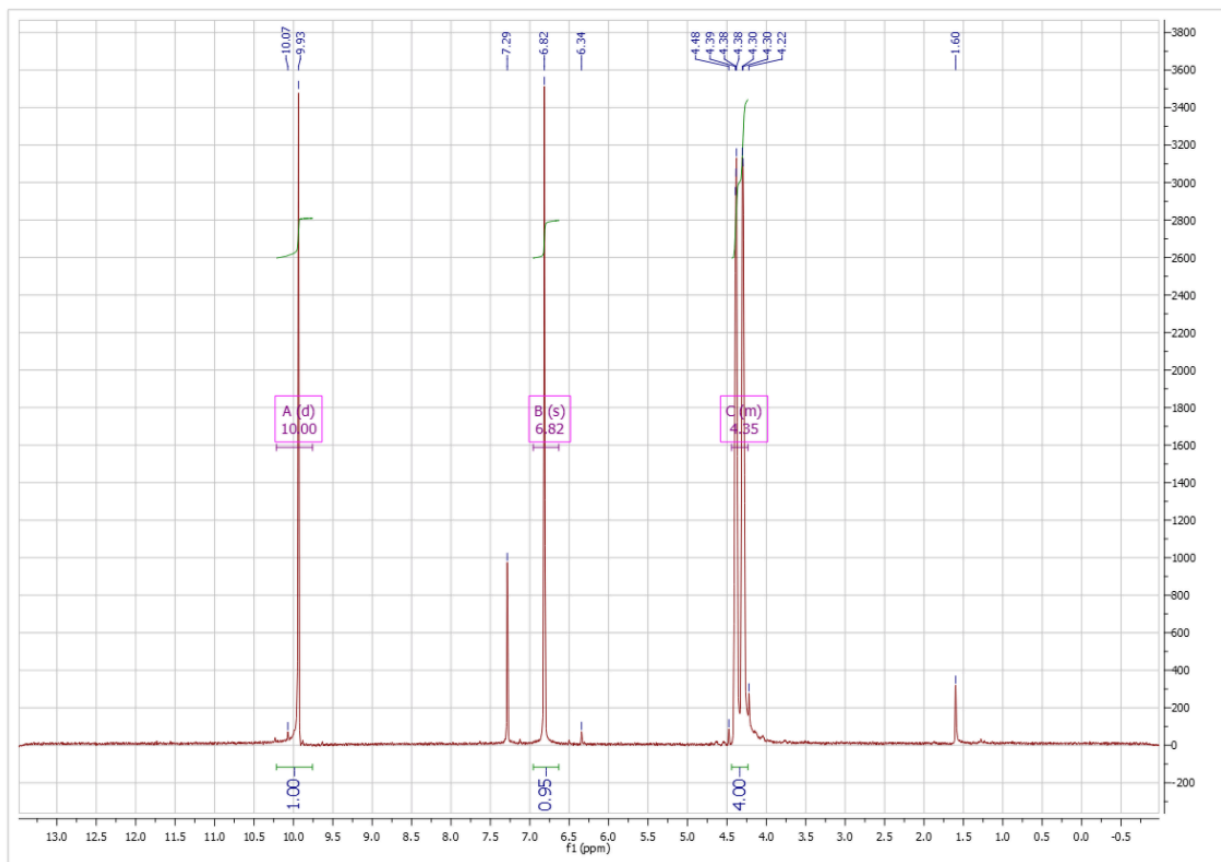
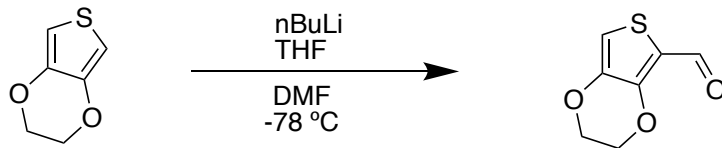
Appendix A-2: 300 MHz ¹H NMR Spectrum for the 2-bromo-3-(dodecyloxy)thiophene (3DDT-Br) in chloroform-d



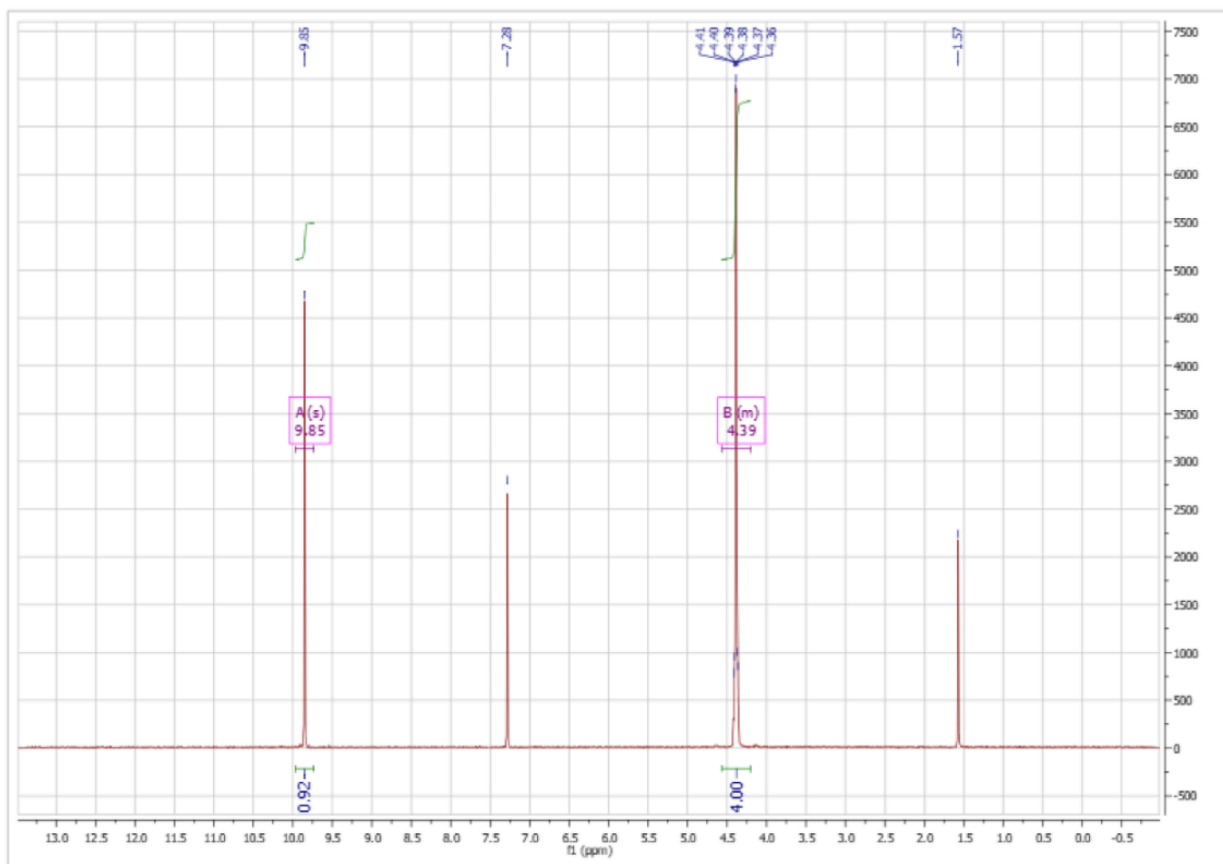
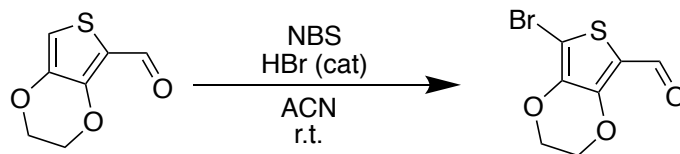
Appendix A-3: 300 MHz ¹H NMR Spectrum for the 3,3'-Bis(dodecyloxy)-2,2'-bithiophene (DDOBT) in chloroform-d



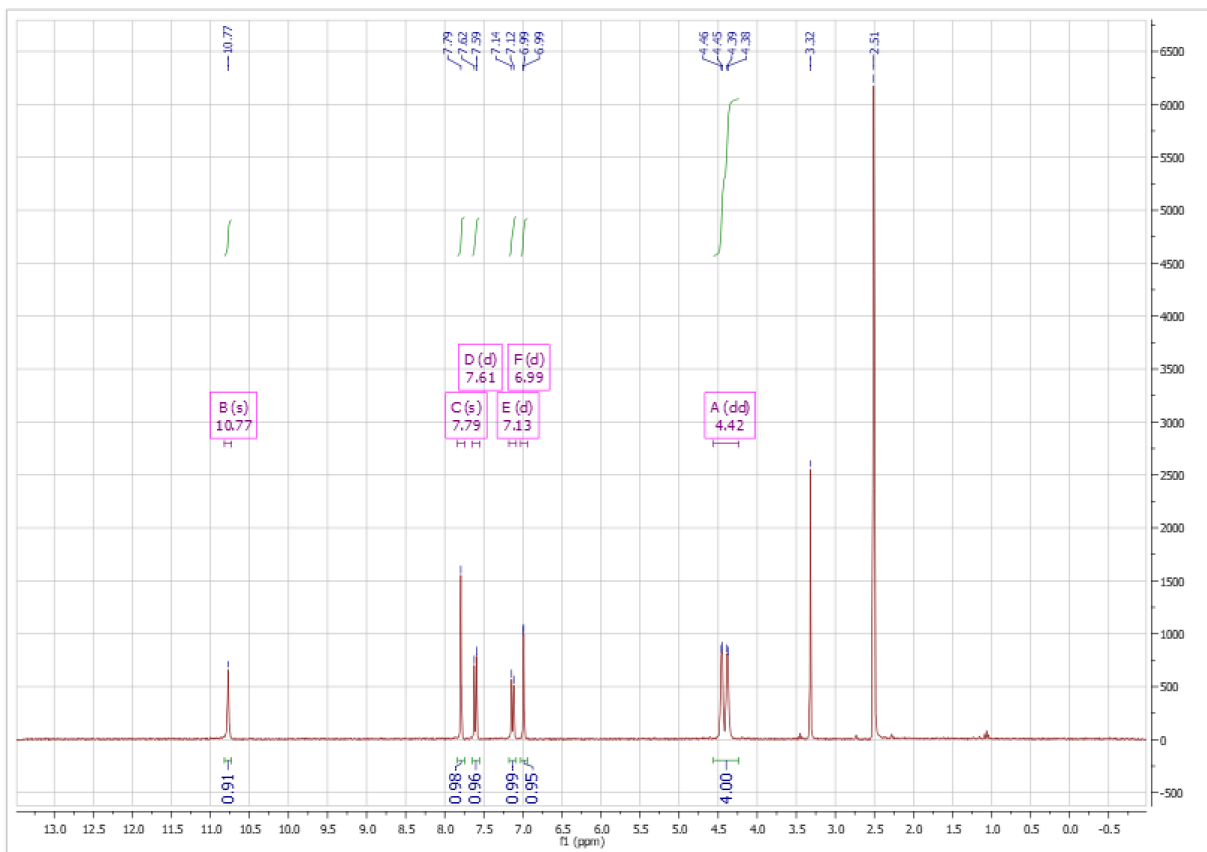
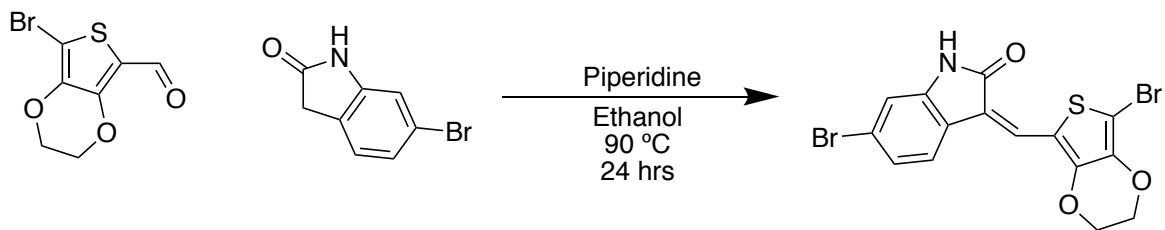
Appendix A-4: 300 MHz ^1H NMR Spectrum for the (3,4'-bis(dodecyloxy)-[2,2'-bithiophene]-5,5'-diyl)bis(trimethylstannane) (DDOBT-TMT) in chloroform-d



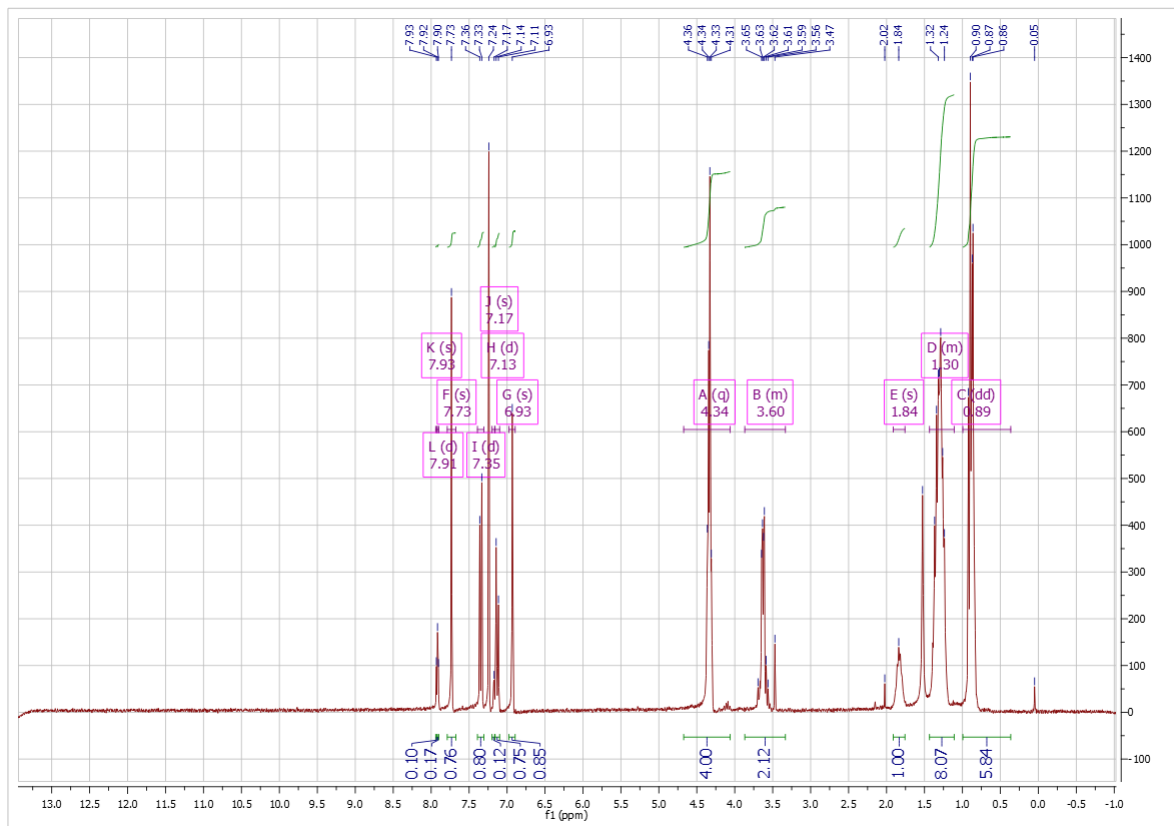
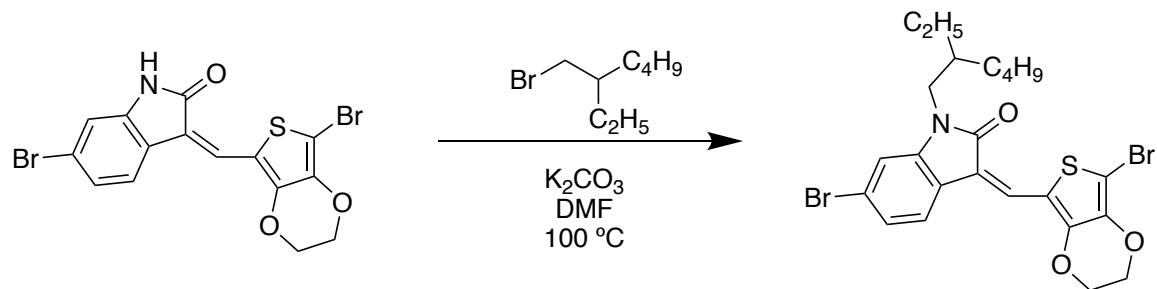
Appendix A-5: 300 MHz ^1H NMR Spectrum for the 2,3-dihydrothieno[3,4-b][1,4]dioxine-5-carbaldehyde (EDOT-CHO) in chloroform- d



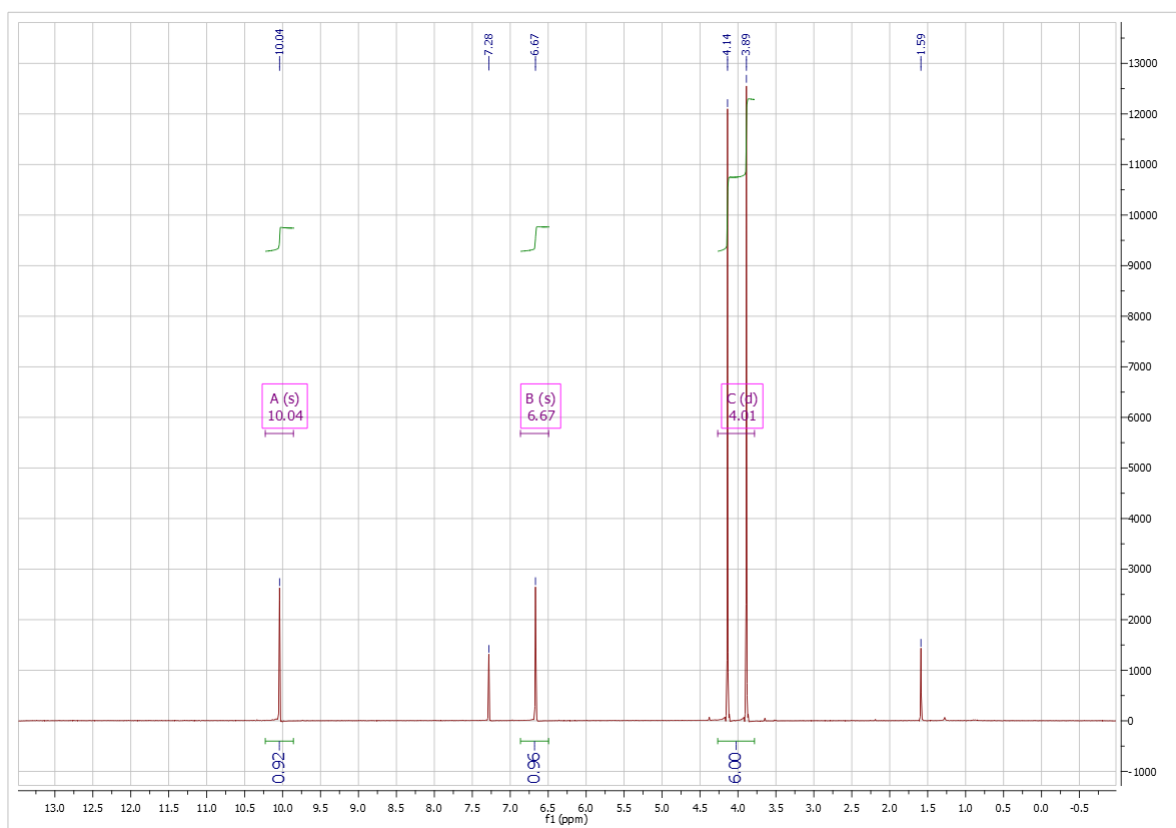
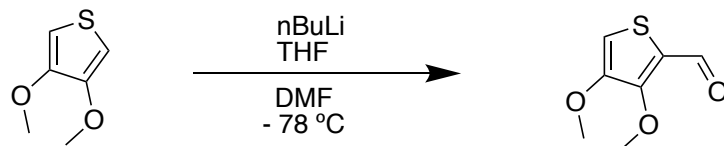
Appendix A-6: 300 MHz ^1H NMR Spectrum for the 7-bromo-2,3-dihydrothieno[3,4-b][1,4]dioxine-5-carbaldehyde (EDOT-CHO-Br) in chloroform-d



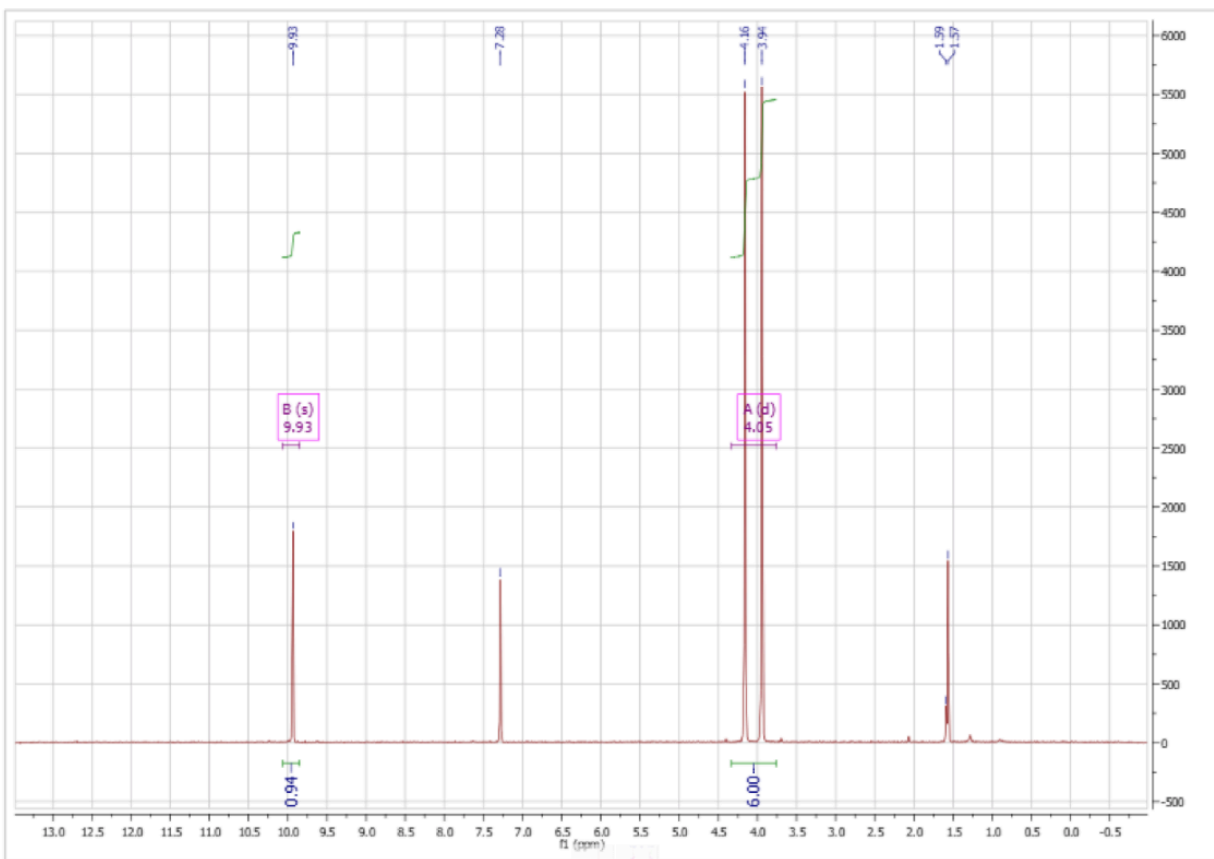
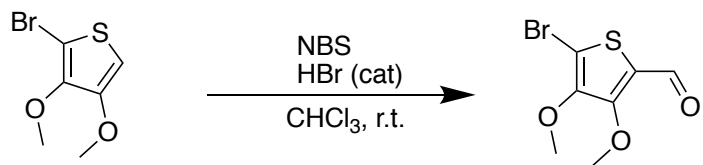
Appendix A-7: 300 MHz ^1H NMR Spectrum of (Z)-6-bromo-3-((7-bromo-2,3-dihydrothieno[3,4-*b*][1,4]dioxin-5-yl)methylene)indolin-2-one (EEI-dBr) in dimethyl sulfoxide- d_6



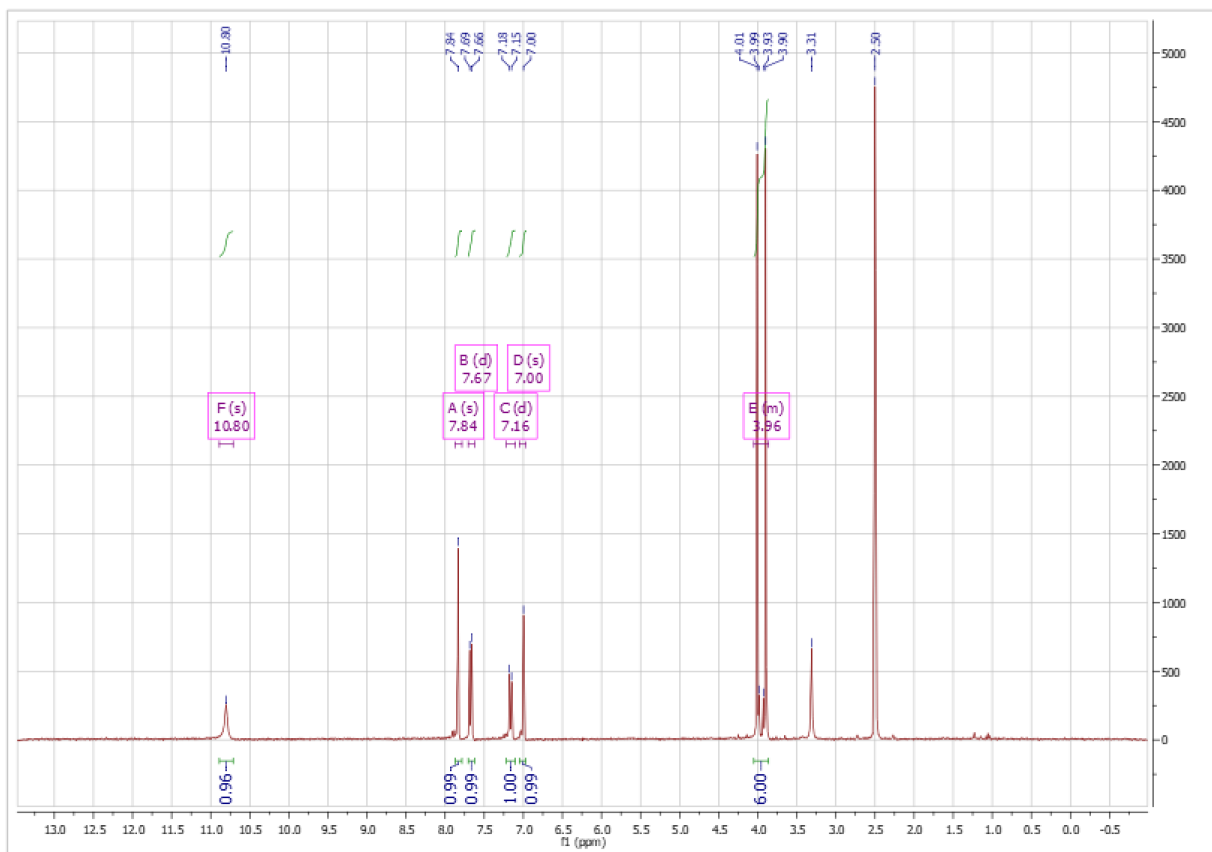
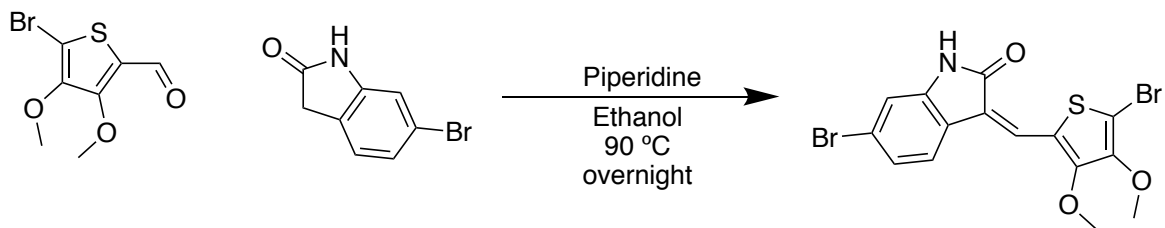
Appendix A-8: 300 MHz ¹H NMR Spectrum of 6-bromo-3-((7-bromo-2,3-dihydrothieno[3,4-b][1,4]dioxin-5-yl)methylene)-1-(2-ethylhexyl)indolin-2-one (M1) in chloroform-*d*



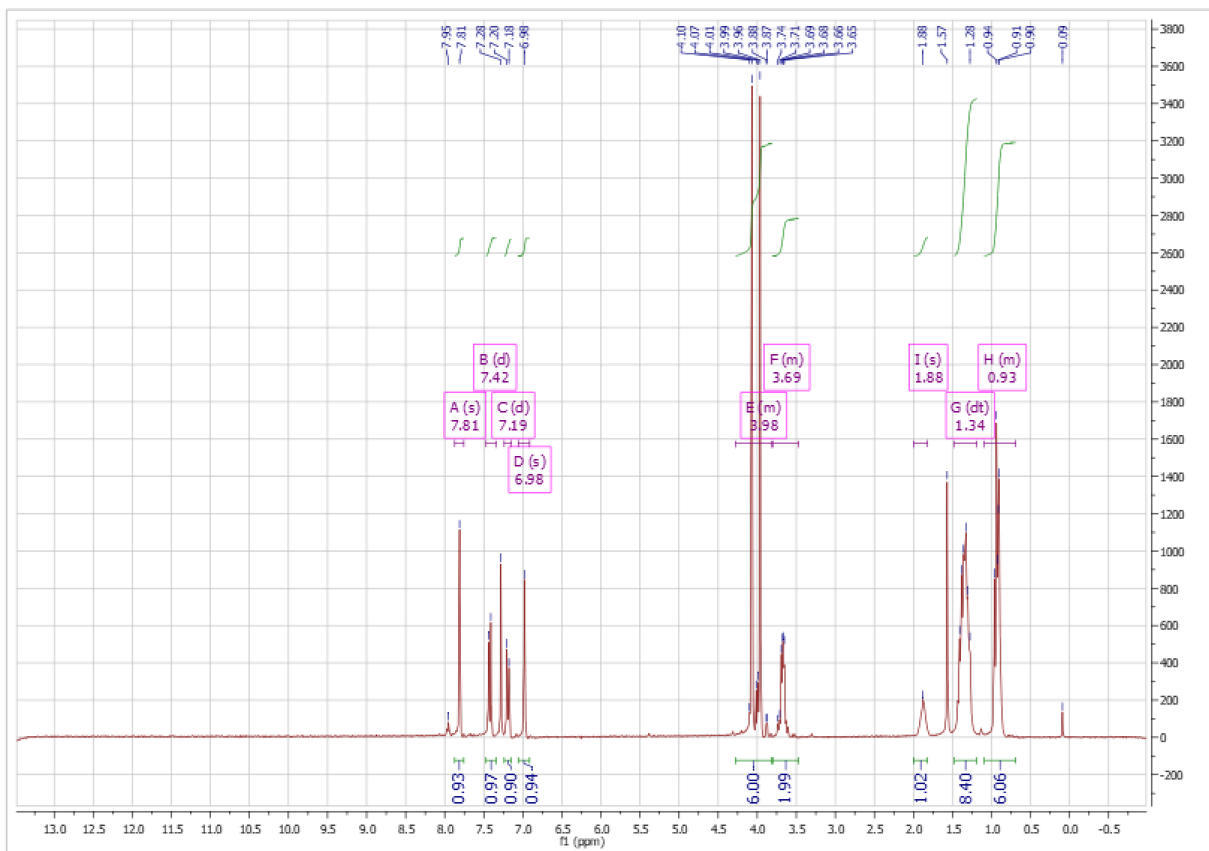
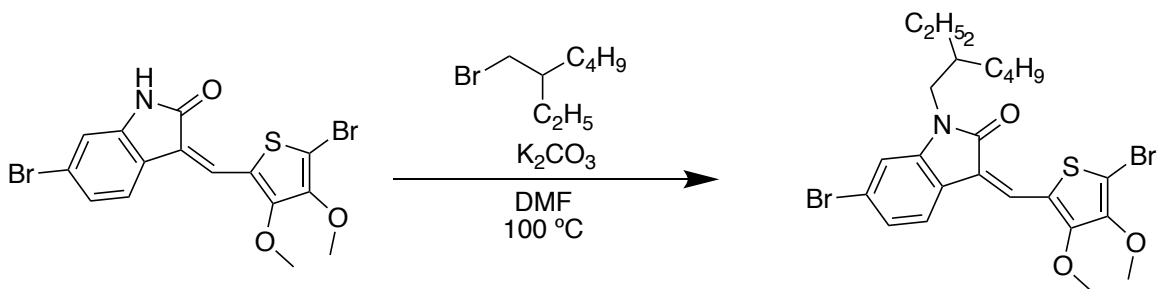
Appendix A-9: 300 MHz ^1H NMR Spectrum of 3,4-dimethoxythiophene-2-carbaldehyde (3,4-DMT-CHO) in chloroform-*d*



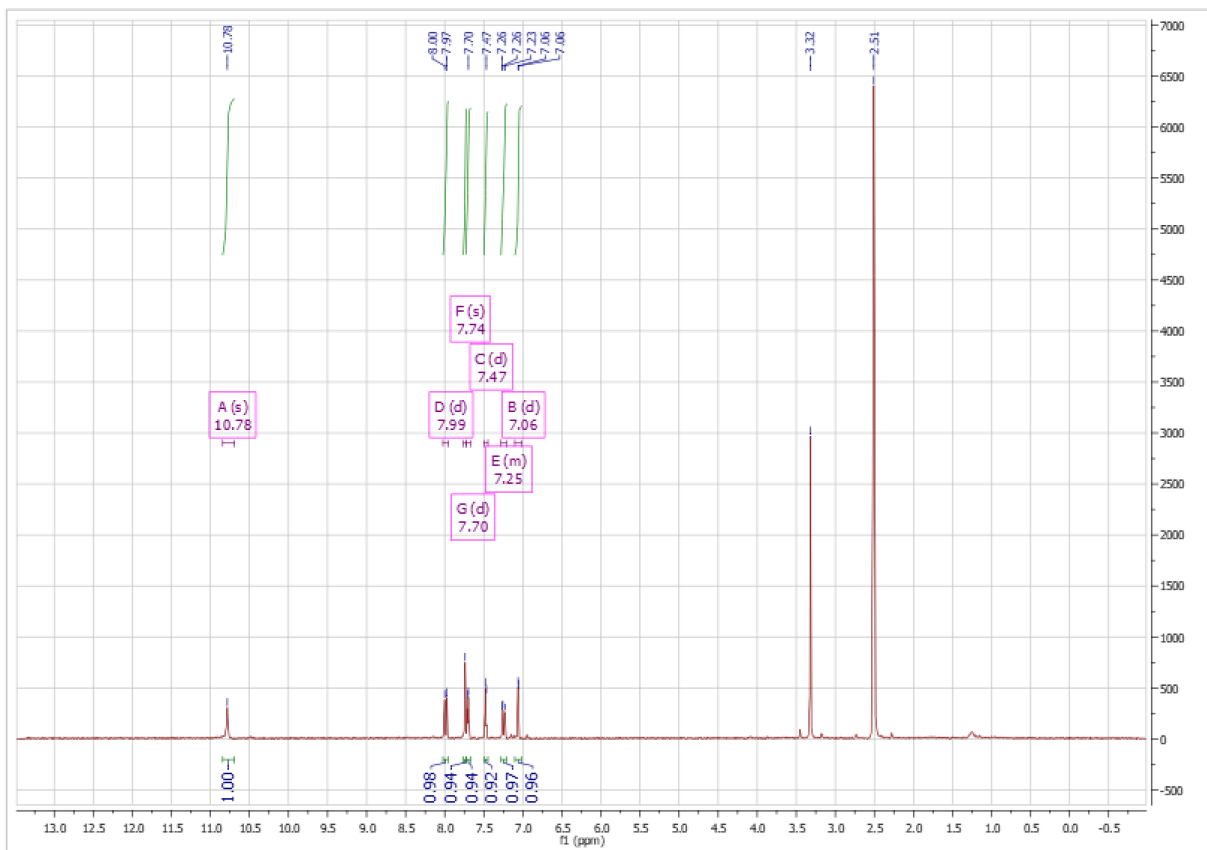
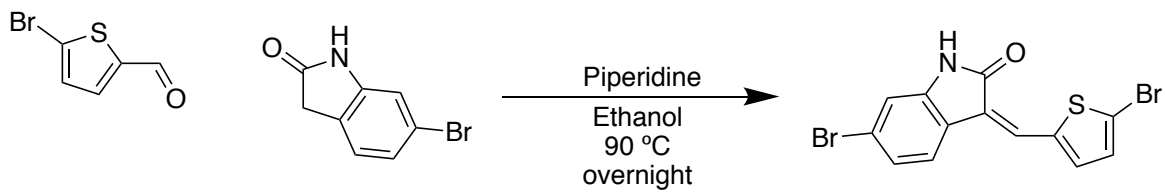
Appendix A-10: 300 MHz ^1H NMR Spectrum of 5-bromo-3,4-dimethoxythiophene-2-carbaldehyde (3,4-DMT-CHO-Br) in chloroform-*d*



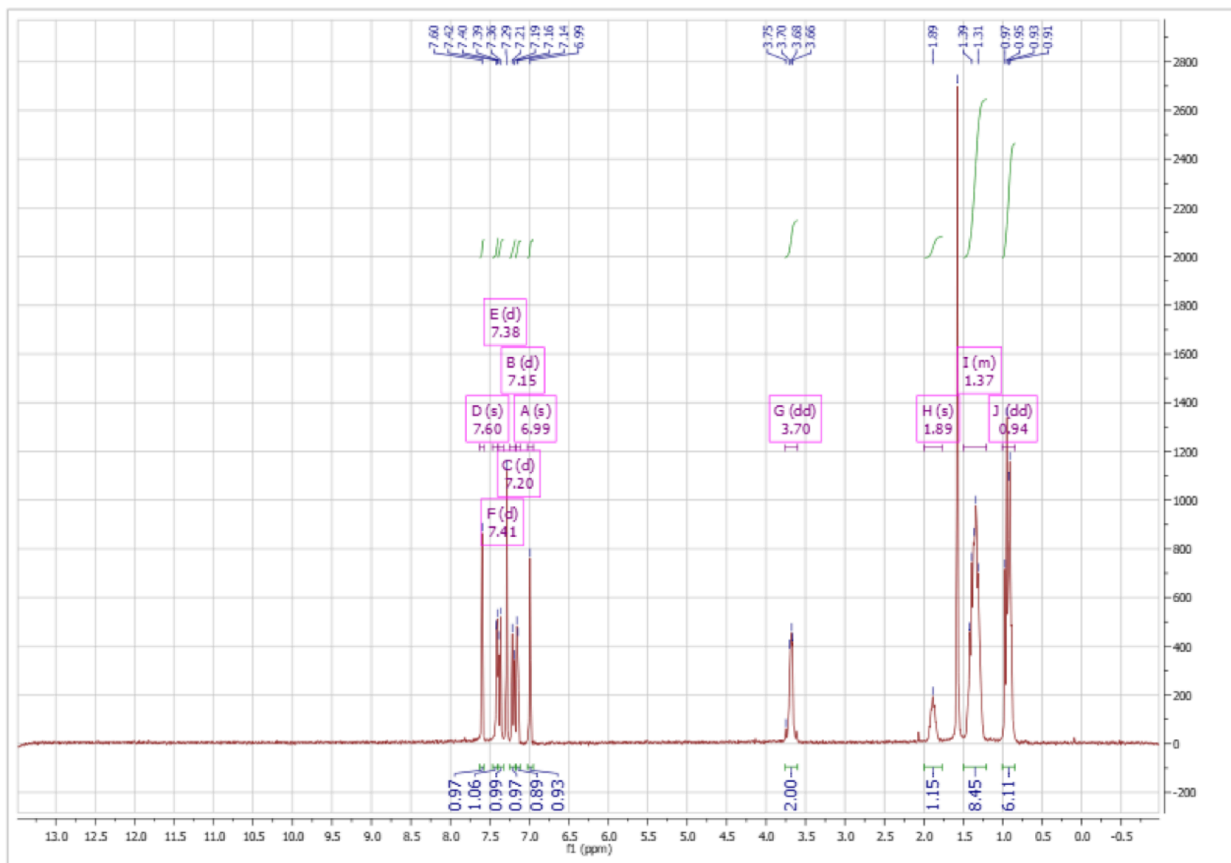
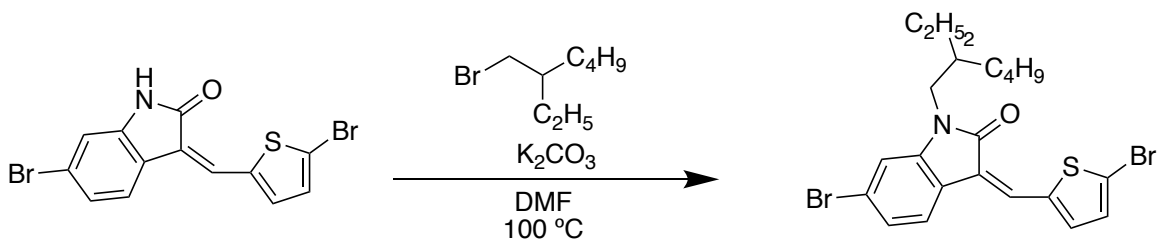
Appendix A-11: 300 MHz ^1H NMR Spectrum of (Z)-6-bromo-3-((5-bromo-3,4-dimethoxythiophen-2-yl)methylene)indolin-2-one (MEI-dBr) in dimethyl sulfoxide- d_6



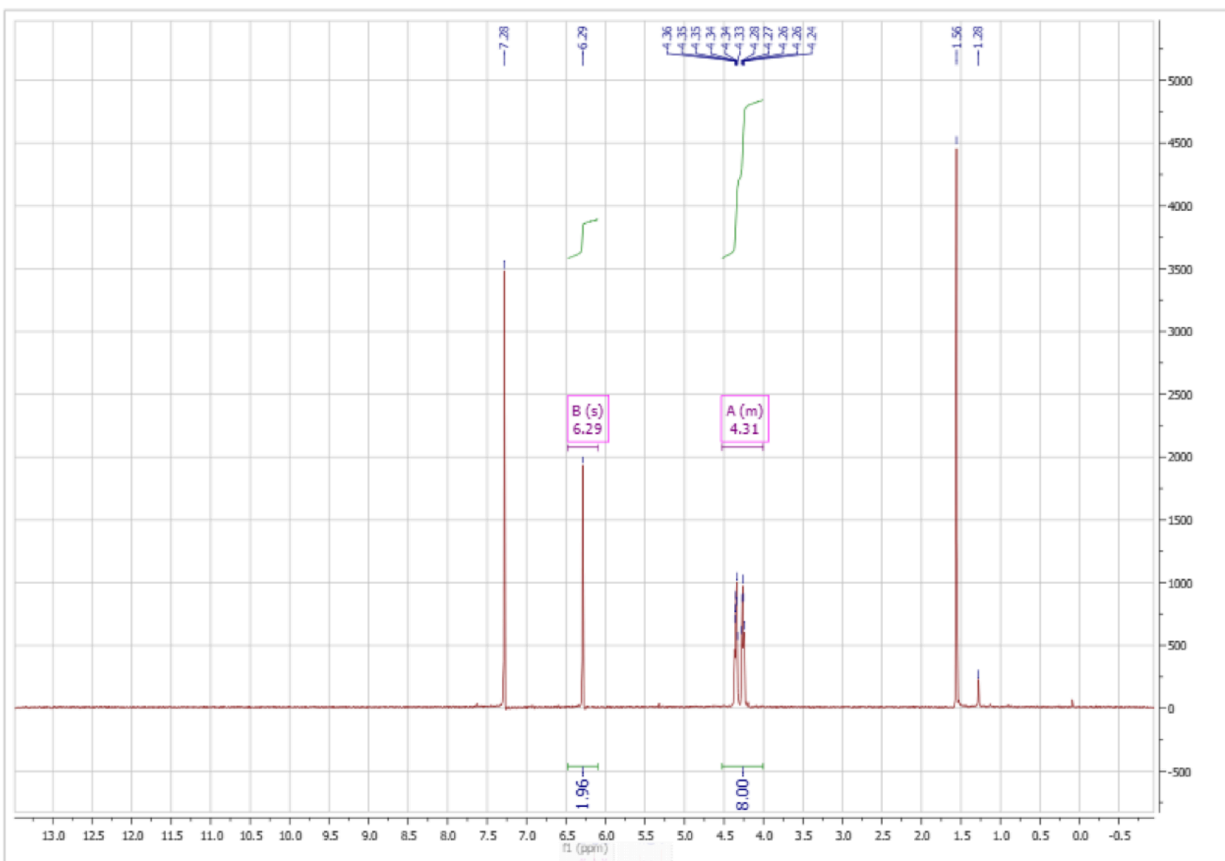
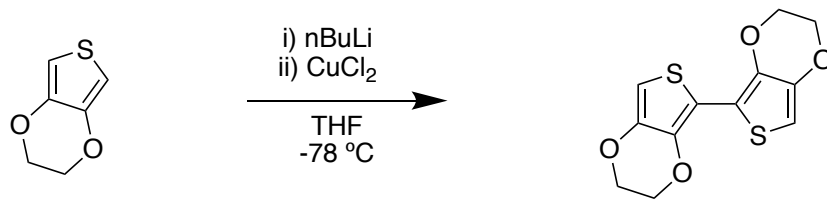
Appendix A-12: 300 MHz ^1H NMR Spectrum of 6-bromo-3-((5-bromo-3,4-dimethoxythiophen-2-yl)methylene)-1-(2-ethylhexyl)indolin-2-one (M2) in chloroform-*d*



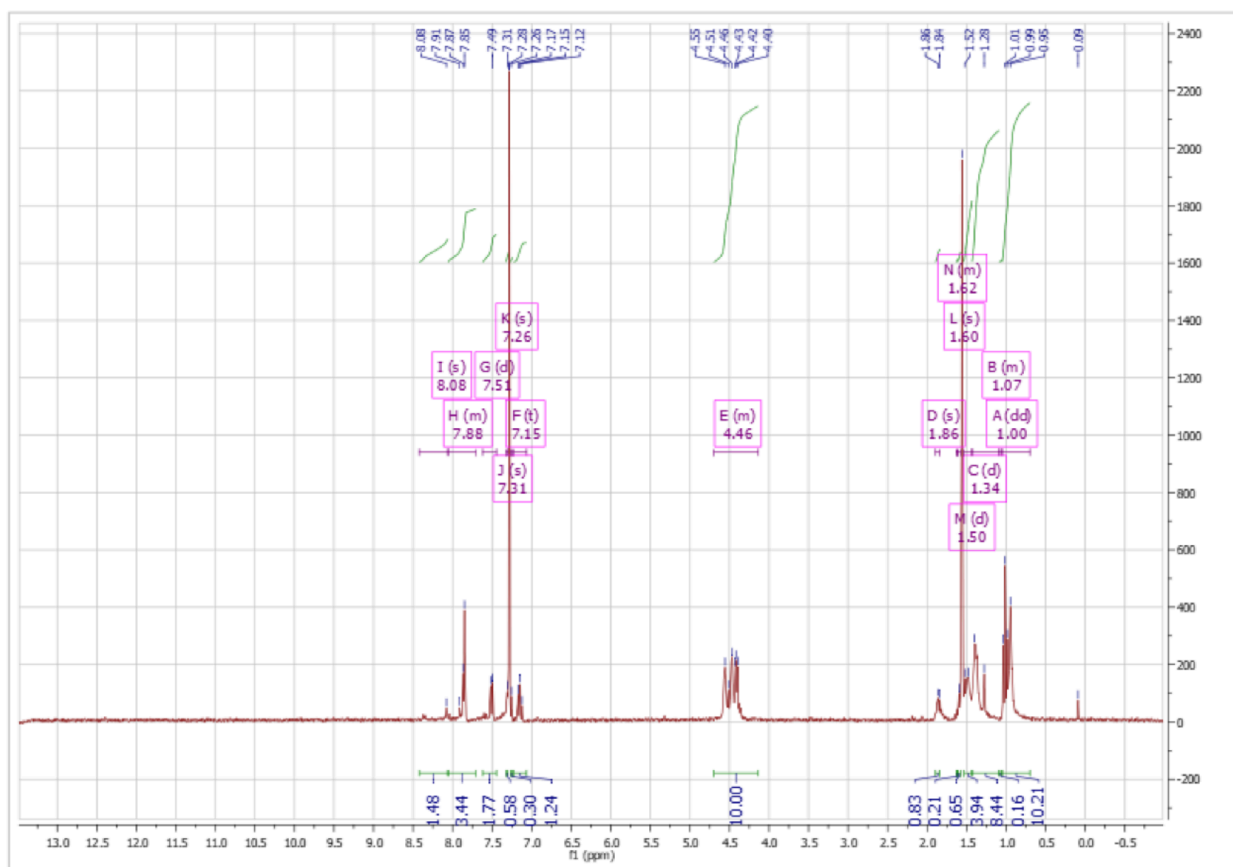
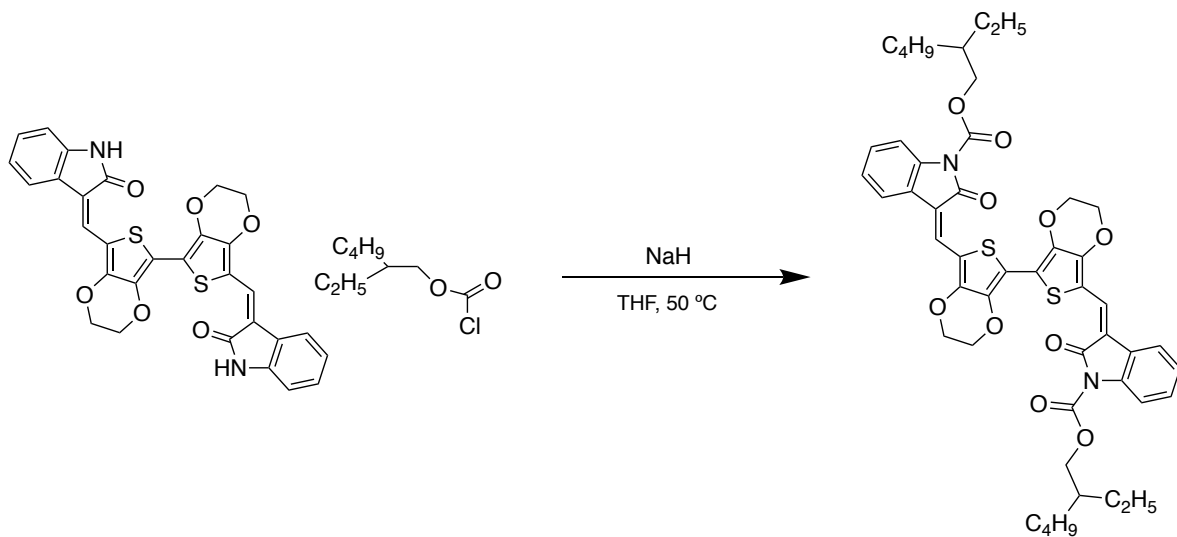
Appendix A-13: 300 MHz ¹H NMR Spectrum of (Z)-6-bromo-3-((5-bromothiophen-2-yl)methylene)indolin-2-one (TEI-dBr) in dimethyl sulfoxide-*d*₆



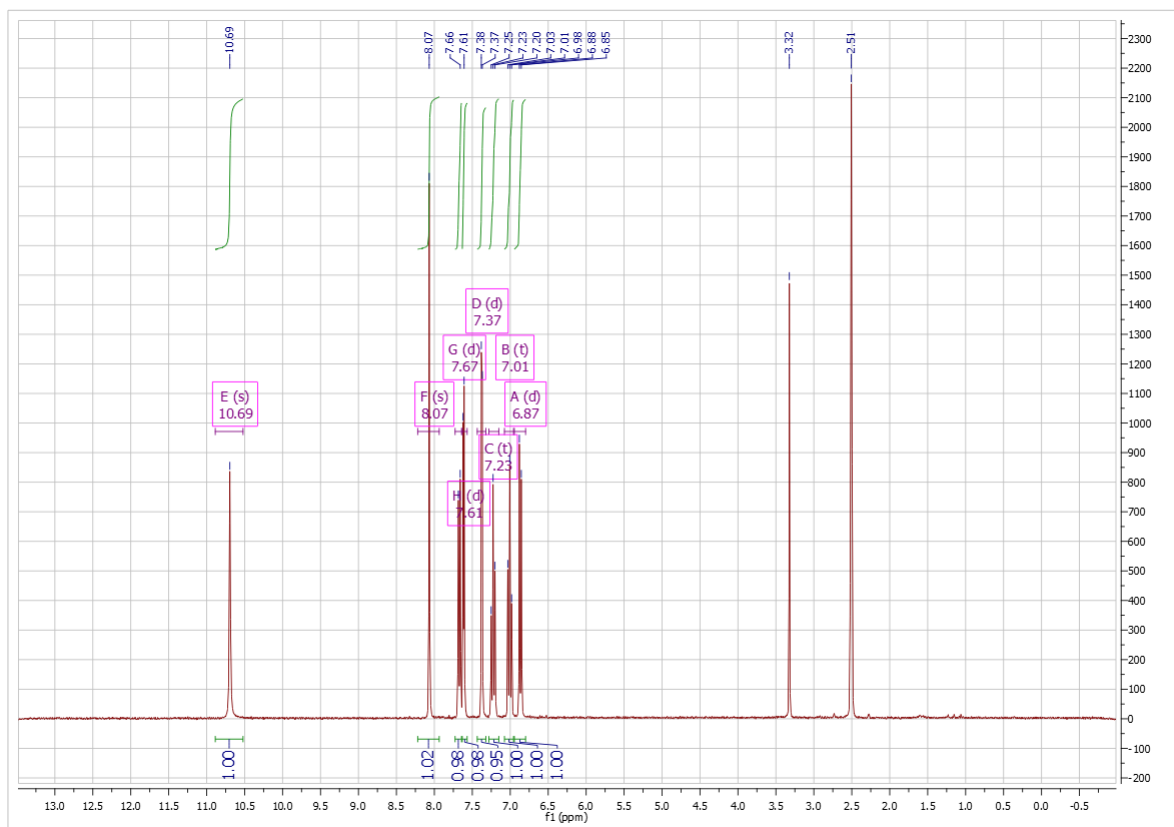
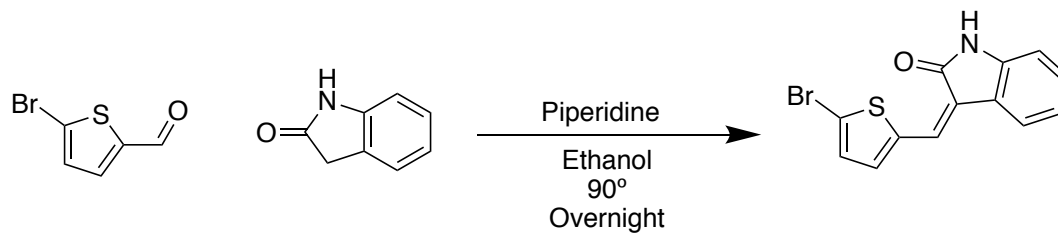
Appendix A-14: 300 MHz ^1H NMR Spectrum of (Z)-6-bromo-3-((5-bromothiophen-2-yl)methylene)-1-(2-ethylhexyl)indolin-2-one (M3)



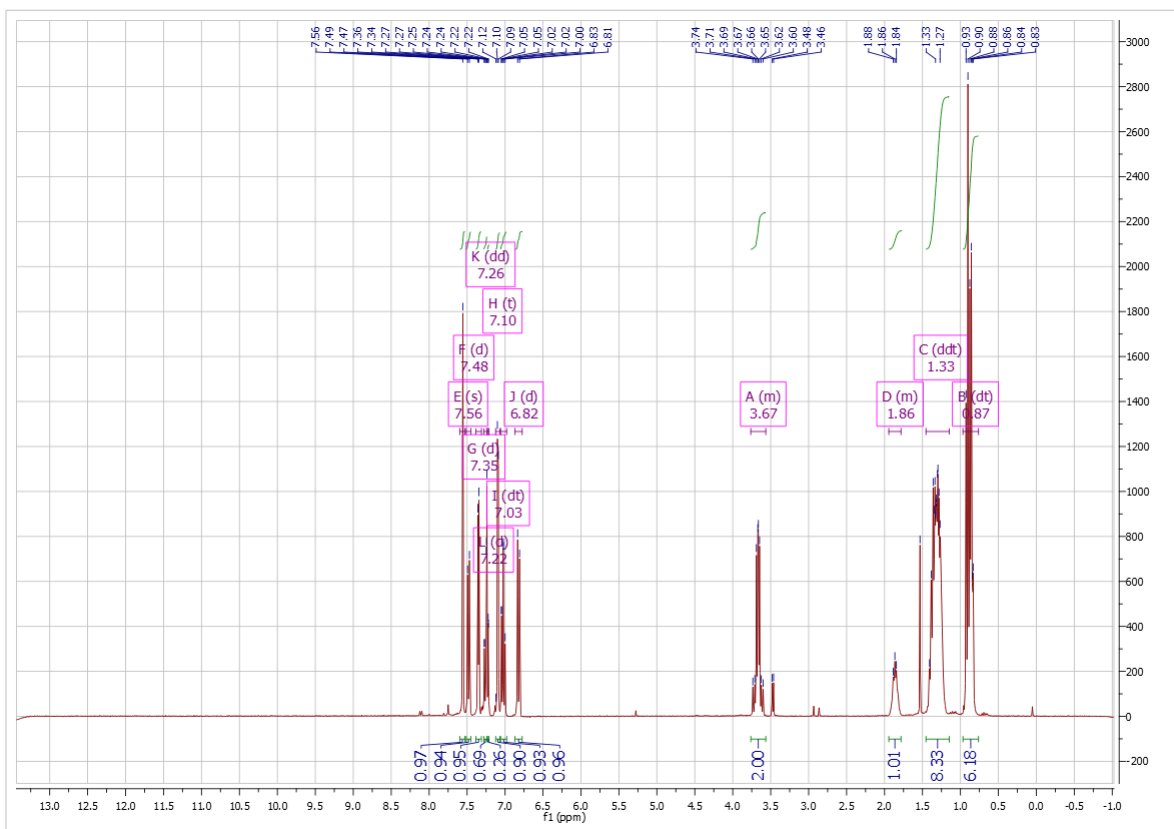
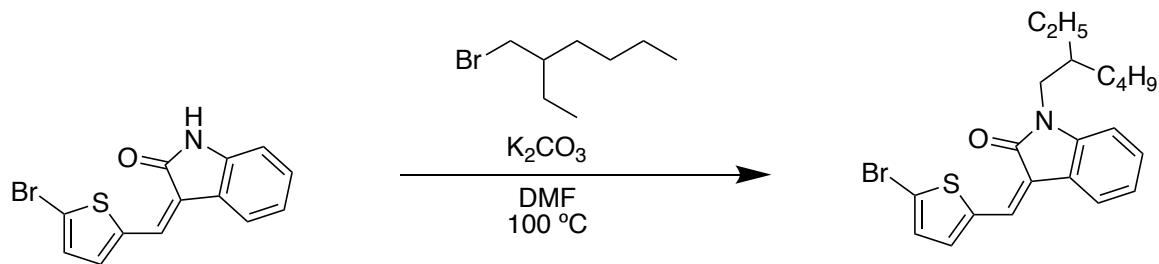
Appendix A-15: 300 MHz ¹H NMR Spectrum of 2,2',3,3'-tetrahydro-5,5'-bithieno[3,4-*b*][1,4]dioxine (BEDOT) in chloroform-*d*



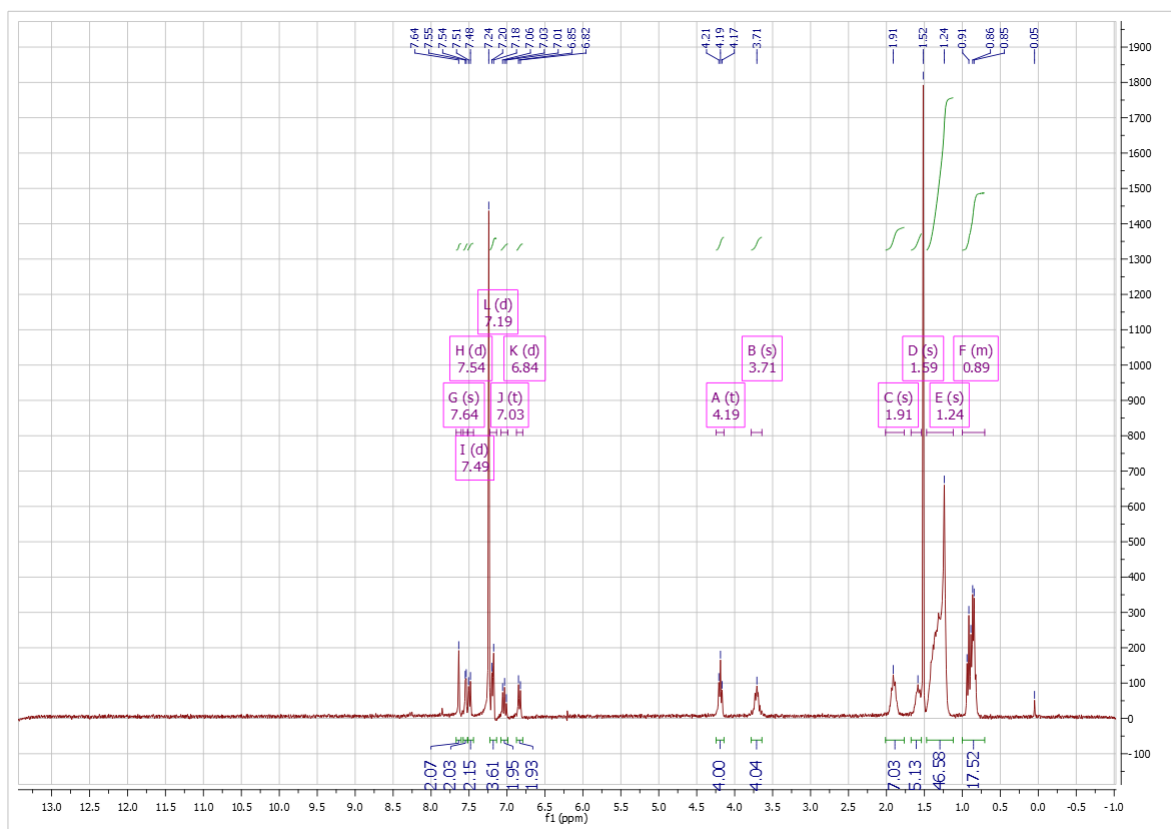
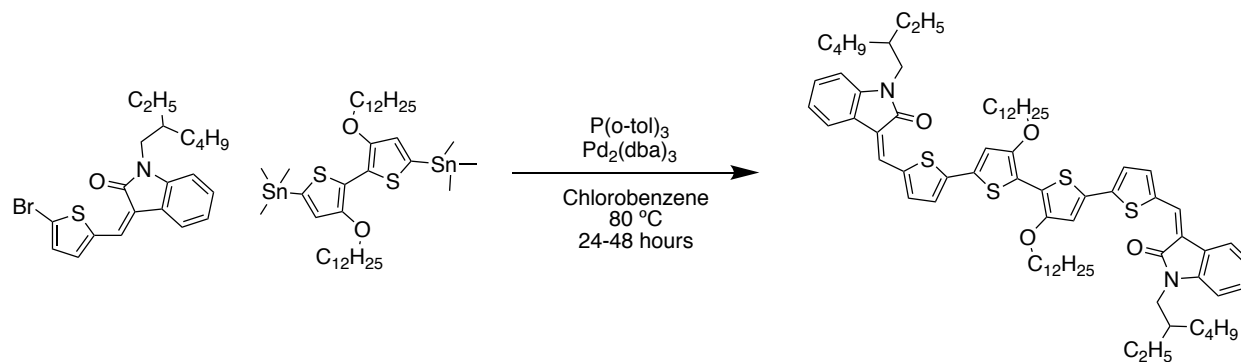
Appendix A-16: 300 MHz ^1H NMR Spectrum of bis(2-ethylhexyl) 3,3'-((2,2',3,3'-tetrahydro-[5,5'-bithieno[3,4-b][1,4]dioxine)-7,7'-diyl)bis(methanelylidene))-bis(2-oxindoline-1-carboxylate) (OG-D1) in chloroform-*d*



Appendix A-17: 300 MHz ^1H NMR Spectrum of 3-((5-bromothiophen-2-yl)methylene)indolin-2-one (TEI-2-Br) in dimethyl sulfoxide- d_6



Appendix A-18: 300 MHz ¹H NMR Spectrum of (Z)-3-((5-bromothiophen-2-yl)methylene)-1-(2-ethylhexyl)indolin-2-one (TEI-2-Br-EH) in chloroform-*d*



Appendix A-19: 300 MHz ^1H NMR Spectrum of 3,3'-((3'',4'-bis(dodecyloxy)-[2,2':5',2'':5'',2'''-quaterthiophene]-5,5'''-diyl)bis(methanelylidene))bis(1-(2-ethylhexyl)indolin-2-one) (OG3) in chloroform-*d*